UNIVERSIDAD DE COSTA RICA
SISTEMA DE ESTUDIOS DE POSGRADO

ESTUDIO DE COHERENCIA Y TRANSPORTE CUÁNTICOS EN LAS DINÁMICAS ENERGÉTICAS DURANTE LA CAPTACIÓN DE ENERGÍA LUMÍNICA EN SISTEMAS FOTOSINTÉTICOS

Tesis sometida a la consideración de la Comisión del Programa de Estudios de Posgrado en Química para optar al grado y título de Maestría Académica en Química

ROBERTO ANDRÉS GONZÁLEZ LEÓN

Ciudad Universitaria Rodrigo Facio, Costa Rica

2022

Dedicatoria

A mi madre Marjorie, y a mi padre Roberto: que sin su apoyo incondicional no habría llegado hasta donde estoy.

A mis hermanos, Kari y Fer, por su compañía, por su confidencia, y por siempre demostrarme cada día que hay que luchar por lo que se quiere.

Agradecimientos

En primera instancia, quiero agradecer a mi director, el profesor Cristopher Camacho. Fue un privilegio trabajar a su lado, y gracias a su paciencia y guía logré realizar este trabajo. Ha sido de gran importancia en mi crecimiento académico y profesional. Le agradezco profundamente por siempre creer en mí y en mi trabajo. A mis lectores, los profesores Mauricio Gutiérrez y Julio Mata, les agradezco su valioso tiempo dedicado a este trabajo y por sus comentarios al respecto. También quiero agradecer a la Vicerrectoría de Investigación, cuyo apoyo económico a través del Proyecto 115-B9461 fue indispensable para la realización de este proyecto.

Gran parte de esta investigación involucró gran cantidad de conocimientos previos que fueron no obtenidos durante mi bachillerato, por lo que gran parte del tiempo de realización consistió en el aprendizaje de estos contenidos y técnicas. En estos esfuerzos, mi pasantía a la Universidad de Ulm fue fundamental. Agradezco al Sistema de Estudios de Posgrado por el financiamiento otorgado para esta pasantía, sobretodo considerando la situación extraordinaria causada por la pandemia de COVID19. Deseo agradecer profundamente a los profesores Martin Plenio y Susana Huelga, quienes me acogieron en el grupo de Control de Dinámicas Cuánticas, al profesor Felipe Caycedo por guiarme al navegar en este fascinante mundo de la Biología Cuántica. Además, quiero agradecer a la Dra. Gerlinde Walliser, secretaria del Centro de Biociencias Cuánticas, cuya colaboración fue indispensable en mi estancia en Ulm.

Deseo agradecer especialmente a mi compañero y confidente Pedro Calderón, quien siempre estuvo presente brindándome su apoyo, su compañía. Sin él, no estaría donde estoy ahora. Finalmente, le agradezco a mi familia, les agradezco por estar siempre a mi lado, por su apoyo incondicional en todas las etapas de este proceso.

"Esta tesis fue aceptada por la Comisión del Programa de Estudios de Posgrado en Química de la Universidad de Costa Rica, como requisito parcial para optar al grado y título de Maestría Académica en Química"

Dr. Federico Muñoz Rojas
Representante de la Decana
Sistema de Estudios de Posgrado

Dr. Cristopher Camacho Leandro
Profesor Guía

Dr. Mauricio Gutiérrez Arguedas
Lector

Dr. Julio Mata Segreda
Lector

Dr. Érick Castellón Elizondo
Representante del Director
Programa de Posgrado en Química

Roberto Andrés González León
Sustentante

Contents

Resumen

La fotosíntesis es uno de los procesos biológicos más ampliamente estudiados en la historia. Su capacidad para fijar carbono en moléculas nutritivas es la base de toda cadena trófica, y su eficiente explotación de la energía solar inspira aplicaciones como las celdas solares o la síntesis de compuestos de importancia biológica.

Durante los primeros milisegundos de la fotosíntesis, la luz solar se absorbe y transfiere a un centro de reacción, donde provee de energía a la conversión de dióxido de carbono en carbohidratos y otras moléculas combustibles. La comprensión de las dinámicas energéticas en este procesos es esencial para el diseño de sistemas similares. En las últimas décadas, técnicas de espectroscopía electrónica ultrarápida y multidimensional han revelado la presencia de fenómenos cuánticos, como el transporte y la coherencia cuántica, durante el transporte de energía en la fotosíntesis; estos se sugieren que contribuyen a su eficiencia inusualmente alta. A pesar de que la presencia de fenómenos en complejos fotosintéticos puede ser investigada empíricamente, su aplicación es limitada debido a la dificultad de la técnica, alto precio de los equipos, análisis de datos complejo y poca aplicabilidad en muestras *in vivo*. En consecuencia, las técnicas *in silico* proveen una plataforma para el estudio de estos fenómeno sin estas limitaciones experimentales.

En este trabajo, se presenta el estudio de la presencia de coherencia y transporte cuánticos en un complejo proteína-pigmento a través de métodos completamente computacionales. Primeramente, se desarrolla y valida una metodología para el cálculo de parámetros espectroscópicos con alta exactitud. A partir de estos, se utilizan ecuaciones cuánticas maestras para obtener las dinámicas de transporte energético, para analizar fenómenos cuánticos y su prevalencia en aras de dilucidar mecanismos y factores que puedan extender su vida media.

Summary

The photosynthesis is one of the most studied biological processes through history. Its capacity to fix carbon into nutritional molecules is the base of all food chains. Its efficient exploitation of the solar energy inspires application such as solar cells, or synthesis of biologically important compounds.

During the first miliseconds of the photosynthesis, sunlight is harvested and transfered to a reaction center, were it powers the conversion of carbon dioxide into carbohydrates and other fuel molecules. The understanding of the dynamics in this process is essential for the design of similar systems. In the last decades, ultrafast multidimensional electronic spectroscopy techniques have revealed the presence of quantum phenomena, such as quantum coherence and transport, during the energy transport in the photosynthesis, which are suggested to contribute to its unusually large efficiency.

Although the presence of quantum phenomena in photosynthetic complexes can be probed empirically, its application is limited by the technique difficulty, highly expensive equipment, complex data analysis and its low transferability to *in vivo* samples. As such, *in silico* techniques provide a platform to study these phenomena without this experimental limitations.

In this work, the study of the presence of quantum coherence and quantum transport in a protein-pigment complex is presented through fully computational methods. First, a methodology is developed and validated for the calculation of highly accurate spectroscopical parameters of the complex. From these, quantum master equations are used to obtain the dynamics of the excitation energy transport, and probe for the quantum effects and its prevalence, in order to elucidate mechanisms and factors that may extend their lifetime.

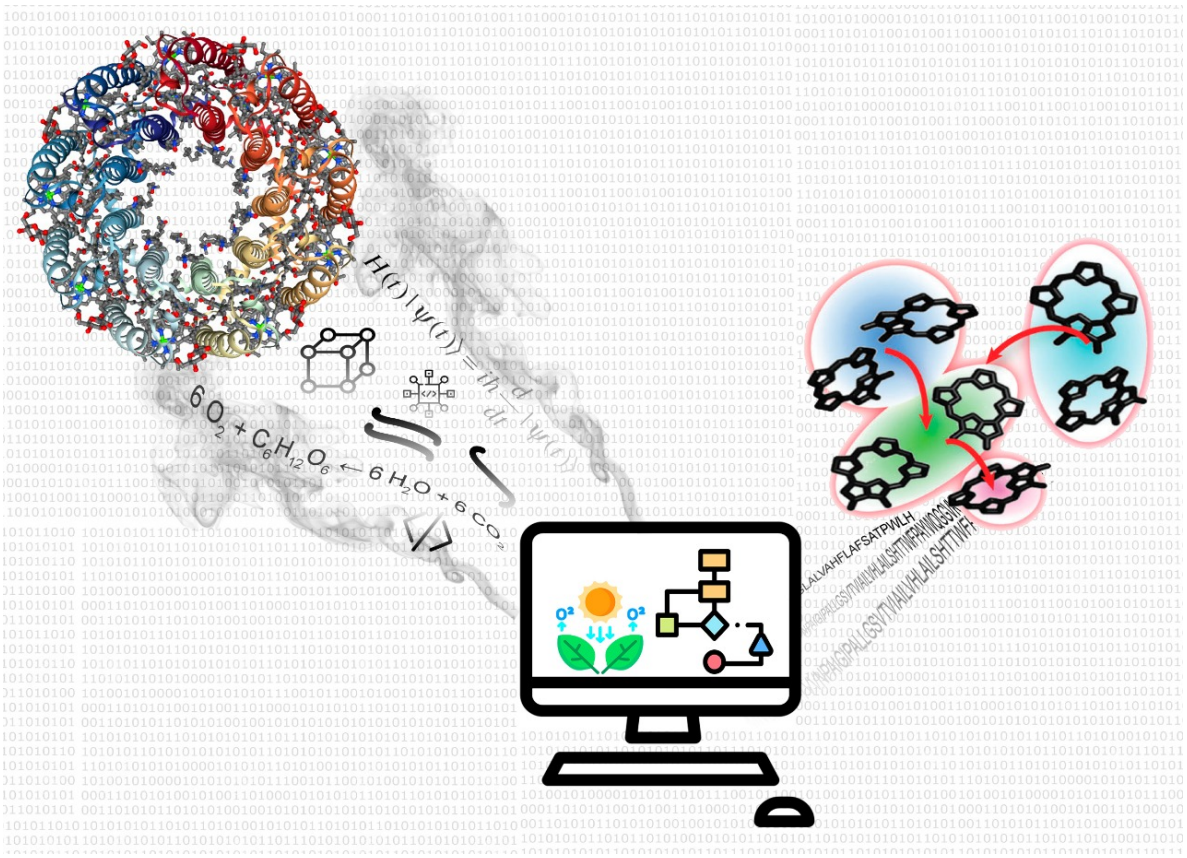

Figure 1: Graphical abstract of the thesis project.

List of Tables

List of Figures

List of Abbreviations

2DES	Two-dimensional Electronic Spectroscopy
AO	Atomic Orbitals
BChl a/b/c/d/e	Bacteriochlorophyll a/b/c/d/e
bil	Bilin
car	Carotenoid
c.c.	Complex Conjugate
CC	Coupled-Cluster
CCSD	Coupled-Cluster Singles and Doubles
CHELP-BOW	Boltzmann-weighted Charges from Electrostatic Potential
Chl a/b/c1/c2/d/e	Chlorophyll a/b/c1/c2/d/e
Chl a – OH	13'2-hydroxyl-chlorophyll a
CT	Charge Transfer
Δ-FLN	Difference Fluorescence Line-Narrowing Spectroscopy
D3BJ	DFTD3 dispersion correction with Becke-Johnson Damping
DFT	Density Functional Theory
DFTB	Density Functional Theory Tight Binding
DLPNO	Domain-based Local Pair Natural Orbital
DMRG	Density Matrix Renormalization Group
EET	Excitation Energy Transfer

EOM	Equation of Motion
FCP	Fucoxanthin and Chlorophyll a/c Polypeptide
FFT	Fast Fourier Transform
FMO	Fenna-Matthews-Olson complex
FTD	Fragment Transition Density
FWMH	Full Width Mid-Height
GGA	Generalized Gradient Approximation
h.c.	Hermitian conjugate
HEOM	Hierarchical Equations of Motion
HF	Hartree-Fock
HRF	Huang-Rhys Factor
ISC	Intersystem crossing
KS	Kohn-Sham
LH1/2	Light-harvesting Complex 1/2 of Purple Bacteria
LHC	Light-harvesting Complex
LHCSR	Stress Related Light-harvesting Complex
LHS	Left Hand Side
MD	Molecular Dynamics
MM	Molecular Mechanics
MMpol	Polarizable Molecular Mechanics
MO	Molecular Orbital
NRMSE	Normalized Root-Mean Squared Error
ODE	Ordinary Differential Equation
PBP	Phycobiliprotein
PBS	Phycobilisome

PCP	Peridinin-chlorophyll Protein
PDA	Point-Dipole Approximation
PDB	Protein Data Bank
PDB ID	Identification Code in the Protein Data Bank
PDE	Partial Differential Equation
PPC	Pigment-Protein Complex
PPP	Pariser-Parr-Pople method
PSI	Photosystem I
PSII	Photosystem II
QC	Quantum Chemical
QM	Quantum Mechanical
QME	Quantum Master Equation
RDM	Reduced Density Matrix
RHS	Right Hand Side
RMSD	Root-Mean Squared Distance
RMSE	Root-Mean Squared Error
RS	Range Separated
RSD	Relative Standard Deviation
SCF	Self Consistent Field
SEET	Singlet Excitation Energy Transfer
STEOM	Second similarity Transformation Equation of Motion
T-TEDOPA	Finite Temperature Time-Evolving Density Operator with Orthogonal Polynomials
TD-DFT	Time-dependent Density Functional Theory
TD-DFTB	Time-dependent Density Functional Theory Tight Binding
TD-DMRG	Time-dependent Density Matrix Renormalization Group

TDA	Tamm-Dancoff Approximation
TDFI	Transition Density Fragment Interaction
TEDOPA	Time-Evolving Density Operator with Orthogonal Polynomials
TEET	Triplet Excitation Energy Transfer
TLS	Two-level System
TMA	Transition Monopole Approximation
TrEsp	Transition Charges from Electrostatic Potential
UV	Ultraviolet
VCP	Violaxanthin-chlorophyll Protein
WSCP	Water Soluble Chlorophyll-Binding Protein
XLH	*Xanthonema* Light-harvesting Complex
ZDO	Zero Differential Overlap
ZINDO	Zerner's Intermediate Neglect of Differential Overlap

UNIVERSIDAD DE COSTA RICA

SEP Sistema de Estudios de Posgrado

Autorización para digitalización y comunicación pública de Trabajos Finales de Graduación del Sistema de Estudios de Posgrado en el Repositorio Institucional de la Universidad de Costa Rica.

Yo, Roberto Andrés González León, con cédula de identidad 116080532, en mi condición de autor del TFG titulado Estudio de coherencia y transporte Cuánticos en las dinámicas energéticas durante la captación de energía lumínica en sistemas fotosintéticos

Autorizo a la Universidad de Costa Rica para digitalizar y hacer divulgación pública de forma gratuita de dicho TFG a través del Repositorio Institucional u otro medio electrónico, para ser puesto a disposición del público según lo que establezca el Sistema de Estudios de Posgrado. **SI** [X] **NO** *[ ]

***En caso de la negativa favor indicar el tiempo de restricción: _____ año (s).**

Este Trabajo Final de Graduación será publicado en formato PDF, o en el formato que en el momento se establezca, de tal forma que el acceso al mismo sea libre, con el fin de permitir la consulta e impresión, pero no su modificación.

Manifiesto que mi Trabajo Final de Graduación fue debidamente subido al sistema digital Kerwá y su contenido corresponde al documento original que sirvió para la obtención de mi título, y que su información no infringe ni violenta ningún derecho a terceros. El TFG además cuenta con el visto bueno de mi Director (a) de Tesis o Tutor (a) y cumplió con lo establecido en la revisión del Formato por parte del Sistema de Estudios de Posgrado.

FIRMA ESTUDIANTE

Nota: El presente documento constituye una declaración jurada, cuyos alcances aseguran a la Universidad, que su contenido sea tomado como cierto. Su importancia radica en que permite abreviar procedimientos administrativos, y al mismo tiempo genera una responsabilidad legal para que quien declare contrario a la verdad de lo que manifiesta, puede como consecuencia, enfrentar un proceso penal por delito de perjurio, tipificado en el artículo 318 de nuestro Código Penal. Lo anterior implica que el estudiante se vea forzado a realizar su mayor esfuerzo para que no sólo incluya información veraz en la Licencia de Publicación, sino que también realice diligentemente la gestión de subir el documento correcto en la plataforma digital Kerwá.

Chapter 1

Introduction

From the birth of Quantum Mechanics (QM) and its experimental studies, one of the premises is that quantum phenomena such as coherence and entanglement cannot have any big relevance in biological processes, owed to their complexity and sources of decoherence, which often escape rigourous mathematical description (Lambert et al., 2013). However, with the development of more powerful tools, modeling constantly bigger biological systems from a physical perspective have been successful. One of the more famous examples is the prediction of DNA properties from purely physical principles by Erwin Schrödinger (1992).

Moreover, the question of the existence of organisms that incorporate quantum phenomena in its functional mechanism, to provide to competitive advantage or process control, remains open and evasive. Quantum Biology emerges from this question, and from its postulation, there have been proposals and tests for different quantum mechanisms to explain the dynamics of several biological process such as photosynthesis, olfaction, vision, proton transfer, enzyme activity and biogeomagnetism (Mohseni et al., 2014; Lambert et al., 2012; Fleming et al., 2011).

Studying the biological process from this perspective can give better insight on previously unknown or unexplained mechanisms, limited by only considering classical analysis. It can also give information of how QM states and dynamics interplay to result in macroscopical highly complex systems.

1.1 Light-Harvesting in Photosynthesis

Photosynthesis is one of most studied biological processes. Using this process, organisms like bacteria, algae and plants, convert solar energy into chemical energy, producing approximately 105 billion tons of biomass anually in the whole planet (B. Green & Parson, 2003). This biomass is the base of all food chains, therefore, the photosynthesis is considered as the base of all life.

The diversity of photoautrotophic organisms is very wide: around 350 000 species of photosynthetic organisms have been described (Sage & Stata, 2015) distributed along Bacteria and Eukarya dominions; the Archaea dominion is excluded, because there are

no known species of archaeas that fix carbon using photosynthetic mechanisms (Bryant & Frigaard, 2006). This diversity is illustrated in Fig. 1.1. Every species present different machinery to explot sunlight, because each has evolved to incorporate certain characteristics and tune their mecanisms to account for the effects of temperature, humidity, precipitation, insolation and even topography (Blankenship, 2010).

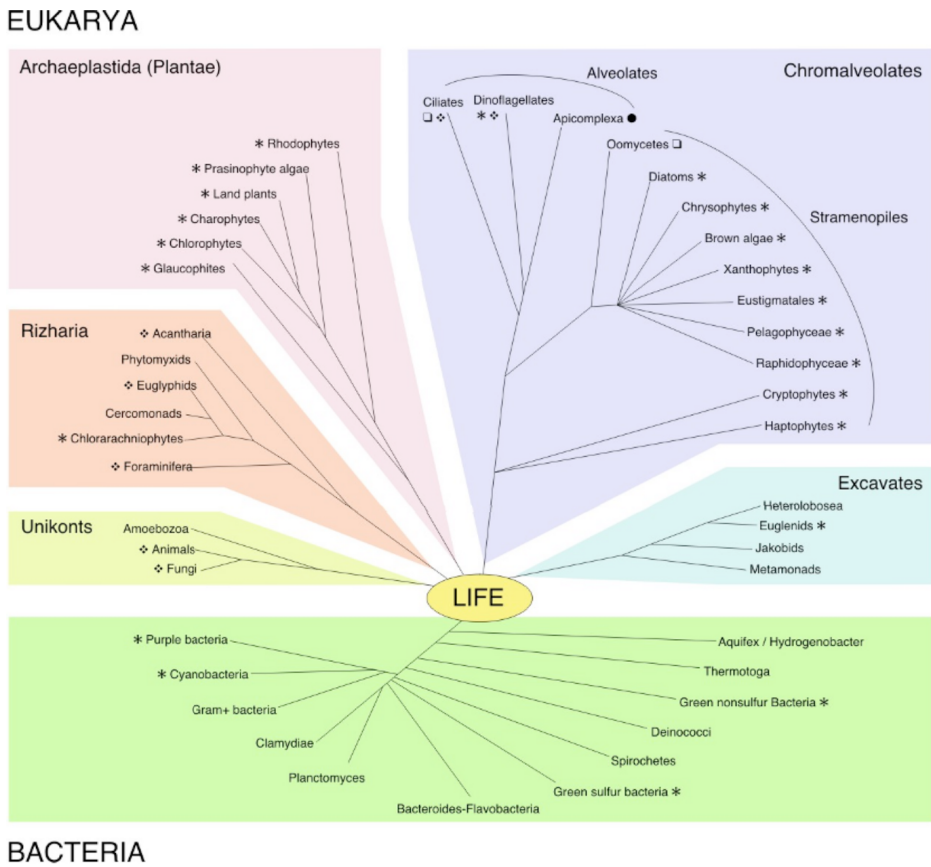

Figure 1.1: Evolutionary tree at class and clade level for the Eukarya and Bacteria dominions. Taken from Collini et al. (2009). The tree annotations indicate the photosynthetic function distributions along groups: $*$ represents organisms with known photosynthetic functions, $\bullet$ organisms with apicoplasts but without photosynthesis-related genes, $\square$ algae species with photosynthetic symbionts or sequestered plastids, ❖ organisms that do not present any plastid but with genes that potentially codify for the photosynthetic proteins.

Photosyntesis convert solar energy and stores it into organic molecules that fuel other metabolic functions, such as cellular respiration. The photosynthesis reaction is, in its most general form (Niel, 1932):

$$CO_2 + 2\,AH_2 \longrightarrow CH_2O + H_2O + 2\,A$$

where AH_2 represents an electron donor in its reduced form, and A its oxidated form. The electron donor varies depending on the photosynthetic species in question, corresponding to water in the oxygenic mechanisms, and other substances such as hydrogen sulfide, sulfite, succinate, lactate, iron(II) (Bryant & Frigaard, 2006) or arsenite (Kulp et al., 2008) in anoxygenic mechanisms.

The photosynthesis process can be summarized into 2 steps: the light-dependent reactions and the light-independent reactions. During the light-dependent phase, initially the light is absorbed by a protein complex incrustrated in the photosynthetic membrane of a plastid. This complex includes pigments: chromophoric molecules that have an electronic structure in some region that allows it to absorb light and store it momentarily in a quasiparticle called exciton. The exciton is transported quickly through an efficient excitonic transport (EET) chain to the reaction center (RC). In the RC, the excitonic energy is used to produce a charge separation reaction between two neighbouring pigments or a pigment and a nearby residue, this captures the light energy from the exciton in a pair of two stable total charges. Both charges are transported by the photosynthetic membrane by following electron transport reactions to produce adenosine triphosphate (ATP) and a reductor, which then enter the light-independent reactions to fix the carbon from CO_2 into fuel molecules (Cogdell et al., 2008; van Amerongen et al., 2000).

The first step of the light-dependent reactions is of interest here, since the EET chains to RC can have quantum efficiencies particularly high, of 95% to even almost 100% (van Amerongen et al., 2000). Compared to other light transmission devices, such as fiber optics, the maximum efficiency of visible light transmission is 92% for coherent and polarized sources and transparent media (Mollers et al., 2009).

To explain this extremely high efficiency of harvest and light transport in natural (wet, complex and non-ideal) conditions, mechanisms including quantum coherence and entanglement have been proposed, in which the energy levels of the chromophores superpose, and efficient transport routes are built in a quantum walk mechanism (Hildner et al., 2013). In contrast, classical theories propose incoherent energy jumps, which would imply energy loss with each jump.

The presence of quantum coherence in photosynthetic complexes was demonstrated for the first time by Engel et al. (2007) using two-dimensional electronic spectroscopy (2DES) at 77 K in the bacteriochlorophyll Fenna-Matthews-Olson complex (FMO) isolated from *Chlorobaculum tepidum*. This new perspective has lead to multiple studies focusing on getting insight on the importance of quantum coherence in improving photosynthetic efficiencies (H. Lee et al., 2009), their prevalence in physiological conditions (Panitchayangkoon et al., 2010) and across the tree of life (Collini, 2012).

1.1.1 Light-Harvesting Complexes

In the first part of the photosynthesis, the energy from sunlight is captured by the photosynthetic membrane, then, this energy is transported to the RC. This job is done by protein complexes called light-harvesting complexes (LHCs). An array of LHCs is an antenna complex, which are synthetized to improve the light-harvesting in the available power spectrum, while also increasing the harvesting sites, and the probability of light absorption and transport without heat relaxation, even in a diffuse source such as sunlight. The diversity of these designs are show in Fig. 1.2.

The LHCs are made of proteins and pigment molecules that absorb sunlight through excitations of their chromophoric groups. This pigments are called "photosynthetic pigments" or "accessory pigments", however, the latter can be missinterpreted, as the role of harvesting or photoprotection of these pigments are vital for the EET (Collini, 2019). In general, they are also called "chromophores" of the LHC. The diversity of LHCs in Nature is vast, considering type, organization and amount of chromophores. Also, LHCs can assemble in complex quaternary structures, denominated "photosynthetic supercomplexes"; they can include different types of LHCs, RCs, and other subunits for photoprotection, electronic transport, among others. Also, in some species, the subunits can form a LHC by themselves (Collini et al., 2009).

Comparing the macrostructures of the protein complexes, almost no similar characteristics are conserved across different types (Cogdell et al., 2008), for example, the LH2 complex present in purple bacteria, is a modular nonamer of apoproteins organized in a ring structure; carotenoids and bacteriochlorophylls function as chromophores and

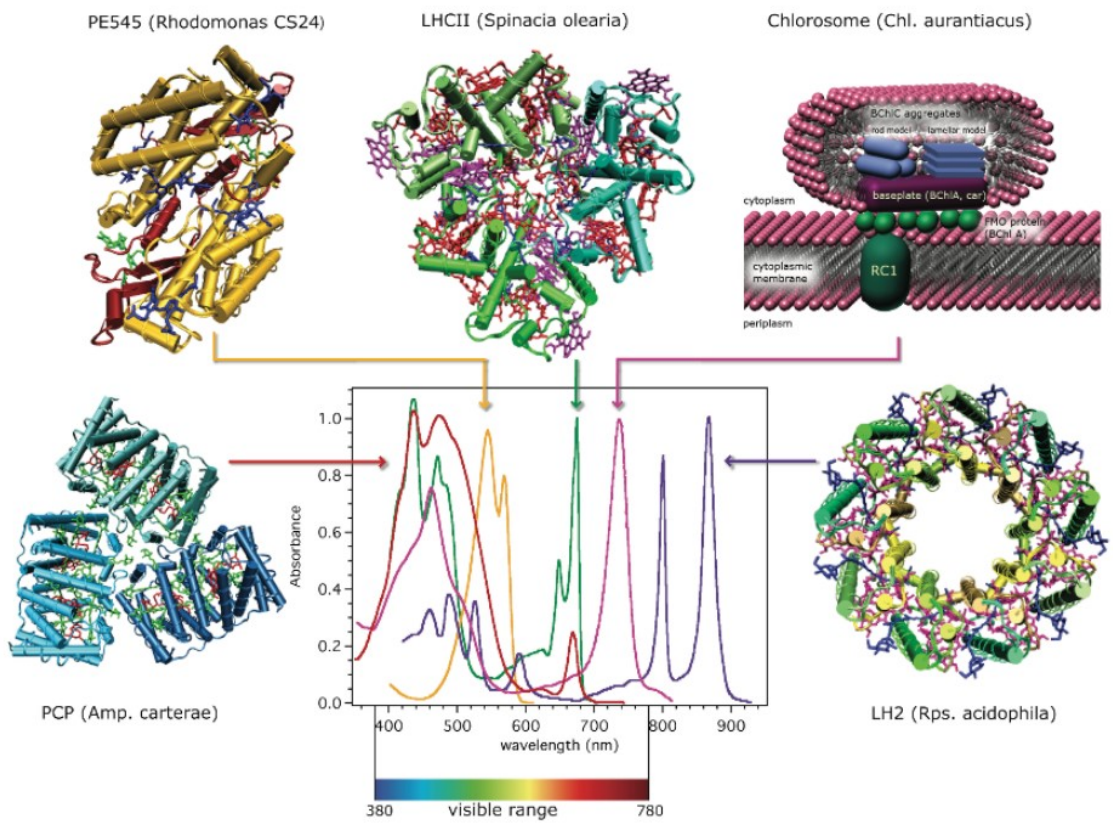

Figure 1.2: Absorption spectra and structure of some representative LHCs at 77 K. Taken from Collini et al. (2009). In parenthesis, the name of the species from which the corresponding structure shown.

are organized by non-covalent interactions inside the monomers (Prince et al., 1997). However, the photosystem II (PSII) of higher plants has a very complex structure, composed by an heterodimer with multiple LHC subunits with different structures, and also electron transport units, RCs, photoprotective units, and others, which can also shift slightly in position depending on the stage (Kern et al., 2018). This diversity is summarized in table 1.1.

Table 1.1: Types of light-harvesting complexes and supercomplexes and their pigments.

LHC Type	Pigments	Reference
B808-865 Complex	BChl a/c + car	Olson et al. (2007) Klappenbach & Pierson (2004)

Table 1.1: Types of light-harvesting complexes and supercomplexes and their pigments. Continued.

LHC Type	Pigments	Reference
Chromophyte chlorophyll a/c-binding LHC (Chl a/c-LHC)	Chl a/c2 + car + bil	Graham & Wilcox (2000) B. R. Green & Durnford (1996)
Chlorosome	BChl a/c/d/e + car	Orf & Blankenship (2013)
Photosystem I (PSI)	Chl a + car	Jordan et al. (2001)
Photosystem II (PSII)	Chl a/b + car	Loll et al. (2005)
Chlorophyll-binding LHC I of higher plants (LHCI)	Chl a/b/d + car + bil	Liu et al. (2004)
Chlorophyll-binding LHC II of higher plants (LHCII)	Chl a/b + car	Drop et al. (2014)
Subunits of the PSII-LHCII (CP24, CP26, CP29, CP43, CP47)	Chl a/b + car	Barera et al. (2012) Bassi et al. (1997)
Fucoxanthin and chlorophyll a/c polypeptide (FCP)	Chl a/c/c1,c2 + car	Graham & Wilcox (2000) Passaquet et al. (1991)
Fenna-Mathews-Olson (FMO) Complex	BChl a/d/e + car	Camara-Artigas et al. (2003)
RC-binding LHC1 of purple bacteria (LH1-RC)	BChl a/b + car	Roszak (2003) Hoogewerf et al. (2003)
LHC2 of purple bacteria (LH2)	BChl a/b + car	Papiz et al. (2003) Cogdell et al. (1996)
Stress Related LHC (LHCSR)	Car	Bailleul et al. (2010) Peers et al. (2009)
Phycobiliprotein (PBP)	Chl a/c2 + car + bil	Kieselbach et al. (2018) Kannaujiya et al. (2017)

Table 1.1: Types of light-harvesting complexes and supercomplexes and their pigments. Continued.

LHC Type	Pigments	Reference
Phycobilisome (PBS)	Chl a/b/c/d + car + bil	Marx & Adir (2013) Gantt (1996)
Peridinin-chlorophyll Protein (PCP)	Chl a/c2 + car	Hiller et al. (1993)
Violaxanthin-chlorophyll Protein (VCP)	Chl a + car	Bína et al. (2014) Wolf et al. (2018)
Xanthonema LHC (XLH)	Chl a + car	Streckaite et al. (2018) Durchan et al. (2012)

Notation: *Chl* = chlorophyll, *BChl* = bacteriochlorophyll, *car* = carotenoid, *bil* = bilin.

During light-harvesting, there exists a competition between several possible destinies of the energy (Fassioli et al., 2013):

1. It can be relaxed through internal conversions and disperse as heat
2. It can be relaxed by photon emission
3. It can be transmitted to another molecule and continue the EET

The competition between these processes occurs in the femtosecond scale, completing the EET process in scales of $0.1 - 10$ ns (Mullineaux et al., 1993; Geacintov et al., 1986) with reported quantum efficiencies for the PSII LHCs of higher plants between 84 and 90%, from light-harvesting to the charge separation in the RC (Wientjes et al., 2013).

The photosynthetic pigments are embedded in a protein scaffold, in which the pigments and cofactors are arranged in precised positions to optimize the EET. Pigments like chlorophyll show almost total self-quenching at concentrations greater than 0.1 mol L^{-1} in solution; however, in LHCs like PSI and PSII, the concentrations are as a high as 0.5 mol L^{-1}, and almost no self-quenching is observed (Beddard & Porter,

1976). Also, the energy transfer is extremely dependent on the distance and interaction between chromophores (Scholes & Ghiggino, 1994). In some cases, the chromophore-protein interaction causes shifting in the absorption spectra of the chromophore, important in the optimization of the absorption probability of the photon, as is the case for BChl a of *Rhodobacter sphaeroides* (Fowler et al., 1992).

Thus, the arrangement of the chromophores inside the LHC is dense, which leads to strong Coulombic interactions (between 10 and 300 cm^{-1} for the LHCII according to Frähmcke & Walla (2006)) that result in an ultrafast EET, and the emergence of quantum phernomena such as quantum coherence and quantum entanglement (Schlau-Cohen et al., 2012).

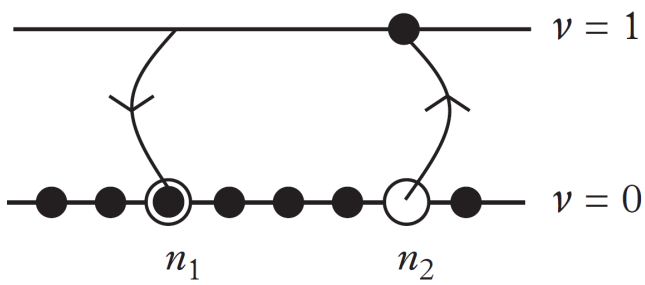

Figure 1.3: Schematic diagram of a Frenkel exciton transport between different sites through a crystal. Each site is shown with its ground ($\nu = 0$) and first excited ($\nu = 1$) states. Taken from Combescot & Shiau (2016).

Because its high density packing inside the LHCs, a solid-state approach is valid, in particular, the excitations in the LHC can be modelled as excitations in a solid crystal. Considering this, the excitation of an electron leaves a positive hole in the ground state, and a bound state between the excited electron and the hole is formed, this is called an exciton, and can even be seen as a quasiparticle. If the exciton is highly localized to a chromophore, the Frenkel exciton model is valid (Frenkel, 1931). Frenkel excitons appear when the spatial extension of the molecular orbitals (MOs) is small compared to the unit cell size, as in organic crystals. In this limit, the crystal can be seen as a set of individual atoms positioned at the crystal lattice nodes, and, therefore, suffer atomic excitations localized around their equilibrium position. Excitons come from the promotion of an electron to an excited state with different position than the ground

state, leaving a hole in their original position; the hole and the electron are bound together by their Coulombic interaction. As Frenkel excitons are highly localized around their origin, they can rapidly recombine by thermal or radiative decay; however, they can jump to other sites if there exist additional Coulombic interaction with them, effectively delocalizing. Following the diagram in Fig. 1.3, the simplest mechanism for exciton transport is the relaxation of the excited electron in the $1 \rightarrow 0$ direction at site n_1, while simultaneously another electron excites at site n_2 in the $0 \rightarrow 1$ (Combescot & Shiau, 2016). In general, these excitations and relaxations can happen at any site and to any excited state, therefore, their complete description is complex.

In LHCs, the pigments are tightly embedded on the protein scaffold, thus, the "organic crystal approach" is valid. However, deviations from this model have to be evaluated, for example, chromophores in LHCs are multiatomic molecules (around 150 atoms per pigment) with complex structures themselves. Also, by considering each pigment a site, the "lattice" is also not symmetrical, and the relative orientation of pigments have to be evaluated. These deviations make the description of the LHC chromophoric aggregate complicated, and robust, high level Quantum Chemical methods are needed to accurately describe their behaviour and the EET phenomena.

1.2 Optical Spectroscopy of PPCs

The optical spectroscopy of PPCs results from the interaction of light with a chromophoric aggregate. Given the rigidity of the protein scaffold, this considers a solid matrix with embedded pigments which interacts with a light beam. The excitation generates an exciton: a bosonic quasiparticle formed between an electron and a hole bound by electrostatic and exchange interactions. Excitons can transfer energy without transporting electric charge; and can be classified given their spatial extent compared to the lattice.

1.2.1 The Frenkel Exciton Model

A chromophoric aggregate consists of a set of N molecules bound by non–covalent interactiones in such a spatial array that their electronic states interact with each other. The chromophores can, in general, be any type of molecule, however, to be considered "pigments" they should be susceptible to electronic optical absorption by UV/Vis light; thus, the probability of absorption sholud be high in those regions. For solar cell applications, the optical absorption spectrum of the pigment should be similar to the one of the Sun at Earth's surface. In photosynthesic complexes, their pigments and their spatial distributions have evolved to harvest the available light in their corresponding habitat.

The excitons in a chromophoric aggregate are bound to a PPC unit, therefore their spatial extent is much smaller than the lattice parameter; these are called Frenkel excitons, and are localized to one or a few pigments at any given time (Frenkel, 1931).

The total aggregate hamiltonian can be written in terms of the molecular hamiltonians $\hat{H}_n$ and the intermolecular Coulombic interactions $\hat{V}_{mn}$, this takes the form (May & Kühn, 2011),

$$\hat{H}_{\text{agg}} = \sum_n \hat{H}_n + \frac{1}{2}\sum_{m,n} \hat{V}_{mn} \tag{1.2.1}$$

Introducing the interacting electronic states of the molecule n, $|\phi_{na}\rangle$ y $|\phi_{nb}\rangle$, then the hamiltonian matrix elements $H_n(ab)$ and the Coulomb matrix elements $J_{mn}(ab, cd)$ are given by,

$$H_n(ab) = \langle\phi_{na}|\,\hat{H}_n\,|\phi_{nb}\rangle \tag{1.2.2}$$

$$J_{mn}(ab, cd) = \langle\phi_{ma}\phi_{nb}|\,\hat{V}_{mn}\,|\phi_{nc}\phi_{md}\rangle \tag{1.2.3}$$

sustituting in (1.2.1),

$$\hat{H}_{\text{agg}} = \sum_n \sum_{a,b} H_n(ab)\,|\phi_{na}\rangle\langle\phi_{nb}| + \frac{1}{2}\sum_{m,n}\sum_{a,b,c,d} J_{mn}(ab, cd)\,|\phi_{ma}\phi_{nb}\rangle\langle\phi_{nc}\phi_{md}| \tag{1.2.4}$$

In natural environments, specially for photosynthetic microorganisms in low insolation habitats, many photosynthetic complexes only sustain one excitation at a time (Blankenship, 2014). Thus, each molecule can be treated as a two-level system (Fig. 1.4) and the Hilbert space of the aggregate quantum states $\mathcal{H}$ is restricted to the subspaces of zero excitations ($\mathcal{H}_0$) and one excitation ($\mathcal{H}_1$), so that $\mathcal{H} = \mathcal{H}_0 \otimes \mathcal{H}_1$.

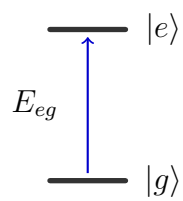

Figure 1.4: Energy levels of a two-level system. The system excitation energy is shown as E_{eg}.

In this approximation, the states are $a = g, e$, where g refers to a ground state and e refers to a first excited state. Substituting,

$$\hat{H}_{\text{agg}} = \sum_{n} \sum_{a=g,e} H_{na} \left|\phi_{na}\right\rangle \left\langle\phi_{na}\right| + \sum_{m,n} J_{mn} \left|\phi_{me}\phi_{ng}\right\rangle \left\langle\phi_{ne}\phi_{mg}\right| \tag{1.2.5}$$

in the Born–Oppenheimer approximation, the nuclear coordinates are fixed at their equilibrium position, thus, the equilibrium potential energy E_{na} and the electronic part of the aggregate hamiltonian is given by,

$$\hat{H}^{(\text{el})}_{\text{agg}} = \sum_{n} \sum_{a=g,e} E_{na} \left|\phi_{na}\right\rangle \left\langle\phi_{na}\right| + \sum_{m,n} J_{mn} \left|\phi_{me}\phi_{ng}\right\rangle \left\langle\phi_{ne}\phi_{mg}\right| \tag{1.2.6}$$

Rearranging the electronic states, the site basis is introduced. In this base, $|n\rangle$ denotes the state where only the chromophore n is excited. Hence,

$$|n\rangle = |\phi_{ne}\rangle \prod_{n \neq m} |\phi_{mg}\rangle \tag{1.2.7}$$

also, the collective ground state of the aggregate is expressed as

$$|0\rangle = \prod_{n} |\phi_{ng}\rangle \tag{1.2.8}$$

In the site basis, equation (1.2.6) is written as,

$$\hat{H}_{\text{agg}} \approx \hat{H}^{(0)}_{\text{agg}} + \hat{H}^{(1)}_{\text{agg}} = E_0 \left|0\right\rangle \left\langle 0\right| + \sum_{m,n} H_{mn} \left|m\right\rangle \left\langle n\right| \tag{1.2.9}$$

the aggregate ground state energy is introduced as,

$$E_0 = \sum_n E_{ng} \tag{1.2.10}$$

The aggregate first excitation hamiltonian $\hat{H}^{(1)}_{\text{agg}}$ is expanded as,

$$\begin{aligned}
\hat{H}^{(1)}_{\text{agg}} &= \sum_{m,n} \left(\delta_{mn} E_0 + E_{mn}\right) \left|m\right\rangle \left\langle n\right| \\
&= \sum_{m,n} \left[\delta_{mn} E_0 + \left(\delta_{mn} E_n + \left(1 - \delta_{mn}\right) J_{mn}\right)\right] \left|m\right\rangle \left\langle n\right| \\
\hat{H}^{(1)}_{\text{agg}} &= \sum_n \left(E_0 + E_n\right) \left|n\right\rangle \left\langle n\right| + \sum_{m \neq n} J_{mn} \left|m\right\rangle \left\langle n\right|
\end{aligned} \tag{1.2.11}$$

thus, the site energy $E_n = E_{ne} - E_{ng}$ corresponds to the vertical excitation energy of first excited state of each chromophore; also called Franck–Condon transition energies. Finally, taking $E_0 = 0$, the aggregate hamiltonian is given by,

$$\hat{H}_{\text{agg}} \approx \hat{H}^{(1)}_{\text{agg}} = \sum_n E_n \left|n\right\rangle \left\langle n\right| + \sum_{m \neq n} J_{mn} \left|m\right\rangle \left\langle n\right| \tag{1.2.12}$$

notice that the hamiltonian on (1.2.12) is completely analogous to the Frenkel hamiltonian for excitations on atomic crystals (Combescot & Shiau, 2016).

The electronic states of the chromophores are combined to give new states, which represent the energy levels of the system that the excitations occupy. These excitations generate a bosonic quasiparticle, via the interaction between the excited electron and the hole it leaves on the ground state: this is called an exciton. The Frenkel excitons are created by interactions between the electronic states localized in the involved chromophores, and the delocalized by Coulombic and Dexter interactions (You & Hsu, 2014). The diagonalization of $\hat{H}_{\text{agg}}$ in (1.2.12) gives the excitonic energy levels depicted

in Fig. 1.5.

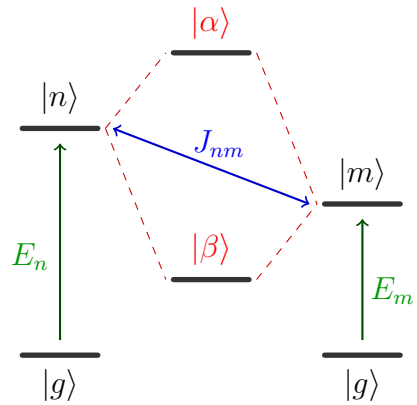

Figure 1.5: Excitonic levels for a two–level dimer. The spectroscopic parameters shown in the Frenkel hamiltonian model are: site energies E_n and E_m, and excitonic coupling J_{mn}.

The excitonic states $|\alpha\rangle$ are given by,

$$\hat{H}_{\text{ex}} |\alpha\rangle = E_\alpha |\alpha\rangle \tag{1.2.13}$$

where E_α are their corresponding energies. The states $|\alpha\rangle$ are expanded in the site basis as,

$$|\alpha\rangle = \sum_n c_\alpha^{(n)} |n\rangle \tag{1.2.14}$$

As $|\alpha\rangle$ are orthogonal, the excitonic hamiltonian satisfies that

$$\hat{H}_{\text{ex}} = \sum_\alpha E_\alpha |\alpha\rangle \langle\alpha| \tag{1.2.15}$$

and the exciton transition dipole moments $\vec{\mu}_\alpha$,

$$\vec{\mu}_\alpha = \sum_n c_\alpha^{(n)} \vec{\mu}_n \tag{1.2.16}$$

where $\vec{\mu}_n$ are the transition dipoles of the $S_0 \to S_1$ transitions of each chromophore.

1.2.2 Excitonic Couplings

The interexcitonic transfer coupling J_{ij} (also called simply "excitonic coupling") between two pigments (i, j) establishes the magnitude of interaction between the excitons E_i and E_j, fully localized at their respective sites. The excitonic coupling allows for the transfer of populations and energy between sites.

When a pigment-protein complex (PPC) interacts with light an excitation energy transfer (EET) process starts. This is a photophysical process in which the electronic excitation energy is transferred from a donor to an acceptor chromophore. This process usually starts with a chromophore being optically excited, then the exciton is subsequently transferred to a nearby site that has a non-null excitonic coupling. This process can happen between singlet or triplet states, which are dubbed SEET and TEET processes respectively (You & Hsu, 2014). SEET is the process involved in the light–harvesting and energy transport in photosynthetic chromophoric aggregates (Peterman et al., 1997). TEET is present in systems where relaxation via intersystem crossing (ISC) stabilizes a triplet state much faster than SEET transfer; this is present in the transfer between triplet oxygen and photoprotective pigments such as carotenoids (Cogdell & Frank, 1987).

Considering the Frenkel hamiltonian, the excitonic coupling is given by,

$$J_{ij} = \langle i | \hat{H}_{agg} | j \rangle \tag{1.2.17}$$

Using first–order perturbation theory in the SEET regimen, the contributions to the excitonic couplings are given by (You & Hsu, 2014),

$$J_{ij} = J_{ij}^{\text{Coul}} + J_{ij}^{\text{exch}} + J_{ij}^{\text{ovlp}} \tag{1.2.18}$$

where J_{ij}^{Coul} is the contribution of Coulombic interactions between electronic transitions; J_{ij}^{exch} is the exchange contribution, also called Dexter coupling, that accounts for the indistinguishability of electrons in the wavefunctions; and J_{ij}^{ovlp} comes from the orbital overlap between the donor and acceptor electron densities.

For an excitation from the ground state $|\Psi_g\rangle$ to the excited state $|\Psi_e\rangle$, the one–particle transition density matrix γ_{eg}^{T} can be expressed as (Curutchet & Mennucci, 2017),

$$\gamma_{eg}^{\mathrm{T}}(\boldsymbol{r},\boldsymbol{r}') = N\int\cdots\int \Psi_e^*(\boldsymbol{r},\boldsymbol{r}_2...\boldsymbol{r}_N)\,\Psi_g(\boldsymbol{r}',\boldsymbol{r}_2...\boldsymbol{r}_N)\,d\boldsymbol{r}_2 d\boldsymbol{r}_3\ldots d\boldsymbol{r}_N \tag{1.2.19}$$

the electron density associated with the electronic transition on a fixed site (transition density) ρ^{T} is given by the diagonal elements of γ_{eg}^{T},

$$\rho^{\mathrm{T}}(\boldsymbol{r}) = \gamma_{eg}^{\mathrm{T}}(\boldsymbol{r},\boldsymbol{r}) \tag{1.2.20}$$

The contributions in (1.2.18) can then be expressed in terms of γ_{eg}^{T} and ρ^{T} (You & Hsu, 2014):

$$J_{ij}^{\mathrm{Coul}} = \int d\boldsymbol{r}\int d\boldsymbol{r}'\rho_i^{\mathrm{T}*}(\boldsymbol{r})\frac{1}{|\boldsymbol{r}-\boldsymbol{r}'|}\rho_j^{\mathrm{T}}(\boldsymbol{r}') \tag{1.2.21}$$

$$J_{ij}^{\mathrm{exch}} = -\int d\boldsymbol{r}\int d\boldsymbol{r}'\gamma_i^{\mathrm{T}*}(\boldsymbol{r},\boldsymbol{r}')\frac{1}{|\boldsymbol{r}-\boldsymbol{r}'|}\gamma_j^{\mathrm{T}}(\boldsymbol{r},\boldsymbol{r}') \tag{1.2.22}$$

and J_{ij}^{ovlp} can be estimated from the overlap integrals, $S_{AB} = \langle\Psi_A\,|\,\Psi_B\rangle$.

1.2.2.1 Coulombic Contributions

It can be considered that in SEET processes generally the Coulombic contribution is much more important than the others, thus,

$$J_{ij} \approx J_{ij}^{\mathrm{Coul}} \tag{1.2.23}$$

In principle, any computational method that allows the calculation of the transition density can be used to directly evaluate the integrals in (1.2.21). However, their direct calculation is often very computationally expensive, therefore other methods are used to approximate them.

In the limit of weak coupling, and when the distance between sites is much bigger than the size of the chromophores, the coupling can be calculated from the interac-

tion between two electric point–dipoles. This is called the point–dipole approximation (PDA), and was proposed by Förster (1948) as part of his theory of EET to explain fluorescence phenomena, based on Fermi's golden rule.

Under PDA, the excitonic coupling is calculated as the energy between the transition dipole $\vec{\mu}_i$ in the electric field produced by another transition dipole $\vec{\mu}_j$, localized at their respective "chromophoric centers". The final expression reads,

$$J_{ij}^{\mathrm{PDA}} = \frac{|\vec{\mu}_i||\vec{\mu}_j|}{4\pi\varepsilon_0}\frac{\kappa}{R_{ij}^3} \tag{1.2.24}$$

where $|\vec{\mu}_i|$ and $|\vec{\mu}_j|$ are their respective dipole lengths, R_{ij} is the distance between chromophoric centers and κ is a purely geometric factor, which considers the relative orientation of the dipoles, and is given by,

$$\kappa = \hat{\mu}_i \cdot \hat{\mu}_j - 3\left(\hat{\mu}_i \cdot \hat{R}_{ij}\right)\left(\hat{\mu}_j \cdot \hat{R}_{ij}\right) \tag{1.2.25}$$

therefore, the quality of the calculated couplings by the PDA method depend on the geometric description of the spatial position on the point dipoles, and also their magnitudes. Besides, this method considers that the dipole lengths are not affected by the presence of another dipole.

A correction for the environment screening can be introduced changing ε_0 to the electrical permittivity of the medium ε_r. However, its most important limitation is that, at short distances, the coupling is greatly overestimated, and when the relative orientation of the dipole is almost perpendicular, the coupling tends to zero, which does not happen in the interaction between transition densities (Curutchet & Mennucci, 2017). Because of the PDA limitations, other methods are proposed to consider the full geometry of the chromophores, and not only their relative orientation along an axis.

Another low cost method to model the excitonic coupling is to decompose the transition density into point–charges localized at the equilibrium positions of the atoms of each chromophore, called transition charges. The excitonic coupling is then the Coulombic energy of interaction between the two sets of transition charges.

There are several protocols to determine the transition charges. One of them is the Transition Monopole Approximation (TMA), proposed by Chang (1977), in which each charge is built from the atomic orbitals (AOs) that contribute to the MOs of the ground and excited states.

Let ϕ_μ be an MO of certain molecule (i or j). Each MO is expressed as a linear combination of AOs χ_i, then,

$$\phi_{\mu,i} = \sum_{I=1}^{N_i} C_{I,\mu}\chi_I \tag{1.2.26}$$

asuming zero differential overlap (ZDO), $\chi_I(\boldsymbol{r})\chi_J(\boldsymbol{r}) = \chi_I\chi_J\delta_{IJ}$ and the form of the Coulombic energy between two charges, the excitonic coupling is given by,

$$J_{ij}^{\mathrm{TMA}} = \frac{1}{4\pi\varepsilon_0}\sum_{I=1}^{N_i}\sum_{J=1}^{N_j} 2C_{I,\nu}^{i}C_{I,\lambda}^{i}C_{J,\nu}^{j}C_{J,\lambda}^{j}\frac{e^2}{|\boldsymbol{R}_I - \boldsymbol{R}_J|} \tag{1.2.27}$$

where $C_{I,\lambda}^{i}$ represents the AO coefficient of the atom I of molecule i in the state λ; hence, λ, ν are the ground and excited states in some given order. From equation (1.2.27), the populations of the AOs can be identified, and the effective transition charges $q_{i,I}(\nu,\lambda)$ are defined as,

$$q_{i,I}(\nu,\lambda) = \sqrt{2}eC_{I,\nu}^{i}C_{I,\lambda}^{i} \tag{1.2.28}$$

Substituting (1.2.28) in (1.2.27), the excitonic coupling can be written as,

$$J_{ij}^{\mathrm{TMA}} = \frac{1}{4\pi\varepsilon_0}\sum_{I=1}^{N_i}\sum_{J=1}^{N_j}\frac{q_{i,I}(\nu,\lambda)\,q_{j,J}(\nu,\lambda)}{|\boldsymbol{R}_I - \boldsymbol{R}_J|} \tag{1.2.29}$$

In this method, it is necessary to calculate the MOs and their decomposition in terms of the AOs, therefore the decomposition method plays a key role in the procedure. Originally, Chang (1977) used a semiempirical approach, in this case, the Pariser–Parr–Pople method (SCF–MO–PPP). Other decomposition schemes can be considered.

In the TrEsp method, the transition density (calculated on the electrostatic potencial of the molecule) of each pigment for the states ν, λ is broken down into a set of transition charges $q(\nu,\lambda)$, first by calculating an electric potential field associated with the transition density and then using the CHELP-BOW method (Sigfridsson & Ryde,

1998) to express the electric field as sourced by point charges at the equilibrium position of the atomic centers. These transition charges are then used as atomic point charges centered at the atomic positions of the pigment, and are rescaled by a constant K so that the transition dipole moment,

$$\vec{\mu}^{\mathrm{TrEsp}} = \sum_{I} q_I\left(\nu, \lambda\right) \boldsymbol{R}_I \tag{1.2.30}$$

gives the same magnitude than some experimental dipole value μ^{exp}, where $\boldsymbol{R}_I$ is the position vector of atom I. Hence,

$$K = \frac{\mu^{\mathrm{exp}}}{\mu^{\mathrm{TrEsp}}}. \tag{1.2.31}$$

Finally, the excitonic coupling is given by the transfer coupling of the two excitons, given by the electric potential energy stored in the set of transition charges of the two pigments at the geometries of the complex. That is,

$$V_{ij}^{\mathrm{TrEsp}} = \frac{K_i K_j}{4\pi\varepsilon_0} \sum_{I,J} \frac{q_{i,I}\left(\nu, \lambda\right) q_{j,J}\left(\nu, \lambda\right)}{\left|\boldsymbol{R}_I - \boldsymbol{R}_J\right|} \tag{1.2.32}$$

Notice that the expression (1.2.32) and (1.2.29) are very similar. However, they differ in two fundamental things:

1. The expression for TrEsp includes correction factors for the calculated transition charges, based on the experimental transition dipoles. In the TMA this correction factor can be introduced as an effective dielectric constant of the environment. Also, one can define the same correction factor K in an analogous way as in equation (1.2.31) using the transition charges of TMA.

2. The way the transition charges are built. In the case of TMA, the transition charges are built directly from atomic orbitals, in contrast with TrEsp, that considers the breaking down of the electric potential surface associated with the calculated transition density into charges at atomic positions. This means that TMA uses a more quantum mechanical argument, and TrEsp a more electrostatic

argument, to calculate the transition charges.

For both the TMA and TrEsp method, the quality of the coupling depends on the quality of the transition charges (thus, the *ab initio* calculations behind them and the localization method), the geometry of coupled pigments and the experimental transition dipole used for rescaling. This kind of discretization suffers from accuracy losses because of the cumulative losses on these factors (Curutchet & Mennucci, 2017). In fact, it was shown that the TrEsp method can underestimate drastically the excitonic couplings, specially at short distances (Olbrich & Kleinekathöfer, 2010). Table 1.2 summarizes the methods and previous estimations of excitonic couplings for type II WSCP pigment dimers.

Table 1.2: Exciton coupling and transition dipoles for type II WSCP pigment dimers reported on the literature.

Reference	**Organism**	**Pigment**	J_{14} **(cm^{-1})**	$\lvert\vec{\mu}_{0\to1}\rvert$ **(D)**	**Method**
Hughes et al. (2006)	*B. oleracea* var. *botrytis*	Chl a	90 ± 20	4.36 ± 0.03	PDA
		Chl d	130 ± 25	5.00 ± 0.06	
Renger et al. (2007)	*B. oleracea* var. *botrytis*	Chl a	84	4.0	TrEsp
		Chl b	72	3.6	
Renger et al. (2009)	*L. virginicum*	Chl a	77	4.0	
		Chl b	69	3.6	
Dinh & Renger (2015)	*B. oleracea* var. *botrytis*	Chl a	77	4.0	
		Chl b	69	3.6	

1.2.2.2 Short–range contributions: Diabatization approaches

The methods previously discussed only deal with Coulombic long–range interactions. As the distance between chromophores becomes smaller, other interactions can become important; thus, the short–range interactions have to be added to the total excitonic coupling. In general, there are three pathways in which the exciton can be transfered from a donor site to an acceptor site (Wehner & Baumeier, 2017), illustrated in Fig. 1.6:

a) Förster-like mechanism: Coulombic interactions between the donor and the acceptor lead to an energy transfer via a virtual photon.

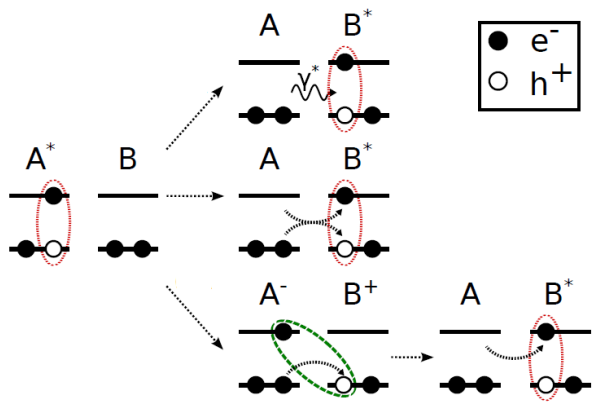

Figure 1.6: Different mechanisms for the excitonic transfer from donor site A to acceptor site B. *Upper:* Förster-like Coulombic excitonic transfer. *Middle:* Dexter-like exchange excitonic transfer. *Lower:* Dexter-like excitonic transfer *via* charge-transfer state. Taken from Wehner & Baumeier (2017).

b) Dexter-like exchange mechanism: exciton transfer through the simultaneous exchange of the electron and the hole from the donor to the acceptor.

c) Dexter-like charge-transfer mediated mechanism: exciton transfer through the exchange of electron and hole in two steps; the first of them leads to an intermediate charge-transfer state.

The PDA, TMA and TrEsp methods only consider Förster-like mechanisms, leading to a general underestimation of the excitonic couplings, specially at short distances (Kitoh-Nishioka et al., 2020; Liess et al., 2017; Błasiak et al., 2015).

The contributions of each term are difficult to calculate explicitly, as they require very expensive integrals, involving the ground and excited state wavefunctions of each chromophore. Other methods have been proposed to overcome this limitations, mainly taking advantage of the integrals that are already efficiently calculated in *ab initio* methods.

One of such alternative approaches is based on the full quantum chemical (QC) calculation at a given level of theory of the whole chromophoric network. This is known as the supermolecule approach (S. J. Jang & Mennucci, 2018). These schemes use the fact that the full QC calculation considers the adiabatic transitions of the whole chromophoric system, whose electronic Hamiltonian eigenvalues yield (in principle) to the exact energies of the excitonic states involved in the excitation dynamics. By

projecting this excitonic Hamiltonian onto the sites basis, one can reach to expressions for the excitonic couplings in terms of the adiabatic states and the site energies of the corresponding diabatic states. As this method does not assume an explicit form for the excitonic couplings, this includes the exchange and overlap interactions along with the Coulombic interactions. The quality of these "exact" total excitonic couplings depends on the accuracy of the level of theory used for the calculation in the "supermolecule" and the individual sites, and also, in the validity of the model Hamiltonian used to describe the electronic Hamiltonian of the whole system.

Consider a molecular system of a two-level dimer, in the Frenkel exciton formulation, the Hamiltonian in the site and excitonic basis is given by,

$$\begin{bmatrix} E_1 & J_{12} \\ J_{12} & E_2 \end{bmatrix}_{\text{site}} \Leftrightarrow \begin{bmatrix} E_+ & 0 \\ 0 & E_- \end{bmatrix}_{\text{exc}} \tag{1.2.33}$$

An electronic structure calculation on the whole system necessarily yields the adiabatic states $\{E_-, E_+\}$, which are the eigenstates of the electronic Hamiltonian in the site basis at the equilibrium geometry. In this framework, the adiabatic excited states of the aggregate are expressed via diabatic excited states. These diabatic states are not necessarily unique in the general multisite, multilevel system, and have to be chosen carefully, considering wavefunction arguments or chemical arguments. For complex multilevel, multiconfigurational systems, extensive localization schemes have to be used to determine the matrix transformation between diabatic and adiabatic states, such as the fragment transition density (FTD) method (Voityuk, 2014b).

In particular, for a two-state dimer model, the diabatic states $\{\phi_i, \phi_j\}$ can be selected to be fully localized in the monomers (Voityuk, 2014a). A unitary transformation connects them to the adiabatic states $\{\psi_i, \psi_j\}$,

$$\begin{bmatrix} \phi_i \\ \phi_j \end{bmatrix} = \begin{bmatrix} \cos\omega & \sin\omega \\ -\sin\omega & \cos\omega \end{bmatrix} \begin{bmatrix} \psi_i \\ \psi_j \end{bmatrix} \Rightarrow \mathbf{\Phi} = \mathbf{\Omega\Psi} \tag{1.2.34}$$

Then, the excitonic coupling is given by,

$$J_{ij}^{Diabat} = \langle \phi_i | \hat{H} | \phi_j \rangle = \frac{E_+ - E_-}{2} \sin 2\omega \tag{1.2.35}$$

where E_+, E_- are the excitonic energies. $\mathbf{\Omega}$ transforms also the transition dipoles of the diabatic ($\{\vec{\mu}_i, \vec{\mu}_j\}$) and adiabatic $\left(\{\vec{M}_i, \vec{M}_j\}\right)$ states, then, the coupling is given by

$$J_{ij}^{Diabat} = (E_+ - E_-) \frac{\left(\vec{M}_i \cdot \vec{M}_j\right)\left(\mu_i^2 - \mu_j^2\right) - \left(\vec{\mu}_i \cdot \vec{\mu}_j\right)\left(M_i^2 - M_j^2\right)}{\left(M_i^2 - M_j^2\right)^2 + 4\left(\vec{M}_i \cdot \vec{M}_j\right)^2} \tag{1.2.36}$$

In completely symmetrical complexes in an isotropic inmediate environment, a particular resonance case in which $\varepsilon_1 = \varepsilon_2$ case is achieved. In the resonance condition, $\mu_i^2 = \mu_j^2$ and the coupling can be determined through the oscillator strengths of the excitonic transitions $\{f_+, f_-\}$ and the angle between the dipoles θ, giving that,

$$J_{ij}^{Diabat} = (E_+ - E_-) \frac{E_+ f_- - E_- f_+}{E_+ f_- + E_- f_+} \frac{1}{2\cos\theta} \tag{1.2.37}$$

Also, the resonance condition assures that the system is at the avoided crossing point, therefore, the direct diagonalization of the Frenkel hamiltonian in the site basis (eq. (1.2.34)) yields the pure adiabatic states. Thus, one can obtain the excitonic coupling from the excitonic splitting as (You & Hsu, 2014),

$$J_{12}^{\text{Diag}} = \frac{|E_+ - E_-|}{2} \tag{1.2.38}$$

Notice that these diabatization approaches depend from electronic structure calculation, therefore, several different methods can be selected to calculate them; from completely wavefunction methods to time-dependent density functional methods.

1.2.3 Linear Optical Absorption

Several spectroscopical techniques can be used to characterize PPCs, however, the most common and least expensive is the linear optical absorption spectroscopy.

In linear absorption spectroscopy, the lineshape of the spectrum represents the interaction between external electromagnetic radiation and the chromophoric aggregate expressed as a linear response of the electric field. Experimentally, the sample is irradiated with a monochromatic light with an initial intensity of I_0, that, after interacting with the sample, is reduced to $I(z)$. According to Beer's law (May & Kühn, 2011),

$$I(z) = I_0 e^{-\alpha z} \tag{1.2.39}$$

where the linear absorption coefficient $\alpha(\omega)$ depends only on the wavelength of the incident light and the refractive index of the system. Assuming randomly oriented aggregates with density n_{agg}, in a media with refractive index n_r,

$$\alpha(\omega) = \frac{4\pi\omega n_{\text{agg}}}{3\hbar n_r c}\text{Re}\left[\int_0^\infty dt e^{i\omega t} C_{\text{d-d}}(t)\right] \tag{1.2.40}$$

where $C_{\text{d-d}}(t)$ is the electric transition dipole-dipole correlation function, which depends on the electric transition dipole moment $\vec{\mu}$ as,

$$C_{\text{d–d}}(t) = \langle \vec{\mu}(t) \cdot \vec{\mu}(0) \rangle_{th} \tag{1.2.41}$$

where $\langle \cdot \rangle_{th}$ corresponds to the thermal distribution average operator. Considering the statistical equilibrium operator in the absence of an external field, $\hat{W}_{\text{eq}} = \frac{e^{\frac{-\hat{H}_{\text{ex}}}{k_{\text{B}}T}}}{\mathcal{Z}}$, with partition function $\mathcal{Z} = \text{Tr}\left[e^{\frac{-\hat{H}_{\text{ex}}}{k_{\text{B}}T}}\right]$, the dipole-dipole correlation function, is expressed using the electric transition moment operator $\hat{\mu}$ as (Dinh & Renger, 2015),

$$C_{\text{d-d}}(t) = \text{Tr}\left[\hat{\mu}(t) \cdot \hat{\mu}(0)\hat{W}_{\text{eq}}\right] = \text{Tr}\left[\hat{\mu}\rho(t)\right] \tag{1.2.42}$$

For a vibronic system, the electronic behavior is given by the projection of the total aggregate state into the ground-state $|0\rangle$, then, the correlation function is written as (May & Kühn, 2011),

$$C_{\text{d–d}}(t) = \text{Tr}_{vib}\left[\text{Tr}_g\left[\hat{W}_{eq} U^\dagger_{\text{agg}}(t)\hat{\mu} U_{\text{agg}}(t)\hat{\mu}\right]\right] \tag{1.2.43}$$

where $\hat{W}_{eq} = \hat{R}_0 |0\rangle \langle 0|$ operates over the ground-state, moreover, $\hat{R}_0$ describes the vibrational equilibirum state of the aggregate, hence,

$$C_{\text{d–d}}(t) = \text{Tr}_{vib}\left[\hat{R}_0 \langle 0| U^{\dagger}_{\text{agg}}(t)\hat{\mu}U_{\text{agg}}(t)\hat{\mu}|0\rangle\right] \tag{1.2.44}$$

in this representation, the transition dipole operator is given by,

$$\hat{\mu} = \sum_n \hat{\mu}_n \equiv \sum_n \vec{\mu}_n |n\rangle \langle 0| + h.c. \tag{1.2.45}$$

substituting in (1.2.44),

$$C_{\text{d–d}}(t) = \sum_{n,m} \text{Tr}_{vib}\left[\hat{R}_0\hat{\mu}^{\dagger}_n \langle n| e^{-i\hat{H}_{\text{ex}}t}|m\rangle \hat{\mu}_m\right] \tag{1.2.46}$$

Changing to the excitonic basis (eq. (1.2.14)) to diagonalize $\hat{H}_{\text{ex}}$,

$$C_{\text{d–d}}(t) = \sum_{\alpha,\beta} \text{Tr}_{vib}\left[\hat{R}_0\hat{\mu}^{\dagger}_\alpha \langle \alpha| e^{-i\hat{H}_{\text{ex}}t}|\beta\rangle \hat{\mu}_\beta\right] \tag{1.2.47}$$

Taking the Condon approximation, the transition dipole moment does not depend on the vibrational modes, thus,

$$C_{\text{d–d}}(t) = \sum_{\alpha,\beta} \vec{\mu}^{\dagger}_\alpha\vec{\mu}_\beta \text{Tr}_{vib}\left[\hat{R}_0 \langle \alpha| e^{-i\hat{H}_{\text{ex}}t}|\beta\rangle\right] \tag{1.2.48}$$

Equation (1.2.48) is general, and can be used for explicit expression of $\hat{R}_0$ in the excitonic basis.

If vibronic coupling is neglected, the excitonic states do not mix, then,

$$\begin{aligned} C_{\text{d–d}}(t) &= \sum_{\alpha,\beta} \delta_{\alpha\beta}\vec{\mu}^{\dagger}_\alpha\vec{\mu}_\beta \text{Tr}_{vib}\left[\hat{R}_0 \langle \alpha| e^{-i\hat{H}_{\text{ex}}t}|\beta\rangle\right] \\ &= \sum_\alpha |\vec{\mu}_\alpha|^2 \text{Tr}_{vib}\left[\hat{R}_0 e^{-iE_\alpha t}\right] \\ C_{\text{d–d}}(t) &= \sum_\alpha \mu^2_\alpha e^{-iE_\alpha t} \end{aligned} \tag{1.2.49}$$

substituting (1.2.49) in (1.2.40),

$$\alpha(\omega) \propto \omega \sum_{\alpha} \mu_{\alpha}^{2} \delta(\hbar\omega - E_{\alpha}) \tag{1.2.50}$$

This gives a distribution of sharp peaks, called a Dirac comb; to get a proper spectrum lineshape, the Dirac delta function is exchanged by a broadening profile function, which considers the effect of the static disorder. To do this, the statistical distibution $\mathcal{F}(E, \sigma)$ is introduced in substitution of $\delta(E, \sigma)$, and its centered at the excitonic levels E_{α} with a standard deviation σ. Thus, the linear absorption optical spectrum, neglecting vibronic coupling, has the form

$$\alpha(\omega) \propto \omega \sum_{\alpha} \mu_{\alpha}^{2} \mathcal{F}(\hbar\omega - E_{\alpha}, \sigma) \tag{1.2.51}$$

for a given distibution $\mathcal{F}(E, \sigma)$.

For the vibronic case, the general time evolution of the transition dipoles has to be considered in equation (1.2.48) via open–quantum system approaches. To consider the continous lineshape, optical response functions dependent on the wavelength of the incident radiation are used. Description of the interaction between the chromophoric system and the electromagnetic radiation follows from the density matrix formalism and its equations of motion (Gelzinis et al., 2015; Schröter et al., 2015; Jing et al., 2013; Polyutov et al., 2012; Chen et al., 2009; Schröder et al., 2007; Lukeš et al., 2006; Schröder et al., 2006; Yang, 2006; Kleinekathöfer et al., 2005; Yang, 2005; Evers et al., 2001; Renger & May, 2000). Other formulations include the path integral formalism (Moix et al., 2015), and perturbative methods that expand the equations of motion like the cumulants method (S. J. Jang, 2019; Ke & Zhao, 2017; Dinh & Renger, 2015; Gelzinis et al., 2015; J. Ma & Cao, 2015; Banchi et al., 2013; S. Jang & Silbey, 2003). Recently, the tensor product formalism has been extended to the prediction of optical spectra through the TD-DMRG method (Jiang et al., 2020; H. Ma et al., 2018; Yao et al., 2018), giving excellent results, but limited to dimers (Xie et al., 2019; Ren et al., 2018).

1.2.4 *In silico* Determination of Frenkel Parameters

The parameters of the hamiltonian in the Frenkel exciton model describe the relevant electronic structure features of the pigments. An excellent estimation of them is essential to predict the optical properties and dynamics of PPCs.

Their determination is usually performed by fitting experimental spectra to a lineshape model using optimization algorithms as the simplex method (Khmelnitskiy et al., 2019) or genetic algorithms (Renger et al., 2007; Adolphs & Renger, 2006; Raszewski et al., 2005). To predict their values from a theoretical paradigm, TD-DFT methods have been used (Schwinn et al., 2020; Khan et al., 2020; Zanetti-Polzi et al., 2017; Plötz et al., 2016; Wang et al., 2007), perturbative methods (Rocca et al., 2010) or vibronic as TDFI (Fujimoto & Balashov, 2017). Other protocols use multireference techniques to describe excitations in highly symmetic pigments (Anda et al., 2016; Kleinschmidt et al., 2009). More expensive methods use the temporal evolution of the transition density, and then the spectrum is obtained through their Fourier transform (Tussupbayev et al., 2015; Peng et al., 2015; Morzan et al., 2014).

With the improvement of the computational capacity, previously prohibitedly expensive methods are now available, for example, the coupled–cluster method (CC) (Caricato et al., 2015; Höfener & Visscher, 2016). However, this methods still demand a lot of computational resources, therefore, TD-DFT is still the most popular method, as it provides good accuracy at a reasonable amount of computational expense (Curutchet & Mennucci, 2017). Nonetheless, TD-DFT results are heavily dependent on the choice of the associated functional (Bokareva et al., 2015; Jacquemin et al., 2014; Okuno et al., 2012).

The effect of the chosen technique is often evaluated on only one of the spectroscopic parameters, with scarce cases of the evaluation of the joint effect on the spectrum (Kocherzhenko et al., 2017).

1.2.5 Time-Dependent Density Functional Theory (TD-DFT)

In the Density Functional Theory (DFT) formalism, the properties of the ground-state of the molecule are uniquely determined by the tridimensional electron density, which is calculated solving the variational problem of minimizing the energy functional. To consider the system response to an external electromagnetic field, the formalism is extended to the time domain. As the system is conservative, this is given by the one-particle Liouville equation,

$$i\frac{\partial}{\partial t}\gamma(t,\boldsymbol{r},\boldsymbol{r}') = \left[\hat{H}_s, \gamma(t,\boldsymbol{r},\boldsymbol{r}')\right] \tag{1.2.52}$$

where $\gamma(t,\boldsymbol{r},\boldsymbol{r}')$ is the one-particle density matrix constructed from Kohn-Sham orbitals $\phi_i(t,\boldsymbol{r})$,

$$\gamma(t,\boldsymbol{r},\boldsymbol{r}') = \sum_i \phi_i(t,\boldsymbol{r})\phi_i^*(t,\boldsymbol{r}') \tag{1.2.53}$$

and the diagonal elements of $\gamma(t,\boldsymbol{r},\boldsymbol{r}')$ yield to the time-dependent electron density of the system $\rho(t,\boldsymbol{r})$.

Eq. (1.2.52) provides a general framework for the response of the electron density to an external potential, however, for vertical transitions, is sufficient to expand $\gamma(t,\boldsymbol{r},\boldsymbol{r}')$ to first-order in the frequency domain, resulting in the linear response equations,

$$\gamma(t) \approx \gamma^{(0)} + \lambda\left(\gamma^{(1)}(\omega)e^{i\omega t} + \gamma^{(1)}(-\omega)e^{-i\omega t}\right) \tag{1.2.54}$$

$$\Rightarrow \left[\hat{H}_s^{(1)}, \gamma^{(0)}\right] + \left[\hat{H}_s^{(0)}, \gamma^{(1)}\right] = \omega\gamma^{(1)} \tag{1.2.55}$$

expanding the linear response density matrix $\gamma^{(1)}$ in Kohn-Sham static orbitals,

$$\gamma^{(1)} = \sum_{ia}\left[X_{ia}^{\omega}\phi_a(\boldsymbol{r})\phi_i(\boldsymbol{r}') + Y_{ia}^{\omega}\phi_i(\boldsymbol{r})\phi_a(\boldsymbol{r}')\right] \tag{1.2.56}$$

where i runs over the occupied orbitals and a over the virtual orbitals. Using the formalism derived by Casida, the transition energies are computed by solving the eigenvalue

problem:

$$\begin{bmatrix} \boldsymbol{A} & \boldsymbol{B} \\ \boldsymbol{B}^* & \boldsymbol{A}^* \end{bmatrix} \begin{bmatrix} \boldsymbol{X} \\ \boldsymbol{Y} \end{bmatrix} = \omega \begin{bmatrix} 1 & 0 \\ 0 & -1 \end{bmatrix} \begin{bmatrix} \boldsymbol{X} \\ \boldsymbol{Y} \end{bmatrix} \tag{1.2.57}$$

the matrices $\boldsymbol{A}$ y $\boldsymbol{B}$ are given by,

$$A_{ia,jb} = \delta_{ij}\delta_{ab}\left(\varepsilon_a - \varepsilon_i\right) + (ia|jb) + (ia|f_{xc}|jb) \tag{1.2.58}$$

$$B_{ia,jb} = (ia|bj) + (ia|f_{xc}|bj) \tag{1.2.59}$$

this calculation can be computationally expensive, therefore a common approximation implemented is the Tamm-Dancoff approximation (TDA), in which the matrix $\boldsymbol{B}$ in eq. (1.2.57) is neglected, thus the eigenvalue problem becomes hermitic and is reduced to,

$$\boldsymbol{AX} = \omega \boldsymbol{X} \tag{1.2.60}$$

Usually, TDA calculations are much faster and give similar results than the full TD-DFT calculation (Curutchet & Mennucci, 2017).

The last term in the $\boldsymbol{A}$ and $\boldsymbol{B}$ matrices is dependent of the f_{xc} function, which corresponds to the exchange-correlation kernel in the adiabatic approximation,

$$f_{xc} = \frac{\partial^2 E_{xc}}{\partial\rho(\boldsymbol{r})\partial\rho(\boldsymbol{r}')} \tag{1.2.61}$$

this term depends on the exchange-correlation energy E_{xc}, hence the expression is dependent on the selection of the functional $E_{xc}\left[\rho(\boldsymbol{r})\right]$, thus, the excitation energies and the involved orbitals also depend on the functional selection.

1.3 Quantum Effects in the EET

The chromophoric system usually is nowhere near isolated, thus, it is imperative to include couplings between electronic and vibrational states (vibronic coupling). To describe these effects, the density matrix formalism is used.

1.3.1 Density Matrix Formalism

For a system with wavefunction $|\Psi(t)\rangle$, the density matrix $\rho(t)$ is defined as,

$$\rho(t) \equiv |\Psi(t)\rangle \langle\Psi(t)| \tag{1.3.1}$$

Then, for an operator $\hat{O}$, its expected value is given by,

$$\left\langle \hat{O} \right\rangle = \langle\Psi| \hat{O} |\Psi\rangle = \langle\Psi| \hat{O} |\Psi\rangle \langle\Psi|\Psi\rangle = \mathrm{Tr}\left[\hat{O}\rho\right] \tag{1.3.2}$$

In the site basis $\{|n\rangle\}$, the wavefunction is expanded as $|\Psi(t)\rangle = \sum_n c_n(t) |n\rangle$, then,

$$\rho(t) = \sum_{nm} c_n(t) c_m^*(t) |n\rangle \langle m| \tag{1.3.3}$$

$$\Rightarrow \left\langle \hat{O}(t) \right\rangle = \sum_{nm} c_n(t) c_m^*(t) \langle m| \hat{O} |n\rangle \tag{1.3.4}$$

However, for statistical ensambles of pure states $|\psi_k\rangle = \sum_n c_n^{(k)} |n\rangle$ each with and occupation probability p_k, then, the density matrix is given by (Breuer & Petruccione, 2002),

$$\rho(t) \equiv \sum_k p_k |\psi_k(t)\rangle \langle\psi_k(t)| \tag{1.3.5}$$

As the ensamble is statistical, the occupation probability of each state is given by a thermal distribution,

$$p_n = \frac{e^{-\beta E_n}}{\mathcal{Z}} \tag{1.3.6}$$

where E_n are the eigenvalues of the system hamiltonian, $\hat{H}\left|n\right\rangle = E_n\left|n\right\rangle$. The statistical equilibrium density matrix is then,

$$\rho_{\text{eq}} = \frac{e^{-\beta\hat{H}}}{\mathcal{Z}} \tag{1.3.7}$$

where the partition function is $\mathcal{Z} = \text{Tr}\left[e^{-\beta\hat{H}}\right]$. The matrix elements of ρ_{eq} are then,

$$\left\langle n\right|\rho_{\text{eq}}\left|m\right\rangle = \left\langle n\right|\frac{e^{-\beta\hat{H}}}{\mathcal{Z}}\left|m\right\rangle = \frac{1}{\mathcal{Z}}\left\langle n\right|e^{-\beta\hat{H}}\left|m\right\rangle = \frac{e^{-\beta E_n}}{\mathcal{Z}}\delta_{nm} = p_n\delta_{nm} \tag{1.3.8}$$

Thus, the thermally averaged expected value of $\hat{O}$ is,

$$\left\langle\hat{O}\right\rangle_{th} = \frac{1}{\mathcal{Z}}\sum_n e^{-\beta E_n}\left\langle n\right|\hat{O}\left|n\right\rangle = \text{Tr}\left[\hat{O}\rho_{\text{eq}}\right] \tag{1.3.9}$$

Notice that ρ_{eq} is the matrix representation of $\hat{W}_{\text{eq}}$, thus $\hat{W}_{\text{eq}}$ is the thermal equilibrium density operator (May & Kühn, 2011).

Also, the correlation function C_{OO} is defined as the thermally averaged expected value of the fluctuation of $\hat{O}$ over a time period,

$$C_{OO}(t) = \left\langle\hat{O}(t)\hat{O}(0)\right\rangle_{th} = \sum_n p_n\left\langle n\right|\hat{O}(t)\hat{O}(0)\left|n\right\rangle \tag{1.3.10}$$

from (1.3.8), $p_n = \left\langle n\right|\rho_{\text{eq}}\left|n\right\rangle$, then,

$$C_{OO}(t) = \text{Tr}\left[\rho_{\text{eq}}\hat{O}(t)\hat{O}(0)\right] = \text{Tr}\left[\hat{O}(t)\hat{O}(0)\rho_{\text{eq}}\right] \tag{1.3.11}$$

Then, the dipole–dipole correlation function is expressed as (Dinh & Renger, 2015),

$$C_{\text{d-d}}(t) = \text{Tr}\left[\hat{\mu}(t)\cdot\hat{\mu}(0)\rho_{\text{eq}}\right] \tag{1.3.12}$$

and therefore, the absorption spectra can be determined from the density matrix dynamics.

1.3.2 Time evolution of the density matrix

The time evolution of a closed quantum system with wavefunction $|\Psi(t)\rangle$ is expressed by time–dependent Schrödinger equation. If the system is a pure state in a Hilbert space $\mathcal{H}$, then (Rivas & Huelga, 2012),

$$\frac{\partial}{\partial t}|\Psi(t)\rangle = -\frac{i}{\hbar}\hat{H}(t)|\Psi(t)\rangle \tag{1.3.13}$$

In terms of the density matrix,

$$\begin{aligned}\frac{\partial\rho(t)}{\partial t} &= \frac{\partial}{\partial t}\left[|\Psi(t)\rangle\langle\Psi(t)|\right] \\ &= \left[\frac{\partial}{\partial t}|\Psi(t)\rangle\right]\langle\Psi(t)| + |\Psi(t)\rangle\left[\frac{\partial}{\partial t}\langle\Psi(t)|\right] \\ &= -\frac{i}{\hbar}\hat{H}(t)|\Psi(t)\rangle\langle\Psi(t)| + \frac{i}{\hbar}|\Psi(t)\rangle\langle\Psi(t)|\hat{H}(t)\end{aligned} \tag{1.3.14}$$

using (1.3.1), the Liouville–von Neumann equation is obtained,

$$\frac{d}{dt}\rho(t) = -\frac{i}{\hbar}\left[\hat{H},\rho(t)\right] \tag{1.3.15}$$

As the hamiltonian is hermitian, the solution of eq. (1.3.13) is given in terms of the time evolution operator $U(t,t_0)$, a unitary operator so that,

$$|\Psi(t)\rangle = U(t,t_0)|\Psi(t_0)\rangle \tag{1.3.16}$$

Substituting the eq. (1.3.1),

$$\rho(t) = U(t,t_0)\,\rho(t_0)\,U(t,t_0)^{\dagger} \tag{1.3.17}$$

In the case of a time–independent hamiltonian, the system is conservative and the solution is direct,

$$U(t,t_0) = \exp\left[-\frac{i(t-t_0)\hat{H}}{\hbar}\right] \tag{1.3.18}$$

However, when the hamiltonian is time–dependent, the system is not conservative and the time evolution operator is formally expressed as a Dyson expansion (Rivas & Huelga, 2012),

$$U\left(t,t_0\right)=\mathcal{T}\exp\left[-\frac{i}{\hbar}\int_{t_0}^{t}\hat{H}\left(t'\right)dt'\right] \tag{1.3.19}$$

where $\mathcal{T}$ is the time–ordering operator. For closed non–conservative quantum systems, analytical solutions of eq. (1.3.19) are limited. Instead, perturbative and series expansion techniques are used to correctly describe the time evolution.

To evaluate the expected value of an operator, from eq. (1.3.2), and substituting eq. (1.3.17),

$$\left\langle\hat{O}(t)\right\rangle=\mathrm{Tr}\left[\hat{O}\rho(t)\right]=\mathrm{Tr}\left[\hat{O}U\rho\left(t_0\right)U^{\dagger}\right]=\mathrm{Tr}\left[U\hat{O}U^{\dagger}\rho\left(t_0\right)\right] \tag{1.3.20}$$

where $\hat{O}(t)=U^{\dagger}\hat{O}U$.

1.3.3 Open Quantum System Dynamics

An open quantum system is one that can exchange matter and energy with other quantum system. Usually, the second quantum system corresponds to an ideal quantum model of the environment in which the first system is embedded. Then, the first system is the one of interest is referred simply as "system" and the second one as the "bath" (Rivas & Huelga, 2012).

In general, for an open system, the time evolution operator is not necesarily unitary. To describe correctly its dynamics, the equation of motion (EOM) of the system density matrix: this is called a quantum master equation (Breuer & Petruccione, 2002).

The formulation in terms of the density matrix starts by considering a quantum system S coupled to another quantum system B that corresponds to the bath, the interaction results in a total system $S+B$ (fig. 1.7). The total system is assumed to be closed, and follows the non-dissipative dynamics.

The state of the system S then changes because of its internal dynamics and its interaction with the environment. This coupling leads to system–bath correlations, that cannot be expressed in general as unitary operators. The dynamics of the subsystem S

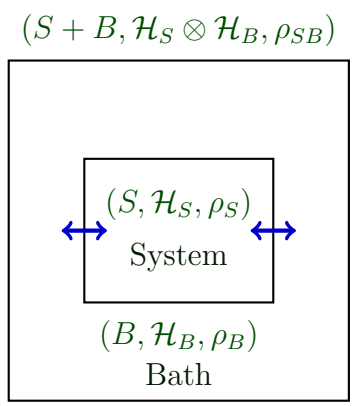

Figure 1.7: Diagram of an open quantum system and its description.

induced by the time evolution of $S+B$ are called reduced system dynamics, therefore, S is often referred as the reduced system.

The Hilbert space of $S+B$ is the tensor product of each subsystem's Hilbert space, that is, $\mathcal{H}_{SB} = \mathcal{H}_S \otimes \mathcal{H}_B$. Then, the total system hamiltonian can written as,

$$\hat{H}(t) = \hat{H}_S \otimes \mathbb{I}_B + \mathbb{I}_S \otimes \hat{H}_B + \hat{H}_{SB}(t) \tag{1.3.21}$$

where $\hat{H}_S$ is the reduced system hamiltonian, $\hat{H}_B$ is the bath hamiltonian, and $\hat{H}_{SB}$ is the hamiltonian that describes the system–bath interaction.

In terms of the density matrix, the dynamics of S are contained in the reduced density matrix ρ_S, that relates to the total system density matrix, ρ_{SB}, through the partial trace over the bath. Thus,

$$\rho_S = \mathrm{Tr}_B\left[\rho_{SB}\right] \tag{1.3.22}$$

Then, the observables of S are expressed as operators of the form $\hat{O} \otimes \mathbb{I}_B$, in eq. (1.3.2),

$$\left\langle \hat{O} \right\rangle = \mathrm{Tr}_S\left[\hat{O}\mathrm{Tr}_B\left[\rho_{SB}\right]\right] = \mathrm{Tr}_S\left[\hat{O}\rho_S\right] \tag{1.3.23}$$

The time evolution of the reduced density matrix is obtained by tracing out the bath from the unitary time evolution of the total system density matrix,

$$\rho_S(t) = \mathrm{Tr}_B\left[U(t,t_0)\,\rho_{SB}(t_0)\,U^\dagger(t,t_0)\right] \tag{1.3.24}$$

substituting in (1.3.15),

$$\frac{d}{dt}\rho_S(t) = -\frac{i}{\hbar}\mathrm{Tr}_B\left[\left[\hat{H}(t), \rho_{SB}(t)\right]\right] \tag{1.3.25}$$

The solution of eq. (1.3.25) can be very difficult, if not impossible, due to the large and complicated structure of the environment and the complex relations to the system. Therefore, several assumptions and approximations about the reduced dynamics are used to simplify and solve the QME.

For instance, one of such assumptions is that the system state only depends on the previous state, therefore, it has no memory of its history. This condition defines a Markovian process, and in this approximation the initial state is a non–correlated product state $\rho_{SB}(t_0) = \rho_S(0) \otimes \rho_B$. Markovian QMEs can be derive from this, like Gorni–Kossakowski–Sudashan–Lindblad (commonly just called simply the Lindblad equation) and the Redfield equation. For non–Markovian process, numerically exact approaches are needed, such as the density matrix renormalization group (DMRG) and hierarchical equations of motion (HEOM) (Ishizaki & Fleming, 2009; Tanimura, 2006; Breuer & Petruccione, 2002; Tanimura & Kubo, 1989).

1.3.4 Quantification of Quantum Phenomena

The presence of quantum phenomena; such as superposition, coherence, interference or entanglement; in macroscopic processes is difficult to probe, as the access to the system is limited by the delicate dynamics of quantum systems and the projective nature of the measurements; as the wavefunction collapses upon measurement.

For the photosynthetic PPC, once the dynamics of the system is modelled, the question to answer is: "the characteristics of this EET can only be explained by the presence of quantum phenomena?". This is specially difficult to demonstrate for biological systems, as the environment is usually very complex, constantly changing and at high temperatures.

To evaluate this question, multiple protocols have been proposed, and can be classified into two categories (C.-M. Li et al., 2012). The first one is the imposition of a

classical restriction: *if the behaviour of the system can be totally explained by classical theories, then it must meet this condition.* For these protocols, conditions proper of classical systems are assumed and then tested in terms of the system. Two of them stand out: if macrorealism and the ability to make non-invasive measurements are imposed, then the system must follow the Leggett-Garg inequality for the system to be considered "classical" (Leggett & Garg, 1985); however, if realism and locality are imposed instead, then the system must follow the Bell inequality to be classical (Bell, 1964). Nevertheless, this type of test present multiple experimental challenges, as the design of non-invasive experiments with very high resolution observables (Wilde et al., 2010) or the simultaneous measurement of different observables in isolation and spatial separation condition (Żukowski & Brukner, 2002).

The second group of protocols are based on deductive logic: *if the dynamics observed correspond sufficiently well with the ones predicted by quantum theory, then the system must be quantum*; similarly for classical systems. Quantum witnesses are found in this second category: functions that are defined from quantum theory and are parametrized in terms of the system observables or states, so that their numerical value serves as a metric that gives direct information about the presence or absense of a particular quantum effect in the system. This allows for the direct evaluation of the quantum characteristics from experimental data, with a quick and effective method, without experimental procedure modifications that increases the overhead in the methodology.

The witnesses have been used to quantify multiple quantum phenomena, for example, they have been used to demostrate the existence of quantum coherence (Monras et al., 2014), quantum entanglement (Hansen et al., 2015), non-locality (Horodecki et al., 1995), quantum discord (Rulli & Sarandy, 2011; Ollivier & Zurek, 2002), quantum teleportation (Salikhov et al., 2007), and even the *quantumness* itself of the system (C.-M. Li et al., 2012).

For PPCs, the presence of quantum coherence has been experimentally observed (Collini et al., 2010), and since then, theoretical examinations have been used to probe for other quantum features in the EET. For example, quantum coherence has been examined through the concurrence witness (Hill & Wootters, 1997) in multiple theoretical

examinations as a basic characterization (Saberi et al., 2016; Bengtson et al., 2016; Oka, 2016; Sarovar et al., 2010). Moreover, other studies have used quantum discord to demonstrate the presence of unequivocally quantum correlations in LHCs (Brádler et al., 2010), or the von Neumann entropy to demostrate the existence of quantum entanglement between the excitonic levels of the chromophoric aggregate (Sarovar et al., 2010), or to demostrate the teleportation of quantum information across the biological membranes through charge separation in transmembrane RCs (Salikhov et al., 2007). The selection of adequate quantum witnesses and their evaluation allows to analyze the influence of quantum phenomena on the EET dynamics of photosynthetic systems.

1.3.5 Quantum Coherence

Two waves are coherent when their frequency and waveform coincide (Griffiths & Schroeter, 2018). As both waves interfere with each other, the coherence implies the correlation between both signals, which show a constant relative phase between them (Glauber, 1963). Coherence is an essential feature of quantum systems, as its in the center of the superposition of quantum states (Huelga & Plenio, 2013).

Several witnesses can be proposed to probe for quantum systems, usually based on functions of the off-diagonal entries of the density matrix, following the physical intuition from the statistical definition of correlation (Baumgratz et al., 2014). For multichromophoric PPCs, the distribution of coherence can be tested usgin the concurrence witness (Sarovar et al., 2010; Hill & Wootters, 1997). In this case, the premise of superposition between the excited states of two chromophores can be interpreted as the 2-qubit entanglement, leading to a global mixed state; thus, the off-diagonal elements of the density matrix should be non-zero. Hence, the concurrence witness for each pair of chromophores (i, j) is given by,

$$C_{ij} = 2\,|\rho_{ij}| \quad ; \quad i \neq j \tag{1.3.26}$$

and proper measures of total coherence are the ones which are monotonically decreasing upon the decrease of coherence, which lead to several measures (Baumgratz et al., 2014).

Two of them are: the L^1-norm of coherence,

$$\mathcal{C}_{L^1} = \sum_{i,j;i\neq j} |\rho_{ij}| \tag{1.3.27}$$

and the relative entropy of coherence,

$$\mathcal{C}_S(\rho) = S(\rho_{diag}) - S(\rho) \tag{1.3.28}$$

where S is the von Neumann entropy and ρ_{diag} denotes the matrix built by only taking the diagonal elements of ρ and setting the rest off-diagonal elements to zero.

The prevalence of quantum coherence has been studied on several PPCs through ultrafast spectroscopic techniques (Schlau-Cohen et al., 2012; Engel et al., 2007). Multiple experimental studies have explored the quantum coherence on cryogenic temperatures (Meneghin et al., 2019, 2018; Dostál et al., 2012), at physiological temperatures (Panitchayangkoon et al., 2010), their dependence on pH (Turner et al., 2012), robustness (Hayes et al., 2011), among other effects. Its functional relevance and potential as a light-harvesting resource is still an active area of research, as no consensus has been reach on the scientific community (Romero et al., 2014; Ai et al., 2013; Calhoun & Fleming, 2011; Hoyer et al., 2010; Sarovar et al., 2010; H. Lee et al., 2009).

1.3.6 Quantum Transport

The term "quantum transport" has been referred to the regimen where the effects of quantum coherence alters the energy transfer dynamics. This means that not only the quantum coherence is present, but also it modulates the excitonic populations on each site. In this sense, the necessary and sufficient condition to sustain quantum transport is the coupling between the quantum coherence and site excitonic occupations in their time evolution (Panitchayangkoon et al., 2011).

The dynamics of quantum transport in a PPC can be observed through the coupling of the coherence and occupations witnesses of the reduced density matrix. In this framework, the transfer of populations of entries in the $\rho_{kl} \to \rho_{ii}$ direction, with $k \neq l$,

indicates quantum transport. This implies that excitonic site occupations are transferred through the zones where quantum coherence is present, impulsing an specific route and quantum coherence drives the dynamics. This reduces the incoherent jumps and intersystem crossings that lead to thermal relaxation. This mechanism is the one suggested to explain the abnormally high efficiencies observed in EET in photosynthetic LHCs (Chin et al., 2013; Hayes et al., 2010; Ishizaki et al., 2010; Caruso et al., 2009; Mohseni et al., 2008; Plenio & Huelga, 2008).

To witness quantum transport, the interplay between the excitonic coherence $\rho_{\alpha\beta}(t)$ between the two excitons $|\alpha\rangle$ and $|\beta\rangle$, and the site populations ρ_{ii} must show the same oscillation frequency, which implies that both phenomena are synchronized (Panitchayangkoon et al., 2011; Hayes et al., 2010).

Chapter 2

Computational Methods

2.1 WSCP Structure Preparation

The studied PPC corresponds to the chlorophyll *b* chromophoric aggregate of the WSCP type II recombinant from cauliflower (*Brassica oleracea* var. *Botrytis*), shown on figure 2.1.

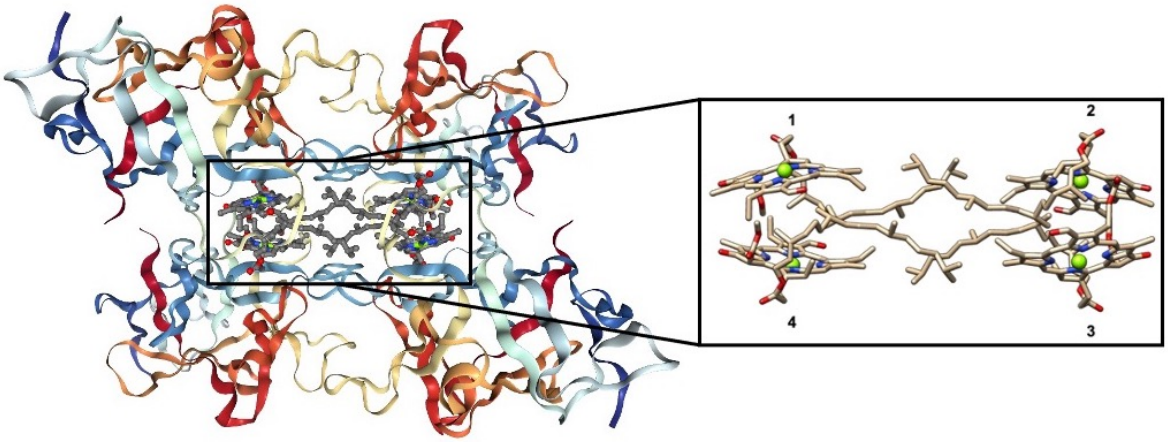

Figure 2.1: Crystal structure of the Class II WSCP-Chl b from cauliflower studied (PDB ID: 6S2Z), and detailed view of the geometry of the chromophoric network.

The most recent XRD crystal structure was used for the Chl b WSCP (Agostini et al., 2019), deposited on the Protein Data Bank (Burley et al., 2021) with code 6S2Z. The experimental coordinates were obtained directly from the PDB website (`https://www.rcsb.org/`) and cleaned using the `pdb4amber` functionality of AmberTools2022 (Case et al., 2022). All hydrogens were added using the MolProbity web service (Williams et al., 2018).

The biological assembly shows that the protein chains self-assemble into a tetramer quaternary structure, however the XRD structure resolves only the monomer. The other subunits are built using C_2 symmetry operations, therefore, the coordinates of each chromophore are equivalent in their own frame of reference with the origin at their center-of-mass. The dimer is built from the coordinates of the two chromophores facing each other (chains A and D of the biological assembly for 6S2Z), including all hydrogens, the chlorin macrocycle, the magnesium center and the phytyl tail. The PDB file was converted to XYZ format using the OpenBabel software (O'Boyle et al., 2011). No geometry optimization was performed, the structure is analyzed as is. The

coordinates used in the calculations are given in the Appendix A.

2.2 TD-DFT Calculations

To determine the Frenkel parameters of the studied PPCs by computational *ab initio* methods, the TD-DFT paradigm was used. The calculation was performed using the all electron def2-TZVP basis sets in every atom. To account for the variety of definitions and parametrizations of functionals, 21 different functionals were considered, divided in 5 categories:

- GGA: BLYP (Becke, 1988; C. Lee et al., 1988), BP86 (Becke, 1988; Perdew, 1986), PBE (Perdew, Burke, & Ernzerhof, 1996; Perdew, Ernzerhof, & Burke, 1996).
- meta-GGA: B97M-V (Mardirossian & Head-Gordon, 2015), B97M-D3BJ (Najibi & Goerigk, 2018), M06-L (Zhao & Truhlar, 2008, 2006), TPSS (Perdew et al., 2004; Tao et al., 2003).
- General Hybrids: BHHLYP (Becke, 1993b), B3LYP (Becke, 1993a), X3LYP (Xu & Goddard, 2004), O3LYP (Hoe et al., 2001; Cohen & Handy, 2001), PBE0 (Adamo & Barone, 1999).
- meta-GGA Hybrids: M06 (Zhao & Truhlar, 2008), M06-2X (Zhao & Truhlar, 2008), TPSSh (Staroverov et al., 2003).
- Range-Separated Hybrids: LC-BLYP (Iikura et al., 2001), ωB97X-V (Mardirossian & Head-Gordon, 2014), ωB97X-D3BJ (Najibi & Goerigk, 2018), CAM-B3LYP (Yanai et al., 2004), CAMh-B3LYP (Shao et al., 2020), Tuned-CAM-B3LYP (Okuno et al., 2012).

Two variations of the calculations were considered: the full TD-DFT calculation and employing the Tamm-Dancoff approximation (TDA). For all available cases, dispersion correction was taken into account by means of the DFTD3 with Becke-Johnson damping (D3BJ): for the functionals O3LYP, X3LYP, M06, M06-L, M06-2X and LC-BLYP, D3BJ corrections are not available. For B97M and ωB97X, the dispersion corrections

are included in the functionals B97M-D3BJ and ωB97X-D3BJ respectively; the functionals B97M-V and ωB97X-V use the VV10 scheme for the dispersion corrections. All calculations were performed with the ORCA 4.2.1 quantum chemical package (Neese, 2018, 2012).

For comparison, the monomer spectra was determined using TD-DFTB, an approximate semiempirical method based on TD-DFT theory. This calculation was performed using the Casida formalism, and the 3ob-3-1 Slater-Koster files, using the D3BJ dispersion. These calculations were performed using the DFTB+ 19.1 suite (Hourahine et al., 2020).

To compare TD-DFT and TD-DFTB results, the transitions obtained were broadened using a Gaussian distribution each peak i centered around $\tilde{\nu}_i$, given by

$$\varepsilon_i\left(\tilde{\nu}\right) = \varepsilon_i^{max}\ \exp\left[-\left(\frac{\tilde{\nu}-\tilde{\nu}_i}{\sigma}\right)^2\right] \tag{2.2.1}$$

where $\varepsilon_i\left(\tilde{\nu}\right)$ is the molar absorptivity at a wavenumber $\tilde{\nu}$ and σ is the full-width mid-height (FWMH). The values of $\varepsilon_i\left(\tilde{\nu}\right)$ were determined from the oscillator strengths f_i using the relation,

$$\varepsilon_i^{max} = \frac{\sqrt{\pi}\, e^2\, N_A}{1000\ \ln 10\, c^2\, m_e}\frac{f_i}{\sigma} \tag{2.2.2}$$

$$= \left(1.3062974 \times 10^8\ \mathrm{L\ mol^{-1}\ cm^{-2}}\right)\frac{f_i}{\sigma} \tag{2.2.3}$$

Both the TD-DFT and TD-DFTB calculated transitions were broadened using the same procedure with the same FWMH ($\sigma = 282\ \mathrm{cm}^{-1}$).

2.3 Frenkel Model Parametrization

Model hamiltonians were obtained, according to the Frenkel exciton approach in eq. (1.2.12). Therefore, the hamiltonian takes only the site energy and the excitonic coupling. By symmetry, the structure is bidimeric, with $J_{14} = J_{23} \gg J_{12}, J_{13}, J_{34}$, therefore, the modeling can be simplified to the dimer case with a 2×2 matrix hamiltonian, by neglecting

all couplings except for J_{14} remaining (Renger et al., 2009).

For the experimental parameters, the site energies are taken from spectroscopical data (Dinh & Renger, 2015), the excitonic couplings were calculated using the TrEsp method employing the previously reported transition charges (Renger et al., 2009, 2007; Madjet et al., 2006), for the rescaling constants, a transition dipole intensity of 3.6 D was used, based on experimental data from Chl b linear absorption spectroscopy (Renger et al., 2007; Knox & Spring, 2003). The TrEsp coupling found in the literature is 72 cm^{-1}, however, this was calculated using the Chl a WSCP structure from *Lepidinium virginicum*, reconstituted with Chl b (PDB ID: 2DRE); in this work, this value was corrected using the coordinates from Chl b WSCP from *Brassica oleracea* var. *botrytis*, which results in a corrected value of 75.3 cm^{-1}.

For the calculated site energies, the transition energy of the vertical $S_0 \rightarrow S_1$ transition of the monomer is taken directly as the site energy. The transition is considered valid only if it is pure and is distinctly higher in intensity and well separated from other transitions, therefore, the highest of the first 10 calculated transitions was selected as the site energy. For the Chl b monomer studied, this criteria is sufficient to ensure the quality of the site energies, however, it should be noted that this is not a general method, and for other systems the transitions have to be carefully analyzed, as dark transitions can play a fundamental role in the EET In addition to this, very diffuse transitions can be calculated, which render the Frenkel approximation invalid in the selected Hilbert space.

In the case of the excitonic couplings, both Coulombic and diabatic methods were evaluated. For the Coulombic methods, the point-dipole approximation (PDA), the transition monopole approximation (TMA) with the transition charges previously reported (Chang, 1977), and the TrEsp method were used. For the PDA, the transition dipole vectors were centered on each magnesium atom of the chlorin macrocycle, and are oriented in the $N_A - N_C$ directions. For both TMA and TrEsp, both methods were rescaled using the 3.6 D experiemental dipole.

The diabatic method employed corresponds to the Fragmented Transition Density (FTD) method (Voityuk, 2014b), for the two-level dimer particular case (Voityuk,

2014a). This method is based on the calculation of the diabatic and adiabatic states, therefore TD-DFT calculations were performed on the monomers and dimers. From the monomers calculations, the diabatic states are obtained, selecting them with the same criteria as the site energies. From the dimer calculation, the adiabatic states are selected as the two most intense transitions from the first 15 excited states calculated, such that the splitting between their transition energies was at least in the order of 10^2 cm^{-1}. As the coupling relies on the full *ab initio* calculation of the supermolecule, one coupling is obtained for each functional. For all selected excited states, their characteristics (transition electric dipole, transition energy, oscillator strength) were used as is, no further rescaling was applied.

2.4 Optimization of Linear Absorption Spectra

For the modeling of the optical spectra, the parametrization takes the hamiltonian and the electric transition dipole of the monomers, according to eq. (1.2.40). The hamiltonian was parametrized using the Frenkel model, as previously specified, making use of experimental and *ab initio* parameters. For the transition dipoles, also both versions were considered, and matched correspondingly for the modelling.

The experimental electric transition dipole strength of 3.6 D was considered in the direction between the nitrogen atoms from the A and C pyrrol rings (N_A–N_C) of each chromophore (Renger et al., 2007), with the Mg at the chromophoric center of the pigment. Also, a variation of the transition dipole vector was considered, using the best fitting angle of $\theta \approx 39°$ determined from the experimental absorption spectra by Dinh & Renger (2015). These vectors coordinates were calculated assuming that:

- The dipole strength is kept at 3.6 D
- The center of each chromophore is kept at the Mg atom
- The C_2 symmetry constraint between the monomers, and therefore, their dipoles
- The vector is fully in the best fitting plane of the chlorin macrocycle of the chlorophyll

- The open angle between the dipoles is fixed at $\theta = 39°$

this solves for the 3 coordinates of both transition dipoles.

For the TD-DFT parameters, the *ab initio* transition dipoles were used directly from the calculation. As this method can only predict energy of the radiation interaction with the molecule up to its magnitude squared, then $\left|\vec{\mu} \cdot \vec{E}\right| = \left|-\vec{\mu} \cdot \vec{E}\right|$, the transition dipoles' direction can be freely inverted. Following the structural information, the transition dipoles are inverted to give an acute opening angle.

The protein static disorder (Stross et al., 2016) greatly influences the optical spectra, as it represents slight equilibrium variations of the structure within the cystal, and produces an inhomogeneous broadening, due to the resulting random variations in the site energies, according to eq. (1.2.51). This effect was considered by using a statistical distribution around the site energies with standard deviation σ.

For the non-vibronic modelling, three distributions were tested for profiling: Gaussian, Lorentzian and Voigtian. The static disorder parameter σ was estimated by varying it between 1.0 and 500.0 cm^{-1} with a 1.0 cm^{-1} step, and comparing the resulting spectra with the experimental one (Dinh & Renger, 2015).

To compare between spectra, three different curve matching metrics were evaluated as possible similarity figures of merit: the L^1-norm, L^2-norm and Procrustes distance (Gower & Dijksterhuis, 2004). For all the spectra, the similarity analysis is performed between the normalized calculated absorption spectrum and the experimental (Dinh & Renger, 2015) measured at 77 K; centering both at their maximum. Maximization of the similarity against the static disorder gives the estimated parameter for the protein.

To evaluate the quality of the parameters obtained by TD-DFT, linear absorption spectra were obtained using the numerically exact simulations through the hierarchical equations of motion (HEOM) method optimized for absorption spectra of the Chl b dimer in WSCP (Caycedo-Soler et al., 2022), considering the experimental spectral density determined by difference flourescense line-narrowing spectroscopy (Δ-FLN) for both pigments (Kell et al., 2013; Pieper et al., 2011). The HEOM calculations were performed by Jaemin Lin, from the Institute of Theoretical Physics and IQST of the

Ulm University. This HEOM simulations consists a fully vibronic modelling with extremely high accuracy. All of the simulated spectra are rescaled for comparison so that the maximum absorption of the spectra is normalized to unity.

The fully vibronic spectra, along with the experimental, was then deconvolved into two absorption peaks, corresponding to the two excitonic bands expected according to the theory. The excitonic splitting and the relative height of the deconvolved bands were compared for TD-DFT parameters and experimental spectra to determined the best protocol to obtain a fully *ab initio* linear absorption spectra of the chromophoric system.

2.5 Closed System Dynamics

In the limit of null coupling to the environment, the hamiltonian of the total system is equivalent to the reduced system, and so, it has the form of the Frenkel hamiltonian previously analyzed (eq. (1.2.12)) and the reduced system dynamics are given by the direct solutions of eq. (1.3.15). Considering that $t_0 = 0$ fs, then the explicit reduced density matrix time evolution is given by,

$$\rho\left(t\right) = \exp\left[-\frac{it\hat{H}_{agg}}{\hbar}\right]\rho_0 \exp\left[\frac{it\hat{H}_{agg}}{\hbar}\right] \tag{2.5.1}$$

where $\rho_0 = \rho\left(t = 0\right)$ represents the initial conditions for the system. Several different choices can be considered for the starting state, in particular:

1. Single local excitation: the initial state is the single vertical excitation localized on one monomer. This is the most usual consideration, following the physical intuition of the process: first a photon excites a single chromophore to start the EET. Considering the site basis, the initial state takes the form $|n\rangle\langle n|$.

2. Single delocalized exciton: the initial state is one of the excitonic levels of the chromophoric aggregate, which is not necessarily localized on a single monomer, according to eq. (1.2.14). Considering the exciton basis, the initial state takes the form $|\alpha\rangle\langle\alpha|$.

3. Thermalized: in this condition, the reduced system is in thermal equilibrium with the bath, therefore the initial state coincides with the statistical equilibrium density matrix, according to eq. (1.3.7).

Here, the Liouville-von Neumann dynamics are analyzed for the Chl b WSCP (PDB ID: 6S2Z) using the previously obtained parameters using the TD-DFT methods. In particular, the functionals ωB97X-D3BJ, CAM-B3LYP and CAMh-B3LYP are considered.

The effects of the static disorder are essential to the description of dynamics, as slight variations can interfere with the delicate quantum dynamics (Cleary & Cao, 2013; Jing et al., 2012; S. Jang et al., 2001; Barvík et al., 1998). This is considered through the statistical average of 10^3 trials of the dynamics simulation. In each trial, the site energies are sampled from a normal distribution around the determined site energies with the optimized σ as standard deviation. The initial condition is set as the single local excitation over the first chromophore in each trial,

$$\rho_0 = |1\rangle \langle 1| = \begin{bmatrix} 1 & 0 \\ 0 & 0 \end{bmatrix} \tag{2.5.2}$$

for the Chl b dimer studied. The reduced system dynamics was simulated from 0 to 3000 fs on each trial with a 1 fs step, obtaining the matrix elements of ρ at each time. Then, the matrices at each fixed time are recursively averaged through the trials.

To evaluate the quantum effects in the dynamics, several quantum witnesses were analyzed. First, the total energy was determined using eq. (1.3.9). The populations of the sites were determined using the absolute values of the corresponding diagonal elements $|\langle n \,|\, \rho\,(t) \,|\, n\rangle|$, while the bipartite coherences between sites was calculated using the absolute values of the relative entropy of coherence, $\mathcal{C}_S\,(\rho\,(t))$, according to eq. (1.3.28). The purity of the state was assessed using the radius of its Bloch vector.

Quantum transport has been evaluated examining the frequencies of the excitonic coherence and populations beating. The excitonic coherence refers to bipartite coherence between the excitonic states, defined by $|\langle + \,|\, \rho\,(t) \,|\, - \rangle|$, where $|\pm\rangle$ are the excitonic states. This graph generally shows a decay added to the beatings, therefore, an exponential fitting was performed on the excitonic coherence data, and substracted to obtain

the pure excitonic coherence beating. For the population and pure coherence beating, their Fourier transform was calculated using the Fast Fourier Transform for discrete data (FFT), to get their frequency components. A peak coincidence between both transforms is shows coincidence in their frequencies.

All witnesses were calculated over the averaged trajectory dynamics.

2.6 Open System Dynamics

To consider the effect of the environment, a first approach using the Redfield QME was employed. In this approach, the excitonic coupling is considered strong and the system-bath coupling is weak. In this limit, the relaxation is considered between excitonic states, and the EET dynamics are given by the Redfield equations (Cheng & Fleming, 2009; Breuer & Petruccione, 2002; Redfield, 1957),

$$\frac{d\rho_{\alpha\beta}(t)}{dt} = -i\omega_{\alpha\beta}\rho_{\alpha\beta}(t) - \sum_{\gamma\delta} R_{\alpha\beta,\gamma\delta}(t)\,\rho_{\gamma\delta}(t) \tag{2.6.1}$$

where $\omega_{\alpha\beta} = \dfrac{E_\beta - E_\alpha}{\hbar}$ is the energy gap frecuency between the excitons, and the matrix elements $\rho_{\alpha\beta}$ are the reduce density matrix (RDM) elements in the exciton basis.

The first term of the right-hand side (RHS) refers to the evolution of coherently associated excitonic states, while the second term is referred as the dissipative term, and summarizes the dynamics of energy dissipation of the reduced system to the bath. The tensor $\hat{R}$ with elements $R_{\alpha\beta,\gamma\delta}(t)$ is the Redfield relaxation tensor and describes the transfer rate from $\rho_{\gamma\delta}$ to $\rho_{\alpha\beta}$ at time t. By taking the weak bath approximation, a second order perturbative approach can be used to yield the tensor elements as,

$$\begin{aligned} R_{\alpha\beta,\gamma\delta} = -\int_0^t d\tau \Big[& \langle \Phi_{\delta\beta}(0)\,\Phi_{\alpha\gamma}(\tau)\rangle\, e^{-i\omega_{\delta\beta}\tau} + \langle \Phi_{\delta\beta}(\tau)\,\Phi_{\alpha\gamma}(0)\rangle\, e^{-i\omega_{\alpha\gamma}\tau} \\ & - \delta_{\delta\beta}\sum_s \langle \Phi_{\delta s}(\tau)\,\Phi_{s\gamma}(0)\rangle\, e^{-i\omega_{s\gamma}\tau} - \delta_{\gamma\alpha}\sum_s \langle \Phi_{\delta s}(0)\,\Phi_{s\beta}(\tau)\rangle\, e^{-i\omega_{\delta s}\tau} \Big] \end{aligned} \tag{2.6.2}$$

where the operators Φ_α correspond to the bath operators coupled to the chromophores. Then, the tensor elements can be interpreted as,

a) $R_{\alpha\alpha,\alpha\alpha}$ describes the depopulation of state $|\alpha\rangle$

b) $R_{\alpha\alpha,\beta\beta}$ describes the population transfer from $|\beta\rangle$ to $|\alpha\rangle$

c) $R_{\alpha\beta,\alpha\beta}\,(\alpha \neq \beta)$ describes the dephasing of the coherence between states $|\alpha\rangle$ and

$|\beta\rangle$, expressed in the decay of coherence $|\alpha\rangle\langle\beta|$

d) $R_{\alpha\beta,\gamma\delta}\left(\omega_{\alpha\beta}-\omega_{\gamma\delta}\neq 0\right)$ describes the coherence transfer directly from $|\gamma\rangle\langle\delta|$ to $|\alpha\rangle\langle\beta|$

At long simulation times, the Redfield tensor relaxation is time-independent, and the coherence transfer terms are neglected, this is called the secular approximation. Also, this implies that the reduced system has no memory, and therefore the system is Markovian.

In the exciton basis, the WSCP dimer is a TLS and the environment can be approximated by a collection of quantum harmonic oscillators which ground states correspond to the collective bath vibrational states of the protein scaffold normal modes. For this system, the exciton states are dubbed $|+\rangle$ for the higher exciton level and $|-\rangle$ for the lower exciton level. Restricting to the secular approximation, eq. 2.6.1 reduces to (May & Kühn, 2011),

$$\frac{d\rho_{++}}{dt} = -k_{+\to-}\rho_{++} + k_{-\to+}\rho_{--} \tag{2.6.3}$$

$$\frac{d\rho_{+-}}{dt} = -i\left(\Omega - i\gamma\right)\rho_{+-} \tag{2.6.4}$$

where $\Omega = \dfrac{E_+ - E_-}{\hbar}$ and the other matrix elements follow the relations,

$$\rho_{--} = 1 - \rho_{++} \tag{2.6.5}$$

$$\rho_{-+} = \rho_{+-}^{*} \tag{2.6.6}$$

the transition rates ($k_{\alpha\to\beta}$) and dephasing rate (γ) are given by,

$$k_{+\to-} = 2\left(1 + n\left(\Omega\right)\right)\mathcal{J}\left(\Omega\right) \tag{2.6.7}$$

$$k_{-\to+} = 2n\left(\Omega\right)\mathcal{J}\left(\Omega\right) \tag{2.6.8}$$

$$\gamma = \frac{1}{2}\left(k_{+\to-} + k_{-\to+}\right) + \gamma^{(\mathrm{pd})} \tag{2.6.9}$$

where the $\gamma^{(\mathrm{pd})}$ correspond to the pure dephasing rate, which comes from elastic interactions between the system and the bath that changes the coherence but not the energy content of the reduced system. The function $n(\omega)$ is the Bose-Einstein distribution function,

$$n(\omega) = \frac{1}{\exp\left[\frac{\hbar\omega}{k_B T}\right] - 1} \tag{2.6.10}$$

which indicates the average number of phonons in the vibrational state with frequency ω.

The function $\mathcal{J}(\omega)$ corresponds to the spectral density, and it describes the coupling strength between an electronic transition and the vibrational modes of the bath, as a function of the bath mode vibrational frequency ω. Therefore, $\mathcal{J}(\omega)$ contains all the necessary information to fully characterize the system-bath interaction.

The spectral density can be decomposed into two parts as $\mathcal{J}(\omega) = \mathcal{J}_l(\omega) + \mathcal{J}_h(\omega)$. The low energy part $\mathcal{J}_l(\omega)$ corresponds to a broad distribution, and the medium-to-high energy part $\mathcal{J}_h(\omega)$ has a discrete structure, with several peaks generally atributed to the intramolecular vibrations effects (Rosnik & Curutchet, 2015).

The low energy part depends on the specific protein, but can be well approximated by lognormal distribution functions (Kell et al., 2013),

$$\mathcal{J}_l(\omega) = \sum_{k=1}^{N} \frac{s_k}{\sigma_k\sqrt{2\pi}}\omega \exp\left[-\left(\frac{\ln\frac{\omega}{\omega_k}}{\sigma_k\sqrt{2}}\right)^2\right] \tag{2.6.11}$$

for the Chl b WSCP, $N = 3$ and $\{s_1, s_2, s_3\} = \{0.39, 0.23, 0.23\}$, $\{\sigma_1, \sigma_2, \sigma_3\} = \{0.40, 0.25, 0.20\}$ and $\{\omega_1, \omega_2, \omega_3\} = \{0.40, 0.25, 0.20\}$ cm^{-1}.

The high energy part can be considered from the experimental resonances observed via Δ-FLN (Kell et al., 2013). For each resonance, its energy ω_k and Huang-Rhys factor s_k is measured and then its broadened using the dressing function,

$$j_k(\omega) = \frac{4 s_k \omega_k \Gamma \omega \left(\omega_k^2 + \Gamma^2\right)}{\pi\left[(\omega + \omega_k)^2 + \Gamma^2\right]\left[(\omega - \omega_k)^2 + \Gamma^2\right]} \tag{2.6.12}$$

then, $\mathcal{J}_h(\omega) = \sum_{k=1}^{M} j_k(\omega)$ for a system with M vibrations, with Γ being the inverse of the characteristic broadening lifetime of the vibrational modes, $\Gamma = \tau_{brd}^{-1}$. For the Chl b WSCP, 55 vibrations have been resolved, their complete distribution is given in Appendix B.

To simplify the structure of the spectral density, a coarse-grained spectral density is considered, where the high-frequency modes are aproximated by a Lorentzian spectral density (Blau et al., 2018),

$$\mathcal{J}_{CG} = \frac{4 s_{CG} \omega_{CG} \Gamma_{CG} \omega \left(\omega_{CG}^2 + \Gamma_{CG}^2\right)}{\pi \left[(\omega + \omega_{CG})^2 + \Gamma_{CG}^2\right] \left[(\omega - \omega_{CG})^2 + \Gamma_{CG}^2\right]} \tag{2.6.13}$$

for the WSCP, the parameters for coarse-graining are $\{\omega_{CG}, s_{CG}\} = \{1350 \text{ cm}^{-1}, 0.49\}$.

Here, 3 spectral densities are used for the simulation: an underdamped density ($\Gamma = (1 \text{ ps})^{-1}$), an overdamped density ($\Gamma = (50 \text{ fs})^{-1}$), and a coarse-grained density ($\Gamma_{CG} = (50 \text{ fs})^{-1}$). Fig. 2.2 shows a comparison between them. The pure dephasing was considered adding typical values according to Caycedo-Soler et al. (2022), using $\gamma^{(\text{pd})} = 0 \text{ ps}^{-1}$ for no pure dephasing, and $\gamma^{(\text{pd})} = (2 \text{ ps})^{-1}$ with finite pure dephasing.

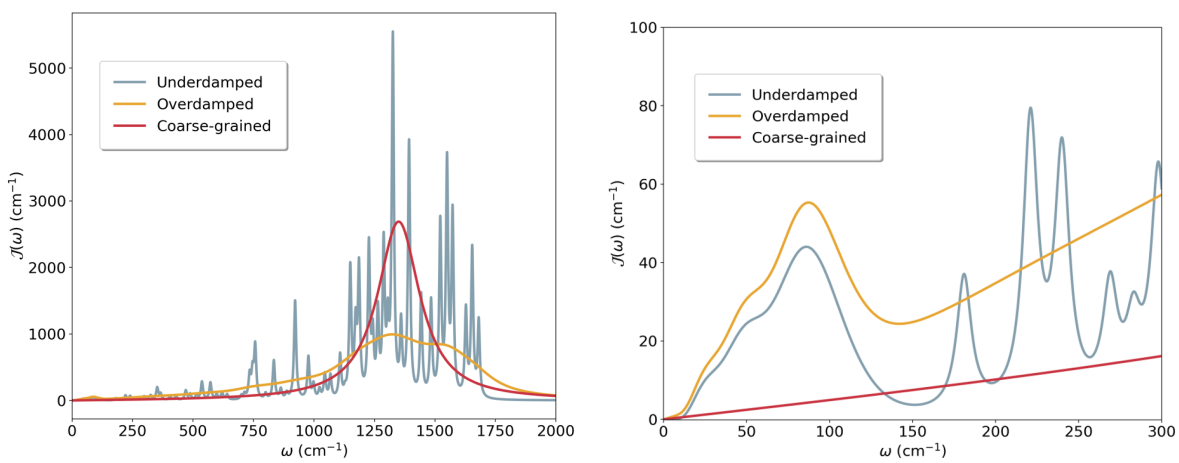

Figure 2.2: Spectral densities for the open system dynamics of the Chl b WSCP. **a)** full frequency range and **b)** low-energy region, respectively.

Considering that experimental measurements are done at low temperature, and by the principle of detailed balance, the upward transition rate is neglected; and the

eq. 2.6.3 can be directly integrated as,

$$\rho_{++}(t) = \rho_{++}(0) \exp\left[-k_{+\to-} t\right] \tag{2.6.14}$$

$$\rho_{+-}(t) = \rho_{+-}(0) \exp\left[-i\left(\Omega - i\gamma\right) t\right] \tag{2.6.15}$$

The matrix elements $\rho_{\alpha\beta}$ in the excitonic basis are related to the matrix elements in the site basis ρ_{mn} via the coefficients in eq. (1.2.14), that is,

$$\rho_{mn} = \sum_{\alpha\beta} c_{\alpha}^{(m)} c_{\beta}^{(n)^*} \rho_{\alpha\beta} \tag{2.6.16}$$

For the approximate Redfield dynamics simulations, only the parameters for ωB97X-D3BJ were considered. The reduced system dynamics was simulated from 0 to 3000 fs, on each trial, and then averaged following the same procedure that for the closed system dynamics. The initial condition is the same that for closed dynamics, but in the excitonic basis,

$$\rho_{0,\pm} = |1\rangle \langle 1|_{\pm} = \frac{1}{2} \begin{bmatrix} 1 & 1 \\ 1 & 1 \end{bmatrix} \tag{2.6.17}$$

For the consideration of the static disorder, 10^3 trials were averaged in the excitonic basis, sampling the site energies from a normal distribution around the determined values with the optimized σ as standard deviation, and diagonalizing the hamiltonian in each trial. The averaged trajectory is then converted to the site basis, and the quantum witnesses calculated for each phenomenon of interest, following the same procedures as those for the closed system dynamics.

Chapter 3

Results and Discussion

3.1 TD-DFT Parametrization

3.1.1 Evaluation of Site energies

Table 3.1 summarized the relative error computed for different DFT functionals when compared to the experimental value of 15198 cm^{-1} (658 nm). For all the categories except GGA functionals, the relative errors are higher for values calculated using TDA than with the full TD-DFT calculation (paired t-test: $p = 4.65 \times 10^{-12}$). For GGA functionals, TDA gives better results than the full TD-DFT, however, previous work has attributed this to cancelation of errors (Shao et al., 2020). This implies that the full TD-DFT calculation is necessary for the accurate simulation of the absorption spectra.

Table 3.1: Normalized root-mean squared error (NRMSE) for the calculated site energies using TD-DFT methods.

Type	Full TD-DFT NRMSE (%)	TDA NRMSE (%)
GGA	3.3	2.3
meta-GGA	8.2	12.2
Hybrid	3.8	11.5
metaH-GGA	3.0	12.0
RS Hybrid	2.6	11.3
Global	4.7	10.8

Analizing across the categories, the relative error is independent on its place in the Jacob's ladder (Mardirossian & Head-Gordon, 2017), yielding to similar values for all the categories with the only exception of the meta-GGA functionals. Fig. 3.1 shows the relative error by functional, from which it is clear that the NRMSE in the meta-GGA group is significantly higher due to the B97M-V/D3BJ functionals. The B97M-V functional has been tested with good results in the prediction of kinetic and thermochemical properties of main-group compounds from the GMTKN55 database (Najibi & Goerigk, 2018), however, there is not enough previous information about its performance on excited states calculations. It should be noticed that for functional B97M-V, the dispersion corrections are parametrized using the VV10 non-local model as part of the correlation; for the D3BJ variant, the corrections are added post-SCF convergence,

conserving the vertical transition energy.

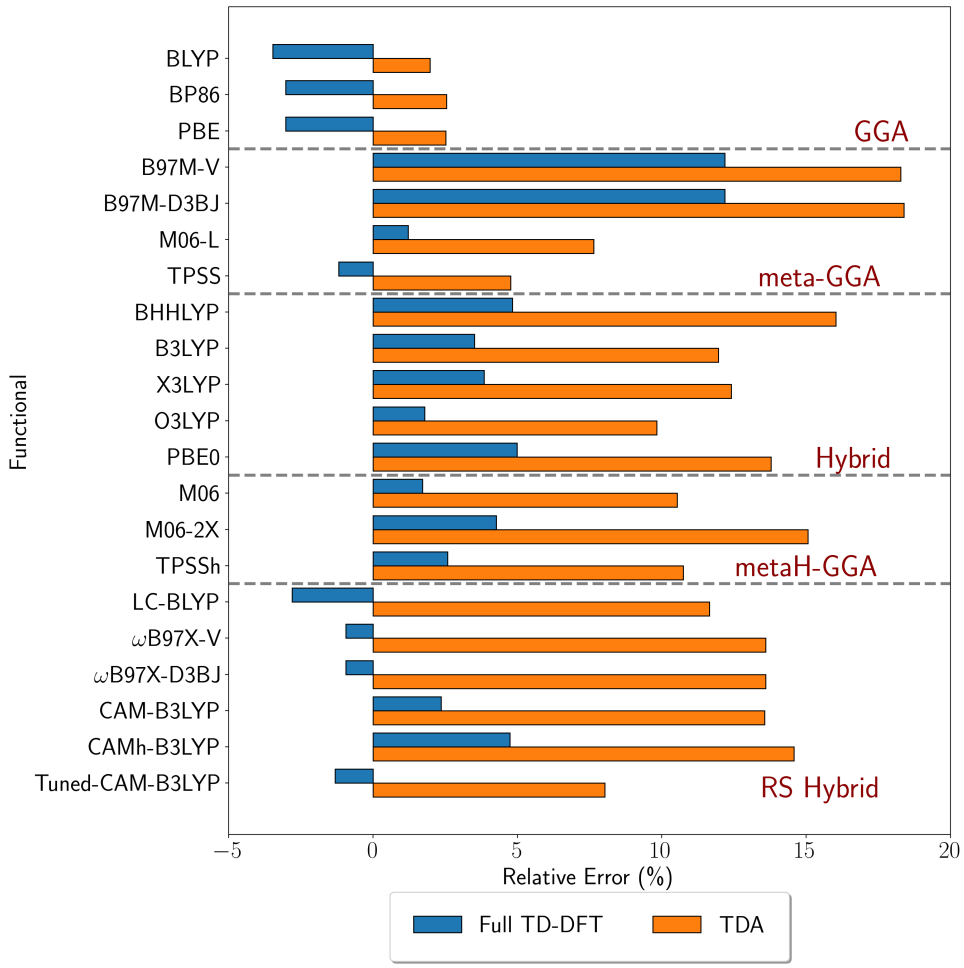

Figure 3.1: Relative errors of the calculated site energies for Chl b WSCP monomer pigment (PDB ID: 6S2Z) using TD-DFT methods.

Range-separated hybrid functionals show slightly better values than the rest of the groups. They are well known to improve the predicted values for vertical transition energies compared to hybrid functionals, correcting the charge-transfer (CT) states behaviour shown by the global hybrid functionals (Chai & Head-Gordon, 2008). This can be specially useful in PPCs, where the excitonic states can coexist with CT like excitations (Curutchet & Mennucci, 2017). In these schemes, the two-electron repulsion is separated into short and long range contributions as,

$$\frac{1}{r_{12}} = \frac{1 - [\alpha + \beta \mathrm{erf}\,(\omega r_{12})]}{r_{12}} + \frac{\alpha + \beta \mathrm{erf}\,(\omega r_{12})}{r_{12}} \tag{3.1.1}$$

The parameters α, β and ω in eq. (3.1.1) have been determined following particular statistical procedures on a benchmark training set. For example, for the CAM-B3LYP functional, the values $\alpha = 0.19$, $\beta = 0.46$ and $\omega = 0.33$ were optimized by minimizing the error for atomization energies of the small G2 set with 53 molecules (Yanai et al., 2004). However, it has been shown that these values are not appropiate for describing excited states of large molecules (Higashi et al., 2014), such as the chromophores in WSCP. To correct this, both CAMh-B3LYP ($\alpha = 0.19$, $\beta = 0.50$, $\omega = 0.33$) and Tuned-CAM-B3LYP ($\alpha = 0.0799$, $\beta = 0.9201$, $\omega = 0.150$) have been used to obtain better excited energies for dyes and biologically important chromophores, however, only the latter actually improves the calculated site energy for the WSCP, reproducing a behaviour previously reported on chlorin pigments upon reducing the value of ω on the CAM-B3LYP functional (Higashi et al., 2014).

The functionals that show better performance are ωB97X-V/D3BJ (-1.0%, -145 cm^{-1}, 6.32 nm), M06-L (1.0%, 149 cm^{-1}, 6.39 nm), TPSS (-1.2%, -182 cm^{-1}, 7.99 nm), Tuned-CAM-B3LYP (-1.3%, -200 cm^{-1}, 8.77 nm), M06 (1.7%, 261 cm^{-1}, 11.1 nm), and O3LYP (1.8%, 271 cm^{-1}, 11.5 nm). The observed errors are typical for TD-DFT calculations employing those functionals (Laurent & Jacquemin, 2013; Jacquemin et al., 2010, 2011, 2009). All of these are within 2% of the reported value. The detailed values are presented in Table 3.2.

Recently, higher-level calculations have been applied to photosynthetic pigments as an alternative to TD-DFT, such as the DLPNO-STEOM-CCSD (Sirohiwal, Berraud-Pache, et al., 2020; Sirohiwal, Neese, & Pantazis, 2020), however, this method shows a comparable accuracy with TD-DFT for the first excited states. Considering the computational cost and that higher-level methods require more extensive and careful considerations (for example, in the definition of the active space), TD-DFT represents the alternative with the most advantages in the *ab initio* calculation.

3.1.2 Evaluation of Excitonic Couplings

Using the T-TEDOPA method, a numerically exact model proposed to include the *full* vibronic contributions to the excitonic dynamics, an excitonic coupling of around

Table 3.2: Calculated site energies and global root-mean squared errors using TD-DFT methods. Experimental site energy of 15198 cm^{-1}.

Type	**Functional**	**Full TD-DFT (cm^{-1})**	**TDA (cm^{-1})**
GGA	BLYP	14669	15497
	BP86	14737	15584
	PBE	14738	15581
meta-GGA	B97M-V	17051	17977
	B97M-D3BJ	17051	17994
	M06-L	15347	16359
	TPSS	15016	15923
Global Hybrid	BHHLYP	15931	17634
	B3LYP	15732	17016
	X3LYP	15783	17084
	O3LYP	15469	16691
	PBE0	15956	17293
metaH-GGA	M06	15459	16800
	M06-2X	15846	17488
	TPSSh	15591	16831
RS Hybrid	LC-BLYP	14771	16969
	ωB97X-V	15054	17265
	ωB97X-D3BJ	15054	17265
	CAM-B3LYP	15557	17259
	CAMh-B3LYP	15919	17415
	Tuned-CAM-B3LYP	14998	16969
RMSE (cm^{-1})		724	1826
NRMSE (%)		4.7	10.8

$J = 140$ cm^{-1} was calculated to be able to predict correctly the absorption spectra of the Chl b dimer of the recombinant type IIa WSCP from cauliflower, according to Caycedo-Soler et al. (2022). This value accounts for the energy redistribution between the zero-phonon transition and its sidebands, and corresponds to a value of that is almost twice the previously determined value of $J = 69$ cm^{-1} by Renger et al. (2007). This is supported also by ZINDO QM/MMpol excited-state calculations along MD trajectories (Rosnik & Curutchet, 2015). Several methods for the calculation of the excitonic couplings are studied to assess the source of this significant discrepancy.

3.1.2.1 Coulombic methods

Table 3.3 contains the Coulombic couplings determined by 3 selected methods. In this case, PDA, TMA and TrEsp methods were used, as detailed in the Computational Methods.

Table 3.3: Excitonic Couplings for the WSCP (PDB ID: 6S2Z) calculated using Coulombic methods.

Method	$\boldsymbol{J_{14}}$ **(cm^{-1})**
PDA ($\theta_{\text{exp}} \approx 35.6°$)	60.0
PDA ($\theta_{\text{Dinh}} \approx 39.0°$)	51.7
TMA	73.6
TrEsp	75.3

The PDA method underestimates the value of excitonic coupling, this can be attributed to the breaking of the point–dipole model because of the short distance between chromophores; however, the calculated values follow the expected tendency, in which the increase in opening angle leads to a decrease of the coupling.

For both TMA and TrEsp the results can be considered equivalent, as both methods consist of the calculation of the energy between two sets of charges. The observed difference between the couplings comes from the methods employed to derive the charges. The normalized distribution of atomic charges in both methods is similar, however, their values are not; this yields to different couplings without considering the rescaling constant K. As previously discussed, the transition charges can be rescaled by a constant so that the calculated transition dipole moment coincides with the experimental transition dipoles. Upon rescaling, both methods yield to almost the same result. The values obtained are slightly higher than the previously reported value of 72 cm^{-1} obtained by Renger et al. (2007), as the latter was calculated using the WSCP structure from *Lepidinium virginicum* adjusted for the change in pigment Chl b (PDB ID: 2DRE).

To analyze the possible reasons for the discrepancies, the assumptions made in the derivation of the TrEsp method are challenged, and their relative importance in the results for the Chl b WSCP are addressed.

One of assumptions is that the transition charges are "recyclable", that is, for a fixed level of theory, the transition charges determined at the equilibrium geometry can be reused for the calculation of the excitonic couplings in any other geometry. This approximation is arguebly plausible: as long as the geometry of the pigment monomer fluctuates around its equilibrium geometry, the effect of geometrical variability on the electronic structure of the molecule and, hence, its transition density should not vary sufficiently enough to require a recalculation of the transition charges. This argument is used to justify the applicability of this method on molecular dynamics (MD) simulations (Olbrich & Kleinekathöfer, 2010).

To asses the validity of this assumption for the WSCP crystal structure, using the transition charges reported by Madjet et al. (2006) and Renger et al. (2007) and the geometries of the respective dimers in the crystal structures, one can reproduce the calculations of the couplings reported by Renger et al. (2007) (using the dipole strength of 4.0 D for Chl a and 3.6 D for Chl b). Then, once the reproducibility has been corroborated, the method with the same parameters can be applied to other systems that show similar structure and verify if the small change in geometry produces a considerably large change in the coupling or not. The results for this test on the different crystal structures of type II WSCP are summarized on table 3.4.

Table 3.4: Excitonic coupling calculated reproducing the conditions in the literature: TrEsp method, using the transition charges in (Madjet et al., 2006) and (Renger et al., 2007) and the geometries of the respective dimers in the crystal structures, using dipole strengths of 4.0 D for Chl a and 3.6 D for Chl b.

PDB Code	**Organism**	**Pigment**	$\boldsymbol{\alpha_{14}}$**(°)**	$\boldsymbol{J_{14}}$ **(cm^{-1})**
6S2Z	*B. oleracea* var. *botrytis*	Chl b	33.62	75.3
2DRE	*L. virginicum*	Chl a	29.37	74.5
6S2Y	*L. virginicum*	Chl b	28.54	85.8
6GIW	*L. virginicum* (L91P)	Chl a	23.17	85.6
6GIX	*L. virginicum* (L91P)	Chl b	24.48	95.4

For the reproducibility assessment, the reference value is the 2DRE value for a Chl a complex. In this case, the reported value of $J_{14} = 77$ cm^{-1} is close to the one calculated of $J_{14} = 77.6$ cm^{-1}, suggesting that the method is reproducible. However, it is unclear from (Renger et al., 2007) if this calculation was made using the geometrical

coordinates of the protein without further mapping to the "open-sandwich" model with the $r_{14} = 10.763$ Å and $\alpha_{14} = 29.37°$ parameters; or if the calculation is done using explicit coordinates. From the fact that no coordinates are available for the 2DRE Chl b complex, the former is suggested. Here, the coupling is calculated using the native coordinates without further mapping. These small changes in the methods of calculation could explain the 0.6 cm^{-1} difference.

Comparing results between 6S2Z and 6S2Y, its clear that upon reducing the angles between the chromophores, the coupling increases. This tendency is conserved in 6GIX, where the angles are reduced even more, and is repeated across the Chl a complexes, 2DRE and 6GIW. Taking the PDA, this coincides with the increase of the geometrical parameter κ, which maximizes for $\alpha = 0°$ for coplanar transition dipole moments. However, this increments are of no more than a 27%. Then, the small changes in the geometries between the models and the real crystal structure would not explain why the coupling has to be *doubled* to reach the T-TEDOPA new value $J = 140$ cm^{-1}.

Another premise is that the transition charges have to be rescaled by a factor that gives the same experimental transition dipole to reach the correct coupling value. To test this, the coupling between pigments i and j without rescaling J^0_{ij} can be calculated and from it, the corresponding rescaling transition dipole $\mu_{ij} = \sqrt{\mu_i \mu_j}$ can be estimated considering the target coupling of $J = 140$ cm^{-1}. These results are summarized on table 3.5, and are only calculated for Chl b complexes, since the target value was only derived for type IIa WSCP reconstituted with Chl b.

Table 3.5: Estimates of experimental rescaling transition dipole moment to reach the proposed coupling of $J = 140$ cm^{-1}. Conditions in the literature: TrEsp method, using the transition charges in Madjet et al. (2006) and Renger et al. (2007) and the geometries of the respective dimers in the crystal structures.

PDB Code	Organism	Pigment	J^0_{14} (cm^{-1})	μ_{14} (D)
6S2Z	*B. oleracea* var. *botrytis*	Chl b	77.5	4.91
6S2Y	*L. virginicum*	Chl b	74.1	4.96
6GIX	*L. virginicum* (L91P)	Chl b	80.7	4.89

From the results on table 3.5, its clear that the coupling calculated without rescaling is near the rescaled one, presented on table 3.4. This is because the calculated transition

dipole for Chl b without rescaling ($\mu_{\text{Chl b}} = 3.67 \pm 0.04$ D) is similar to rescaling factor of 3.6 D used in the literature. To reach the target value of 140 cm^{-1}, the rescaling transition dipole has to be raised up to a minimum of 4.85 D, which represents an increase of ca. 35% from the reported value by Knox & Spring (2003).

It is difficult to precise the source of the discrepancy in the transition dipole values. The transition dipole can, in principle, be determined directly from the absorption spectra of the molecule. However, if the environment can polarize, the transition properties of the chromophores are changed and the Coulomb interactions are screened (Curutchet & Mennucci, 2017). The screening factor f is introduced to compensate for this effect (Hsu et al., 2001; Knox & van Amerongen, 2002; Adolphs & Renger, 2006; Renger et al., 2007; Friedl et al., 2022), describing the change of dipole strengths due to the chromophore interaction with the surrounding dielectric medium, so that $\vec{\mu} \cdot \vec{E} = f\mu_0 E$, where E is the average electrical field acting on the transition dipole $\vec{\mu}$ and μ_0 is the corresponding molecular transition dipole strength in the vacuum (Knox & van Amerongen, 2002).

Several approaches have been proposed to calculate the screening factor, as it can either increase or the decrease the excitonic coupling (Hsu et al., 2001). For example, an "empty cavity" approach calculates the correction screening factor to the local field around the pigment, considering it enclosed in an empty spherical cavity subjected to an external homogeneous field. For such a model, f is given by (Curutchet & Mennucci, 2017),

$$f = \frac{3\varepsilon}{2\varepsilon + 1} \tag{3.1.2}$$

with ε the dielectric constant of the medium (in this case, the solvent or the protein scaffold). This particular model is used to obtain the vacuum dipole of Chl a (4.6 D) and Chl b (3.8 D) further adjusted on Renger et al. (2007) to the ones used in Table 3.4. This leads to an effective screening factor of $f = 0.87$ for Chl a and $f = 0.95$ for Chl b, which correspond to effective dielectric constants of $\varepsilon = 0.69$ and $\varepsilon = 0.86$ using the empty cavity model. The argument for the selection these screening factors is not clear on Renger et al. (2007). The article states that the screening factor is selected "similar" to the one of BChl a determined in Adolphs & Renger (2006), but the latter

sets a dielectric constant of $\varepsilon = 2$ and a screening factor of $f = 0.8$. The artificial increase of the screening factor is not explained on Renger et al. (2007), neither is the relation of the screening factor to the dielectric constant, if any is used.

As stated before, other methods could lead to a different screening factors. In fact, extrapolating directly from the linear empirical relation given by Knox & Spring (2003), a protein refractive index of $n \approx 1.4954-1.5889$ can be derived for $\mu = 4.85-5.11$ D, this corresponds to a protein dielectric constant of $\varepsilon \approx 2.24 - 2.52$, which is in the range ($\sim 2 - 4$) of the internal dielectric region of a protein, according to the microscopic description literature (Laberge, 1998) and are close to the ones used ($\varepsilon = 3$) in previous works (Hughes et al., 2006). Recently, a large scale semiempirical calculation study derived a mean dielectric constant of 3.23 ± 0.04 for more than 150000 proteins (Amin & Küpper, 2020). This variability on the optimal value used for the dielectric constant of the protein reflects the lack of consensus on the matter, reaching values from the ones stated to as high as $\varepsilon \approx 15-40$ (Pitera et al., 2001), this is largely due to the dependence of the dielectric constant on the specific definition and model used to calculate it (Schutz & Warshel, 2001). Perhaps a better description of the dielectric constant of a protein is a field that reflects the complex protein structure and electrostatic properties of its residue sequence. This approach has lead to better results than using an homogeneous dielectric constant in pK_a's prediction for tritable residues (L. Li et al., 2013).

All this calls for a more accurate description of the electrostatic properties of the protein scaffold and their relation to the transition dipole strength of the chromophore through better screening factors to *fully* explain the difference in excitonic couplings. Further research is recommended on this topic.

It has been reported that fully Coulombic methods (as TrEsp, TMA and their extensions as Poisson-TrEsp) significantly underestimate the total coupling, due to ignoring the short-range interactions (Kitoh-Nishioka et al., 2020; Fornari et al., 2017), which are enhanced in PPCs due to short distances, high orbital overlap, and high Coulombic couplings (Fornari et al., 2017). Therefore, the excitonic coupling is also calculated using diabatic approaches.

3.1.2.2 Diabatic methods

For the diabatic approach, the supermolecule model for dimers (Voityuk, 2014a) was used to estimate the couplings. In general, this method relies on the calculation of the excitonic states through a full TD-DFT calculation on the dimer, as well as over each monomer. TD-DFT has the advantage that the output gives the electric transition dipole moment coordinates, and also the energy and oscillator strength of the excitation. Therefore, the estimation of the coupling can be done using the transformation between states and their properties, avoiding extensive calculations of integrals between densities. Notice that this method works on the assumption that the diabatic states are fully localized on the monomers and the diabatic states are fully delocalized in the dimer. For the Chl b WSCP dimer studied, this can be seen in Fig. 3.2, where the MOs follow this scheme.

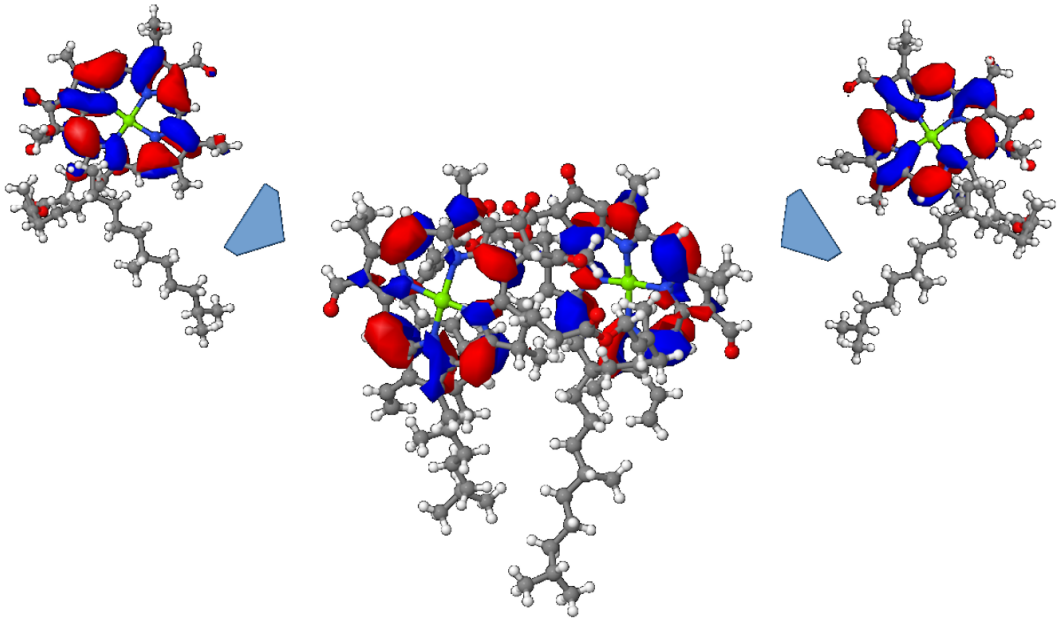

Figure 3.2: Molecular orbitals of the first excited states of the monomers and dimer of the Chl b WSCP, determined at TD-DFT/PBE0/def2-TZVP level of theory.

The diabatization procedure also relies on the description of the supermolecule states, as being fully delocalized between chromophores; and representative of the excitonic states distribution as predicted by the Frenkel hamiltonian. Depending of the particular functional, density functional methods can lead to inaccurate description

of the states. As a comparison, the linear absorption spectra of the Chl b dimer of WSCP was calculated at TD-DFT/PBE0/def2-TZVP level, and also using TD-DFTB: a semiempirical version of TD-DFT which employs the tight-binding approximation, implemented on the DFTB+ suite (Hourahine et al., 2020; Niehaus et al., 2001). Both spectra are plotted on Fig. 3.3 using a Gaussian broadening. Both spectra show very different features: TD-DFT methods show only two transitions in the range of interest, with a predicted peak after broadening around 630 nm. It is clear that TD-DFTB predicts several more transitions in the excitonic band, against the expected two from the Frenkel theory. Also, the predicted peak after broadening is more shifted to the red. This can be attributed to the approximations made from the TD-DFT theory to get to the TD-DFTB level. As DFT is a level of theory that has a higher accuracy than DFTB, the former results are the ones recommended.

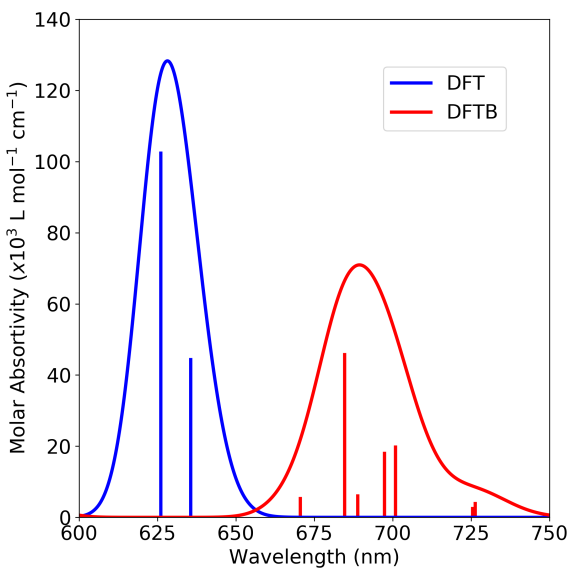

Figure 3.3: Absorption spectra for the 1–4 Chl b dimer of WSCP (PDB ID: 6S2Z) obtained using TD-DFT/PBE0/def2-TZVP and TD-DFTB methods. Verticals sticks show transition position and relative oscillator strength. Spectra plotted with Gaussian broadening with FWMH = 35 meV.

With all the advantages from this TD-DFT based diabatic method, come several disadvantages. As the calculations on the monomers and aggregate are done separately, typical errors present in TD-DFT calculations are present in all three separate calculations, increasing the possible deviations in the final result. Thus, quality metrics

are proposed to evaluate the validity of the excitonic coupling. For instance, the R parameter evaluates the ratio,

$$R = \frac{M_i^2 + M_j^2}{\mu_i^2 + \mu_j^2} \tag{3.1.3}$$

For the ideal case it follows that $R = 1$, therefore, a sufficient criteria is that the deviation $|R - 1|$ is less than certain limit. A suggested limit (Voityuk, 2014a) of 20% is applied in this work, beyond which the approximation is rendered invalid and the coupling is discarded. Moreover, in the particular case of the Chl b WSCP system studied, the coordinates of both chromophores are the same in their center-of-mass, therefore $\mu_i^2 = \mu_j^2$, and the different equations proposed for the estimation of the diabatic excitonic coupling (eq. (1.2.36)–(1.2.38)) should give similar results. As such, also a 20% maximum RSD is expected between expressions.

Using both criteria, values obtained using all GGA funcionals, as well as B97M-V, B97M-D3BJ, X3LYP and M06, are discarded (see table 3.6). These functionals fail one or both criteria, which suggest that their description of the $S_0 \rightarrow S_1$ is not good enough to estimate valid excitonic couplings. As the diabatic states are not necessarily unique nor optimal, forcing the selection of the S_1 states results in the failure of the estimation, specially in diffuse transitions. Other methods of choosing the diabatic states have been proposed using transition charges (Fornari et al., 2016; Aragó & Troisi, 2015a,b).

The values determined by diabatization strategies for WSCP are closer to the one obtained using the T-TEDOPA procedure. This suggests that the short-range interactions have been greatly underestimated for this dimer. Other studies suggest that the contribution of short-range interactions can be around 15% of the total excitonic coupling, and can be as high as 70% for more closely coupled chromophores (Fornari et al., 2017). In particular, they state that if the minimum intermolecular distance is less than 7 Å, then the short-range interactions are significantly different than the method's intrinsical errors. For the WSCP Chl b 1–4 dimer, the minimum intermolecular distance is of 0.97 Å (1.16 Å without considering H atoms); thus, short-range interactions are considered to be important.

Figure 3.4b shows the predicted excitonic coupling values by TD-DFT methods. In general, these methods gives higher couplings with respect to the ones determined by

Table 3.6: Calculated diabatic excitonic couplings and quality metrics using TD-DFT methods. In red, values that discard the respective coupling as valid, according to criteria outlined in the main text.

Type	Functional	J_{14} (cm^{-1})	R	%RSD
GGA	BLYP	55.7	0.802	21.24
	BP86	54.4	0.800	25.06
	PBE	53.2	0.800	26.84
meta-GGA	B97M-V	3.8	0.017	107.93
	B97M-D3BJ	98.2	0.125	39.03
	M06-L	81.8	0.819	4.86
	TPSS	60.4	0.814	19.00
Global Hybrid	BHHLYP	148.8	0.845	3.25
	B3LYP	104.8	0.821	1.27
	X3LYP	140.3	0.781	9.28
	O3LYP	88.5	0.829	6.08
	PBE0	118.1	0.834	3.91
metaH-GGA	M06	90.2	0.717	8.31
	M06-2X	131.4	0.826	4.37
	TPSSh	88.9	0.830	6.89
RS Hybrid	LC-BLYP	131.1	0.844	4.17
	ωB97X-V	139.5	0.848	3.89
	ωB97X-D3BJ	139.5	0.848	3.89
	CAM-B3LYP	135.6	0.844	3.62
	CAMh-B3LYP	129.8	0.841	3.65
	Tuned-CAM-B3LYP	112.3	0.833	3.87

Coulombic methods, this supports that the short-range contributions have been greatly overlooked in previous reports. Range-separated hybrids predict the best couplings compared to the 140 cm^{-1} target, and most of them give results near the target, consistent with the observed behaviour with the site energies.

The excitonic coupling depends not only on the magnitude but on the relative direction of the transition dipoles, this represents the opening angle between transition dipoles. Examining previously reported transition dipoles (Madjet et al., 2006; Dinh & Renger, 2015) the calculated opening angle is significantly different, almost doubling the reported angle. Figure 3.4 shows that the predicted direction and opening angle across functionals is very similar (average opening angle: $\theta = (65 \pm 6)^\circ$), therefore the deviations cannot account for the full variability in the excitonic couplings.

The length of the calculated transition dipoles determined ranges from 1.60 D to

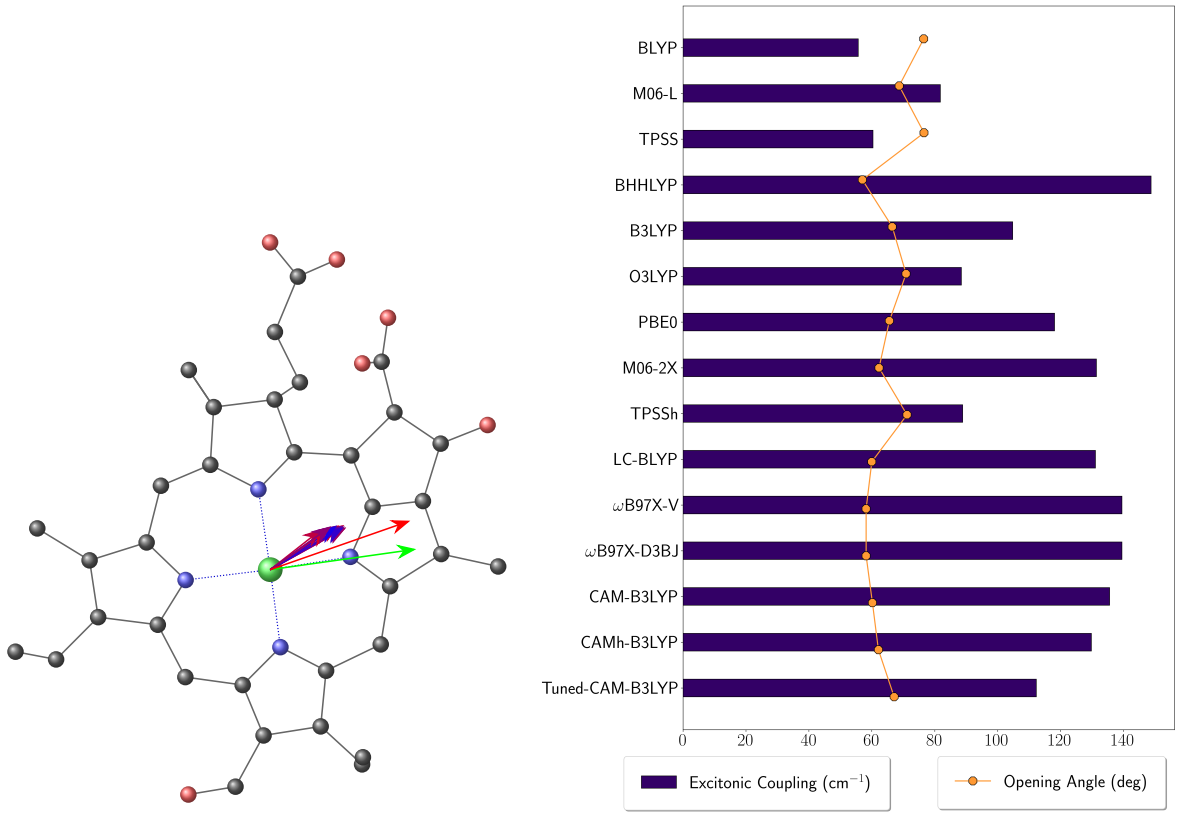

(a) ***(b)***

Figure 3.4: Excitonic couplings estimation by diabatic methods. **a)** Electric transition dipole moments determined by TD-DFT methods (group of blue to purple vectors) on the Chl b from WSCP structure. For reference, the transition dipole moment on the $N_A \rightarrow N_C$ axis (bright green) and the optimized for 39° of opening angle. Hydrogen atoms and phytyl tail have been omitted for clarity. **b)** Values of excitonic couplings and opening angle for valid functionals.

2.20 D, which is significantly lower compared to experimental data (Knox & Spring, 2003; Renger et al., 2007). Previously reported values (Renger et al., 2007; Friedl et al., 2022) of f range from around 0.80 to 1.40 for WSCP. However, taking the TD-DFT dipoles as the ones on the dielectric media, and the experimental (Knox & Spring, 2003) as the one on vacuum, predicted $f = 0.44 - 0.60$, which differ significantly. Thus, the introduction of the screening factor cannot explain the discrepancies between diabatic and Coulombic couplings.

Since neither the opening angle nor the dipole strength can explain the variability of the excitonic couplings, we attribute the increasing and variability of the determined excitonic couplings to the full supermolecule calculation, that accounts for all the

short-range and long-range contributions. Taking $J_{14} = 140$ cm^{-1} as reference, the the functionals which predict better couplings are ωB97X-V/D3BJ (-0.4%, -0.5 cm^{-1}), CAM-B3LYP (-3.1%, -4.4 cm^{-1}), M06-2X (-6.1%, -8.6 cm^{-1}), LC-B3LYP (-6.4%, -8.9 cm^{-1}), CAMh-B3LYP (-7.3%, -10.2 cm^{-1}), and PBE0 (-16%, -21.9 cm^{-1}); which show that range–separated functionals give the most accurate excitonic couplings through the diabatic method, in line with the results for site energies.

3.1.3 Optimization of Linear Absorption Spectra

3.1.3.1 Estimation of the static disorder

The parameters previously obtained are used to predict the linear absorption spectra of Chl b WSCP using HEOM simulations (Caycedo-Soler et al., 2022). However, first the estimation of the static disorder parameters σ is necessary. This is performed neglecting the vibronic coupling according to equation (1.2.51).

The effect of the static disorder of the protein (Stross et al., 2016) is taken into account through statistical distributions around the site energies with standard deviation σ. Three distributions where considered:

- Gaussian profile:

$$\mathcal{F}(E,\sigma) = \frac{1}{\sigma\sqrt{2\pi}} e^{-\frac{E^2}{2\sigma^2}} \tag{3.1.4}$$

- Lorentzian profile:

$$\mathcal{F}(E,\sigma) = \frac{2}{\pi}\frac{\sigma}{4E^2+\sigma^2} \tag{3.1.5}$$

- Voigt profile:

$$\mathcal{F}(E,\sigma) = \int_{-\infty}^{\infty} \mathcal{G}(E',\sigma)\,\mathcal{L}(E-E',\sigma)\,dE' \tag{3.1.6}$$

  where $\mathcal{G}(E,\sigma)$ and $\mathcal{L}(E,\sigma)$ are the Gaussian and Lorentzian profiles.

The estimation of σ comes from the optimization of the predicted spectra against the experimental. The election of the statistical distribution in (1.2.51) changes the shape of the predicted spectra. Fig. 3.5 shows the effect for the 3 different distributions used, obtained with the experimental site energy (15198 cm^{-1}) and TrEsp recalculated

coupling (75.3 cm^{-1}). Analogous curves for the TD-DFT derived parameters are shown on Appendix C. Notice that for the Lorentzian shows sharper peaks than Gaussian and Voigtian profiles, however, they are broader at the base. Also, Lorentzian profiles conserves the shoulder at much higher values of σ, while overestimating the shoulder height. For the Gaussian case, the shoulder only shows for $\sigma \leq 75$ cm^{-1}; for the Voigtian, the shoulder occurs at even lower values of σ and both peaks fuse rapidly with increasing σ.

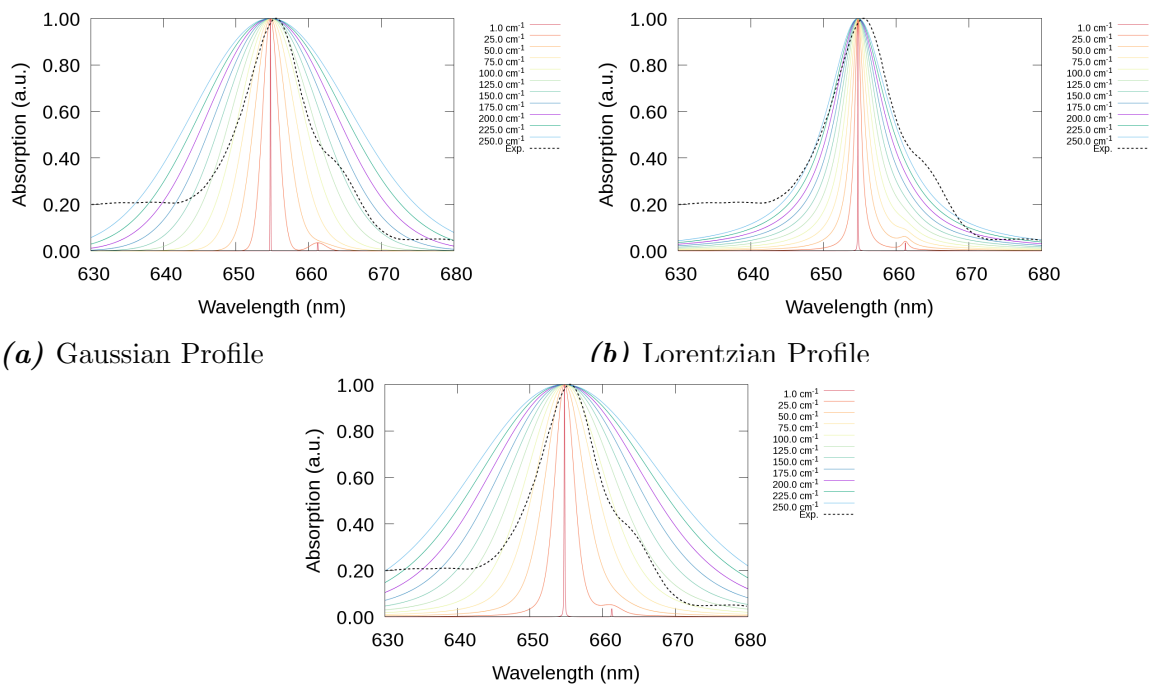

(a) Gaussian Profile

(b) Lorentzian Profile

(c) Voigtian Profile

Figure 3.5: Simulated spectra for approximate lineshapes of absorption spectra in the non-vibronic case. Effect of the statistical distribution and static disorder parameter σ. *Conditions:* experimental site energy (15198 cm^{-1}) and TrEsp recalculated coupling (75.3 cm^{-1}).

The optimization of σ is performed by numerical iteration for every distribution and parameter set for each functional, minimizing the distance between the calculated and experimental spectra with respect to σ. Several metrics can be proposed to perform the shape comparison, based on the spatial distance between their corresponding points (Efrat et al., 2007; Vlachos et al., 2002): the lesser the distance, the greater the similarity.

A simple procedure to obtain the distance is calculating the Procrustes distance (Gower

& Dijksterhuis, 2004), which consists of the cartesian measure between 2 sets of points in n dimensions. Let $\mathcal{S}_1$ and $\mathcal{S}_2$ be two shapes in 2 dimensions so that the points $\{(x_i, y_i)\} \in \mathcal{S}_1$ and $\{(u_i, v_i)\} \in \mathcal{S}_2$, each set of k points, then to calculate the Procrustes distance between $\mathcal{S}_1$ and $\mathcal{S}_2$, 3 transformations are performed:

1. Traslation: both shapes are centered around their centroids $(\overline{x}, \overline{y})$ and $(\overline{u}, \overline{v})$, defined as,

$$\overline{x} = \sum_i \frac{x_i}{k} \quad ; \quad \overline{y} = \sum_i \frac{y_i}{k} \quad ; \quad \overline{u} = \sum_i \frac{u_i}{k} \quad ; \quad \overline{v} = \sum_i \frac{v_i}{k} \tag{3.1.7}$$

then, the transformations are so that,

$$(x_i, y_i) \mapsto (x_i - \overline{x}, y_i - \overline{y}) \quad ; \quad (u_i, v_i) \mapsto (u_i - \overline{u}, v_i - \overline{v}) \tag{3.1.8}$$

2. Scaling: both shapes are resized to the same scale. The statistical size of each shape can be estimated from the RMSD of the points. Let it be α_i for $\mathcal{S}_i$, then,

$$\alpha_1 = \sqrt{\frac{\sum_i (x_i - \overline{x})^2 + (y_i - \overline{y})^2}{k}} \quad ; \quad \alpha_2 = \sqrt{\frac{\sum_i (u_i - \overline{u})^2 + (v_i - \overline{v})^2}{k}} \tag{3.1.9}$$

then, the shape is divided by its size, so that both shapes are rescaled to size 1,

$$(x_i, y_i) \mapsto \left(\frac{x_i - \overline{x}}{\alpha_1}, \frac{y_i - \overline{y}}{\alpha_1} \right) \quad ; \quad (u_i, v_i) \mapsto \left(\frac{u_i - \overline{u}}{\alpha_2}, \frac{v_i - \overline{v}}{\alpha_2} \right) \tag{3.1.10}$$

3. Rotation: both shapes are rotated to the same orientation. To do this, one of the shape has to be selected as the reference, and the other is rotated to match the first one. Let $\{(X_i, Y_i)\}$ and $\{(U_i, V_i)\}$ be the traslated and rescaled sets, and take the first one as the reference, then the rotated shape with points $\{(W_i, Z_i)\}$ is given by,

$$\begin{bmatrix} W_i \\ Z_i \end{bmatrix} = \begin{bmatrix} \cos\theta & -\sin\theta \\ \sin\theta & \cos\theta \end{bmatrix} \begin{bmatrix} U_i \\ V_i \end{bmatrix} \tag{3.1.11}$$

the optimal rotation angle can be determined by minimizing the RMSD between

the rotated shape and the reference using a least squares procedure, then,

$$\tan\theta = \frac{\sum_i (Y_i U_i - X_i V_i)}{\sum_i (X_i U_i + Y_i V_i)} \tag{3.1.12}$$

After the transformations, the Procrustes distance d_P between both shapes is given by the Cartesian distance of the mapped points, given by,

$$d_P = \sqrt{\sum_i \left[(W_i - X_i)^2 + (V_i - Y_i)^2\right]} \tag{3.1.13}$$

in this case, the reference figure is the experimental linear absorption spectrum.

From measure theory, other metrics can be defined. In the case of two functions f, g that belong in a L^p metric space, both belong to the same equivalence class if the norm of their substraction is zero (Rudin, 1987; Wheeden & Zygmund, 1977), that is,

$$\left(\int |f - g|^p d\mu\right)^{\frac{1}{p}} = 0 \tag{3.1.14}$$

then, the more similar the functions, the norm of their substraction is closest to zero. The expression $||f||_p = \left(\int |f|^p d\mu\right)^{\frac{1}{p}}$ is called the L^p-norm of the metric space.

In particular, the Procrustes distance, the L^1–norm and the L^2–norm have been evaluated as similarity metrics between the estimated and experimental spectra. An example of the behaviour of the 3 metrics is shown of Fig. 3.6; analogous curves for the rest TD-DFT derived parameters are shown on Appendix C. For all conditions and metrics, the graph is different, however, in the vicinity of the minima, all of them form a well. For Lorentzian profiles, all metrics have similar graphs and are wider than for Gaussian and Voigtian profiles. Procrustes metric show narrower minima in all cases, which increases its method sensitivity, thus, this is the preferred metric.

Fig. 3.7 compares the different behaviour of the Procrustes distance for the different profiles. The distance is calculated for a wide range of values for σ, and then the minimal value is taken as optimal for every distribution. Curves for the rest TD-DFT derived parameters are shown on Appendix C. Again, Lorentzian profiling shows

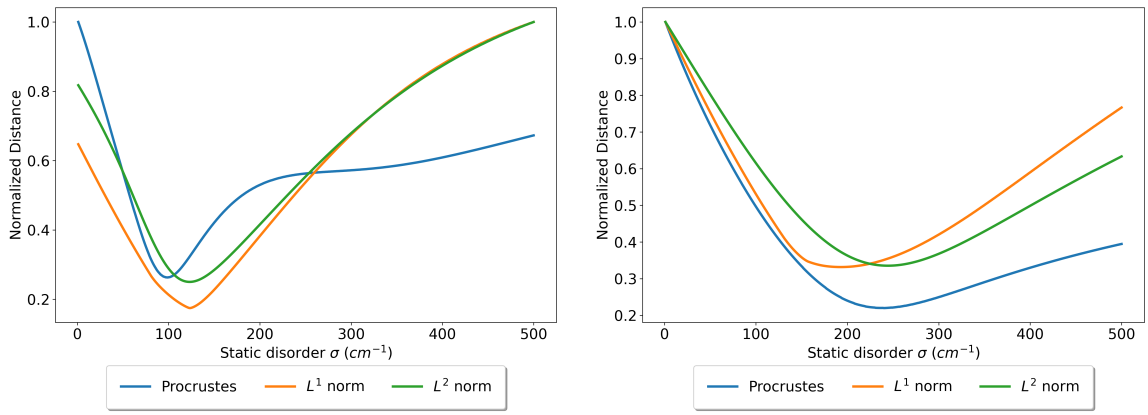

(a) Gaussian Profile

(b) Lorentzian Profile

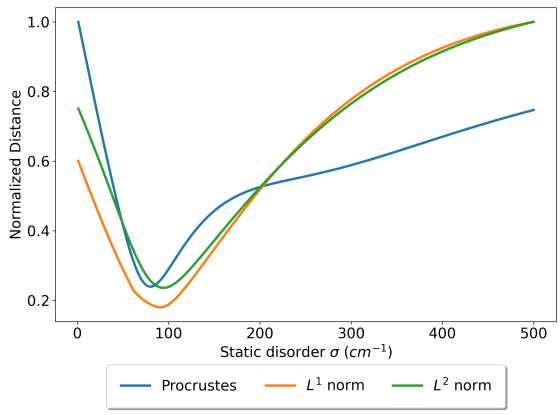

(c) Voigtian Profile

Figure 3.6: Behaviour of different similarity metrics for the optimization of approximate spectral lineshapes. Effect of the statistical distribution and static disorder parameter σ. *Conditions:* experimental site energy (15198 cm^{-1}) and ωB97X-D3BJ recalculated coupling (139.5 cm^{-1}).

remarkably different results than Gaussian and Voigtian, with much wider and shallower minimum, this suggest that the Lorentz distribution is completely inadequate for the approximation. Gaussian and Voigtian profiling show very similar results, with Voigtian giving slightly deeper minimum, which suggest a better spectrum.

Examining the results for the optimal values in table 3.7, similar optimal values are found across all the functionals, with percentual relative standard deviation (%RSD) of around 10% for static disorders and Procrustes distances alike. This indicates that the static disorder can be estimated as an independent parameter from the TD-DFT functional, only associated with the PPC and profiling. Comparing the averages, the Lorentzian profile give a slightly lower Procrustes distance, however, the corresponding

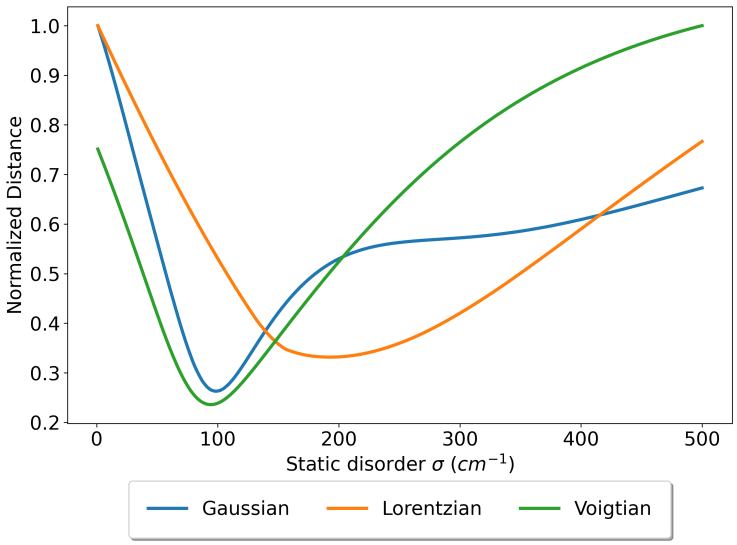

Figure 3.7: Example of the numerical optimization of σ by minimization of the Procrustes distance. *Conditions:* experimental site energy (15198 cm^{-1}) and ωB97X-D3BJ recalculated coupling (139.5 cm^{-1}).

static disorder is more than doubled from previous studies for WSCP (Dinh & Renger, 2015; Renger et al., 2009, 2007) an other PPCs (Khmelnitskiy et al., 2019; Adolphs & Renger, 2006; Raszewski et al., 2005; Novoderezhkin et al., 1999), which suggests is unphysical and an artifact of the numerical optimization, owing also to its low sensitivity, in accordance with previously seen behaviour. Therefore, the Lorentzian profile is discarded. For the other two profiles, the results are similar, but different statistically (paired t-test: $p = 0.00282$). Hence, the Voigtian profile gives better results, which optimized value for the static disorder is (72 ± 7) cm^{-1}, in accordance with previous studies (Caycedo-Soler et al., 2022).

Table 3.7: Optimal static disorder parameters σ (in cm^{-1}) and minimal Procrustes distances for the sets of parameters determined using TD-DFT methods.

Type	**Functional**	**Gaussian**		**Lorentzian**		**Voigtian**	
		σ	*Distance*	σ	*Distance*	σ	*Distance*
meta-GGA	M06-L	81	0.422	192	0.348	65	0.390
	TPSS	85	0.405	249	0.341	71	0.366
Global Hybrid	BHHLYP	106	0.334	254	0.271	87	0.298
	B3LYP	81	0.399	206	0.333	67	0.366
	O3LYP	79	0.459	191	0.382	62	0.423
	PBE0	87	0.396	217	0.334	72	0.364
metaH-GGA	M06-2X	96	0.371	235	0.312	78	0.339
	TPSSh	83	0.459	195	0.386	65	0.427
RS Hybrid	LC-BLYP	93	0.362	225	0.309	65	0.427
	ωB97X-V	98	0.346	238	0.292	80	0.314
	ωB97X-D3BJ	98	0.346	238	0.292	80	0.314
	CAM-B3LYP	96	0.358	234	0.299	78	0.325
	CAMh-B3LYP	94	0.366	235	0.305	77	0.333
	Tuned-CAM-B3LYP	81	0.430	203	0.370	66	0.400
Average		90	0.390	222	0.327	72	0.363
%RSD		9.4	10.6	9.7	10.9	10.5	12.3

3.1.3.2 Vibronic Spectra

Optical processes dynamics are highly affected by vibronic effects, therefore, the correct lineshape theory must include the full description of all important PPC vibrations and their interplay with the excited states of the chromophores (May & Kühn, 2011). The Hierarchical equations of motion (HEOM) is an infinite set of Partial Differential Equations (PDEs) that describe the time-evolution of the reduced density matrix of the chromophoric aggregate in the bath of vibrational motions of its protein scaffold, by considering a linear coupling between the quantum system and the thermal bath of quantum harmonic oscillators (Jing et al., 2013; Chen et al., 2009).

Fig. 3.8 shows selected spectra obtained by numerically exact simulations, performed employing the HEOM method. The spectra for the rest TD-DFT derived parameters are shown on Appendix C. Qualitatively, functionals with $J_{14} \approx 140$ cm^{-1} show the correct features: the peak with a shoulder to red side, and a planar side to the blue side of the peak; meanwhile, lower excitonic couplings cannot reproduce the same behaviour, as is the case of TPSS. Neither functional can predict the relative height of the peak and its shoulder faithfully.

For a shifted hamiltonian with $E = 0$ cm^{-1}, using equation (1.2.16), the higher (+) and lower (−) exciton dipole strenghts $\mu_\pm$ are given by,

$$\mu_\pm = \mu\sqrt{1 \pm \cos\theta} \tag{3.1.15}$$

where μ is the dipole strength of the monomer transition. This shows that the ratio of strengths (which determined the relative height of the peaks) is given by,

$$\frac{\mu_+}{\mu_-} = \sqrt{\frac{1+\cos\theta}{1-\cos\theta}} = \left|\cot\frac{\theta}{2}\right| \tag{3.1.16}$$

which decreases rapidly with increasing angle for $0 \leq \theta \leq \frac{\pi}{2}$. The ratio for the experimental data is approximately 2.86 (1/0.35), which solves for $\theta \approx 39°$, that coincides with previous estimates (Dinh & Renger, 2015; Caycedo-Soler et al., 2022). The TD-DFT estimate for the opening angle is at least 60% higher, which leads to the discrepancies

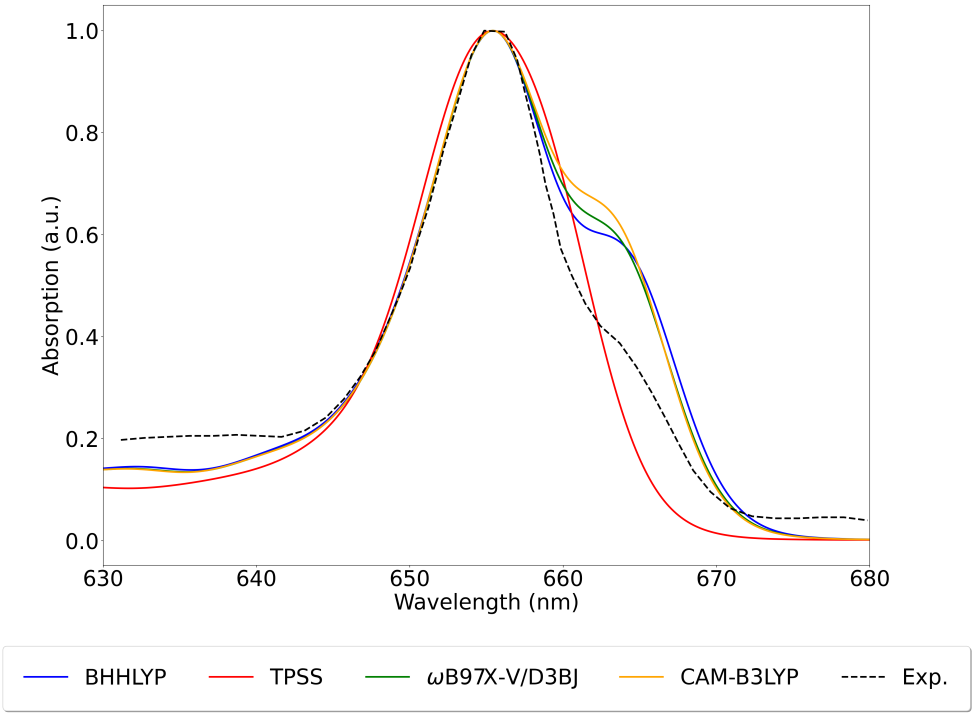

Figure 3.8: Simulated spectra for numerically exact lineshapes of linear absorption in the full vibronic picture. All site energies have been shifted so that the highest peak coincides with the experimental.

in the relative height of the peaks, reducing the ratio to 1.57 (1/0.64) on average. This comparison can be seen in Fig. 3.9. Therefore, the increase in opening angle explains the difference in relative height.

The orientation of the predicted transition dipoles by TD-DFT has not been explored thouroughly in the literature, but comparison to high level wavefunction theory calculations show deviations of around 9° on average, with maximal values near 34° for similar functionals (Robinson, 2018). This amount of errors in both the monomer transition dipoles could explain the large predicted opening angle. Methods to achieve better orientations of the transition dipoles have to be studied further, as small conformational changes can lead to large changes in the transition dipole (Brand et al., 2011).

To analyze the quality of HEOM-predicted spectra with TD-DFT parameters, de-

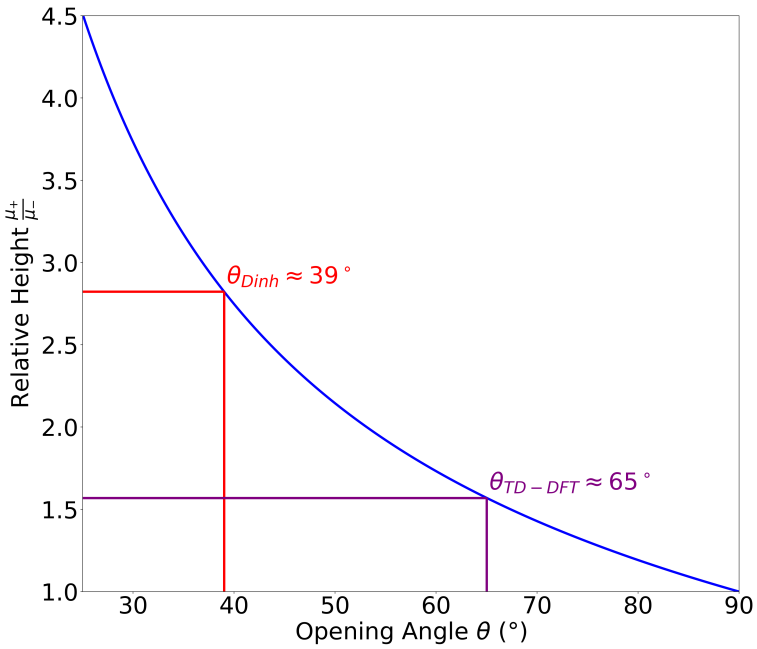

Figure 3.9: Dependence of the theoretical relative height between the peak and shoulder with the opening angle.

convolution of the spectra was performed into two Voigtian peaks of the form,

$$V(\omega) = A_0 \,\mathrm{Re}\left[W\left(\frac{\omega - \omega_0 + i\gamma}{\sigma\sqrt{2}}\right)\right] \tag{3.1.17}$$

where A_0 is the area under the peak, ω_0 is the frequency of the peak center, γ and σ are related to the underlying broadening through the standard deviations of respective Lorentzian and Gaussian profiles, and $W(z)$ is the Faddeeva function,

$$W(z) = e^{-z^2}\left(1 + \frac{2i}{\sqrt{\pi}}\int_0^z e^{t^2}dt\right) \tag{3.1.18}$$

The experimental spectra shows an almost horizontal zone between 630 nm and 640 nm, which leads to poor results in the curve-fitting procedure. To consider this effect, an artificial baseline $B(\omega)$ is inserted on the blue side of the major peak only, given by,

$$B(\omega) = (m\omega + b)\left[1 - H_s(\omega)\right] \tag{3.1.19}$$

where m and b define the linear regression of the first 1000 data points of each spectrum,

and $H_s(\omega)$ is the softened Heaviside function,

$$H_s(\omega) = 1 - \frac{1}{1 + e^{\lambda(\omega - \omega_s)}} \tag{3.1.20}$$

where λ is the softening parameter, which determines how sharp is the jump, and ω_s is the switch frequency at which the baseline is switched off. Thus, the full absorption spectra fitting function for deconvolution is,

$$\alpha(\omega) = B(\omega) + V_1(\omega) + V_2(\omega) \tag{3.1.21}$$

The curve-fitting was performed minimizing the residuals using the least-squares method. From each fit, 12 parameters are adjusted: 4 for each Voigtian peak $(A_0, \omega_0, \sigma, \gamma)$, and 4 for the baseline $(m, b, \lambda, \omega_s)$. Examples of the curve-fitting results are shown in Fig. 3.10. The curves for the rest of the functionals are shown on Appendix C.

From each peak, the center of the peak ω_0 and its height h_{max} are extracted, and compared to the experimental analogues, using the excitonic splitting E and the relative height P, defined as,

$$E = \omega_{0,+} - \omega_{0,-} \qquad ; \qquad P = \frac{h_{max,+}}{h_{max,-}} \tag{3.1.22}$$

as quality performance metrics. Fig. 3.11a shows the behaviour of the errors of both figures across the functionals, making the distance to the center the measurement of the full deviations. It is clear that range-separated hybrids perform best, as they are clustered near the center fo the graph, which is in line with the observations on the performance for both site energies and excitonic couplings. Meanwhile, meta-GGA and metaH-GGA functionals perform the worst, as a consequence of the lower J_{14} predicted by these functionals. Global hybrids give mixed results: functionals like PBE0 have distances similar to RS Hybrids, however, this behaviour does not reproduce in other functionals of the same category.

A combined measurement of both contributions to the errors is the distance to the

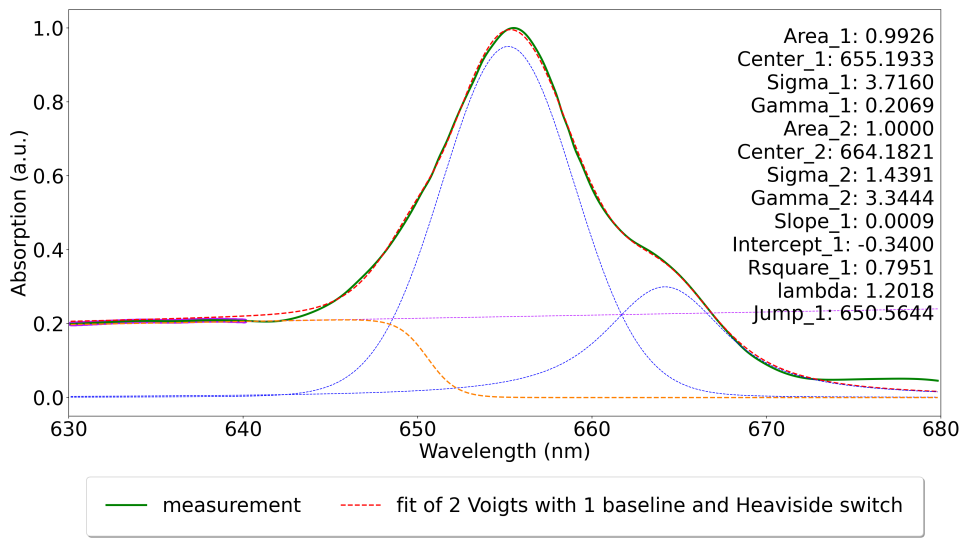

(a) Experimental

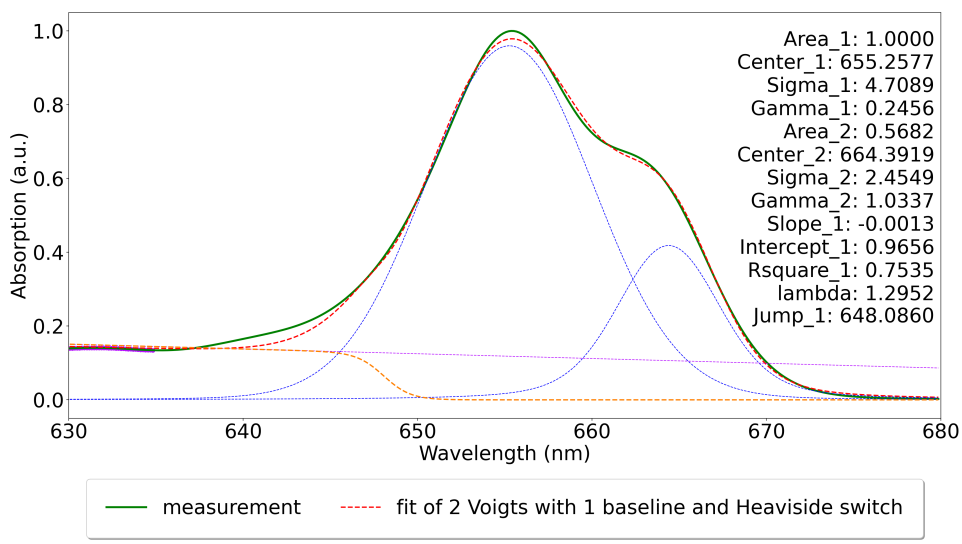

(b) CAM-B3LYP

Figure 3.10: Deconvolution of simulated spectra for HEOM lineshapes obtained for experimental data and CAM-B3LYP calculated spectroscopical parameters.

center of the relative error plot, is given by,

$$d_{error} = \sqrt{\left(\frac{E}{E_{exp}} - 1\right)^2 + \left(\frac{P}{P_{exp}} - 1\right)^2} \tag{3.1.23}$$

This error distance is the one shown on Fig. 3.11b. It is clear that for meta-GGA functionals the distances are much greater than for the rest of functionals. The RS

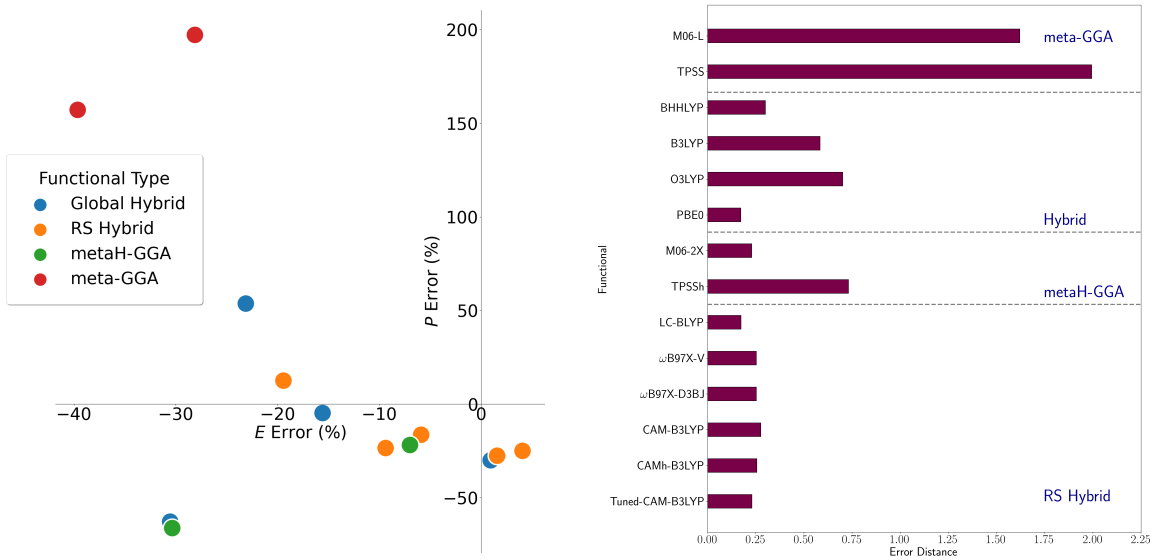

(a) ***(b)***

Figure 3.11: Relative errors for quality figures of merit for TD-DFT derived parameters in the prediction of linear absorption spectra, predicted HEOM lineshape theory. **a)** Metric percentage relative errors compared to the deconvolution of experimental data. **b)** Error distance as a measurement of the total deviation from experimental data.

hybrids perform the best, with very similar distances (%RSD = 17%), being LC-BLYP the best functional, followed by Tuned-CAM-B3LYP, ωB97X-V/D3BJ, CAMh-B3LYP and CAM-B3LYP.

Global hybrid functionals have very different performances between them. This variability is usually associated with the relative amount of Hartree-Fock (HF) exchange in the exchange–correlation contributions, and several benchmarks select functionals according to their HF exchange percentage (Laurent & Jacquemin, 2013; Jacquemin et al., 2009). For the functionals here assessed the HF exchanges are 50% for BHHLYP, 20% for B3LYP, 12% for O3LYP and 25% for PBE0. Thus, a positive correlation can be observed for the first 3 functionals between their performance and HF exchange, however, for PBE0 the error distance is abnormally low, being also the lowest of all the functionals across all categories. PBE0 is a functional that minimizes the effect of the self-interaction errors in the calculation of excited states, which explains the outlier behaviour (Adamo & Barone, 1999).

3.2 Quantum Effects in the WSCP EET

3.2.1 Liouville-von Neumann Dynamics

A first approach to analyze the EET dynamics in the system, is the limit of null coupling between the system and the bath, which leads to a closed system with non-dissipative dynamics. This gives information about the quantum characteristics of the system, and how the different parameters interplay with each other.

The energy landscape for the aggregate (Fig. 3.12a) shows significantly different energies for every functional, however the energy splittings are very similar, which suggests that the dynamics would also be similar for all cases. As the system is closed, the dynamics are non-dissipative and this energy must be conservative. This coincides with the behaviour observed in Fig. 3.12b, where the energy remains almost constant, owing its variability to the static disorder of the system. The disorder of the aggregate generates a statistical distribution of the hamiltonian, which implies a noisy distribution of the total energy. Indeed, the %RSD of all the energy values along the simulation is not greater than 0.01% for each tested functional. Notice that the value of energy depends on the functional, which coincides with the site energy of the first site, as indicated by the starting condition selected and the conservative nature of the system.

The EET dynamics can be seen directly from the site populations ($\rho_{nn}(t) = |\langle n| \rho(t) |n\rangle|$) and coherences. The former denotes the probability that the system is in certain state $|n\rangle$ at some time t, and the latter, the interaction between states. Fig. 3.13a and 3.13b show the dynamics for the site populations on the first site, for both the case with and without static disorder. In all cases, the population starts at 1, as expected, and oscillates sinusoidally around an offset of 0.5. This is a direct consequence of the form of the time-dependent Schrödinger equation and the initial state selected: for an initial state that is a superposition of the eigenstates of the system Hamiltonian, the time evolution yields a superposition of oscillations, or wave packet. The difference in phases of each coherent oscillation in the superposition produces the quantum beating observed in the populations, which indicates that the initial populations travel from one site

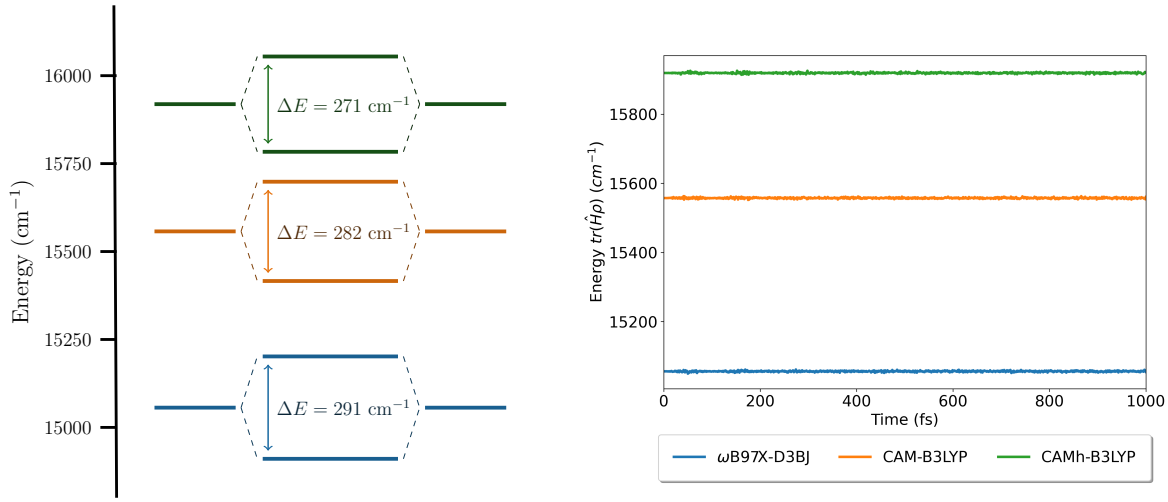

(a) ***(b)***

Figure 3.12: Energy distribution for the closed system dynamics of the Chl b WSCP. **a)** Energy landscape of the excitonic system determined from TD-DFT parameters. **b)** Total energy dynamics. Color symbology is the same for **a)** and **b)**.

to the other, back and forth with certain frequency. If the starting state were a pure eigenstate of the hamiltonian, then the time evolution would yield a time-independent solution for the populations (May & Kühn, 2011).

In both figures 3.13a and 3.13b the 3 oscillations do not have the same frequency Ω. The order is as follows Ω (CAMh-B3LYP) $<$ Ω (CAM-B3LYP) $<$ Ω (ωB97X-D3BJ), which is the same order than the energy splitting calculated. The inclusion of the static disorder results in a damping of the amplitude of the oscillations. This is owed to the difference in site energies in each trial: each sample lead to a different phase relation with the same average frecuency, as the phase relations are averaged out for several trials, the result is a dephasing of the population and the amplitude decays exponentially (May & Kühn, 2011).

The populations dynamics can also be analyzed from the coherence witness, in this case, the relative entropy of coherence $\mathcal{C}_S$, according to eq. 1.3.28. Fig. 3.13c and 3.13d show the coherence dynamics in the site basis. The selection of the basis is extremely important, and must be considered in the interpretation of the results, as the witness quantifies the coherence between the basis states. As expected, the coherence starts at 0, since the starting state is a pure basis state. The oscillations are also present in this witness, however, the wave shape changes to a $\sin^2 \Omega t$ type. The maximal value for the

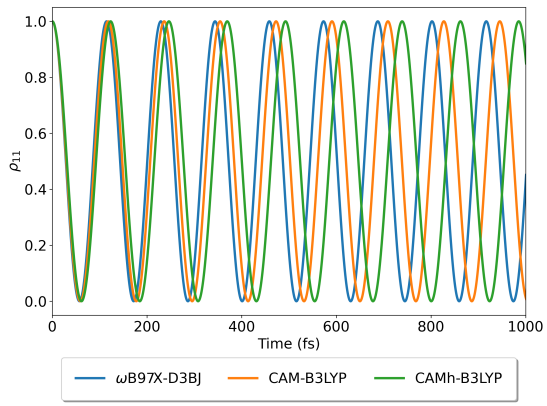

(a) Populations with $\sigma = 0$ cm^{-1}

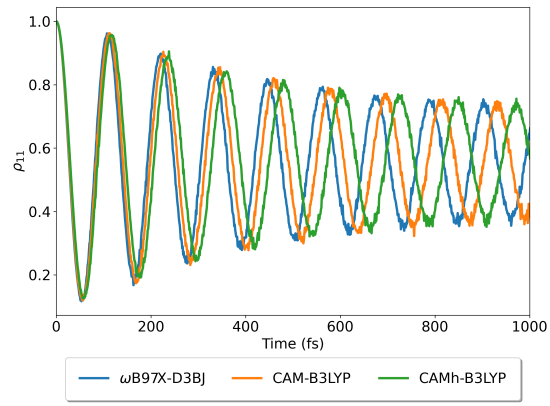

(b) Populations with $\sigma \neq 0$ cm^{-1}

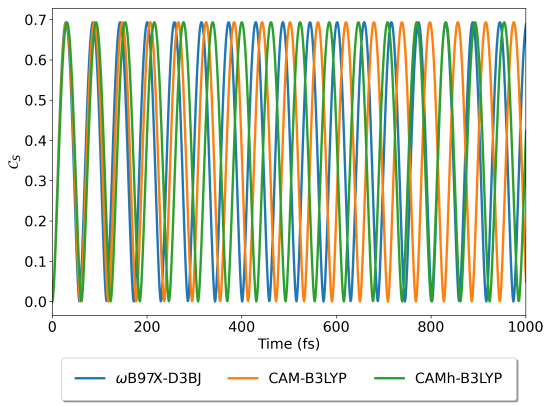

(c) Coherences with $\sigma = 0$ cm^{-1}

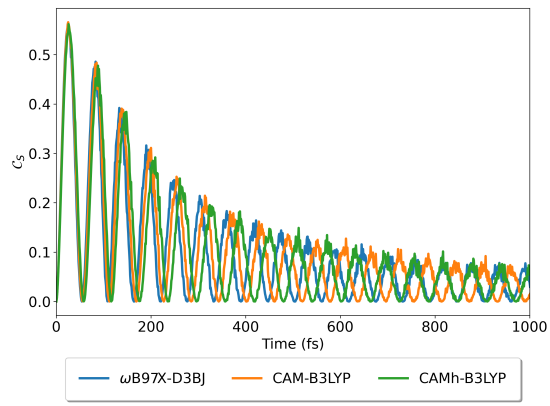

(d) Coherences with $\sigma \neq 0$ cm^{-1}

Figure 3.13: Populations and coherence for the closed system dynamics of the Chl b WSCP, and dependence with the TD-DFT parameters. The populations shown are for the first site, and the relative entropy of coherence is considered as coherence witness. **a)** and **b)** show population dynamics without and with static disorder, respectively. **c)** and **d)** show coherence dynamics without and with static disorder, respectively.

coherence corresponds to the maximum value of the von Neumann entropy,

$$S(\rho) = -\mathrm{Tr}\left[\rho \ln \rho\right] \tag{3.2.1}$$

which in this case maximizes to $\ln 2 \approx 0.69$. The differences in frequencies are still present in the coherences, and follow the same order than before. The addition of the static disorder also produces a decay in the amplitude of the oscillations, however, the damping is more pronounced than in the populations. As stated before, this can be attributed to the dephasing of the multiple waves averaged, however it is clear that this is more correctly described as the decoherence of states due to the static disorder.

To further examine the effect of the static disorder, one can consider the purity of the state: the measurement of how much a state is a mixed. For a completely pure state, $\mathrm{Tr}\left[\rho^2\right] = 1$, while for a mixed state $\mathrm{Tr}\left[\rho^2\right] < 1$. The degree of mixing $\gamma = \mathrm{Tr}\left[\rho^2\right]$ can be used to decide whether a system is mixed or not, for the maximally mixed state in a Hilbert space of dimension N,

$$\rho_{\text{max. mixed}} = \frac{1}{N} I_N \Rightarrow \gamma = \frac{1}{N} \tag{3.2.2}$$

then, $\frac{1}{N} \leq \gamma \leq 1$. However, this measure is not necesarily monotonically decreasing upon mixing. To realize a more adequate witness of purity, the depiction of the state on the Bloch sphere can be analyzed (Nielsen & Chuang, 2010). For an arbitrary state with a density matrix ρ in the Hilbert space for $N = 2$, then,

$$\rho = \frac{I_2 + \vec{R} \cdot \vec{\sigma}}{2} \tag{3.2.3}$$

where $\vec{R} = (R_x, R_y, R_z)$ is the Bloch vector and $\vec{\sigma} = (X, Y, Z)$ is the vector which entries are the Pauli matrices. Then, the degree of purity is,

$$\gamma = \frac{1 + R_{Bloch}^2}{2} \tag{3.2.4}$$

where $R_{Bloch} = |\vec{R}|$, and therefore the state is pure when $R_{Bloch} = 1$, and the state is maximally mixed when $R_{Bloch} = 0$. Hence, the length of the Bloch vector decreases monotonically in the interval $[0, 1]$ when the state becomes less pure. Notice that the length of the Bloch vector can be recovered from,

$$R_{Bloch} = \sqrt{\left(\mathrm{Tr}\left[\rho X\right]\right)^2 + \left(\mathrm{Tr}\left[\rho Y\right]\right)^2 + \left(\mathrm{Tr}\left[\rho Z\right]\right)^2} \tag{3.2.5}$$

Fig. 3.14a and 3.14b show the purity dynamics without and with static disorder, using R_{Bloch} as a purity witness according to eq. (3.2.5). It is clear that for the case without static disorder the state remains pure in all cases, as the state system is set as pure at the beginning, and the unitary evolution does not alter the purity of the system,

as is the case of the closed system. However, the inclusion of the state disorder now produces an ensemble of wavefunctions, all valid for the system, as they represent the variability introduced in the static disorder and the dephasing. The beatings are still conserved, moreover, the frequencies of oscillation also follow the same order than for the populations and coherences. Also, the purity of the system starts at 1, as expected by the initial condition set; but the center of the oscillations decays exponentially. This is a clear indicative of the ensemble nature of the quantum state for the aggregate.

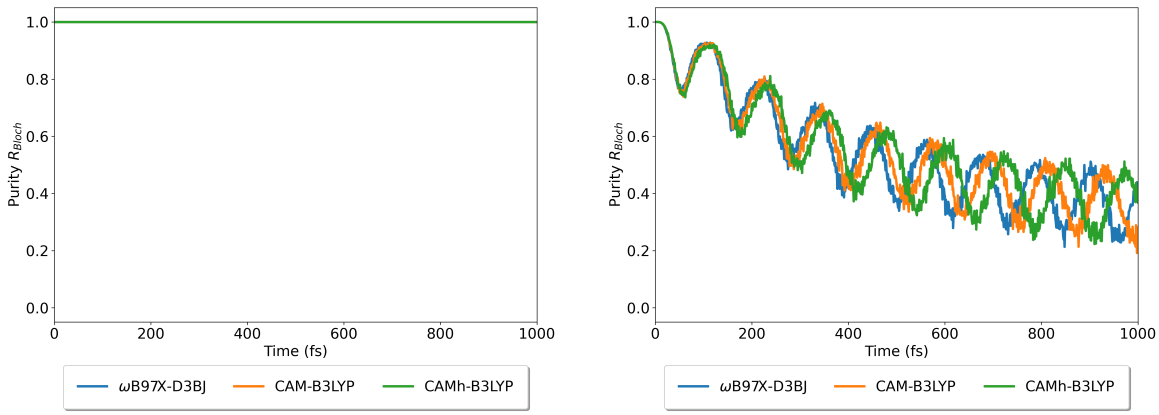

(a) Purity with $\sigma = 0$ cm^{-1} ***(b)*** Purity with $\sigma \neq 0$ cm^{-1}

Figure 3.14: Purity for the closed system dynamics of the Chl b WSCP, and dependence with the TD-DFT parameters. The radius of the Bloch vector is used as purity witness. **a)** and **b)** show purity dynamics without and with static disorder, respectively.

For the evaluation of quantum transport, the excitonic states are obtained from diagonalization of the average hamiltonian. As the Chl b WSCP is a dimer, the resulting aggregate is a two-level system (TLS), where the higher and lower excitons are represented by the states $|+\rangle$ and $|-\rangle$, respectively. The excitonic coherence is then given by,

$$\mathcal{C}_{ext} = \rho_{\pm} = |\langle + \,|\, \rho\,(t)\,|\, - \rangle| \tag{3.2.6}$$

where $\rho_{\pm}$ represents the density matrix in the excitonic basis, this means that matrix elements $\rho_{\alpha\beta}$ of $\rho_{\pm}$ are related to the matrix elements in the site basis ρ_{mn} via the coefficients in eq. (1.2.14), that is,

$$\rho_{\alpha\beta} = \sum_{mn} c_{\alpha}^{(m)} c_{\beta}^{(n)^*} \rho_{mn} \tag{3.2.7}$$

Fig. 3.15 show the excitonic coherence dynamics, for the case with no static disorder, the excitonic coherence is constant a 0.5, which shows that the exciton is constantly delocalized between the two sites. Including the static disorder, makes the excitonic coherence decay exponentially and oscillates, sign of the decoherence phenomenon as discussed previously.

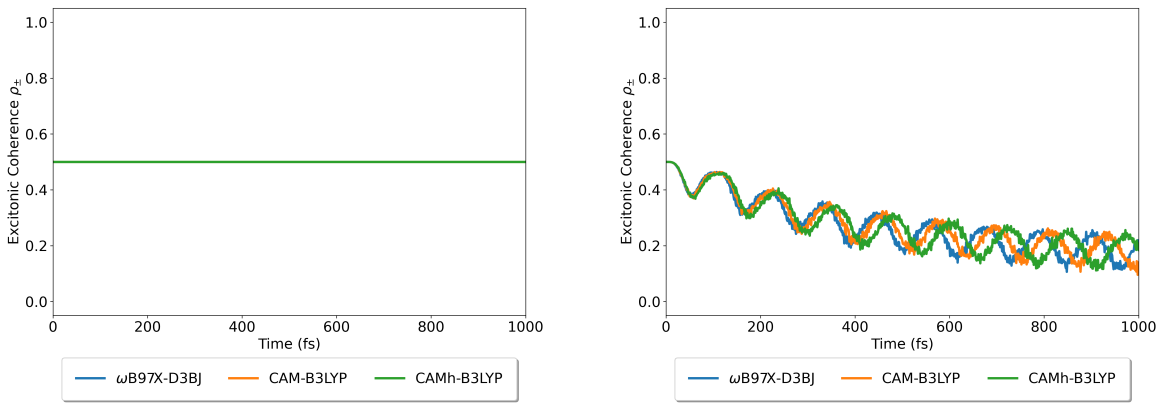

(a) Excitonic coherence with $\sigma = 0$ cm^{-1} ***(b)*** Excitonic coherence with $\sigma \neq 0$ cm^{-1}

Figure 3.15: Excitonic coherence for the closed system dynamics of the Chl b WSCP, and dependence with the TD-DFT parameters. The relative entropy of coherence of ρ in the exciton basis is used as a coherence witness. **a)** and **b)** show excitonic coherence dynamics without and with static disorder, respectively.

As stated before, to witness quantum transport, the excitonic coherence most drive the population dynamics, and therefore must have the same beating frequency. As the excitonic coherence shows a decay mixed with the beating, an exponential fitting of the data is performed to extract only the coherence beating. Fig. 3.16 shows an example of this procedure. For the ordered condition ($\sigma = 0$ cm^{-1}), the excitonic coherence is constant, and no beating is observed, therefore, the procedure fails.

Fourier analysis is performed on the population and excitonic coherence beating trajectories. Using the FFT, the frequency content of both signals is analyzed: to show coherence between them, their oscillation frequency and waveform most be the same. As the populations oscillate as an underdamped sine wave, only one frequency peak is expected; however, the excitonic coherence beating shows fast oscillations of almost constant amplitude around their average line, which also oscillates with a much slower frequency, therefore, two peaks are expected in the Fourier transform. Fig. 3.17 shows

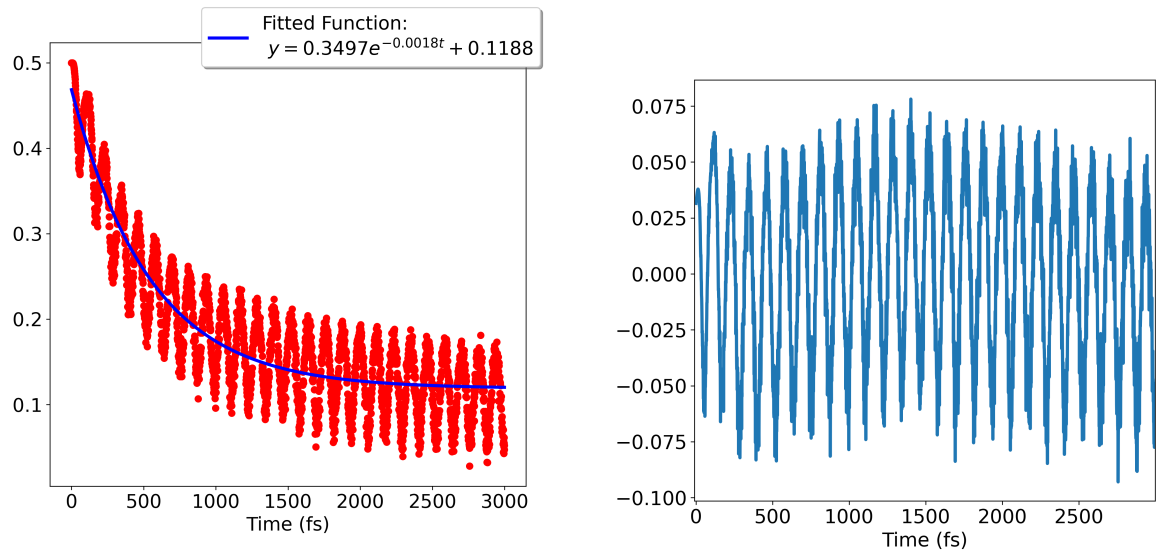

(a) Excitonic coherence fit ***(b)*** Extracted beating

Figure 3.16: Excitonic coherence beating extraction for the closed system dynamics of the Chl b WSCP. The exponential fit of the excitonic coherence is shown on **a)**, and **b)** shows the excitonic coherence beating extracted. *Conditions:* TD-DFT/CAM-B3LYP parameters with $\sigma = 78$ cm^{-1}.

the FFTs of both witnesses for the analyzed conditions.

It is clear from Fig. 3.17 that the beating frequency of both witnesses coincide, which is a sign of the presence of quantum transport phenomena. This behaviour is independent on the choice of parameters, and therefore, it suggests that is a characteristic of the system in a closed conservative regimen.

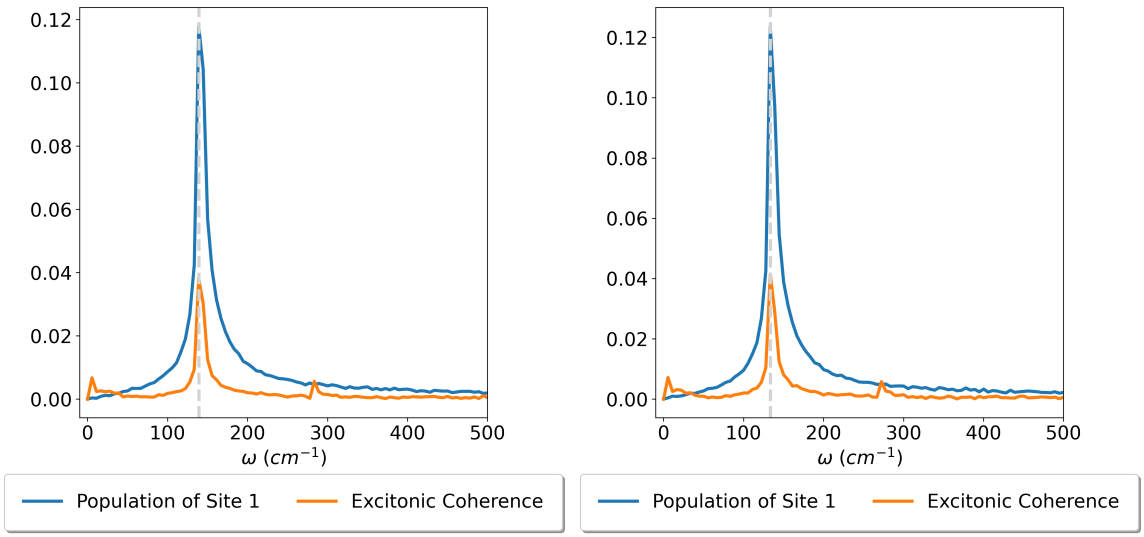

(a) CAM-B3LYP

(b) CAMh-B3LYP

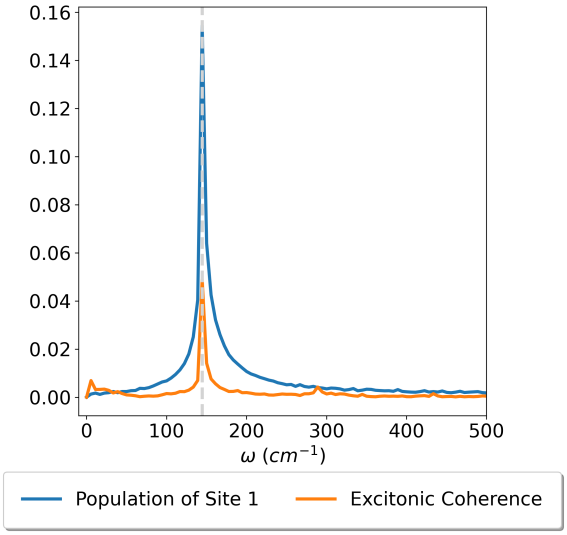

(c) ωB97X-V/D3BJ

Figure 3.17: Quantum transport evaluation in the Chl b WSCP for closed system dynamics, and dependence on the TD-DFT parameters. The FFT of the population of site 1 and the excitonic coherence beating are shown. Dotted lined shows the frequency of the population beating.

3.2.2 Approximate Redfield Dynamics

The presence of a protein scaffold around the pigments in the WSCP leads to vibronic dynamics due to the coupling between the EET and the vibrational motions that change the electronic structure of each chromophore in time. This interaction then produces decoherence of the excitonic states, and has to be considered to accurately describe the EET dynamics. Therefore, an open quantum system approach has to be used to describe the dissipative dynamics. Here, the approximate secular Redfield dynamics is used for the low temperature two-level system (TLS), considering that the experimental spectra are measured at 77 K.

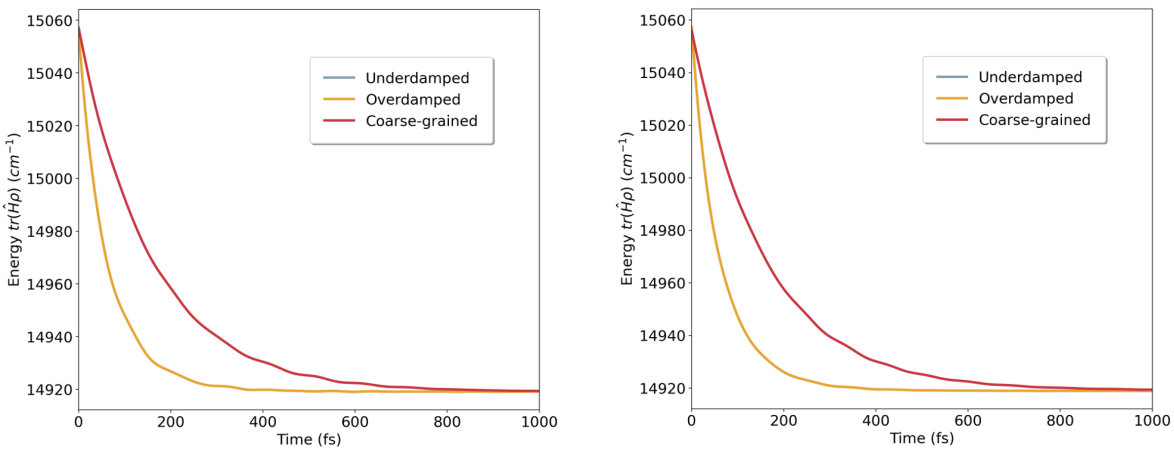

(a) $\gamma^{(\mathrm{pd})} = 0\ \mathrm{ps}^{-1}$ ***(b)*** $\gamma^{(\mathrm{pd})} = (2\ \mathrm{ps})^{-1}$

Figure 3.18: Energy for the open system dynamics of the Chl b WSCP, and dependence on the spectral density selection. **a)** and **b)** show energy dynamics without and with pure dephasing, respectively.

Fig. 3.18 shows the energy dynamics for the open system. It is clear than in this regimen, energy is lost to the environment until an equilibrium is achieved, consecuence of the dissipative dynamics. As in the Redfield approach, the coupling to the environment is considered weak, the excitonic coupling is much higher than the environmental coupling, therefore the energy lost corresponds only to the excitonic coupling. This is a particular case for the resonant condition of the monomers: for a more general case, the energy value for the equilibrium is E_-, and the energy loss is half the excitonic splitting, $\dfrac{E_+ - E_-}{2}$.

The amount of energy lost to the environment is independent on the spectral den-

sity selection, nor the addition of pure dephasing affects it. However, the time to reach equilibirium is affected by the former. For the overdamped system, the equilibrium time is much shorter than for the underdamped and coarse-grained cases; this is expected, as the overdamped modes oscillate much faster, and so does the energy disperses. For underdamped and coarse-grained conditions, the behaviour is the same, this is consequence of similar values of $\mathcal{J}(\Omega)$.

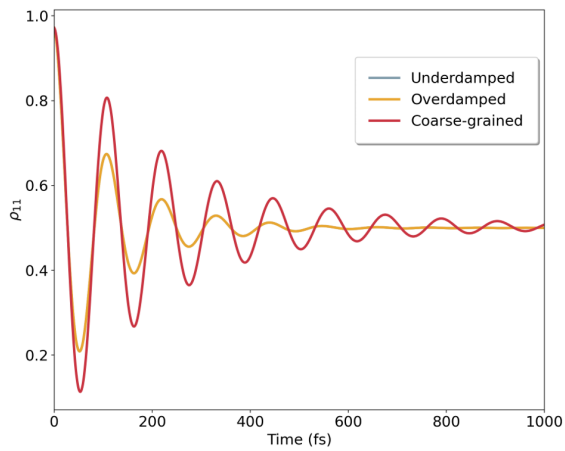

(a) Populations, $\gamma^{(\mathrm{pd})} = 0\ \mathrm{ps}^{-1}$

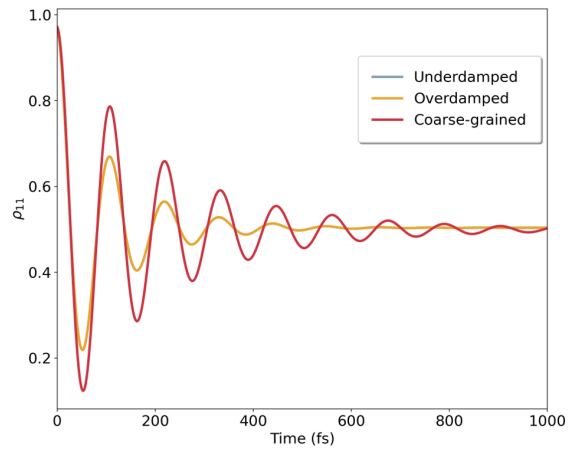

(b) Populations, $\gamma^{(\mathrm{pd})} = (2\ \mathrm{ps})^{-1}$

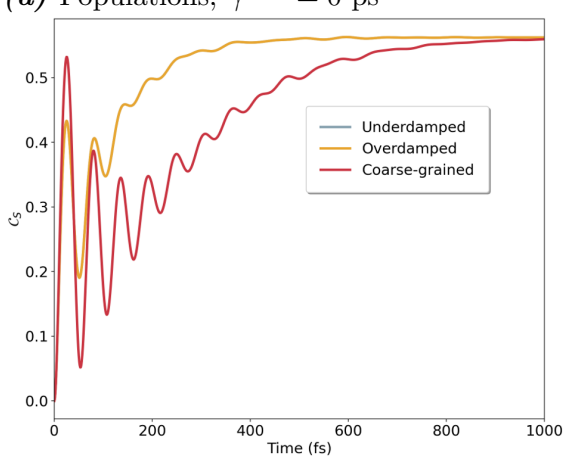

(c) Coherence, $\gamma^{(\mathrm{pd})} = 0\ \mathrm{ps}^{-1}$

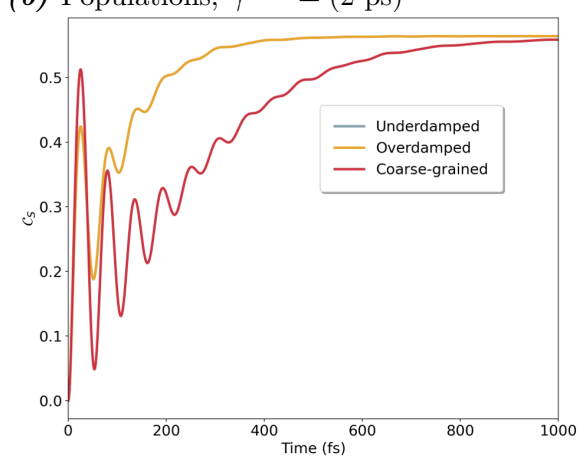

(d) Coherence,$\gamma^{(\mathrm{pd})} = (2\ \mathrm{ps})^{-1}$

Figure 3.19: Populations and coherences for the open system dynamics of the Chl b WSCP, and dependence on the spectral density selection. **a)** and **b)** show populations for the first site dynamics without and with pure dephasing, respectively. For the bipartite coherence, the relative entropy of coherence is used as witness. **c)** and **d)** show coherence dynamics without and with pure dephasing, respectively.

It is worth noting that the coarsed-grained and the underdamped spectral densities have very different lineshapes, but result in the same behaviour: as the approximation

used here only needs one point of the spectral densities, all the complex attributes are lost. Higher level, numerically exact calculations can lead to different results by considering the contributions of the rest of couplings (Caycedo-Soler et al., 2022).

The population and coherence dynamics for the open system are shown on Fig. 3.19. The populations show the same underdamped sinusoidal wave behaviour than in the closed system case, however, their amplitude decrease much faster; even faster in the case of overdamped vibrations. This implies that the coupling to the environment suppresses the beating, and forces the system to reach equilibrium much faster. The addition of pure dephasing only slightly reduces the observed amplitudes, which implies that pure dephasing also contributes to the damping.

During the first femtoseconds of the dynamics, the coherences show similar oscillations than in the closed case. However, they are also damped because of the coupling to the environment. In this case, the value of the coherences without the beating increases until its stabilizes to a maximally coherent state. For a TLS, this state is of the form (Bai & Du, 2015),

$$|\phi\rangle = \frac{1}{\sqrt{2}} \left(|1\rangle \langle 1| + |2\rangle \langle 2| \right) \tag{3.2.8}$$

which coincides with the equilibrium state suggested by the populations, and also, is consistent with the Markovian nature of the secular approach used in the simulation. For the coherences, the same effect of the pure dephasing is observed as in the case of the populations, where only slightly damps the oscillations.

Finally, Fig. 3.20 show the quantum transport evaluation for the open system, performed with the same procedure than in the closed system case. For all the spectral densities, presence of quantum transport is clear in the case of no pure dephasing, however, the addition of it completely suppresses the presence of quantum transport. This suggests that pure dephasing is the principal mechanism that breaks quantum transport. Further research is suggested with numerically exact, non-Markovian methods to study in detail the relative importance of decoherence mecanisms in the presence of quantum transport.

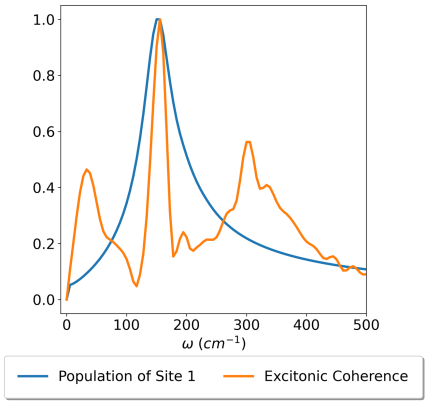

(a) Underdamped, $\gamma^{(\mathrm{pd})} = 0\ \mathrm{ps}^{-1}$

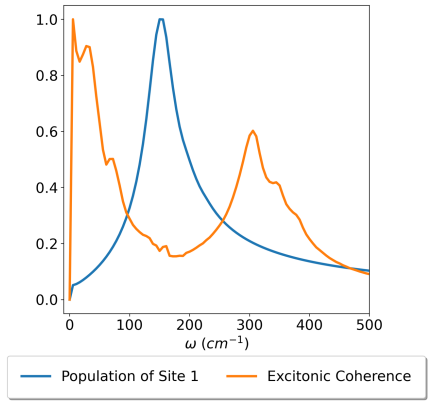

(b) Underdamped, $\gamma^{(\mathrm{pd})} = (2\ \mathrm{ps})^{-1}$

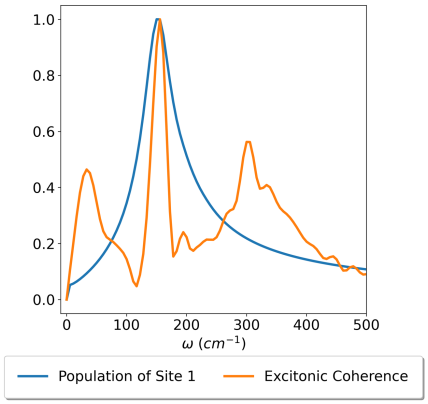

(c) Overdamped, $\gamma^{(\mathrm{pd})} = 0\ \mathrm{ps}^{-1}$

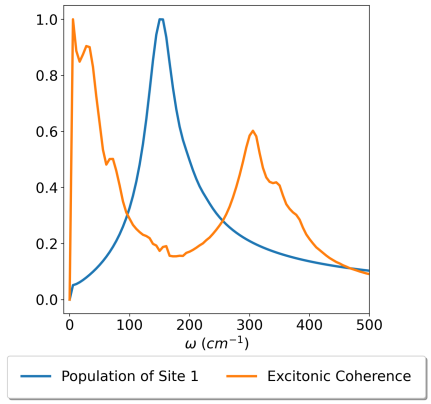

(d) Overdamped, $\gamma^{(\mathrm{pd})} = (2\ \mathrm{ps})^{-1}$

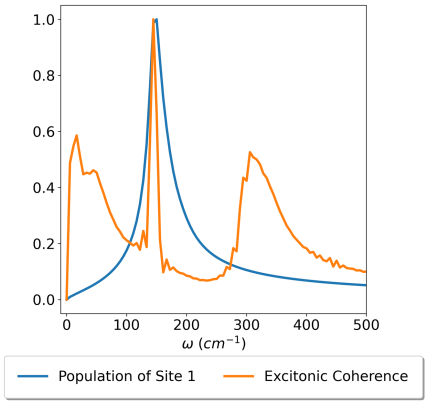

(e) Coarse-grained, $\gamma^{(\mathrm{pd})} = 0\ \mathrm{ps}^{-1}$

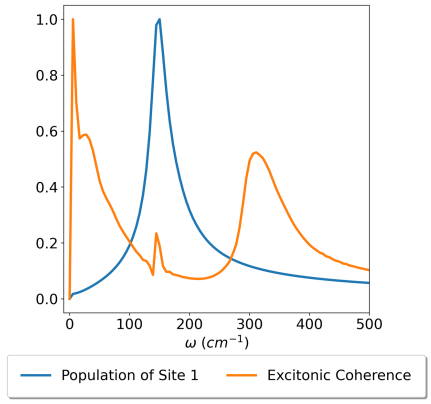

(f) Coarse-grained, $\gamma^{(\mathrm{pd})} = (2\ \mathrm{ps})^{-1}$

Figure 3.20: Quantum transport evaluation in the Chl b WSCP for open system dynamics, and dependence on the spectral density selection. **a)** and **b)** shows the evaluation for the underdamped spectral density ($\tau_{brd} = 1$ ps) without and with pure dephasing, respectively. **c)** and **d)** shows the evaluation for the overdamped spectral density ($\tau_{brd} = 50$ fs) without and with pure dephasing, respectively. **e)** and **f)** shows the evaluation for the coarse-grained spectral density ($\tau_{brd} = 50$ fs) without and with pure dephasing, respectively.

Chapter 4

Concluding Remarks

In this work, the quantification of presence and prevalence of quantum effects in PPCs was evaluated through Quantum Chemical and Computational techniques.

First, the relevant spectroscopical parameters for the chromophoric aggregates were obtained using *ab initio* methods in the Frenkel model framework. For the site energies, the calculations show excellent agreement with the experimental values at the TD-DFT/def2-TZVP level, with better values predicted by range-separated hybrid functionals. It was also demonstrated that the Tamm Dancoff approximation is insufficient for the quantitative prediction of site energies. For completion, it is recommended to perform calculations employing double hydrid methods and parametrizations for range separated functionals to assess their performance.

For the prediction of the excitonic couplings, a numerically exact fully vibronic method was considered as reference for the evaluation of different techniques. Coulombic methods give almost half of the reference value, which is not explained by structural differences; however, the influence of the dielectric properties of the protein scaffold on the transition dipole moment is not clear, which can affect the rescaling of the couplings.

Diabatic methodologies, using TD-DFT calculations, show excellent results for the calculation of the excitonic couplings. This is attributed to the inclusion of long and short range interactions, in contrast to the Coulombic methods, that only account for long range interactions. Range separated functionals give better results overall, while global hybrids give mixed results; it is recommended to fully study the nature of the predicted excited states to understand the source of these discrepancies.

For the prediction of the linear absorption spectra of the PPC, first, the static disorder was estimated using a non-vibronic model. It was demonstrated that this parameter can be estimated independently of the TD-DFT functional, and is dependent on the statistical distribution selected for the broadening. Voigtian broadening show the best results, with the Procrustes distance as the best metric to asses quality of the spectra. The static disorder obtained coincides with previous reports. Vibronic linear absorption spectra were simulated using the obtained parameters, showing that range-separated functionals give the best results in the accurate prediction of the spectra; with the ex-

ception of the relative height of the peaks, which shows significant discrepancies, owing to the opening angle predicted. It is recommended to investigate the source of this discrepancies and possible solutions to give more accurate transition dipoles.

To study the presence of quantum coherence and transport in the EET dynamics, the time evolution of the system was obtained under closed and open system paradigms. The closed system dynamics show that in this regimen the energy is conservative. The populations and coherence show sinusoidal oscillations with a frequency dependent on the excitonic splitting. The introduction of the static disorder effects leads to dephasing and decoherence in the dynamics, resulting in a mixing of the states in a statistical ensamble. Through Fourier analysis, it was shown that the closed system presents quantum transport in the disordered case, independently of the functional selected for the parameters calculation.

The approximate Redfield dynamics simulation shows that the coupling to the environment damps the quantum beatings and rapidly forces the system to an equilibrium state, which corresponds to a maximally coherent state. The use of overdamped spectral densities greatly lowers the lifetime of the oscillations, while pure dephasing only slightly contributes to the damping. The evaluation of quantum transport shows that the absence of pure dephasing allows the quantum transport, while its inclusion completely suppresses it. Further research is recommended using numerically exact, non-Markovian methods to fully account for the intermediate couplings to the environment and vibronic effects, in order to fully assess the relative importance of decoherence and dephasing sources to the suppression of quantum transport.

References

Adamo, C., & Barone, V. (1999, April). Toward reliable density functional methods without adjustable parameters: The PBE0 model. The Journal of Chemical Physics, 110(13), 6158–6170. Retrieved 2020-11-27, from http://aip.scitation.org/doi/10.1063/1.478522 doi: 10.1063/1.478522

Adolphs, J., & Renger, T. (2006, October). How Proteins Trigger Excitation Energy Transfer in the FMO Complex of Green Sulfur Bacteria. Biophysical Journal, 91(8), 2778–2797. Retrieved 2019-04-08, from https://linkinghub.elsevier.com/retrieve/pii/S0006349506719932 doi: 10.1529/biophysj.105.079483

Agostini, A., Meneghin, E., Gewehr, L., Pedron, D., Palm, D. M., Carbonera, D., ... Collini, E. (2019, December). How water-mediated hydrogen bonds affect chlorophyll a/b selectivity in Water-Soluble Chlorophyll Protein. Scientific Reports, 9(1), 18255. Retrieved 2020-03-02, from http://www.nature.com/articles/s41598-019-54520-4 doi: 10.1038/s41598-019-54520-4

Ai, Q., Yen, T.-C., Jin, B.-Y., & Cheng, Y.-C. (2013, August). Clustered Geometries Exploiting Quantum Coherence Effects for Efficient Energy Transfer in Light Harvesting. The Journal of Physical Chemistry Letters, 4(15), 2577–2584. Retrieved 2019-04-08, from http://pubs.acs.org/doi/10.1021/jz4011477 doi: 10.1021/jz4011477

Amin, M., & Küpper, J. (2020, January). Variations in Proteins Dielectric Constants. arXiv:2001.07053 [physics]. Retrieved 2020-03-03, from http://arxiv.org/abs/2001.07053 (arXiv: 2001.07053)

Anda, A., Hansen, T., & De Vico, L. (2016, March). Multireference Excitation Energies for Bacteriochlorophylls A within Light Harvesting System 2. Journal of Chemical Theory and Computation, 12(3), 1305–1313. Retrieved 2020-11-26, from https://pubs.acs.org/doi/10.1021/acs.jctc.5b01104 doi: 10.1021/acs.jctc.5b01104

Aragó, J., & Troisi, A. (2015a, January). Dynamics of the Excitonic Coupling in Organic Crystals. Physical Review Letters, 114(2), 026402. Retrieved 2020-11-29, from https://link.aps.org/doi/10.1103/PhysRevLett.114.026402 doi: 10.1103/PhysRevLett.114.026402

Aragó, J., & Troisi, A. (2015b, April). Excitonic couplings between molecular crystal pairs by a multistate approximation. The Journal of Chemical Physics, 142(16), 164107. Retrieved 2020-11-29, from http://aip.scitation.org/doi/10.1063/1.4919241 doi: 10.1063/1.4919241

Bai, Z., & Du, S. (2015, November). Maximally coherent states. Quantum Information and Computation, 15(15&16), 1355–1364. Retrieved from https://doi.org/10.26421/qic15.15-16-6 doi: 10.26421/qic15.15-16-6

Bailleul, B., Rogato, A., de Martino, A., Coesel, S., Cardol, P., Bowler, C., ... Finazzi, G. (2010, October). An atypical member of the light-harvesting complex stress-related protein family modulates diatom responses to light. Proceedings of the National Academy of Sciences, 107(42), 18214–18219. Retrieved 2019-05-10, from http://www.pnas.org/cgi/doi/10.1073/pnas.1007703107 doi: 10.1073/pnas.1007703107

Banchi, L., Costagliola, G., Ishizaki, A., & Giorda, P. (2013, May). An analytical continuation approach for evaluating emission lineshapes of molecular aggregates and the adequacy of multichromophoric Förster theory. The Journal of Chemical Physics, 138(18), 184107. Retrieved 2020-08-24, from http://aip.scitation.org/doi/10.1063/1.4803694 doi: 10.1063/1.4803694

Barera, S., Pagliano, C., Pape, T., Saracco, G., & Barber, J. (2012, December). Characterization of PSII-LHCII supercomplexes isolated from pea thylakoid membrane

by one-step treatment with - and -dodecyl-D-maltoside. Philosophical Transactions of the Royal Society B: Biological Sciences, 367(1608), 3389–3399. Retrieved 2019-05-10, from http://rstb.royalsocietypublishing.org/cgi/doi/10.1098/rstb.2012.0056 doi: 10.1098/rstb.2012.0056

Barvík, I., Warns, C., & Reineker, P. (1998, February). Exciton transfer in disordered molecular aggregates: Computer modeling of optical line shapes in ring bacteria antenna systems. Journal of Luminescence, 76-77, 331–334. Retrieved 2020-08-24, from https://linkinghub.elsevier.com/retrieve/pii/S0022231397002202 doi: 10.1016/S0022-2313(97)00220-2

Błasiak, B., Maj, M., Cho, M., & Góra, R. W. (2015, July). Distributed Multipolar Expansion Approach to Calculation of Excitation Energy Transfer Couplings. J. Chem. Theory Comput., 11(7), 3259–3266. Retrieved 2020-04-06, from https://pubs.acs.org/doi/10.1021/acs.jctc.5b00216 doi: 10.1021/acs.jctc.5b00216

Bassi, R., Sandona, D., & Croce, R. (1997, August). Novel aspects of chlorophyll a/b-binding proteins. Physiol Plant, 100(4), 769–779. Retrieved 2019-05-11, from http://doi.wiley.com/10.1111/j.1399-3054.1997.tb00004.x doi: 10.1111/j.1399-3054.1997.tb00004.x

Baumgratz, T., Cramer, M., & Plenio, M. B. (2014, Sep). Quantifying coherence. Phys. Rev. Lett., 113, 140401. Retrieved from https://link.aps.org/doi/10.1103/PhysRevLett.113.140401 doi: 10.1103/PhysRevLett.113.140401

Becke, A. D. (1988, September). Density-functional exchange-energy approximation with correct asymptotic behavior. Physical Review A, 38(6), 3098–3100. Retrieved 2020-11-27, from https://link.aps.org/doi/10.1103/PhysRevA.38.3098 doi: 10.1103/PhysRevA.38.3098

Becke, A. D. (1993a, April). Density-functional thermochemistry. III. The role of exact exchange. The Journal of Chemical Physics, 98(7), 5648–5652. Retrieved 2020-11-27, from http://aip.scitation.org/doi/10.1063/1.464913 doi: 10.1063/1.464913

Becke, A. D. (1993b, January). A new mixing of Hartree–Fock and local density-functional theories. The Journal of Chemical Physics, 98(2), 1372–1377. Retrieved 2020-11-27, from http://aip.scitation.org/doi/10.1063/1.464304 doi: 10.1063/1.464304

Beddard, G. S., & Porter, G. (1976, March). Concentration quenching in chlorophyll. Nature, 260, 366–367.

Bell, J. S. (1964). On the Einstein-Podolsky-Rosen paradox. Physics, 1(3), 195–200.

Bengtson, C., Stenrup, M., & Sjöqvist, E. (2016, December). Quantum nonlocality in the excitation energy transfer in the Fenna-Matthews-Olson complex: Bengtson et al. International Journal of Quantum Chemistry, 116(23), 1763–1771. Retrieved 2019-04-22, from http://doi.wiley.com/10.1002/qua.25221 doi: 10.1002/qua.25221

Blankenship, R. E. (2010, October). Early Evolution of Photosynthesis. Plant Physiology, 154(2), 434–438. Retrieved 2019-04-26, from http://www.plantphysiol.org/cgi/doi/10.1104/pp.110.161687 doi: 10.1104/pp.110.161687

Blankenship, R. E. (2014). Molecular Mechanisms of Photosynthesis (2nd ed.). USA: Wiley-Blackwell. Retrieved 2019-05-02, from https://www.wiley.com/en-us/Molecular+Mechanisms+of+Photosynthesis%2C+2nd+Edition-p-9781405189767

Blau, S. M., Bennett, D. I. G., Kreisbeck, C., Scholes, G. D., & Aspuru-Guzik, A. (2018, April). Local protein solvation drives direct down-conversion in phycobiliprotein PC645 via incoherent vibronic transport. Proc Natl Acad Sci USA, 115(15), E3342–E3350. Retrieved 2020-02-26, from http://www.pnas.org/lookup/doi/10.1073/pnas.1800370115 doi: 10.1073/pnas.1800370115

Bína, D., Gardian, Z., Herbstová, M., Kotabová, E., Koník, P., Litvín, R., ... Vácha, F. (2014, June). Novel type of red-shifted chlorophyll a antenna complex from Chromera velia: II. Biochemistry and spectroscopy. Biochimica et Biophysica Acta (BBA) - Bioenergetics, 1837(6), 802–810. Retrieved 2019-05-10, from https://linkinghub

.elsevier.com/retrieve/pii/S0005272814000139 doi: 10.1016/j.bbabio.2014.01.011

Bokareva, O. S., Grell, G., Bokarev, S. I., & Kühn, O. (2015, April). Tuning Range-Separated Density Functional Theory for Photocatalytic Water Splitting Systems. Journal of Chemical Theory and Computation, 11(4), 1700–1709. Retrieved 2020-11-26, from https://pubs.acs.org/doi/10.1021/acs.jctc.5b00068 doi: 10.1021/acs.jctc.5b00068

Brand, C., Meerts, W. L., & Schmitt, M. (2011, April). How and why do transition dipole moment orientations depend on conformer structure? The Journal of Physical Chemistry A, 115(34), 9612–9619. Retrieved from https://doi.org/10.1021/jp200492s doi: 10.1021/jp200492s

Brádler, K., Wilde, M. M., Vinjanampathy, S., & Uskov, D. B. (2010, December). Identifying the quantum correlations in light-harvesting complexes. Physical Review A, 82(6), 062310. Retrieved 2019-04-22, from https://link.aps.org/doi/10.1103/PhysRevA.82.062310 doi: 10.1103/PhysRevA.82.062310

Breuer, H.-P., & Petruccione, F. (2002). The Theory of Open Quantum Systems. Oxford University Press. (Google-Books-ID: 0Yx5VzaMYm8C)

Bryant, D. A., & Frigaard, N.-U. (2006, November). Prokaryotic photosynthesis and phototrophy illuminated. Trends in Microbiology, 14(11), 488–496. Retrieved 2019-04-27, from https://linkinghub.elsevier.com/retrieve/pii/S0966842X06002265 doi: 10.1016/j.tim.2006.09.001

Burley, S. K., Bhikadiya, C., Bi, C., Bittrich, S., Chen, L., Crichlow, G. V., ... Zhuravleva, M. (2021, January). RCSB protein data bank: powerful new tools for exploring 3D structures of biological macromolecules for basic and applied research and education in fundamental biology, biomedicine, biotechnology, bioengineering and energy sciences. Nucleic Acids Res., 49(D1), D437–D451.

Calhoun, T. R., & Fleming, G. R. (2011, April). Quantum coherence in photosynthetic complexes. physica status solidi (b), 248(4), 833–838. Retrieved 2019-04-08, from http://doi.wiley.com/10.1002/pssb.201000856 doi: 10.1002/pssb.201000856

Camara-Artigas, A., Blankenship, R. E., & Allen, J. P. (2003). The structure of the FMO protein from Chlorobium tepidum at 2.2 Å resolution. Photosynthesis Research, 75, 49–55.

Caricato, M., Curutchet, C., Mennucci, B., & Scalmani, G. (2015, November). Electronic Couplings for Resonance Energy Transfer from CCSD Calculations: From Isolated to Solvated Systems. Journal of Chemical Theory and Computation, 11(11), 5219–5228. Retrieved 2020-11-26, from https://pubs.acs.org/doi/10.1021/acs.jctc.5b00720 doi: 10.1021/acs.jctc.5b00720

Caruso, F., Chin, A. W., Datta, A., Huelga, S. F., & Plenio, M. B. (2009). Highly efficient energy excitation transfer in light-harvesting complexes: The fundamental role of noise-assisted transport. The Journal of Chemical Physics, 131(10), 105106. Retrieved from https://aip.scitation.org/doi/abs/10.1063/1.3223548 doi: 10.1063/1.3223548

Case, D., Aktulga, H., Belfon, K., Ben-Shalom, J., Berryman, J., Brozel, S., ... Kollman, P. (2022). Amber 2022. University of California, San Francisco.

Caycedo-Soler, F., Mattioni, A., Lim, J., Renger, T., Huelga, S. F., & Plenio, M. B. (2022, May). Exact simulation of pigment-protein complexes unveils vibronic renormalization of electronic parameters in ultrafast spectroscopy. Nature Communications, 13(1). Retrieved from https://doi.org/10.1038/s41467-022-30565-4 doi: 10.1038/s41467-022-30565-4

Chai, J.-D., & Head-Gordon, M. (2008, February). Systematic optimization of long-range corrected hybrid density functionals. The Journal of Chemical Physics, 128(8), 084106. Retrieved 2021-02-06, from http://aip.scitation.org/doi/10.1063/1.2834918 doi: 10.1063/1.2834918

Chang, J. C. (1977). Monopole effects on electronic excitation interactions between large molecules. I. Application to energy transfer in chlorophylls. The Journal of Chemical Physics, 67(9), 3901–3909. Retrieved 2020-03-30, from http://scitation.aip.org/content/aip/journal/jcp/67/9/10.1063/1.435427 doi: 10.1063/1.435427

Chen, L., Zheng, R., Shi, Q., & Yan, Y. (2009). Optical line shapes of molecular aggregates: Hierarchical equations of motion method. The Journal of Chemical Physics, 131(9), 094502. Retrieved 2020-08-12, from http://scitation.aip.org/content/aip/journal/jcp/131/9/10.1063/1.3213013 doi: 10.1063/1.3213013

Cheng, Y.-C., & Fleming, G. R. (2009, May). Dynamics of Light Harvesting in Photosynthesis. Annual Review of Physical Chemistry, 60(1), 241–262. Retrieved 2018-03-20, from http://www.annualreviews.org/doi/10.1146/annurev.physchem.040808.090259 doi: 10.1146/annurev.physchem.040808.090259

Chin, A. W., Prior, J., Rosenbach, R., Caycedo-Soler, F., Huelga, S. F., & Plenio, M. B. (2013, February). The role of non-equilibrium vibrational structures in electronic coherence and recoherence in pigment–protein complexes. Nat. Phys., 9(2), 113–118.

Cleary, L., & Cao, J. (2013, December). Optimal thermal bath for robust excitation energy transfer in disordered light-harvesting complex 2 of purple bacteria. New Journal of Physics, 15(12), 125030. Retrieved 2020-08-12, from https://iopscience.iop.org/article/10.1088/1367-2630/15/12/125030 doi: 10.1088/1367-2630/15/12/125030

Cogdell, R. J., & Frank, H. A. (1987). How carotenoids function in photosynthetic bacteria. Biochimica et Biophysica Acta (BBA) - Reviews on Bioenergetics, 895(2), 63-79. Retrieved from https://www.sciencedirect.com/science/article/pii/S0304417387800083 doi: https://doi.org/10.1016/S0304-4173(87)80008-3

Cogdell, R. J., Fyfe, P. K., Barrett, S. J., Prince, S. M., Freer, A. A., Isaacs, N. W., ... Hunter, C. N. (1996, May). The purple bacterial photosynthetic unit. Photosynth

Res, 48(1-2), 55–63. Retrieved 2019-05-10, from http://link.springer.com/10.1007/BF00040996 doi: 10.1007/BF00040996

Cogdell, R. J., Gardiner, A. T., Hashimoto, H., & Brotosudarmo, T. H. P. (2008). A comparative look at the first few milliseconds of the light reactions of photosynthesis. Photochemical & Photobiological Sciences, 7(10), 1150. Retrieved 2019-04-08, from http://xlink.rsc.org/?DOI=b807201a doi: 10.1039/b807201a

Cohen, A. J., & Handy, N. C. (2001, April). Dynamic correlation. Molecular Physics, 99(7), 607–615. Retrieved 2020-11-27, from http://www.tandfonline.com/doi/abs/10.1080/00268970010023435 doi: 10.1080/00268970010023435

Collini, E. (2012, June). Differences among coherent dynamics in evolutionary related light-harvesting complexes: evidence for subtle quantum-mechanical strategies for energy transfer optimization. In T. Durt & V. N. Zadkov (Eds.), (p. 84400A). Brussels, Belgium. Retrieved 2019-03-24, from http://proceedings.spiedigitallibrary.org/proceeding.aspx?doi=10.1117/12.927850 doi: 10.1117/12.927850

Collini, E. (2019, March). Carotenoids in Photosynthesis: The Revenge of the "Accessory" Pigments. Chem, 5(3), 494–495. Retrieved 2019-04-22, from https://linkinghub.elsevier.com/retrieve/pii/S2451929419300701 doi: 10.1016/j.chempr.2019.02.013

Collini, E., Curutchet, C., Mirkovic, T., & Scholes, G. D. (2009). Electronic Energy Transfer in Photosynthetic Antenna Systems. In I. Burghardt, V. May, D. A. Micha, & E. R. Bittner (Eds.), Energy Transfer Dynamics in Biomaterial Systems (Vol. 93, pp. 3–34). Berlin, Heidelberg: Springer Berlin Heidelberg. Retrieved 2019-03-24, from http://link.springer.com/10.1007/978-3-642-02306-4_1 doi: 10.1007/978-3-642-02306-4_1

Collini, E., Wong, C. Y., Wilk, K. E., Curmi, P. M. G., Brumer, P., & Scholes, G. D. (2010, February). Coherently wired light-harvesting in photosynthetic marine algae at ambient temperature. Nature, 463(7281), 644–647. Retrieved 2017-11-18,

from http://www.nature.com/doifinder/10.1038/nature08811 doi: 10.1038/nature08811

Combescot, M., & Shiau, S.-Y. (2016). Excitons and cooper pairs: two composite bosons in many-body physics. New York, NY: Oxford University Press.

Curutchet, C., & Mennucci, B. (2017, January). Quantum Chemical Studies of Light Harvesting. Chemical Reviews, 117(2), 294–343. Retrieved 2019-04-22, from http://pubs.acs.org/doi/10.1021/acs.chemrev.5b00700 doi: 10.1021/acs.chemrev.5b00700

Dinh, T.-C., & Renger, T. (2015, January). Towards an exact theory of linear absorbance and circular dichroism of pigment-protein complexes: Importance of non-secular contributions. The Journal of Chemical Physics, 142(3), 034104. Retrieved 2020-02-25, from http://aip.scitation.org/doi/10.1063/1.4904928 doi: 10.1063/1.4904928

Dostál, J., Mančal, T., Augulis, R.-n., Vácha, F., Pšenčík, J., & Zigmantas, D. (2012, July). Two-Dimensional Electronic Spectroscopy Reveals Ultrafast Energy Diffusion in Chlorosomes. Journal of the American Chemical Society, 134(28), 11611–11617. Retrieved 2019-04-08, from http://pubs.acs.org/doi/10.1021/ja3025627 doi: 10.1021/ja3025627

Drop, B., Webber-Birungi, M., Yadav, S. K., Filipowicz-Szymanska, A., Fusetti, F., Boekema, E. J., & Croce, R. (2014, January). Light-harvesting complex II (LHCII) and its supramolecular organization in Chlamydomonas reinhardtii. Biochimica et Biophysica Acta (BBA) - Bioenergetics, 1837(1), 63–72. Retrieved 2019-05-10, from https://linkinghub.elsevier.com/retrieve/pii/S0005272813001291 doi: 10.1016/j.bbabio.2013.07.012

Durchan, M., Tichý, J., Litvín, R., Šlouf, V., Gardian, Z., Hříbek, P., ... Polívka, T. (2012, August). Role of Carotenoids in Light-Harvesting Processes in an Antenna Protein from the Chromophyte *Xanthonema debile*. J. Phys. Chem. B, 116(30), 8880–

8889. Retrieved 2019-05-10, from http://pubs.acs.org/doi/10.1021/jp3042796 doi: 10.1021/jp3042796

Efrat, A., Fan, Q., & Venkatasubramanian, S. (2007, April). Curve Matching, Time Warping, and Light Fields: New Algorithms for Computing Similarity between Curves. Journal of Mathematical Imaging and Vision, 27(3), 203–216. Retrieved 2020-09-30, from http://link.springer.com/10.1007/s10851-006-0647-0 doi: 10.1007/s10851-006-0647-0

Engel, G. S., Calhoun, T. R., Read, E. L., Ahn, T.-K., Mančal, T., Cheng, Y.-C., ... Fleming, G. R. (2007, April). Evidence for wavelike energy transfer through quantum coherence in photosynthetic systems. Nature, 446(7137), 782–786. Retrieved 2019-04-08, from http://www.nature.com/articles/nature05678 doi: 10.1038/nature05678

Evers, F., Giraud-Girard, J., Grimme, S., Manz, J., Monte, C., Oppel, M., ... Zimmermann, P. (2001, March). Absorption and Fluorescence Excitation Spectra of 9-(N-carbazolyl)-anthracene: Effects of Intramolecular Vibrational Redistribution and Diabatic Transitions Involving Electron Transfer. The Journal of Physical Chemistry A, 105(12), 2911–2924. Retrieved 2020-08-24, from https://pubs.acs.org/doi/10.1021/jp003879d doi: 10.1021/jp003879d

Fassioli, F., Dinshaw, R., Arpin, P. C., & Scholes, G. D. (2013, December). Photosynthetic light harvesting: excitons and coherence. Journal of The Royal Society Interface, 11(92), 20130901–20130901. Retrieved 2019-04-08, from http://rsif.royalsocietypublishing.org/cgi/doi/10.1098/rsif.2013.0901 doi: 10.1098/rsif.2013.0901

Fleming, G. R., Scholes, G. D., & Cheng, Y.-C. (2011). Quantum effects in biology. Procedia Chemistry, 3(1), 38–57. Retrieved 2018-03-20, from http://linkinghub.elsevier.com/retrieve/pii/S1876619611000507 doi: 10.1016/j.proche.2011.08.011

Fornari, R. P., Aragó, J., & Troisi, A. (2016, April). Exciton Dynamics in Phthalocyanine Molecular Crystals. The Journal of Physical Chemistry C, 120(15), 7987–7996. Retrieved 2020-11-29, from https://pubs.acs.org/doi/10.1021/acs.jpcc.6b01298 doi: 10.1021/acs.jpcc.6b01298

Fornari, R. P., Rowe, P., Padula, D., & Troisi, A. (2017, August). Importance and Nature of Short-Range Excitonic Interactions in Light Harvesting Complexes and Organic Semiconductors. Journal of Chemical Theory and Computation, 13(8), 3754–3763. Retrieved 2020-11-29, from https://pubs.acs.org/doi/10.1021/acs.jctc.7b00328 doi: 10.1021/acs.jctc.7b00328

Fowler, G. J. S., Visschers, R. W., Grief, G. G., van Grondelle, R., & Hunter, C. N. (1992, February). Genetically modified photosynthetic antenna complexes with blueshifted absorbance bands. Nature, 355, 848–850.

Frenkel, J. (1931, January). On the Transformation of light into Heat in Solids. I. Phys. Rev., 37(1), 17–44. Retrieved 2019-05-02, from https://link.aps.org/doi/10.1103/PhysRev.37.17 doi: 10.1103/PhysRev.37.17

Frähmcke, J. S., & Walla, P. J. (2006, October). Coulombic couplings between pigments in the major light-harvesting complex LHC II calculated by the transition density cube method. Chemical Physics Letters, 430(4-6), 397–403. Retrieved 2019-05-01, from https://linkinghub.elsevier.com/retrieve/pii/S0009261406013273 doi: 10.1016/j.cplett.2006.09.009

Friedl, C., Fedorov, D. G., & Renger, T. (2022). Towards a quantitative description of excitonic couplings in photosynthetic pigment–protein complexes: quantum chemistry driven multiscale approaches. Physical Chemistry Chemical Physics, 24(8), 5014–5038. Retrieved from https://doi.org/10.1039/d1cp03566e doi: 10.1039/d1cp03566e

Förster, T. (1948). Intermolecular energy migration and fluorescence. Annals of Physics, 437(1-2), 55-75. Retrieved from https://onlinelibrary.wiley.com/doi/abs/10.1002/andp.19484370105 doi: https://doi.org/10.1002/andp.19484370105

Fujimoto, K. J., & Balashov, S. P. (2017, March). Vibronic coupling effect on circular dichroism spectrum: Carotenoid–retinal interaction in xanthorhodopsin. The Journal of Chemical Physics, 146(9), 095101. Retrieved 2020-04-06, from http://aip.scitation.org/doi/10.1063/1.4977045 doi: 10.1063/1.4977045

Gantt, E. (1996, May). Pigment protein complexes and the concept of the photosynthetic unit: Chlorophyll complexes and phycobilisomes. Photosynth Res, 48(1-2), 47–53. Retrieved 2019-05-10, from http://link.springer.com/10.1007/BF00040995 doi: 10.1007/BF00040995

Geacintov, N. E., Breton, J., & Knox, R. S. (1986). Energy migration and exciton trapping in green plant photosynthesis. Photosynth Res, 10(3), 233–242. Retrieved 2019-05-01, from http://link.springer.com/10.1007/BF00118288 doi: 10.1007/BF00118288

Gelzinis, A., Abramavicius, D., & Valkunas, L. (2015, April). Absorption lineshapes of molecular aggregates revisited. The Journal of Chemical Physics, 142(15), 154107. Retrieved 2020-08-12, from http://aip.scitation.org/doi/10.1063/1.4918343 doi: 10.1063/1.4918343

Glauber, R. J. (1963, Jun). The quantum theory of optical coherence. Phys. Rev., 130, 2529–2539. Retrieved from https://link.aps.org/doi/10.1103/PhysRev.130.2529 doi: 10.1103/PhysRev.130.2529

Gower, J. C., & Dijksterhuis, G. B. (2004). Procrustes problems (No. 30). Oxford ; New York: Oxford University Press. (OCLC: ocm53156636)

Graham, L. E., & Wilcox, L. W. (2000). Algae. Upper Saddler River, NJ: Prentice Hall.

Green, B., & Parson, W. W. (Eds.). (2003). Light-Harvesting Antennas in Photosynthesis. Springer Netherlands. Retrieved 2019-04-25, from https://www.springer.com/us/book/9780792363354

Green, B. R., & Durnford, D. G. (1996, June). The Chlorophyll- Carotenoid proteins of oxygenic photosynthesis. Annu. Rev. Plant. Physiol. Plant. Mol. Biol., 47(1), 685–714. Retrieved 2019-05-10, from http://www.annualreviews.org/doi/10.1146/annurev.arplant.47.1.685 doi: 10.1146/annurev.arplant.47.1.685

Griffiths, D. J., & Schroeter, D. F. (2018). Introduction to quantum mechanics (3rd ed.). Cambridge University Press.

Hansen, L. O., Hauge, A., Myrheim, J., & Sollid, P. O. (2015, December). Extremal entanglement witnesses. International Journal of Quantum Information, 13(08), 1550060. Retrieved 2019-04-22, from http://www.worldscientific.com/doi/abs/10.1142/S0219749915500604 doi: 10.1142/S0219749915500604

Hayes, D., Panitchayangkoon, G., Fransted, K. A., Caram, J. R., Wen, J., Freed, K. F., & Engel, G. S. (2010, June). Dynamics of electronic dephasing in the Fenna–Matthews–Olson complex. New J. Phys., 12(6), 065042. Retrieved 2019-06-13, from http://stacks.iop.org/1367-2630/12/i=6/a=065042?key=crossref.e48a640b7ecb24af36c75fd8005b8c8f doi: 10.1088/1367-2630/12/6/065042

Hayes, D., Wen, J., Panitchayangkoon, G., Blankenship, R. E., & Engel, G. S. (2011). Robustness of electronic coherence in the Fenna–Matthews–Olson complex to vibronic and structural modifications. Faraday Discussions, 150, 459. Retrieved 2019-04-08, from http://xlink.rsc.org/?DOI=c0fd00030b doi: 10.1039/c0fd00030b

Höfener, S., & Visscher, L. (2016, February). Wave Function Frozen-Density Embedding: Coupled Excitations. Journal of Chemical Theory and Computation, 12(2), 549–557. Retrieved 2020-11-26, from https://pubs.acs.org/doi/10.1021/acs.jctc.5b00821 doi: 10.1021/acs.jctc.5b00821

Higashi, M., Kosugi, T., Hayashi, S., & Saito, S. (2014, September). Theoretical Study on Excited States of Bacteriochlorophyll *a* in Solutions with Density Functional Assessment. The Journal of Physical Chemistry B, 118(37), 10906–10918. Retrieved 2020-11-26, from https://pubs.acs.org/doi/10.1021/jp507259g doi: 10.1021/jp507259g

Hildner, R., Brinks, D., Nieder, J. B., Cogdell, R. J., & van Hulst, N. F. (2013, June). Quantum Coherent Energy Transfer over Varying Pathways in Single Light-Harvesting Complexes. Science, 340(6139), 1448–1451. Retrieved 2019-04-29, from http://www.sciencemag.org/cgi/doi/10.1126/science.1235820 doi: 10.1126/science.1235820

Hill, S., & Wootters, W. K. (1997, June). Entanglement of a Pair of Quantum Bits. Physical Review Letters, 78(26), 5022–5025. Retrieved 2019-04-22, from https://link.aps.org/doi/10.1103/PhysRevLett.78.5022 doi: 10.1103/PhysRevLett.78.5022

Hiller, R. G., Wrench, P. M., Gooley, A. P., Shoebridge, G., & Breton, J. (1993, January). The major intrinsic light-harvesting protein of Amphidinium: characterization and relation to other light-harvesting proteins. Photochem Photobiol, 57(1), 125–131. Retrieved 2019-05-10, from http://doi.wiley.com/10.1111/j.1751-1097.1993.tb02267.x doi: 10.1111/j.1751-1097.1993.tb02267.x

Hoe, W.-M., Cohen, A. J., & Handy, N. C. (2001). Assessment of a new local exchange functional optx. Chemical Physics Letters, 341(3), 319-328. Retrieved from https://www.sciencedirect.com/science/article/pii/S0009261401005814 doi: https://doi.org/10.1016/S0009-2614(01)00581-4

Hoogewerf, G. J., Jung, D. O., & Madigan, M. T. (2003, January). Evidence for limited species diversity of bacteriochlorophyll *b* -containing purple nonsulfur anoxygenic phototrophs in freshwater habitats. FEMS Microbiology Letters, 218(2), 359–364. Retrieved 2019-05-11, from https://academic.oup.com/femsle/article-lookup/doi/10.1016/S0378-1097(02)01195-3 doi: 10.1016/S0378-1097(02)01195-3

Horodecki, R., Horodecki, P., & Horodecki, M. (1995). Violating Bell inequality by mixed spin-1/2 states: necessary and sufficient condition. Physical Letters A, 200, 340–344.

Hourahine, B., Aradi, B., Blum, V., Bonafé, F., Buccheri, A., Camacho, C., ... Frauenheim, T. (2020). Dftb+, a software package for efficient approximate density

functional theory based atomistic simulations. The Journal of Chemical Physics, 152(12), 124101. Retrieved from https://doi.org/10.1063/1.5143190 doi: 10.1063/1.5143190

Hoyer, S., Sarovar, M., & Birgitta Whaley, K. (2010, June). Limits of quantum speedup in photosynthetic light harvesting. New Journal of Physics, 12(6), 065041. Retrieved 2019-04-08, from http://stacks.iop.org/1367-2630/12/i=6/a=065041?key=crossref.5b6ba9502742a0295ecde7083c39955e doi: 10.1088/1367-2630/12/6/065041

Hsu, C.-P., Fleming, G. R., Head-Gordon, M., & Head-Gordon, T. (2001, February). Excitation energy transfer in condensed media. The Journal of Chemical Physics, 114(7), 3065–3072. Retrieved 2020-03-03, from http://aip.scitation.org/doi/10.1063/1.1338531 doi: 10.1063/1.1338531

Huelga, S., & Plenio, M. (2013, July). Vibrations, quanta and biology. Contemporary Physics, 54(4), 181–207. Retrieved 2019-04-08, from http://www.tandfonline.com/doi/abs/10.1080/00405000.2013.829687 doi: 10.1080/00405000.2013.829687

Hughes, J. L., Razeghifard, R., Logue, M., Oakley, A., Wydrzynski, T., & Krausz, E. (2006, March). Magneto-Optic Spectroscopy of a Protein Tetramer Binding Two Exciton-Coupled Chlorophylls. Journal of the American Chemical Society, 128(11), 3649–3658. Retrieved 2020-02-25, from https://pubs.acs.org/doi/10.1021/ja056576b doi: 10.1021/ja056576b

Iikura, H., Tsuneda, T., Yanai, T., & Hirao, K. (2001, August). A long-range correction scheme for generalized-gradient-approximation exchange functionals. The Journal of Chemical Physics, 115(8), 3540–3544. Retrieved 2020-11-27, from http://aip.scitation.org/doi/10.1063/1.1383587 doi: 10.1063/1.1383587

Ishizaki, A., Calhoun, T. R., Schlau-Cohen, G. S., & Fleming, G. R. (2010). Quantum coherence and its interplay with protein environments in photosynthetic electronic energy transfer. Physical Chemistry Chemical Physics, 12, 7319–7337.

Ishizaki, A., & Fleming, G. R. (2009, June). Unified treatment of quantum coherent and incoherent hopping dynamics in electronic energy transfer: Reduced hierarchy equation approach. The Journal of Chemical Physics, 130(23), 234111. Retrieved 2019-03-24, from http://aip.scitation.org/doi/10.1063/1.3155372 doi: 10.1063/1.3155372

Jacquemin, D., Moore, B., Planchat, A., Adamo, C., & Autschbach, J. (2014, April). Performance of an Optimally Tuned Range-Separated Hybrid Functional for 0–0 Electronic Excitation Energies. Journal of Chemical Theory and Computation, 10(4), 1677–1685. Retrieved 2020-11-26, from https://pubs.acs.org/doi/10.1021/ct5000617 doi: 10.1021/ct5000617

Jacquemin, D., Perpète, E. A., Ciofini, I., & Adamo, C. (2011, January). Assessment of the ωB97 family for excited-state calculations. Theoretical Chemistry Accounts, 128(1), 127–136. Retrieved 2020-11-20, from http://link.springer.com/10.1007/s00214-010-0783-x doi: 10.1007/s00214-010-0783-x

Jacquemin, D., Perpète, E. A., Ciofini, I., Adamo, C., Valero, R., Zhao, Y., & Truhlar, D. G. (2010). On the Performances of the M06 Family of Density Functionals for Electronic Excitation Energies. Journal of Chemical Theory and Computation, 6, 2071–2085.

Jacquemin, D., Wathelet, V., Perpète, E. A., & Adamo, C. (2009, September). Extensive TD-DFT Benchmark: Singlet-Excited States of Organic Molecules. Journal of Chemical Theory and Computation, 5(9), 2420–2435. Retrieved 2020-04-19, from https://pubs.acs.org/doi/10.1021/ct900298e doi: 10.1021/ct900298e

Jang, S., Dempster, S. E., & Silbey, R. J. (2001, July). Characterization of the Static Disorder in the B850 Band of LH2. The Journal of Physical Chemistry B, 105(28), 6655–6665. Retrieved 2019-04-22, from https://pubs.acs.org/doi/10.1021/jp010169e doi: 10.1021/jp010169e

Jang, S., & Silbey, R. J. (2003, May). Theory of single molecule line shapes of multichromophoric macromolecules. The Journal of Chemical Physics, 118(20), 9312–9323.

Retrieved 2020-08-24, from http://aip.scitation.org/doi/10.1063/1.1569239 doi: 10.1063/1.1569239

Jang, S. J. (2019, July). Fourth order expressions for the electronic absorption lineshape of molecular excitons. The Journal of Chemical Physics, 151(4), 044110. Retrieved 2020-08-12, from http://aip.scitation.org/doi/10.1063/1.5100986 doi: 10.1063/1.5100986

Jang, S. J., & Mennucci, B. (2018, August). Delocalized excitons in natural light-harvesting complexes. Reviews of Modern Physics, 90(3), 035003. Retrieved 2020-04-06, from https://link.aps.org/doi/10.1103/RevModPhys.90.035003 doi: 10.1103/RevModPhys.90.035003

Jiang, T., Li, W., Ren, J., & Shuai, Z. (2020, May). Finite Temperature Dynamical Density Matrix Renormalization Group for Spectroscopy in Frequency Domain. The Journal of Physical Chemistry Letters, 11(10), 3761–3768. Retrieved 2020-08-24, from https://pubs.acs.org/doi/10.1021/acs.jpclett.0c00905 doi: 10.1021/acs.jpclett.0c00905

Jing, Y., Chen, L., Bai, S., & Shi, Q. (2013, January). Equilibrium excited state and emission spectra of molecular aggregates from the hierarchical equations of motion approach. The Journal of Chemical Physics, 138(4), 045101. Retrieved 2020-08-24, from http://aip.scitation.org/doi/10.1063/1.4775843 doi: 10.1063/1.4775843

Jing, Y., Zheng, R., Li, H.-X., & Shi, Q. (2012, January). Theoretical Study of the Electronic–Vibrational Coupling in the Q_y States of the Photosynthetic Reaction Center in Purple Bacteria. The Journal of Physical Chemistry B, 116(3), 1164–1171. Retrieved 2019-04-08, from http://pubs.acs.org/doi/10.1021/jp209575q doi: 10.1021/jp209575q

Jordan, P., Fromme, P., Witt, H. T., Klukas, O., Saenger, W., & Krauß, N. (2001, June). Three-dimensional structure of cyanobacterial photosystem i at 2.5 Å resolution. Nature, 411(6840), 909–917. Retrieved from https://doi.org/10.1038/35082000 doi: 10.1038/35082000

Kannaujiya, V. K., Sundaram, S., & Sinha, R. P. (2017). Phycobiliproteins: Recent Developments and Future Applications. Springer. (Google-Books-ID: njxEDwAAQBAJ)

Ke, Y., & Zhao, Y. (2017, May). Hierarchy of stochastic Schrödinger equation towards the calculation of absorption and circular dichroism spectra. The Journal of Chemical Physics, 146(17), 174105. Retrieved 2020-08-12, from http://aip.scitation.org/doi/10.1063/1.4982230 doi: 10.1063/1.4982230

Kell, A., Feng, X., Reppert, M., & Jankowiak, R. (2013, June). On the shape of the phonon spectral density in photosynthetic complexes. The Journal of Physical Chemistry B, 117(24), 7317–7323. Retrieved from https://doi.org/10.1021/jp405094p doi: 10.1021/jp405094p

Kern, J., Chatterjee, R., Young, I. D., Fuller, F. D., Lassalle, L., Ibrahim, M., ... Yachandra, V. K. (2018, November). Structures of the intermediates of Kok's photosynthetic water oxidation clock. Nature, 563(7731), 421–425. Retrieved 2019-05-13, from http://www.nature.com/articles/s41586-018-0681-2 doi: 10.1038/s41586-018-0681-2

Khan, M. U., Mehboob, M. Y., Hussain, R., Afzal, Z., Khalid, M., & Adnan, M. (2020, July). Designing spirobifullerene core based three-dimensional cross shape acceptor materials with promising photovoltaic properties for high-efficiency organic solar cells. International Journal of Quantum Chemistry. Retrieved 2020-08-24, from https://onlinelibrary.wiley.com/doi/abs/10.1002/qua.26377 doi: 10.1002/qua.26377

Khmelnitskiy, A., Reinot, T., & Jankowiak, R. (2019, January). Mixed Upper Exciton State of the Special Pair in Bacterial Reaction Centers. The Journal of Physical Chemistry B, 123(4), 852–859. Retrieved 2020-02-25, from https://pubs.acs.org/doi/10.1021/acs.jpcb.8b12542 doi: 10.1021/acs.jpcb.8b12542

Kieselbach, T., Cheregi, O., Green, B. R., & Funk, C. (2018, March). Proteomic analysis of the phycobiliprotein antenna of the cryptophyte alga Guillardia theta

cultured under different light intensities. Photosynthesis Research, 135(1-3), 149–163. Retrieved 2019-04-22, from http://link.springer.com/10.1007/s11120-017-0400-0 doi: 10.1007/s11120-017-0400-0

Kitoh-Nishioka, H., Shigeta, Y., Itoh, S., & Kimura, A. (2020, January). Excitonic Coupling on a Heliobacterial Symmetrical Type-I Reaction Center: Comparison with Photosystem I. J. Phys. Chem. B, 124(2), 389–403. Retrieved 2020-04-06, from https://pubs.acs.org/doi/abs/10.1021/acs.jpcb.9b11290 doi: 10.1021/acs.jpcb.9b11290

Klappenbach, J. A., & Pierson, B. K. (2004, January). Phylogenetic and physiological characterization of a filamentous anoxygenic photoautotrophic bacterium *Candidatus Chlorothrix halophila* gen. nov., sp. nov., recovered from hypersaline microbial mats. Archives of Microbiology, 181(1), 17–25. Retrieved 2019-05-10, from http://link.springer.com/10.1007/s00203-003-0615-7 doi: 10.1007/s00203-003-0615-7

Kleinekathöfer, U., Schröder, M., & Schreiber, M. (2005, April). Absorption spectra for a model light-harvesting system using non-Markovian theories. Journal of Luminescence, 112(1-4), 461–464. Retrieved 2020-08-24, from https://linkinghub.elsevier.com/retrieve/pii/S0022231304003898 doi: 10.1016/j.jlumin.2004.09.074

Kleinschmidt, M., Marian, C. M., Waletzke, M., & Grimme, S. (2009, January). Parallel multireference configuration interaction calculations on mini-β-carotenes and β-carotene. The Journal of Chemical Physics, 130(4), 044708. Retrieved 2020-11-26, from http://aip.scitation.org/doi/10.1063/1.3062842 doi: 10.1063/1.3062842

Knox, R. S., & Spring, B. Q. (2003, May). Dipole Strengths in the Chlorophylls. Photochemistry and Photobiology, 77(5), 497–501. Retrieved 2020-02-26, from http://doi.wiley.com/10.1562/0031-8655%282003%290770497DSITC2.0.CO2 doi: 10.1562/0031-8655(2003)0770497DSITC2.0.CO2

Knox, R. S., & van Amerongen, H. (2002). Refractive Index Dependence of the Förster Resonance Excitation Transfer Rate. Journal of Physical Chemistry B, 106, 5289–5293.

Kocherzhenko, A. A., Sosa Vazquez, X. A., Milanese, J. M., & Isborn, C. M. (2017, August). Absorption Spectra for Disordered Aggregates of Chromophores Using the Exciton Model. Journal of Chemical Theory and Computation, 13(8), 3787–3801. Retrieved 2019-10-13, from https://pubs.acs.org/doi/10.1021/acs.jctc.7b00477 doi: 10.1021/acs.jctc.7b00477

Kulp, T. R., Hoeft, S. E., Asao, M., Madigan, M. T., Hollibaugh, J. T., Fisher, J. C., ... Oremland, R. S. (2008, August). Arsenic(III) Fuels Anoxygenic Photosynthesis in Hot Spring Biofilms from Mono Lake, California. Science, 321(5891), 967–970. Retrieved 2019-04-29, from http://www.sciencemag.org/cgi/doi/10.1126/science.1160799 doi: 10.1126/science.1160799

Laberge, M. (1998). Intrinsic protein electric fields: basic non-covalent interactions and relationship to protein-induced Stark effects. Biochimica et Biophysica Acta, 1386, 305–330.

Lambert, N., Chen, Y.-N., Cheng, Y.-C., Li, C.-M., Chen, G.-Y., & Nori, F. (2012, May). Functional quantum biology in photosynthesis and magnetoreception. arXiv:1205.0883 [physics, physics:quant-ph, q-bio]. Retrieved 2019-04-08, from http://arxiv.org/abs/1205.0883 (arXiv: 1205.0883)

Lambert, N., Chen, Y.-N., Cheng, Y.-C., Li, C.-M., Chen, G.-Y., & Nori, F. (2013, January). Quantum biology. Nature Physics, 9(1), 10–18. Retrieved 2018-03-20, from http://www.nature.com/articles/nphys2474 doi: 10.1038/nphys2474

Laurent, A. D., & Jacquemin, D. (2013). TD-DFT benchmarks: A review. International Journal of Quantum Chemistry, 113, 2019–2039.

Lee, C., Yang, W., & Parr, R. G. (1988, January). Development of the Colle-Salvetti correlation-energy formula into a functional of the electron density. Physical

Review B, 37(2), 785–789. Retrieved 2020-11-27, from https://link.aps.org/doi/10.1103/PhysRevB.37.785 doi: 10.1103/PhysRevB.37.785

Lee, H., Cheng, Y.-C., & Fleming, G. R. (2009). Quantum Coherence Accelerating Photosynthetic Energy Transfer. In P. Corkum, S. Silvestri, K. A. Nelson, E. Riedle, & R. W. Schoenlein (Eds.), Ultrafast Phenomena XVI (Vol. 92, pp. 607–609). Berlin, Heidelberg: Springer Berlin Heidelberg. Retrieved 2019-04-08, from http://link.springer.com/10.1007/978-3-540-95946-5_197 doi: 10.1007/978-3-540-95946-5_197

Leggett, A. J., & Garg, A. (1985, March). Quantum mechanics versus macroscopic realism: Is the flux there when nobody looks? Phys. Rev. Lett., 54(9), 857–860. Retrieved 2019-06-17, from https://link.aps.org/doi/10.1103/PhysRevLett.54.857 doi: 10.1103/PhysRevLett.54.857

Li, C.-M., Lambert, N., Chen, Y.-N., Chen, G.-Y., & Nori, F. (2012, December). Witnessing Quantum Coherence: from solid-state to biological systems. Scientific Reports, 2(1), 885. Retrieved 2019-04-08, from http://www.nature.com/articles/srep00885 doi: 10.1038/srep00885

Li, L., Li, C., Zhang, Z., & Alexov, E. (2013, April). On the Dielectric "Constant" of Proteins: Smooth Dielectric Function for Macromolecular Modeling and Its Implementation in DelPhi. J. Chem. Theory Comput., 9(4), 2126–2136. Retrieved 2020-03-03, from https://pubs.acs.org/doi/10.1021/ct400065j doi: 10.1021/ct400065j

Liess, A., Lv, A., Arjona-Esteban, A., Bialas, D., Krause, A.-M., Stepanenko, V., ... Würthner, F. (2017, March). Exciton Coupling of Merocyanine Dyes from H- to J-type in the Solid State by Crystal Engineering. Nano Lett., 17(3), 1719–1726. Retrieved 2020-04-06, from https://pubs.acs.org/doi/10.1021/acs.nanolett.6b04995 doi: 10.1021/acs.nanolett.6b04995

Liu, Z., Yan, H., Wang, K., Kuang, T., Zhang, J., Gui, L., ... Chang, W. (2004, March). Crystal structure of spinach major light-harvesting complex at 2.72 Å resolution.

Nature, 428(6980), 287–292. Retrieved 2019-05-10, from http://www.nature.com/articles/nature02373 doi: 10.1038/nature02373

Loll, B., Kern, J., Saenger, W., Zouni, A., & Biesiadka, J. (2005, December). Towards complete cofactor arrangement in the 3.0 Å resolution structure of photosystem II. Nature, 438(7070), 1040–1044. Retrieved 2019-05-10, from http://www.nature.com/articles/nature04224 doi: 10.1038/nature04224

Lukeš, V., Pálszegi, T., Milota, F., Sperling, J., & Kauffmann, H. F. (2006, February). Density Matrix Analysis, Simulation, and Measurements of Electronic Absorption and Fluorescence Spectra of Spirobifluorenes. The Journal of Physical Chemistry A, 110(5), 1775–1782. Retrieved 2020-08-24, from https://pubs.acs.org/doi/10.1021/jp054507d doi: 10.1021/jp054507d

Ma, H., Luo, Z., & Yao, Y. (2018, April). The time-dependent density matrix renormalisation group method. Molecular Physics, 116(7-8), 854–868. Retrieved 2020-08-24, from https://www.tandfonline.com/doi/full/10.1080/00268976.2017.1406165 doi: 10.1080/00268976.2017.1406165

Ma, J., & Cao, J. (2015, March). Förster resonance energy transfer, absorption and emission spectra in multichromophoric systems. I. Full cumulant expansions and system-bath entanglement. The Journal of Chemical Physics, 142(9), 094106. Retrieved 2020-08-12, from http://aip.scitation.org/doi/10.1063/1.4908599 doi: 10.1063/1.4908599

Madjet, M. E., Abdurahman, A., & Renger, T. (2006, August). Intermolecular Coulomb Couplings from Ab Initio Electrostatic Potentials: Application to Optical Transitions of Strongly Coupled Pigments in Photosynthetic Antennae and Reaction Centers. The Journal of Physical Chemistry B, 110(34), 17268–17281. Retrieved 2019-04-22, from https://pubs.acs.org/doi/10.1021/jp0615398 doi: 10.1021/jp0615398

Mardirossian, N., & Head-Gordon, M. (2014). ωB97X-V: A 10-parameter, range-separated hybrid, generalized gradient approximation density functional with nonlocal correlation, designed by a survival-of-the-fittest strategy. Physical Chemistry

Chemical Physics, 16(21), 9904. Retrieved 2020-11-27, from http://xlink.rsc.org/?DOI=c3cp54374a doi: 10.1039/c3cp54374a

Mardirossian, N., & Head-Gordon, M. (2015, February). Mapping the genome of meta-generalized gradient approximation density functionals: The search for B97M-V. The Journal of Chemical Physics, 142(7), 074111. Retrieved 2020-11-27, from http://aip.scitation.org/doi/10.1063/1.4907719 doi: 10.1063/1.4907719

Mardirossian, N., & Head-Gordon, M. (2017, October). Thirty years of density functional theory in computational chemistry: an overview and extensive assessment of 200 density functionals. Molecular Physics, 115(19), 2315–2372. Retrieved 2020-11-20, from https://www.tandfonline.com/doi/full/10.1080/00268976.2017.1333644 doi: 10.1080/00268976.2017.1333644

Marx, A., & Adir, N. (2013, March). Allophycocyanin and phycocyanin crystal structures reveal facets of phycobilisome assembly. Biochimica et Biophysica Acta (BBA) - Bioenergetics, 1827(3), 311–318. Retrieved 2019-05-11, from https://linkinghub.elsevier.com/retrieve/pii/S000527281201081X doi: 10.1016/j.bbabio.2012.11.006

May, V., & Kühn, O. (2011). Charge and Energy Transfer Dynamics in Molecular Systems (3rd ed.). Germany: John Wiley & Sons, Inc.

Meneghin, E., Pedron, D., & Collini, E. (2019, March). Characterization of the coherent dynamics of bacteriochlorophyll a in solution. Chemical Physics, 519, 85–91. Retrieved 2019-03-24, from https://linkinghub.elsevier.com/retrieve/pii/S0301010418311005 doi: 10.1016/j.chemphys.2018.12.008

Meneghin, E., Volpato, A., Cupellini, L., Bolzonello, L., Jurinovich, S., Mascoli, V., ... Collini, E. (2018, December). Coherence in carotenoid-to-chlorophyll energy transfer. Nature Communications, 9(1), 3160. Retrieved 2019-04-08, from http://www.nature.com/articles/s41467-018-05596-5 doi: 10.1038/s41467-018-05596-5

Mohseni, M., Omar, Y., Engel, G. S., & Plenio, M. B. (Eds.). (2014). Quantum Effects in Biology. Reino Unido: Cambridge University Press.

Mohseni, M., Rebentrost, P., Lloyd, S., & Aspuru-Guzik, A. (2008, November). Environment-assisted quantum walks in photosynthetic energy transfer. The Journal of Chemical Physics, 129(17), 174106. Retrieved 2019-04-08, from http://aip.scitation.org/doi/10.1063/1.3002335 doi: 10.1063/1.3002335

Moix, J. M., Ma, J., & Cao, J. (2015, March). Förster resonance energy transfer, absorption and emission spectra in multichromophoric systems. III. Exact stochastic path integral evaluation. The Journal of Chemical Physics, 142(9), 094108. Retrieved 2020-08-24, from http://aip.scitation.org/doi/10.1063/1.4908601 doi: 10.1063/1.4908601

Mollers, I., Jager, D., Gaudino, R., Nocivelli, A., Kragl, H., Ziemann, O., ... Randel, S. (2009, August). Plastic optical fiber technology for reliable home networking: overview and results of the EU project pof-all. IEEE Commun. Mag., 47(8), 58–68.

Monras, A., Checińska, A., & Ekert, A. (2014, June). Witnessing quantum coherence in the presence of noise. New J. Phys., 16(6), 063041. Retrieved 2019-05-05, from http://stacks.iop.org/1367-2630/16/i=6/a=063041?key=crossref.808d53abbdb14feacca57ac8235bf2b1 doi: 10.1088/1367-2630/16/6/063041

Morzan, U. N., Ramírez, F. F., Oviedo, M. B., Sánchez, C. G., Scherlis, D. A., & Lebrero, M. C. G. (2014, April). Electron dynamics in complex environments with real-time time dependent density functional theory in a QM-MM framework. The Journal of Chemical Physics, 140(16), 164105. Retrieved 2020-11-26, from http://aip.scitation.org/doi/10.1063/1.4871688 doi: 10.1063/1.4871688

Mullineaux, C. W., Pascal, A. A., Horton, P., & Holzwarth, A. R. (1993, February). Excitation-energy quenching in aggregates of the LHC II chlorophyll-protein complex: a time-resolved fluorescence study. Biochimica et Biophysica Acta (BBA) - Bioenergetics, 1141(1), 23–28. Retrieved 2019-05-01, from https://linkinghub

.elsevier.com/retrieve/pii/000527289390184H doi: 10.1016/0005-2728(93)90184-H

Najibi, A., & Goerigk, L. (2018, November). The Nonlocal Kernel in van der Waals Density Functionals as an Additive Correction: An Extensive Analysis with Special Emphasis on the B97M-V and ωB97M-V Approaches. Journal of Chemical Theory and Computation, 14(11), 5725–5738. Retrieved 2020-11-20, from https://pubs.acs.org/doi/10.1021/acs.jctc.8b00842 doi: 10.1021/acs.jctc.8b00842

Neese, F. (2012, January). The ORCA program system. WIREs Computational Molecular Science, 2(1), 73–78. Retrieved 2020-11-26, from https://onlinelibrary.wiley.com/doi/abs/10.1002/wcms.81 doi: 10.1002/wcms.81

Neese, F. (2018, January). Software update: the ORCA program system, version 4.0. WIREs Computational Molecular Science, 8(1). Retrieved 2020-11-26, from https://onlinelibrary.wiley.com/doi/abs/10.1002/wcms.1327 doi: 10.1002/wcms.1327

Niehaus, T. A., Suhai, S., Della Sala, F., Lugli, P., Elstner, M., Seifert, G., & Frauenheim, T. (2001, Feb). Tight-binding approach to time-dependent density-functional response theory. Phys. Rev. B, 63, 085108. Retrieved from https://link.aps.org/doi/10.1103/PhysRevB.63.085108 doi: 10.1103/PhysRevB.63.085108

Niel, C. B. (1932). On the morphology and physiology of the purple and green sulphur bacteria. Archiv für Mikrobiologie, 3(1), 1–112. Retrieved 2019-04-27, from http://link.springer.com/10.1007/BF00454965 doi: 10.1007/BF00454965

Nielsen, M. A., & Chuang, I. L. (2010). Quantum computation and quantum information (10th anniversary ed ed.). Cambridge ; New York: Cambridge University Press.

Novoderezhkin, V., Monshouwer, R., & van Grondelle, R. (1999, November). Exciton (De)Localization in the LH2 Antenna of *Rhodobacter* sphaeroides As Revealed by Relative Difference Absorption Measurements of the LH2 Antenna and the B820

Subunit. The Journal of Physical Chemistry B, 103(47), 10540–10548. Retrieved 2020-03-25, from https://pubs.acs.org/doi/10.1021/jp9844415 doi: 10.1021/jp9844415

O'Boyle, N. M., Banck, M., James, C. A., Morley, C., Vandermeersch, T., & Hutchison, G. R. (2011, October). Open babel: An open chemical toolbox. J. Cheminform., 3(1), 33.

Oka, H. (2016, September). Role of an elliptical structure in photosynthetic energy transfer: Collaboration between quantum entanglement and thermal fluctuation. Scientific Reports, 6(1), 26058. Retrieved 2019-04-22, from http://www.nature.com/articles/srep26058 doi: 10.1038/srep26058

Okuno, K., Shigeta, Y., Kishi, R., Miyasaka, H., & Nakano, M. (2012, May). Tuned CAM-B3LYP functional in the time-dependent density functional theory scheme for excitation energies and properties of diarylethene derivatives. Journal of Photochemistry and Photobiology A: Chemistry, 235, 29–34. Retrieved 2020-11-20, from https://linkinghub.elsevier.com/retrieve/pii/S101060301200130X doi: 10.1016/j.jphotochem.2012.03.003

Olbrich, C., & Kleinekathöfer, U. (2010, September). Time-Dependent Atomistic View on the Electronic Relaxation in Light-Harvesting System II. J. Phys. Chem. B, 114(38), 12427–12437. Retrieved 2020-02-28, from https://pubs.acs.org/doi/10.1021/jp106542v doi: 10.1021/jp106542v

Ollivier, H., & Zurek, W. H. (2002). Quantum Discord: A Measure of the Quantumness of Correlations. PHYSICAL REVIEW LETTERS, 88(1), 4.

Olson, T. L., van de Meene, A. M. L., Francis, J. N., Pierson, B. K., & Blankenship, R. E. (2007, June). Pigment Analysis of "Candidatus Chlorothrix halophila," a Green Filamentous Anoxygenic Phototrophic Bacterium. Journal of Bacteriology, 189(11), 4187–4195. Retrieved 2019-05-10, from http://jb.asm.org/cgi/doi/10.1128/JB.01712-06 doi: 10.1128/JB.01712-06

Orf, G. S., & Blankenship, R. E. (2013, October). Chlorosome antenna complexes from green photosynthetic bacteria. Photosynthesis Research, 116(2-3), 315–331. Retrieved 2019-04-08, from http://link.springer.com/10.1007/s11120-013-9869-3 doi: 10.1007/s11120-013-9869-3

Panitchayangkoon, G., Hayes, D., Fransted, K. A., Caram, J. R., Harel, E., Wen, J., ... Engel, G. S. (2010, July). Long-lived quantum coherence in photosynthetic complexes at physiological temperature. Proceedings of the National Academy of Sciences, 107(29), 12766–12770. Retrieved 2019-04-08, from http://www.pnas.org/cgi/doi/10.1073/pnas.1005484107 doi: 10.1073/pnas.1005484107

Panitchayangkoon, G., Voronine, D. V., Abramavicius, D., Caram, J. R., Lewis, N. H. C., Mukamel, S., & Engel, G. S. (2011, December). Direct evidence of quantum transport in photosynthetic light-harvesting complexes. Proceedings of the National Academy of Sciences, 108(52), 20908–20912. Retrieved 2019-04-08, from http://www.pnas.org/cgi/doi/10.1073/pnas.1105234108 doi: 10.1073/pnas.1105234108

Papiz, M. Z., Prince, S. M., Howard, T., Cogdell, R. J., & Isaacs, N. W. (2003, March). The Structure and Thermal Motion of the B800–850 LH2 Complex from Rps.acidophila at 2.0Å Resolution and 100k: New Structural Features and Functionally Relevant Motions. Journal of Molecular Biology, 326(5), 1523–1538. Retrieved 2019-05-11, from https://linkinghub.elsevier.com/retrieve/pii/S002228360300024X doi: 10.1016/S0022-2836(03)00024-X

Passaquet, C., Thomas, J., Caron, L., Hauswirth, N., Puel, F., & Berkaloff, C. (1991, March). Light harvesting complexes in brown algae: Biochemical characterization and inmunological relationships. FEBS Journal, 280(1), 21–26.

Peers, G., Truong, T. B., Ostendorf, E., Busch, A., Elrad, D., Grossman, A. R., ... Niyogi, K. K. (2009, November). An ancient light-harvesting protein is critical for the regulation of algal photosynthesis. Nature, 462(7272), 518–521. Retrieved 2019-05-12, from http://www.nature.com/articles/nature08587 doi: 10.1038/nature08587

Peng, B., Lingerfelt, D. B., Ding, F., Aikens, C. M., & Li, X. (2015, March). Real-Time TDDFT Studies of Exciton Decay and Transfer in Silver Nanowire Arrays. The Journal of Physical Chemistry C, 119(11), 6421–6427. Retrieved 2020-11-26, from https://pubs.acs.org/doi/10.1021/acs.jpcc.5b00263 doi: 10.1021/acs.jpcc.5b00263

Perdew, J. P. (1986, June). Density-functional approximation for the correlation energy of the inhomogeneous electron gas. Physical Review B, 33(12), 8822–8824. Retrieved 2020-11-27, from https://link.aps.org/doi/10.1103/PhysRevB.33.8822 doi: 10.1103/PhysRevB.33.8822

Perdew, J. P., Burke, K., & Ernzerhof, M. (1996, October). Generalized Gradient Approximation Made Simple. Physical Review Letters, 77(18), 3865–3868. Retrieved 2020-11-27, from https://link.aps.org/doi/10.1103/PhysRevLett.77.3865 doi: 10.1103/PhysRevLett.77.3865

Perdew, J. P., Ernzerhof, M., & Burke, K. (1996, December). Rationale for mixing exact exchange with density functional approximations. The Journal of Chemical Physics, 105(22), 9982–9985. Retrieved 2020-11-27, from http://aip.scitation.org/doi/10.1063/1.472933 doi: 10.1063/1.472933

Perdew, J. P., Tao, J., Staroverov, V. N., & Scuseria, G. E. (2004, April). Meta-generalized gradient approximation: Explanation of a realistic nonempirical density functional. The Journal of Chemical Physics, 120(15), 6898–6911. Retrieved 2020-11-27, from http://aip.scitation.org/doi/10.1063/1.1665298 doi: 10.1063/1.1665298

Peterman, E. J., Monshouwer, R., van Stokkum, I. H., van Grondelle, R., & van Amerongen, H. (1997). Ultrafast singlet excitation transfer from carotenoids to chlorophylls via different pathways in light-harvesting complex ii of higher plants. Chemical Physics Letters, 264(3), 279-284. Retrieved from https://www.sciencedirect.com/science/article/pii/S0009261496013346 doi: https://doi.org/10.1016/S0009-2614(96)01334-6

Pieper, J., Rätsep, M., Trostmann, I., Schmitt, F.-J., Theiss, C., Paulsen, H., ... Renger, G. (2011, April). Excitonic Energy Level Structure and Pigment-Protein Interactions in the Recombinant Water-Soluble Chlorophyll Protein. II. Spectral Hole-Burning Experiments. The Journal of Physical Chemistry B, 115(14), 4053–4065. Retrieved 2020-02-25, from https://pubs.acs.org/doi/10.1021/jp111457t doi: 10.1021/jp111457t

Pitera, J. W., Falta, M., & van Gunsteren, W. F. (2001, June). Dielectric Properties of Proteins from Simulation: The Effects of Solvent, Ligands, pH, and Temperature. Biophysical Journal, 80(6), 2546–2555. Retrieved 2020-03-03, from https://linkinghub.elsevier.com/retrieve/pii/S0006349501762261 doi: 10.1016/S0006-3495(01)76226-1

Plenio, M. B., & Huelga, S. F. (2008, November). Dephasing-assisted transport: quantum networks and biomolecules. New Journal of Physics, 10(11), 113019. Retrieved 2019-05-05, from http://stacks.iop.org/1367-2630/10/i=11/a=113019?key=crossref.36d81b34c2b44449dc5f16ebd1e681ac doi: 10.1088/1367-2630/10/11/113019

Plötz, P.-A., Polyutov, S. P., Ivanov, S. D., Fennel, F., Wolter, S., Niehaus, T., ... Kühn, O. (2016). Biphasic aggregation of a perylene bisimide dye identified by exciton-vibrational spectra. Physical Chemistry Chemical Physics, 18(36), 25110–25119. Retrieved 2020-08-24, from http://xlink.rsc.org/?DOI=C6CP04898F doi: 10.1039/C6CP04898F

Polyutov, S., Kühn, O., & Pullerits, T. (2012, February). Exciton-vibrational coupling in molecular aggregates: Electronic versus vibronic dimer. Chemical Physics, 394(1), 21–28. Retrieved 2020-08-24, from https://linkinghub.elsevier.com/retrieve/pii/S0301010411005520 doi: 10.1016/j.chemphys.2011.12.006

Prince, S. M., Papiz, M. Z., Freer, A. A., McDermott, G., Hawthornthwaite-Lawless, A. M., Cogdell, R. J., & Isaacs, N. W. (1997). Apoprotein Structure in the LH2

Complex from Rhodopseudomonas acidophila Strain 10050: Modular Assembly and Protein Pigment Interactions. Journal of Molecular Biology, 268, 412–423.

Raszewski, G., Saenger, W., & Renger, T. (2005, February). Theory of Optical Spectra of Photosystem II Reaction Centers: Location of the Triplet State and the Identity of the Primary Electron Donor. Biophysical Journal, 88(2), 986–998. Retrieved 2020-03-25, from https://linkinghub.elsevier.com/retrieve/pii/S0006349505731702 doi: 10.1529/biophysj.104.050294

Redfield, A. G. (1957, January). On the Theory of Relaxation Processes. IBM J. Res. & Dev., 1(1), 19–31. Retrieved 2019-06-16, from http://ieeexplore.ieee.org/lpdocs/epic03/wrapper.htm?arnumber=5392713 doi: 10.1147/rd.11.0019

Ren, J., Shuai, Z., & Kin-Lic Chan, G. (2018, October). Time-Dependent Density Matrix Renormalization Group Algorithms for Nearly Exact Absorption and Fluorescence Spectra of Molecular Aggregates at Both Zero and Finite Temperature. Journal of Chemical Theory and Computation, 14(10), 5027–5039. Retrieved 2020-08-24, from https://pubs.acs.org/doi/10.1021/acs.jctc.8b00628 doi: 10.1021/acs.jctc.8b00628

Renger, T., Madjet, M. E., Müh, F., Trostmann, I., Schmitt, F.-J., Theiss, C., ... Renger, G. (2009, July). Thermally Activated Superradiance and Intersystem Crossing in the Water-Soluble Chlorophyll Binding Protein. The Journal of Physical Chemistry B, 113(29), 9948–9957. Retrieved 2020-02-25, from https://pubs.acs.org/doi/10.1021/jp901886w doi: 10.1021/jp901886w

Renger, T., & May, V. (2000, May). Simulations of Frequency-Domain Spectra: Structure-Function Relationships in Photosynthetic Pigment-Protein Complexes. Physical Review Letters, 84(22), 5228–5231. Retrieved 2020-08-24, from https://link.aps.org/doi/10.1103/PhysRevLett.84.5228 doi: 10.1103/PhysRevLett.84.5228

Renger, T., Trostmann, I., Theiss, C., Madjet, M. E., Richter, M., Paulsen, H., ... Renger, G. (2007, September). Refinement of a Structural Model of a Pigment-

Protein Complex by Accurate Optical Line Shape Theory and Experiments. The Journal of Physical Chemistry B, 111(35), 10487–10501. Retrieved 2020-02-25, from https://pubs.acs.org/doi/10.1021/jp0717241 doi: 10.1021/jp0717241

Rivas, A., & Huelga, S. F. (2012). Open Quantum Systems: An Introduction. Berlin, Heidelberg: Springer Berlin Heidelberg. Retrieved 2020-08-13, from http://link.springer.com/10.1007/978-3-642-23354-8 doi: 10.1007/978-3-642-23354-8

Robinson, D. (2018, August). Comparison of the transition dipole moments calculated by TDDFT with high level wave function theory. Journal of Chemical Theory and Computation, 14(10), 5303–5309. Retrieved from https://doi.org/10.1021/acs.jctc.8b00335 doi: 10.1021/acs.jctc.8b00335

Rocca, D., Lu, D., & Galli, G. (2010, October). *Ab* initio calculations of optical absorption spectra: Solution of the Bethe–Salpeter equation within density matrix perturbation theory. The Journal of Chemical Physics, 133(16), 164109. Retrieved 2020-08-24, from http://aip.scitation.org/doi/10.1063/1.3494540 doi: 10.1063/1.3494540

Romero, E., Augulis, R., Novoderezhkin, V. I., Ferretti, M., Thieme, J., Zigmantas, D., & van Grondelle, R. (2014, September). Quantum coherence in photosynthesis for efficient solar-energy conversion. Nature Physics, 10(9), 676–682. Retrieved 2019-04-08, from http://www.nature.com/articles/nphys3017 doi: 10.1038/nphys3017

Rosnik, A. M., & Curutchet, C. (2015, November). Theoretical characterization of the spectral density of the water-soluble chlorophyll-binding protein from combined quantum mechanics/molecular mechanics molecular dynamics simulations. Journal of Chemical Theory and Computation, 11(12), 5826–5837. Retrieved from https://doi.org/10.1021/acs.jctc.5b00891 doi: 10.1021/acs.jctc.5b00891

Roszak, A. W. (2003, December). Crystal Structure of the RC-LH1 Core Complex from Rhodopseudomonas palustris. Science, 302(5652), 1969–1972. Retrieved 2019-05-11, from http://www.sciencemag.org/cgi/doi/10.1126/science.1088892 doi: 10.1126/science.1088892

Rudin, W. (1987). Real and complex analysis (3rd ed ed.). New York: McGraw-Hill.

Rulli, C. C., & Sarandy, M. S. (2011, October). Global quantum discord in multipartite systems. Physical Review A, 84(4), 042109. Retrieved 2019-04-22, from https://link.aps.org/doi/10.1103/PhysRevA.84.042109 doi: 10.1103/PhysRevA.84.042109

Saberi, M., Harouni, M. B., Roknizadeh, R., & Latifi, H. (2016, July). Energy transfer and quantum correlation dynamics in FMO light-harvesting complex. Molecular Physics, 114(14), 2123–2131. Retrieved 2019-04-22, from http://www.tandfonline.com/doi/full/10.1080/00268976.2016.1185548 doi: 10.1080/00268976.2016.1185548

Sage, R. F., & Stata, M. (2015, January). Photosynthetic diversity meets biodiversity: The C4 plant example. Journal of Plant Physiology, 172, 104–119. Retrieved 2019-04-26, from https://linkinghub.elsevier.com/retrieve/pii/S0176161714002363 doi: 10.1016/j.jplph.2014.07.024

Salikhov, K. M., Golbeck, J. H., & Stehlik, D. (2007, March). Quantum teleportation across a biological membrane by means of correlated spin pair dynamics in photosynthetic reaction centers. Applied Magnetic Resonance, 31(1-2), 237–252. Retrieved 2019-04-22, from http://link.springer.com/10.1007/BF03166259 doi: 10.1007/BF03166259

Sarovar, M., Ishizaki, A., Fleming, G. R., & Whaley, K. B. (2010, June). Quantum entanglement in photosynthetic light-harvesting complexes. Nature Physics, 6(6), 462–467. Retrieved 2019-04-08, from http://www.nature.com/articles/nphys1652 doi: 10.1038/nphys1652

Schlau-Cohen, G. S., Dawlaty, J. M., & Fleming, G. R. (2012, January). Ultrafast Multidimensional Spectroscopy: Principles and Applications to Photosynthetic Systems. IEEE Journal of Selected Topics in Quantum Electronics, 18(1), 283–295. Retrieved 2019-04-08, from http://ieeexplore.ieee.org/document/5742965/ doi: 10.1109/JSTQE.2011.2112640

Scholes, G. D., & Ghiggino, K. P. (1994, April). Electronic Interactions and Interchromophore Excitation Transfer. J. Phys. Chem., 98(17), 4580–4590. Retrieved 2019-05-01, from http://pubs.acs.org/doi/abs/10.1021/j100068a017 doi: 10.1021/j100068a017

Schröder, M., Kleinekathöfer, U., & Schreiber, M. (2006, February). Calculation of absorption spectra for light-harvesting systems using non-Markovian approaches as well as modified Redfield theory. The Journal of Chemical Physics, 124(8), 084903. Retrieved 2020-08-24, from http://aip.scitation.org/doi/10.1063/1.2171188 doi: 10.1063/1.2171188

Schröder, M., Schreiber, M., & Kleinekathöfer, U. (2007, July). A time-dependent modified Redfield theory for absorption spectra applied to light-harvesting systems. Journal of Luminescence, 125(1-2), 126–132. Retrieved 2020-08-24, from https://linkinghub.elsevier.com/retrieve/pii/S0022231306005771 doi: 10.1016/j.jlumin.2006.08.086

Schrödinger, E. (1992). What is Life? (2nd ed.). Reino Unido: Cambridge University Press.

Schröter, M., Ivanov, S., Schulze, J., Polyutov, S., Yan, Y., Pullerits, T., & Kühn, O. (2015, March). Exciton-vibrational coupling in the dynamics and spectroscopy of Frenkel excitons in molecular aggregates. Physics Reports, 567, 1–78. Retrieved 2020-08-12, from https://linkinghub.elsevier.com/retrieve/pii/S0370157314004104 doi: 10.1016/j.physrep.2014.12.001

Schutz, C. N., & Warshel, A. (2001, September). What are the dielectric "constants" of proteins and how to validate electrostatic models? Proteins, 44(4), 400–417. Retrieved 2020-03-03, from http://doi.wiley.com/10.1002/prot.1106 doi: 10.1002/prot.1106

Schwinn, K., Ferré, N., & Huix-Rotllant, M. (2020). UV-visible absorption spectrum of FAD and its reduced forms embedded in cryptochrome protein. Physical Chemistry

Chemical Physics, 22, 12447–12455. Retrieved 2020-08-24, from http://xlink.rsc.org/?DOI=C6CP06015C doi: 10.1039/C6CP06015C

Shao, Y., Mei, Y., Sundholm, D., & Kaila, V. R. I. (2020, January). Benchmarking the Performance of Time-Dependent Density Functional Theory Methods on Biochromophores. Journal of Chemical Theory and Computation, 16(1), 587–600. Retrieved 2020-11-20, from https://pubs.acs.org/doi/10.1021/acs.jctc.9b00823 doi: 10.1021/acs.jctc.9b00823

Sigfridsson, E., & Ryde, U. (1998). Comparison of methods for deriving atomic charges from the electrostatic potential and moments. Journal of Computational Chemistry, 19(4), 377–396.

Sirohiwal, A., Berraud-Pache, R., Neese, F., Izsák, R., & Pantazis, D. A. (2020, October). Accurate Computation of the Absorption Spectrum of Chlorophyll *a* with Pair Natural Orbital Coupled Cluster Methods. The Journal of Physical Chemistry B, 124(40), 8761–8771. Retrieved 2020-11-20, from https://pubs.acs.org/doi/10.1021/acs.jpcb.0c05761 doi: 10.1021/acs.jpcb.0c05761

Sirohiwal, A., Neese, F., & Pantazis, D. A. (2020, October). Protein Matrix Control of Reaction Center Excitation in Photosystem II. Journal of the American Chemical Society, 142(42), 18174–18190. Retrieved 2020-11-20, from https://pubs.acs.org/doi/10.1021/jacs.0c08526 doi: 10.1021/jacs.0c08526

Staroverov, V. N., Scuseria, G. E., Tao, J., & Perdew, J. P. (2003, December). Comparative assessment of a new nonempirical density functional: Molecules and hydrogen-bonded complexes. The Journal of Chemical Physics, 119(23), 12129–12137. Retrieved 2020-11-27, from http://aip.scitation.org/doi/10.1063/1.1626543 doi: 10.1063/1.1626543

Streckaite, S., Gardian, Z., Li, F., Pascal, A. A., Litvin, R., Robert, B., & Llansola-Portoles, M. J. (2018, November). Pigment configuration in the light-harvesting protein of the xanthophyte alga Xanthonema debile. Photosynth Res, 138(2), 139–

148. Retrieved 2019-05-10, from http://link.springer.com/10.1007/s11120-018-0557-1 doi: 10.1007/s11120-018-0557-1

Stross, C., Van der Kamp, M. W., Oliver, T. A. A., Harvey, J. N., Linden, N., & Manby, F. R. (2016, November). How Static Disorder Mimics Decoherence in Anisotropy Pump-Probe Experiments on Purple-Bacteria Light Harvesting Complexes. The Journal of Physical Chemistry B, 120(44), 11449–11463. Retrieved 2020-08-17, from https://pubs.acs.org/doi/10.1021/acs.jpcb.6b09916 doi: 10.1021/acs.jpcb.6b09916

Tanimura, Y. (2006, August). Stochastic Liouville, Langevin, Fokker–Planck, and Master Equation Approaches to Quantum Dissipative Systems. Journal of the Physical Society of Japan, 75(8), 082001. Retrieved 2019-04-22, from https://journals.jps.jp/doi/10.1143/JPSJ.75.082001 doi: 10.1143/JPSJ.75.082001

Tanimura, Y., & Kubo, R. (1989, January). Time Evolution of a Quantum System in Contact with a Nearly Gaussian-Markoffian Noise Bath. Journal of the Physical Society of Japan, 58(1), 101–114.

Tao, J., Perdew, J. P., Staroverov, V. N., & Scuseria, G. E. (2003, September). Climbing the Density Functional Ladder: Nonempirical Meta–Generalized Gradient Approximation Designed for Molecules and Solids. Physical Review Letters, 91(14), 146401. Retrieved 2020-11-26, from https://link.aps.org/doi/10.1103/PhysRevLett.91.146401 doi: 10.1103/PhysRevLett.91.146401

Turner, D. B., Dinshaw, R., Lee, K.-K., Belsley, M. S., Wilk, K. E., Curmi, P. M. G., & Scholes, G. D. (2012). Quantitative investigations of quantum coherence for a light-harvesting protein at conditions simulating photosynthesis. Physical Chemistry Chemical Physics, 14(14), 4857. Retrieved 2019-04-22, from http://xlink.rsc.org/?DOI=c2cp23670b doi: 10.1039/c2cp23670b

Tussupbayev, S., Govind, N., Lopata, K., & Cramer, C. J. (2015, March). Comparison of Real-Time and Linear-Response Time-Dependent Density Functional Theories for

Molecular Chromophores Ranging from Sparse to High Densities of States. Journal of Chemical Theory and Computation, 11(3), 1102–1109. Retrieved 2020-11-26, from https://pubs.acs.org/doi/10.1021/ct500763y doi: 10.1021/ct500763y

Żukowski, M., & Brukner, C. (2002, May). Bell's Theorem for General N -Qubit States. Physical Review Letters, 88(21), 210401. Retrieved 2019-04-22, from https://link.aps.org/doi/10.1103/PhysRevLett.88.210401 doi: 10.1103/PhysRevLett.88.210401

van Amerongen, H., Valkunas, L., & van Grondelle, R. (2000). Photosynthetic excitons. World Scientific Publishing Co. Pte. Ltd. Retrieved 2019-04-29, from https://research.vu.nl/en/publications/photosynthetic-excitons

Vlachos, M., Kollios, G., & Gunopulos, D. (2002). Discovering similar multidimensional trajectories. In Proceedings 18th International Conference on Data Engineering (pp. 673–684). San Jose, CA, USA: IEEE Comput. Soc. Retrieved 2020-09-30, from http://ieeexplore.ieee.org/document/994784/ doi: 10.1109/ICDE.2002.994784

Voityuk, A. A. (2014a, January). Estimation of Electronic Coupling for Singlet Excitation Energy Transfer. The Journal of Physical Chemistry C, 118(3), 1478–1483. Retrieved 2020-04-06, from https://pubs.acs.org/doi/10.1021/jp410802d doi: 10.1021/jp410802d

Voityuk, A. A. (2014b, June). Fragment transition density method to calculate electronic coupling for excitation energy transfer. The Journal of Chemical Physics, 140(24), 244117. Retrieved 2020-04-06, from http://aip.scitation.org/doi/10.1063/1.4884944 doi: 10.1063/1.4884944

Wang, F., Yam, C. Y., Chen, G., Wang, X., Fan, K., Niehaus, T. A., & Frauenheim, T. (2007, July). Linear scaling time-dependent density-functional tight-binding method for absorption spectra of large systems. Physical Review B, 76(4), 045114. Retrieved 2020-08-24, from https://link.aps.org/doi/10.1103/PhysRevB.76.045114 doi: 10.1103/PhysRevB.76.045114

Wehner, J., & Baumeier, B. (2017, April). Intermolecular Singlet and Triplet Exciton Transfer Integrals from Many-Body Green's Functions Theory. J. Chem. Theory Comput., 13(4), 1584–1594. Retrieved 2020-04-06, from https://pubs.acs.org/doi/10.1021/acs.jctc.6b00935 doi: 10.1021/acs.jctc.6b00935

Wheeden, R. L., & Zygmund, A. (1977). Measure and Integral: An Introduction to Real Analysis (No. 43). New York, USA: Marcel Dekker.

Wientjes, E., van Amerongen, H., & Croce, R. (2013, September). Quantum Yield of Charge Separation in Photosystem II: Functional Effect of Changes in the Antenna Size upon Light Acclimation. J. Phys. Chem. B, 117(38), 11200–11208. Retrieved 2019-05-01, from http://pubs.acs.org/doi/10.1021/jp401663w doi: 10.1021/jp401663w

Wilde, M. M., McCracken, J. M., & Mizel, A. (2010, May). Could light harvesting complexes exhibit non-classical effects at room temperature? Proceedings of the Royal Society A: Mathematical, Physical and Engineering Sciences, 466(2117), 1347–1363. Retrieved 2019-04-08, from http://www.royalsocietypublishing.org/doi/10.1098/rspa.2009.0575 doi: 10.1098/rspa.2009.0575

Williams, C. J., Headd, J. J., Moriarty, N. W., Prisant, M. G., Videau, L. L., Deis, L. N., ... Richardson, D. C. (2018, January). MolProbity: More and better reference data for improved all-atom structure validation. Protein Science, 27(1), 293–315. Retrieved 2021-02-03, from http://doi.wiley.com/10.1002/pro.3330 doi: 10.1002/pro.3330

Wolf, B. M., Niedzwiedzki, D. M., Magdaong, N. C. M., Roth, R., Goodenough, U., & Blankenship, R. E. (2018, March). Characterization of a newly isolated freshwater Eustigmatophyte alga capable of utilizing far-red light as its sole light source. Photosynth Res, 135(1-3), 177–189. Retrieved 2019-05-10, from http://link.springer.com/10.1007/s11120-017-0401-z doi: 10.1007/s11120-017-0401-z

Xie, X., Liu, Y., Yao, Y., Schollwöck, U., Liu, C., & Ma, H. (2019, December). Time-dependent density matrix renormalization group quantum dynamics

for realistic chemical systems. The Journal of Chemical Physics, 151(22), 224101. Retrieved 2020-08-24, from http://aip.scitation.org/doi/10.1063/1.5125945 doi: 10.1063/1.5125945

Xu, X., & Goddard, W. A. (2004, March). The X3LYP extended density functional for accurate descriptions of nonbond interactions, spin states, and thermochemical properties. Proceedings of the National Academy of Sciences, 101(9), 2673–2677.

Yanai, T., Tew, D. P., & Handy, N. C. (2004, July). A new hybrid exchange–correlation functional using the Coulomb-attenuating method (CAM-B3LYP). Chemical Physics Letters, 393(1-3), 51–57. Retrieved 2020-11-27, from https://linkinghub.elsevier.com/retrieve/pii/S0009261404008620 doi: 10.1016/j.cplett.2004.06.011

Yang, M. (2005, September). A reduced density-matrix theory of absorption line shape of molecular aggregate. The Journal of Chemical Physics, 123(12), 124705. Retrieved 2020-08-12, from http://aip.scitation.org/doi/10.1063/1.2046668 doi: 10.1063/1.2046668

Yang, M. (2006, September). Influence of energy transfer on the intensity pattern of vibronic excitation studied by reduced density-matrix theory. Journal of Molecular Spectroscopy, 239(1), 108–114. Retrieved 2020-08-24, from https://linkinghub.elsevier.com/retrieve/pii/S0022285206001871 doi: 10.1016/j.jms.2006.06.004

Yao, Y., Sun, K.-W., Luo, Z., & Ma, H. (2018, January). Full Quantum Dynamics Simulation of a Realistic Molecular System Using the Adaptive Time-Dependent Density Matrix Renormalization Group Method. The Journal of Physical Chemistry Letters, 9(2), 413–419. Retrieved 2020-08-24, from https://pubs.acs.org/doi/10.1021/acs.jpclett.7b03224 doi: 10.1021/acs.jpclett.7b03224

You, Z.-Q., & Hsu, C.-P. (2014, January). Theory and calculation for the electronic coupling in excitation energy transfer. International Journal of Quantum Chemistry,

114(2), 102–115. Retrieved 2020-04-19, from http://doi.wiley.com/10.1002/qua.24528 doi: 10.1002/qua.24528

Zanetti-Polzi, L., Aschi, M., Daidone, I., & Amadei, A. (2017, February). Theoretical modeling of the absorption spectrum of aqueous riboflavin. Chemical Physics Letters, 669, 119–124. Retrieved 2020-08-24, from https://linkinghub.elsevier.com/retrieve/pii/S000926141630971X doi: 10.1016/j.cplett.2016.12.022

Zhao, Y., & Truhlar, D. G. (2006, November). A new local density functional for main-group thermochemistry, transition metal bonding, thermochemical kinetics, and noncovalent interactions. The Journal of Chemical Physics, 125(19), 194101. Retrieved 2020-11-27, from http://aip.scitation.org/doi/10.1063/1.2370993 doi: 10.1063/1.2370993

Zhao, Y., & Truhlar, D. G. (2008, May). The M06 suite of density functionals for main group thermochemistry, thermochemical kinetics, noncovalent interactions, excited states, and transition elements: two new functionals and systematic testing of four M06-class functionals and 12 other functionals. Theoretical Chemistry Accounts, 120(1-3), 215–241. Retrieved 2020-11-27, from http://link.springer.com/10.1007/s00214-007-0310-x doi: 10.1007/s00214-007-0310-x

Appendices

Appendix A

Coordinate Files

A.1 6S2Z Chl b dimer

```
272
PDB ID: 6s2zFH    Chain: AD    Ligand: CHL    ID: 1001
MG   11.312   3.415   15.292
 C   13.274   3.48   18.06
 C   8.663   3.899   17.325
 C   9.255   2.753   12.689
 C   13.989   2.054   13.481
 N   11.025   3.866   17.237
 C   11.892   3.973   18.135
 C   11.419   4.528   19.414
 C   9.942   4.464   19.23
 C   9.86   4.044   17.832
 C   9.339   3.415   20.128
 C   12.03   5.859   19.83
 C   11.425   6.505   21.05
 C   11.983   6.137   22.392
 O   12.926   6.67   22.805
```

```
O    11.308    5.202    23.219
N    9.261    3.37    15.041
C    8.317    3.551    15.951
C    6.935    3.393    15.517
C    7.143    3.052    14.141
C    8.588    3.067    13.957
C    5.668    3.529    16.291
C    6.124    2.768    13.117
C    5.14    1.973    13.304
N    11.558    2.562    13.414
C    10.644    2.351    12.497
C    11.15    1.735    11.275
C    12.534    1.53    11.494
C    12.665    2.056    12.843
C    10.47    1.341    10.034
O    9.328    1.556    9.844
C    13.537    0.906    10.574
C    13.557    -0.567    10.747
N    13.255    2.873    15.602
C    14.216    2.339    14.891
C    15.454    2.119    15.67
C    15.011    2.63    16.954
C    13.79    3.018    16.815
C    16.834    1.621    15.369
C    15.441    2.851    18.345
O    16.577    2.621    18.796
C    14.32    3.427    19.101
C    14.011    2.644    20.329
O    14.164    3.098    21.395
O    13.541    1.325    20.289
```

```
C    13.547    0.54    21.421
C    11.843    4.148    23.965
C    10.68    3.524    24.654
C    10.616    2.22    24.889
C    11.729    1.347    24.508
C    9.442    1.618    25.548
C    8.779    0.644    24.613
C    8.529    1.166    23.223
C    7.881    0.09    22.374
C    8.843    -0.526    21.384
C    6.634    0.602    21.693
C    5.555    0.757    22.707
C    4.232    0.778    22.003
C    3.144    1.441    22.819
C    2.773    0.638    24.038
C    1.925    1.643    21.949
C    0.955    2.629    22.576
C    -0.303    2.81    21.744
C    -1.022    4.074    22.153
C    -1.59    4.764    20.962
C    -2.145    3.715    23.055
H    10.477    6.299    21.056
H    12.977    5.725    19.992
H    0.712    2.32    23.463
H    11.954    6.477    19.086
H    2.198    1.966    21.076
H    9.473    5.288    19.437
H    11.711    4.034    20.196
H    -2.758    3.124    22.59
H    -1.798    3.266    23.841
```

```
H    -2.614    4.52    23.324
H    -0.874    4.995    20.349
H    -2.219    4.176    20.516
H    -2.047    5.572    21.243
H    -0.39    4.662    22.595
H    9.719    2.549    19.915
H    -0.073    2.851    20.803
H    -0.888    2.045    21.86
H    1.394    3.487    22.685
H    1.48    0.792    21.81
H    2.453    -0.236    23.765
H    3.552    0.533    24.606
H    2.075    1.099    24.529
H    3.484    2.294    23.13
H    4.327    1.245    21.158
H    3.966    -0.132    21.796
H    9.53    3.632    21.054
H    5.585    0.026    23.344
H    5.681    1.577    23.21
H    6.813    1.452    21.262
H    6.355    -0.015    20.998
H    9.179    0.162    20.788
H    9.585    -0.93    21.861
H    8.384    -1.206    20.866
H    7.617    -0.621    22.979
H    7.956    1.948    23.261
H    9.365    1.447    22.82
H    8.379    3.388    19.995
H    9.331    -0.151    24.551
H    7.932    0.371    24.999
```

```
H    9.714    1.165    26.361
H    8.814    2.311    25.806
H    11.872    1.404    23.55
H    12.534    1.627    24.972
H    11.52    0.431    24.75
H    9.945    4.089    24.94
H    12.295    3.508    23.393
H    12.498    4.469    24.605
H    14.76    1.85    12.928
H    14.456    0.447    21.746
H    13.0    0.955    22.106
H    13.189    -0.336    21.209
H    14.472    4.302    19.492
H    16.784    0.715    15.026
H    17.248    2.195    14.706
H    17.365    1.63    16.18
H    13.794    -0.782    11.663
H    12.679    -0.928    10.547
H    14.211    -0.955    10.145
H    8.712    2.82    11.888
H    13.321    1.126    9.654
H    14.418    1.27    10.753
H    10.981    0.887    9.346
H    4.497    1.822    12.594
H    5.037    1.521    14.156
H    6.203    3.207    12.256
H    5.663    2.889    17.019
H    5.603    4.428    16.651
H    4.912    3.36    15.707
H    11.506    7.466    20.948
```

```
138  H    7.92    4.039    17.932
139 MG    11.312    -3.415    23.258
140  C    13.274    -3.48    20.49
141  C    8.663    -3.899    21.225
142  C    9.255    -2.753    25.861
143  C    13.989    -2.054    25.069
144  N    11.025    -3.866    21.313
145  C    11.892    -3.973    20.415
146  C    11.419    -4.528    19.136
147  C    9.942    -4.464    19.32
148  C    9.86    -4.044    20.718
149  C    9.339    -3.415    18.422
150  C    12.03    -5.859    18.72
151  C    11.425    -6.505    17.5
152  C    11.983    -6.137    16.158
153  O    12.926    -6.67    15.745
154  O    11.308    -5.202    15.331
155  N    9.261    -3.37    23.509
156  C    8.317    -3.551    22.599
157  C    6.935    -3.393    23.033
158  C    7.143    -3.052    24.409
159  C    8.588    -3.067    24.593
160  C    5.668    -3.529    22.259
161  C    6.124    -2.768    25.433
162  C    5.14    -1.973    25.246
163  N    11.558    -2.562    25.136
164  C    10.644    -2.351    26.053
165  C    11.15    -1.735    27.275
166  C    12.534    -1.53    27.056
167  C    12.665    -2.056    25.707
```

```
C    10.47    -1.341    28.516
O    9.328    -1.556    28.706
C    13.537    -0.906    27.976
C    13.557    0.567    27.803
N    13.255    -2.873    22.948
C    14.216    -2.339    23.659
C    15.454    -2.119    22.88
C    15.011    -2.63    21.596
C    13.79    -3.018    21.735
C    16.834    -1.621    23.181
C    15.441    -2.851    20.205
O    16.577    -2.621    19.754
C    14.32    -3.427    19.449
C    14.011    -2.644    18.221
O    14.164    -3.098    17.155
O    13.541    -1.325    18.261
C    13.547    -0.54    17.129
C    11.843    -4.148    14.585
C    10.68    -3.524    13.896
C    10.616    -2.22    13.661
C    11.729    -1.347    14.042
C    9.442    -1.618    13.002
C    8.779    -0.644    13.937
C    8.529    -1.166    15.327
C    7.881    -0.09    16.176
C    8.843    0.526    17.166
C    6.634    -0.602    16.857
C    5.555    -0.757    15.843
C    4.232    -0.778    16.547
C    3.144    -1.441    15.731
```

```
198 C    2.773    -0.638    14.512
199 C    1.925    -1.643    16.601
200 C    0.955    -2.629    15.974
201 C    -0.303    -2.81    16.806
202 C    -1.022    -4.074    16.397
203 C    -1.59    -4.764    17.588
204 C    -2.145    -3.715    15.495
205 H    10.477    -6.299    17.494
206 H    12.977    -5.725    18.558
207 H    0.712    -2.32    15.087
208 H    11.954    -6.477    19.464
209 H    2.198    -1.966    17.474
210 H    9.473    -5.288    19.113
211 H    11.711    -4.034    18.354
212 H    -2.758    -3.124    15.96
213 H    -1.798    -3.266    14.709
214 H    -2.614    -4.52    15.226
215 H    -0.874    -4.995    18.201
216 H    -2.219    -4.176    18.034
217 H    -2.047    -5.572    17.307
218 H    -0.39    -4.662    15.955
219 H    9.719    -2.549    18.635
220 H    -0.073    -2.851    17.747
221 H    -0.888    -2.045    16.69
222 H    1.394    -3.487    15.865
223 H    1.48    -0.792    16.74
224 H    2.453    0.236    14.785
225 H    3.552    -0.533    13.944
226 H    2.075    -1.099    14.021
227 H    3.484    -2.294    15.42
```

```
228 H    4.327    -1.245    17.392
229 H    3.966    0.132    16.754
230 H    9.53    -3.632    17.496
231 H    5.585    -0.026    15.206
232 H    5.681    -1.577    15.34
233 H    6.813    -1.452    17.288
234 H    6.355    0.015    17.552
235 H    9.179    -0.162    17.762
236 H    9.585    0.93    16.689
237 H    8.384    1.206    17.684
238 H    7.617    0.621    15.571
239 H    7.956    -1.948    15.289
240 H    9.365    -1.447    15.73
241 H    8.379    -3.388    18.555
242 H    9.331    0.151    13.999
243 H    7.932    -0.371    13.551
244 H    9.714    -1.165    12.189
245 H    8.814    -2.311    12.744
246 H    11.872    -1.404    15.0
247 H    12.534    -1.627    13.578
248 H    11.52    -0.431    13.8
249 H    9.945    -4.089    13.61
250 H    12.295    -3.508    15.157
251 H    12.498    -4.469    13.945
252 H    14.76    -1.85    25.622
253 H    14.456    -0.447    16.804
254 H    13.0    -0.955    16.444
255 H    13.189    0.336    17.341
256 H    14.472    -4.302    19.058
257 H    16.784    -0.715    23.524
```

```
258 H    17.248    -2.195    23.844
259 H    17.365    -1.63    22.37
260 H    13.794    0.782    26.887
261 H    12.679    0.928    28.003
262 H    14.211    0.955    28.405
263 H    8.712    -2.82    26.662
264 H    13.321    -1.126    28.896
265 H    14.418    -1.27    27.797
266 H    10.981    -0.887    29.204
267 H    4.497    -1.822    25.956
268 H    5.037    -1.521    24.394
269 H    6.203    -3.207    26.294
270 H    5.663    -2.889    21.531
271 H    5.603    -4.428    21.899
272 H    4.912    -3.36    22.843
273 H    11.506    -7.466    17.602
274 H    7.92    -4.039    20.618
```

Appendix B

Spectral Densities

B.1 Parameters for the modeling of Chl b WSCP spectral density

Table B.1: Parameters for the log-normal approximation of the low-energy part of the spectral density of the Chl b WSCP from Δ-FLN. Taken from Kell et al. (2013).

$\boldsymbol{k}$	$\boldsymbol{s_k}$	ω_k **(cm^{-1})**	$\boldsymbol{\sigma_k}$
1	0.39	26	0.40
2	0.23	51	0.25
3	0.23	85	0.20

Table B.2: Frequencies and Huang-Rhys factors of the Chl b WSCP from Δ-FLN. Taken from Pieper et al. (2011).

Energy (cm^{-1})	**HRF**	**Energy (cm^{-1})**	**HRF**
181	0.0173	221	0.0246
240	0.0182	269	0.0064
283	0.0036	298	0.0104
325	0.0112	352	0.0249
366	0.0112	405	0.0061
430	0.0050	470	0.0075
488	0.0061	515	0.0045
537	0.0157	572	0.0132
598	0.0036	620	0.0047
641	0.0033	700	0.0019
713	0.0025	734	0.0107
746	0.0112	757	0.0229
800	0.0022	834	0.0140
863	0.0033	887	0.0019
922	0.0291	977	0.0110
998	0.0036	1023	0.0022
1045	0.0056	1068	0.0050
1108	0.0087	1128	0.0011
1150	0.0244	1172	0.0121
1186	0.0226	1227	0.0249
1243	0.0090	1264	0.0126
1288	0.0224	1305	0.0093
1326	0.0509	1360	0.0093
1393	0.0328	1443	0.0121
1484	0.0107	1522	0.0185
1550	0.0241	1573	0.0182
1628	0.0081	1654	0.0135
1681	0.0067		

Appendix C

Linear Absorption Spectra Optimization

C.1 Estimation of the static disorder parameter

C.1.1 Spectra dependence on the statistical distribution

The spectra for all valid parameters are presented, and their dependence on the static disorder and statistical distribution selected. All site energies have been shifted so that the site energy matches the experimental one (15198 cm^{-1}).

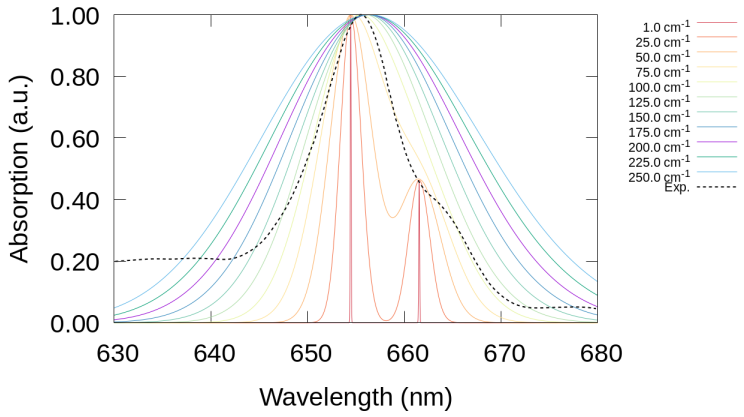

(a) Gaussian Profile

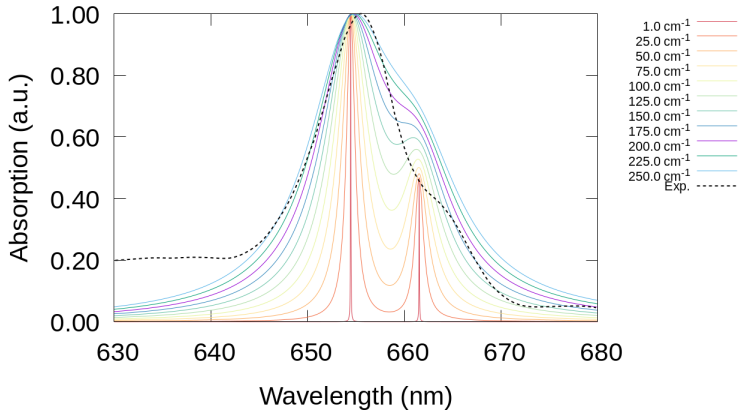

(b) Lorentzian Profile

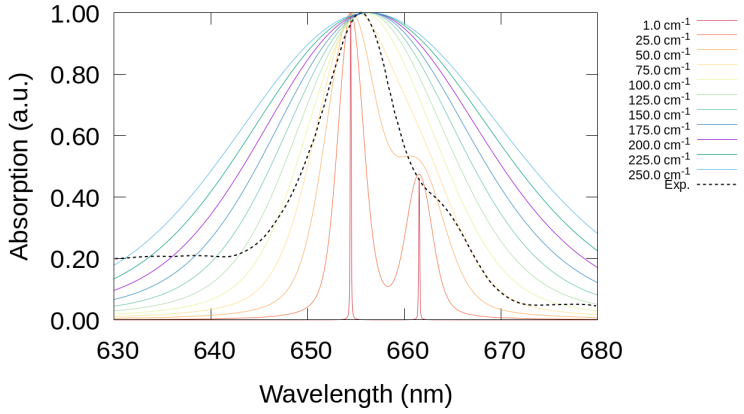

(c) Voigtian Profile

Figure C.1: Simulated spectra for approximate lineshapes of absorption spectra in the non-vibronic case. Effect of the statistical distribution and static disorder parameter σ. *Conditions:* site energy and diabatic excitonic coupling using functional M06-L.

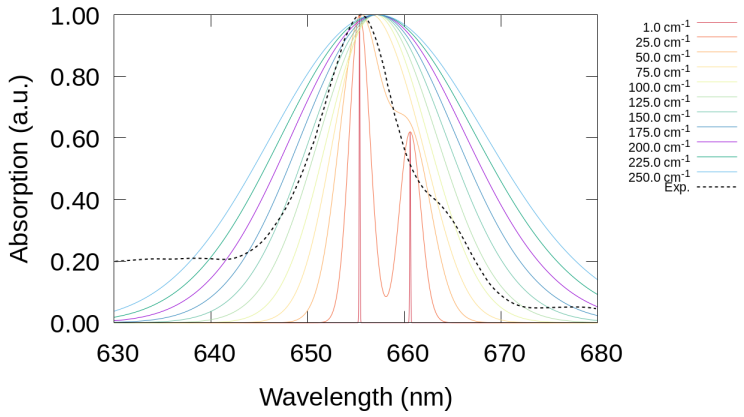

(a) Gaussian Profile

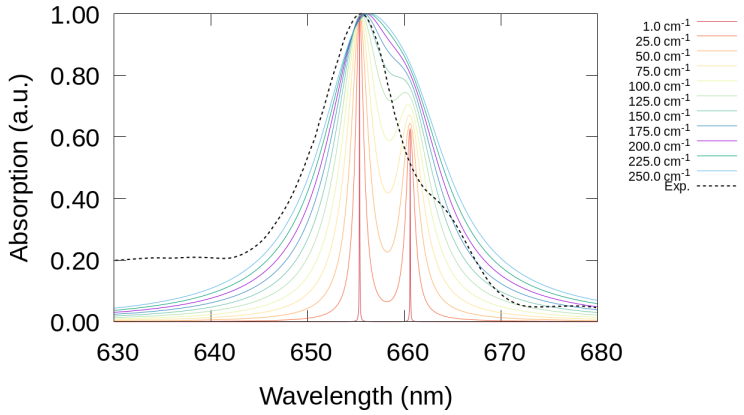

(b) Lorentzian Profile

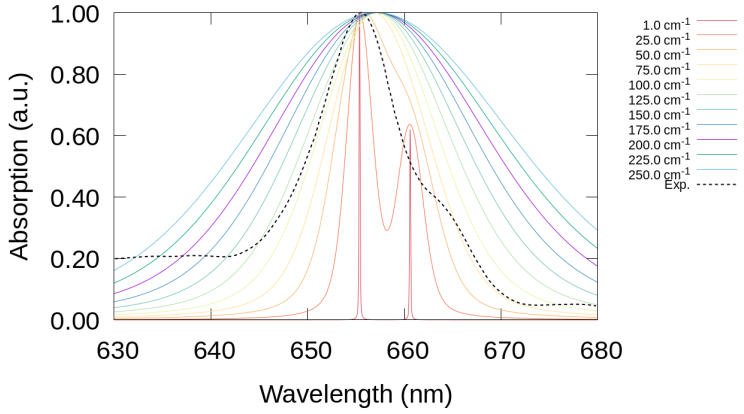

(c) Voigtian Profile

Figure C.2: Simulated spectra for approximate lineshapes of absorption spectra in the non-vibronic case. Effect of the statistical distribution and static disorder parameter σ. *Conditions:* site energy and diabatic excitonic coupling using functional TPSS.

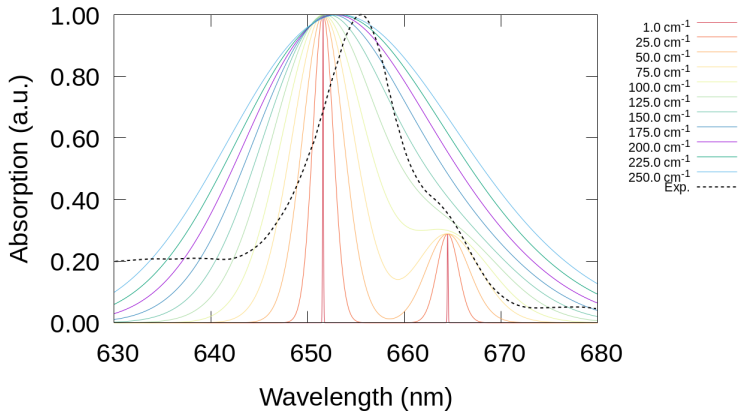

(a) Gaussian Profile

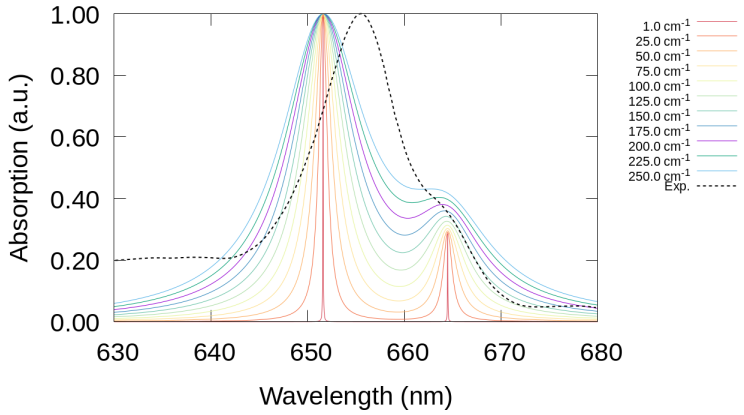

(b) Lorentzian Profile

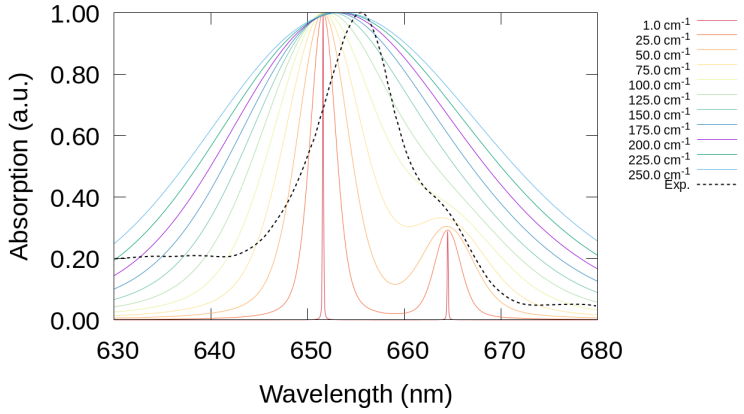

(c) Voigtian Profile

Figure C.3: Simulated spectra for approximate lineshapes of absorption spectra in the non-vibronic case. Effect of the statistical distribution and static disorder parameter σ. *Conditions:* site energy and diabatic excitonic coupling using functional BHHLYP.

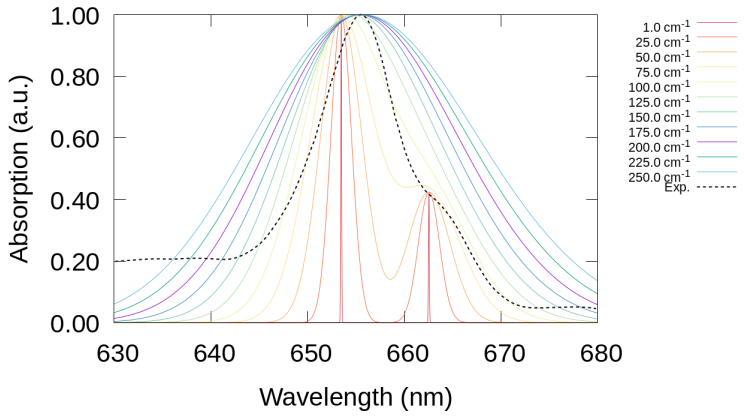

(a) Gaussian Profile

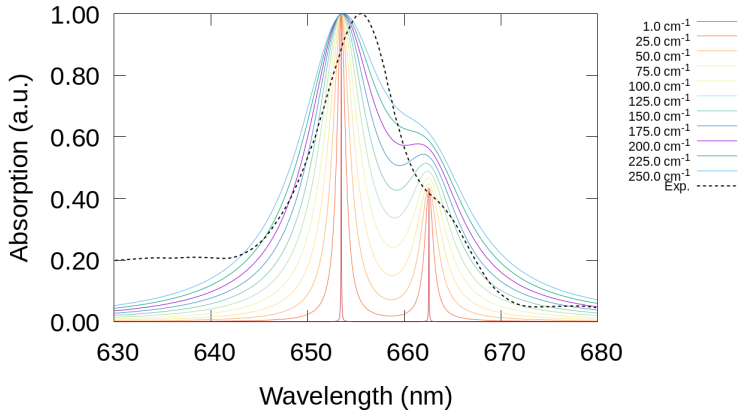

(b) Lorentzian Profile

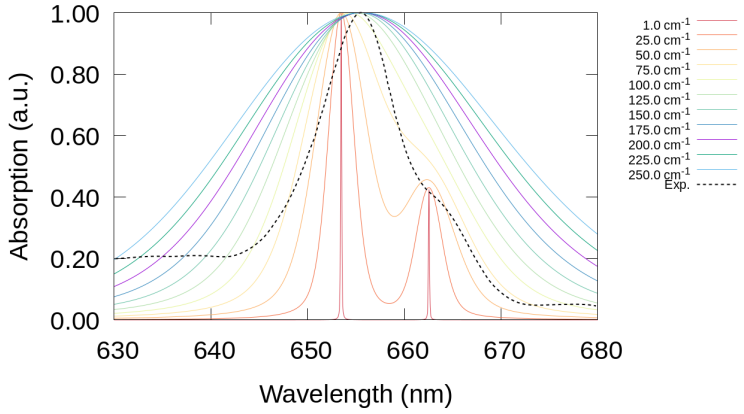

(c) Voigtian Profile

Figure C.4: Simulated spectra for approximate lineshapes of absorption spectra in the non-vibronic case. Effect of the statistical distribution and static disorder parameter σ. *Conditions:* site energy and diabatic excitonic coupling using functional B3LYP.

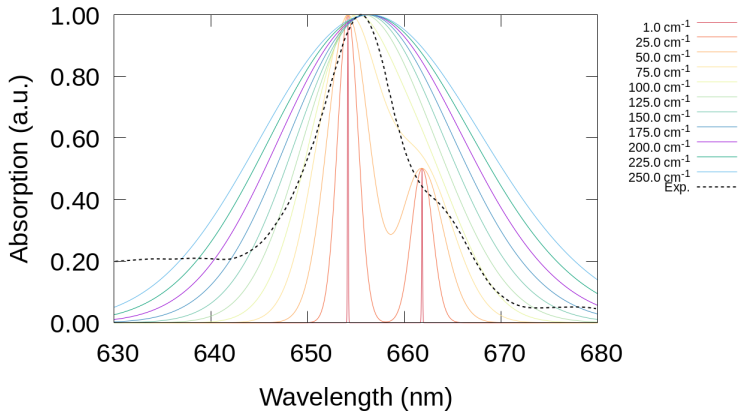

(a) Gaussian Profile

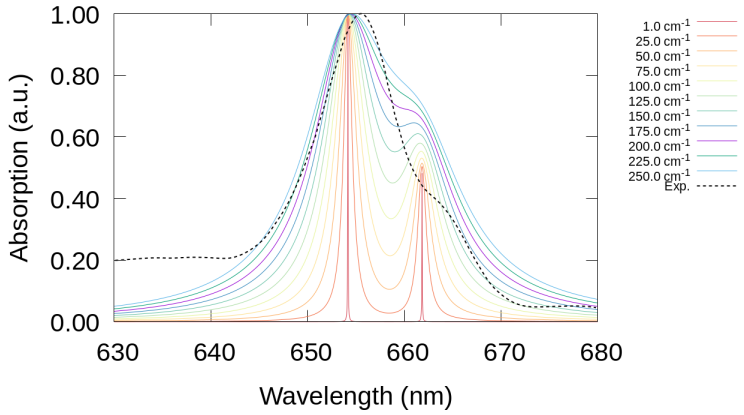

(b) Lorentzian Profile

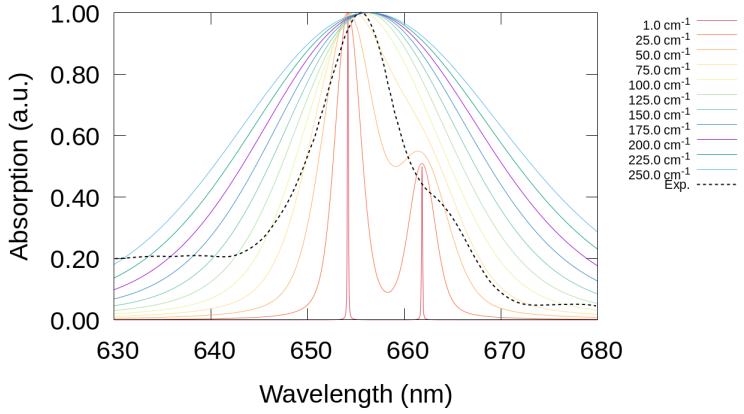

(c) Voigtian Profile

Figure C.5: Simulated spectra for approximate lineshapes of absorption spectra in the non-vibronic case. Effect of the statistical distribution and static disorder parameter σ. *Conditions:* site energy and diabatic excitonic coupling using functional O3LYP.

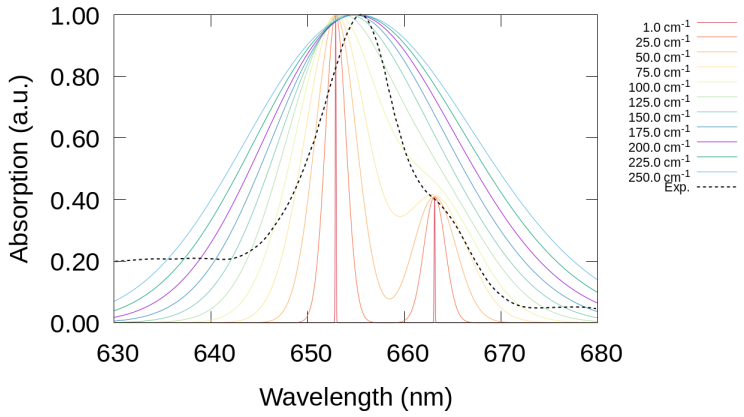

(a) Gaussian Profile

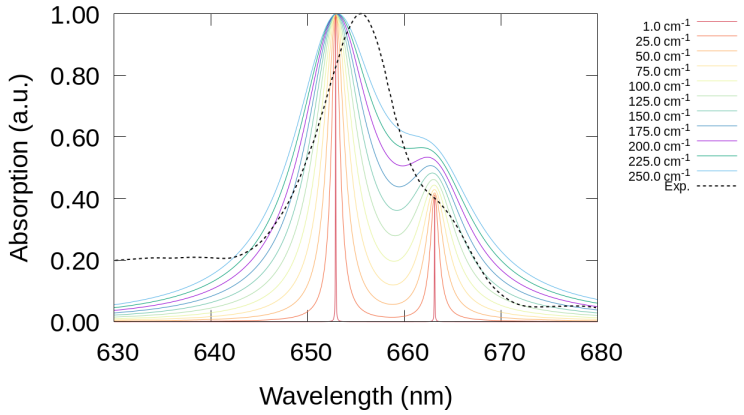

(b) Lorentzian Profile

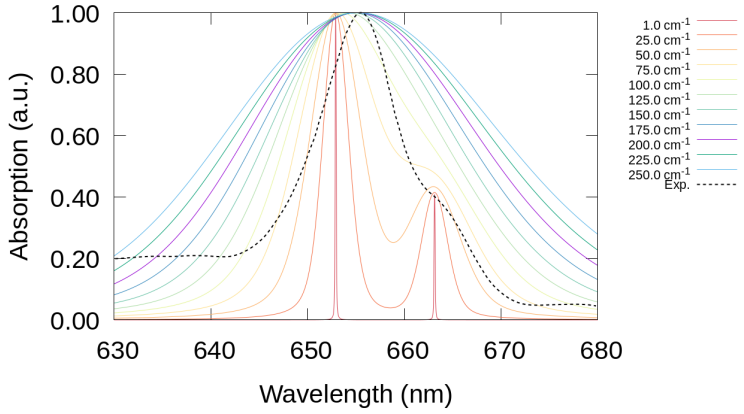

(c) Voigtian Profile

Figure C.6: Simulated spectra for approximate lineshapes of absorption spectra in the non-vibronic case. Effect of the statistical distribution and static disorder parameter σ. *Conditions:* site energy and diabatic excitonic coupling using functional PBE0.

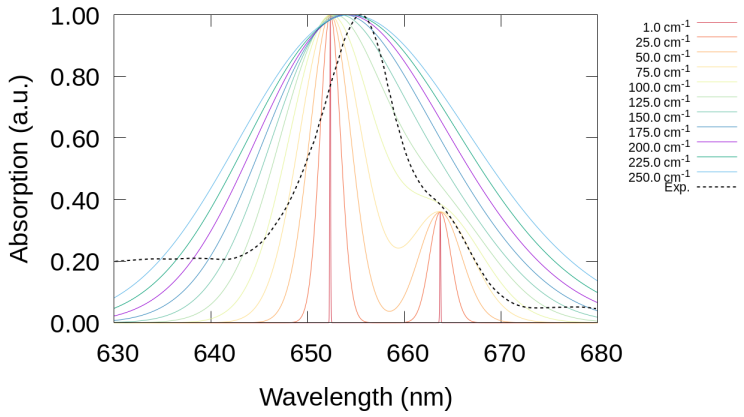

(a) Gaussian Profile

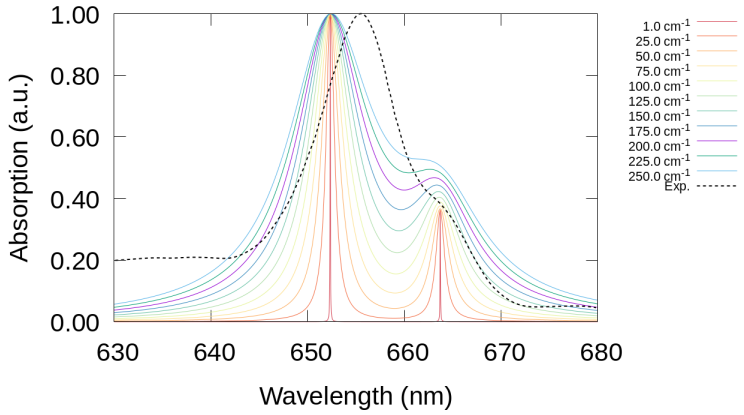

(b) Lorentzian Profile

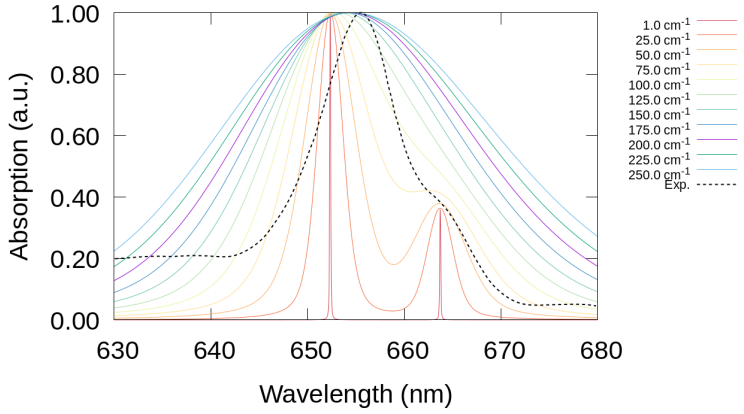

(c) Voigtian Profile

Figure C.7: Simulated spectra for approximate lineshapes of absorption spectra in the non-vibronic case. Effect of the statistical distribution and static disorder parameter σ. *Conditions:* site energy and diabatic excitonic coupling using functional M06-2X.

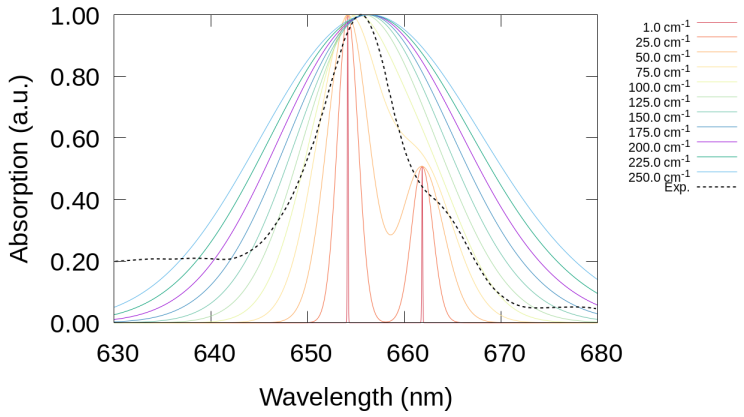

(a) Gaussian Profile

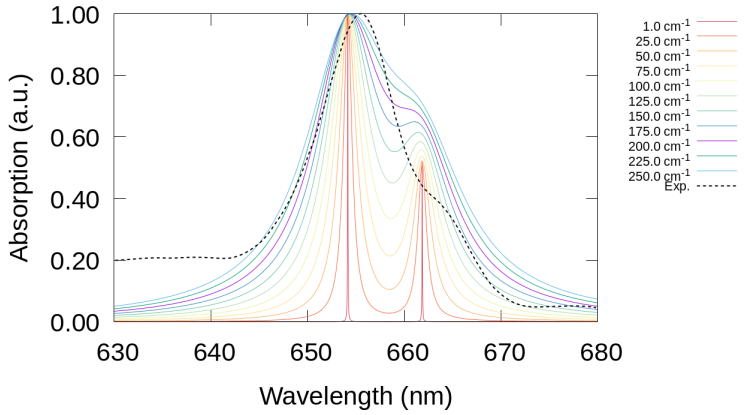

(b) Lorentzian Profile

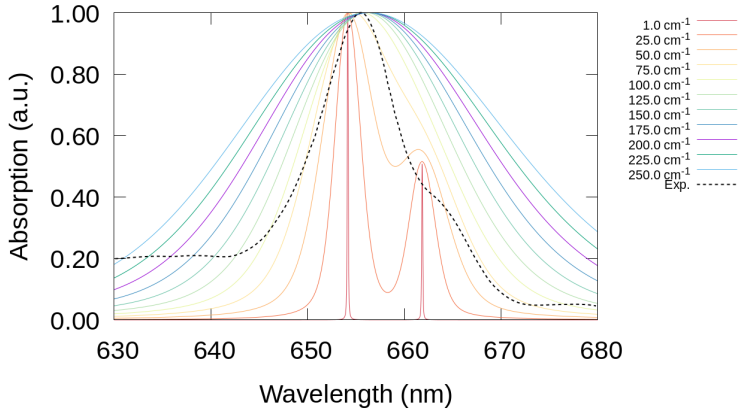

(c) Voigtian Profile

Figure C.8: Simulated spectra for approximate lineshapes of absorption spectra in the non-vibronic case. Effect of the statistical distribution and static disorder parameter σ. *Conditions:* site energy and diabatic excitonic coupling using functional TPSSh.

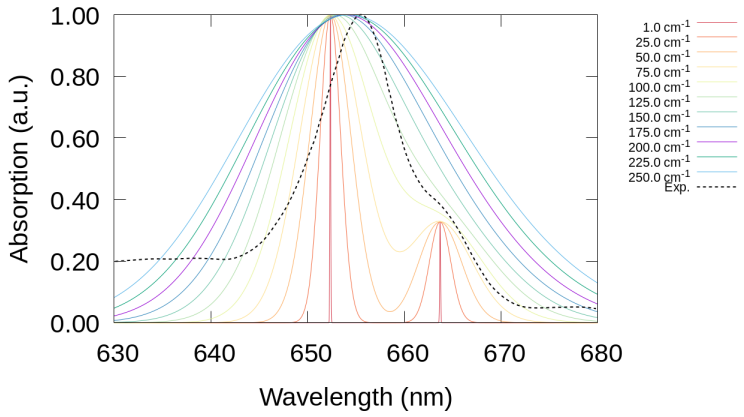

(a) Gaussian Profile

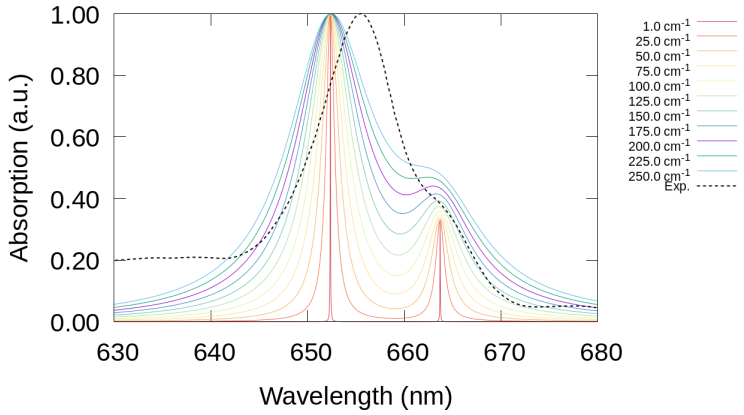

(b) Lorentzian Profile

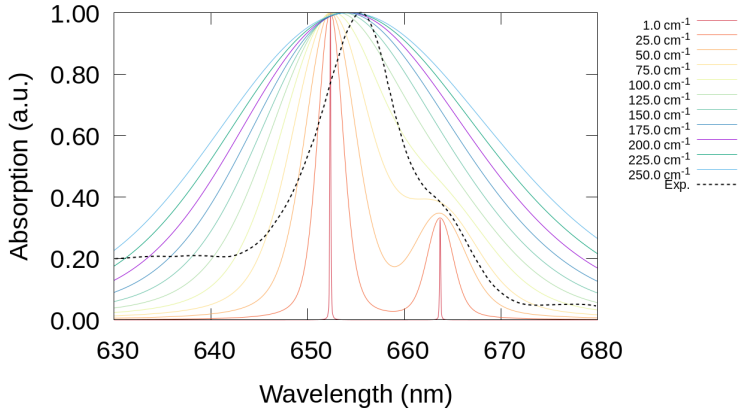

(c) Voigtian Profile

Figure C.9: Simulated spectra for approximate lineshapes of absorption spectra in the non-vibronic case. Effect of the statistical distribution and static disorder parameter σ. *Conditions:* site energy and diabatic excitonic coupling using functional LC-BLYP.

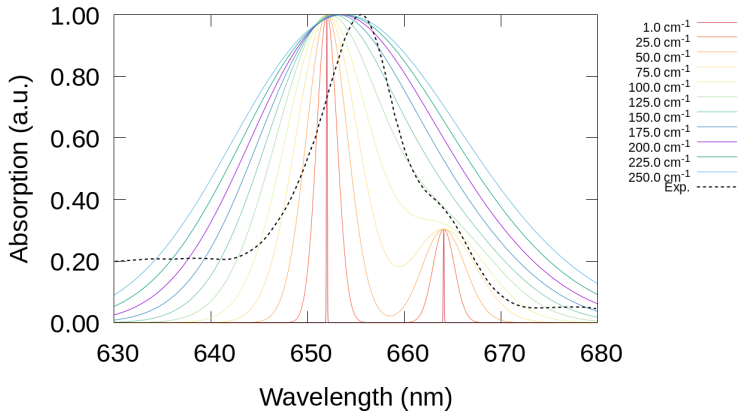

(a) Gaussian Profile

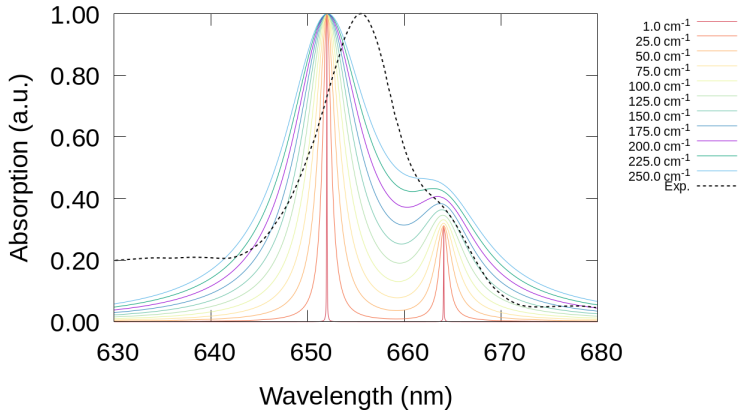

(b) Lorentzian Profile

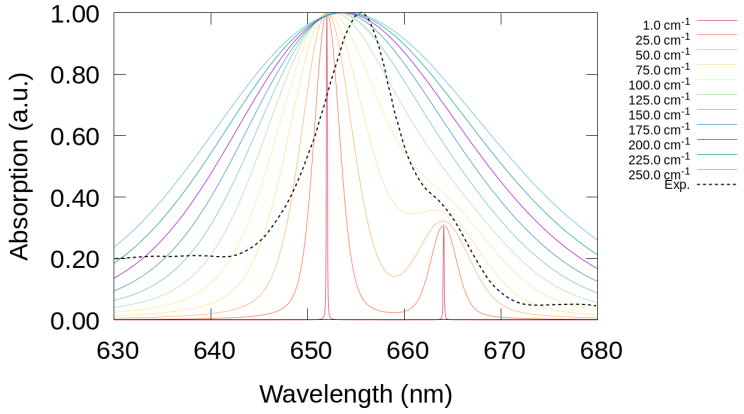

(c) Voigtian Profile

Figure C.10: Simulated spectra for approximate lineshapes of absorption spectra in the non-vibronic case. Effect of the statistical distribution and static disorder parameter σ. *Conditions:* site energy and diabatic excitonic coupling using functional ωB97X-V.

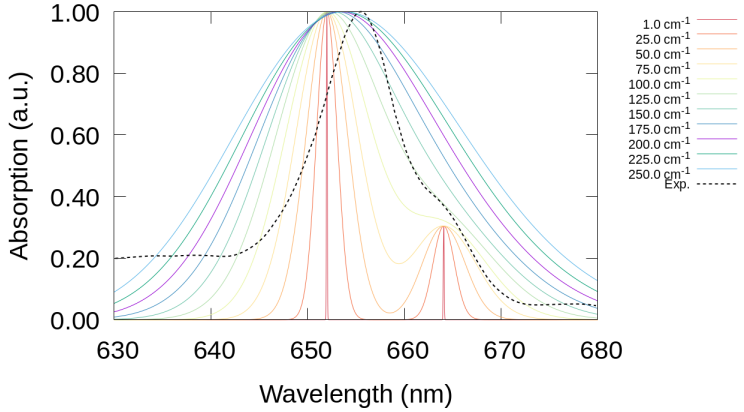

(a) Gaussian Profile

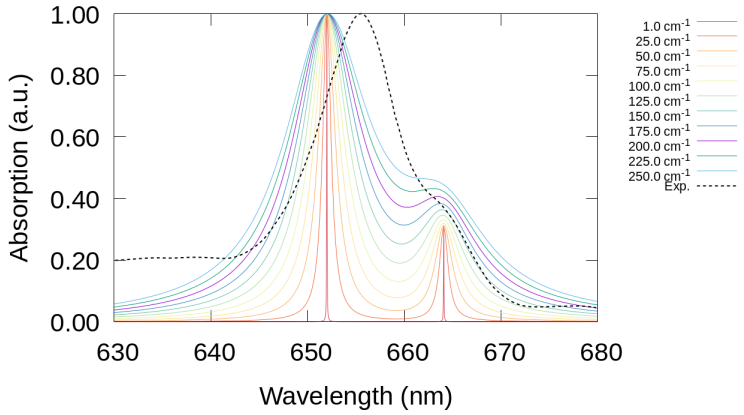

(b) Lorentzian Profile

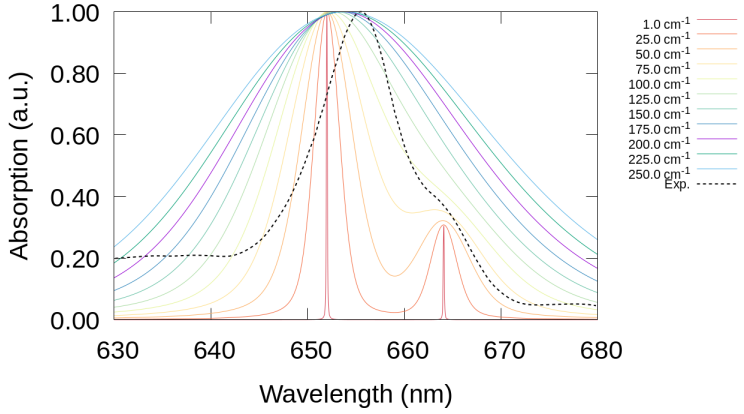

(c) Voigtian Profile

Figure C.11: Simulated spectra for approximate lineshapes of absorption spectra in the non-vibronic case. Effect of the statistical distribution and static disorder parameter σ. *Conditions:* site energy and diabatic excitonic coupling using functional ωB97X-D3BJ.

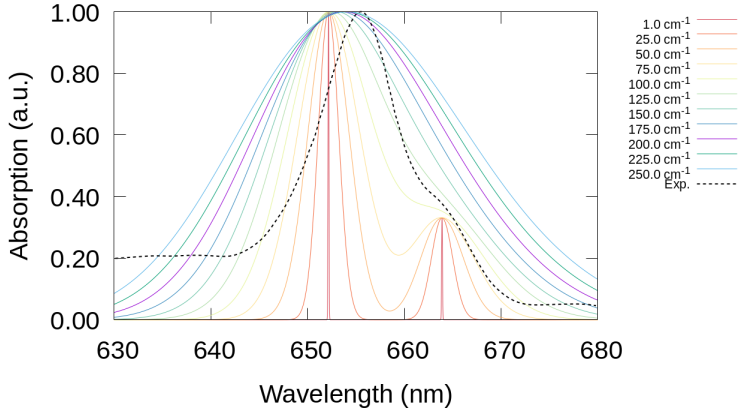

(a) Gaussian Profile

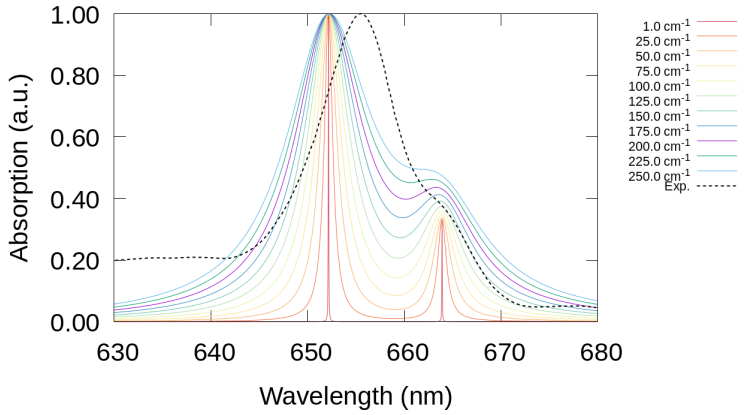

(b) Lorentzian Profile

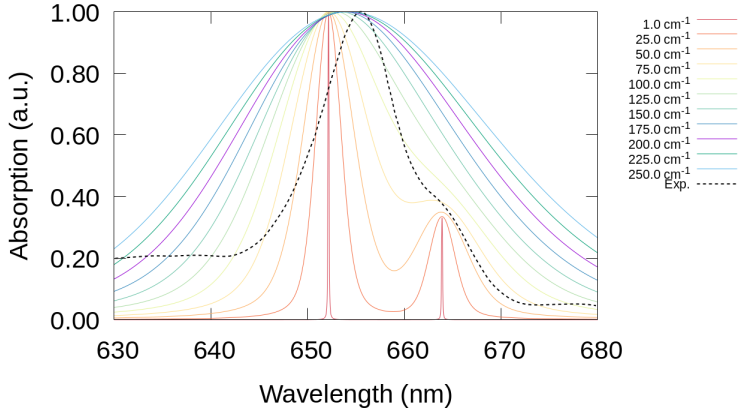

(c) Voigtian Profile

Figure C.12: Simulated spectra for approximate lineshapes of absorption spectra in the non-vibronic case. Effect of the statistical distribution and static disorder parameter σ. *Conditions:* site energy and diabatic excitonic coupling using functional CAM-B3LYP.

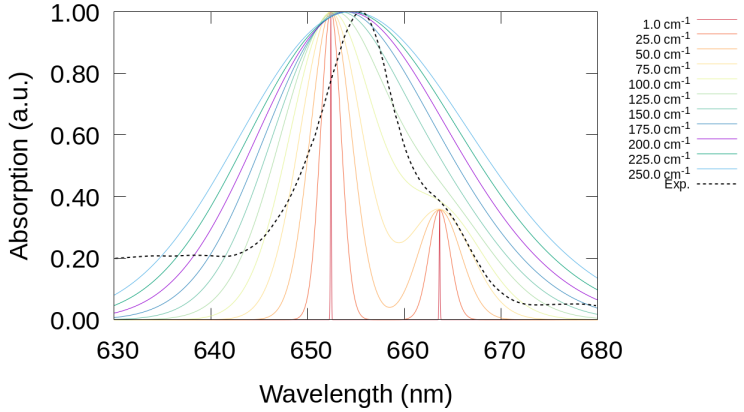

(a) Gaussian Profile

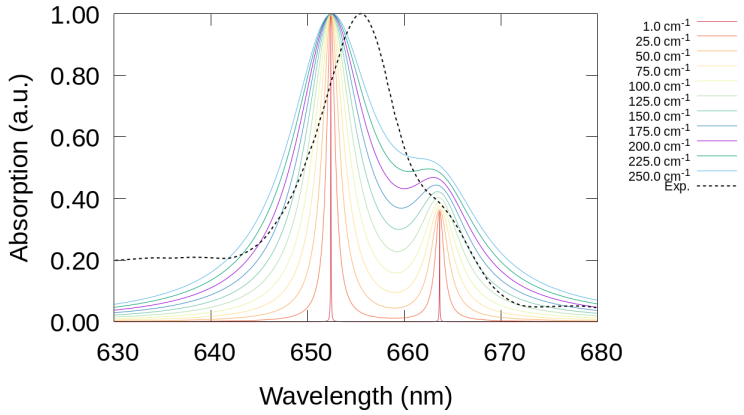

(b) Lorentzian Profile

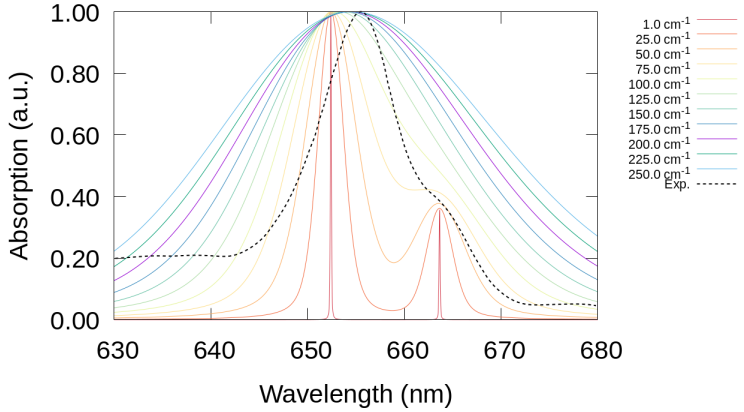

(c) Voigtian Profile

Figure C.13: Simulated spectra for approximate lineshapes of absorption spectra in the non-vibronic case. Effect of the statistical distribution and static disorder parameter σ. *Conditions:* site energy and diabatic excitonic coupling using functional CAMh-B3LYP.

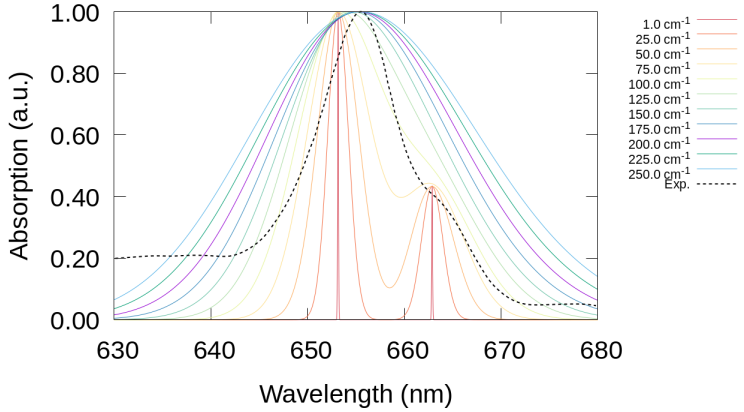

(a) Gaussian Profile

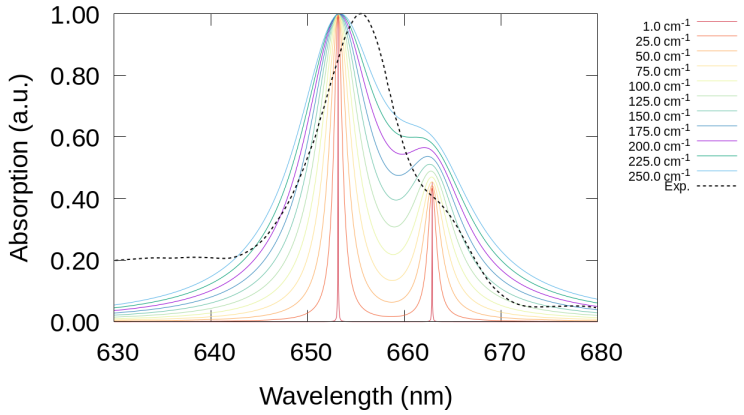

(b) Lorentzian Profile

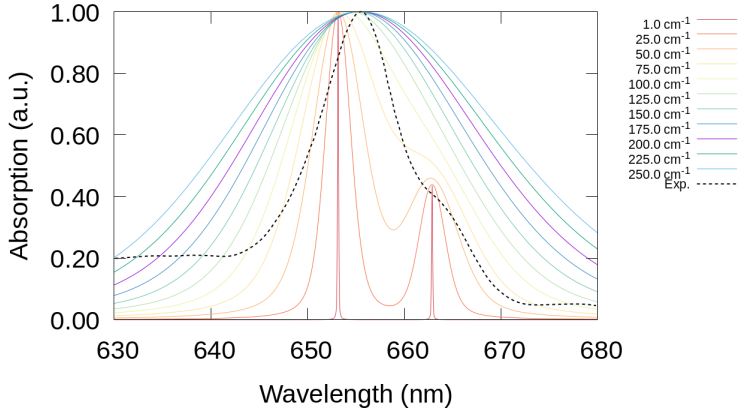

(c) Voigtian Profile

Figure C.14: Simulated spectra for approximate lineshapes of absorption spectra in the non-vibronic case. Effect of the statistical distribution and static disorder parameter σ. *Conditions:* site energy and diabatic excitonic coupling using functional Tuned-CAM-B3LYP.

C.1.2 Similarity metrics behaviour

Comparison of the different similarity metrics is presented, and their dependence on the static disorder and statistical distribution selected. All site energies have been shifted so that the site energy matches the experimental one (15198 cm^{-1}).

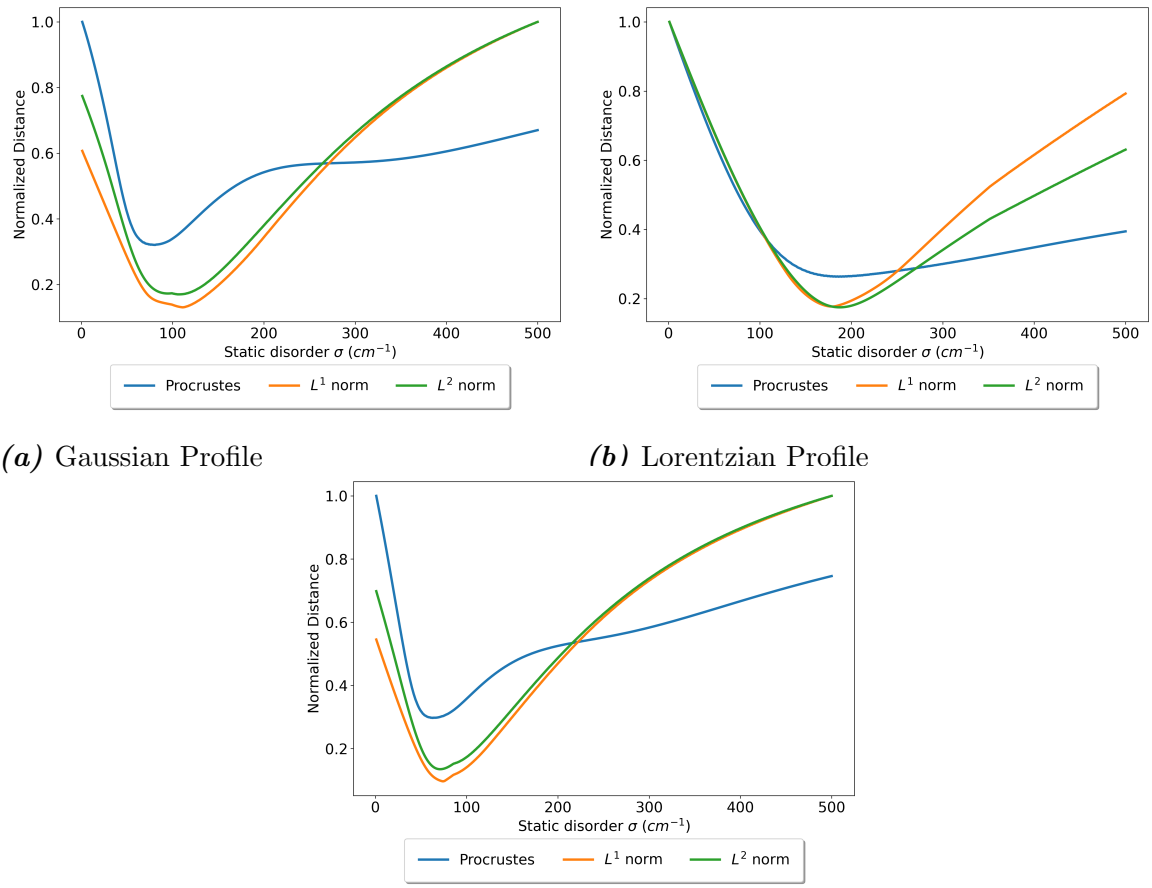

(a) Gaussian Profile

(b) Lorentzian Profile

(c) Voigtian Profile

Figure C.15: Behaviour of different similarity metrics for the optimization of approximate spectral lineshapes. Effect of the statistical distribution and static disorder parameter σ. *Conditions:* experimental site energy and diabatic excitonic coupling using functional M06-L.

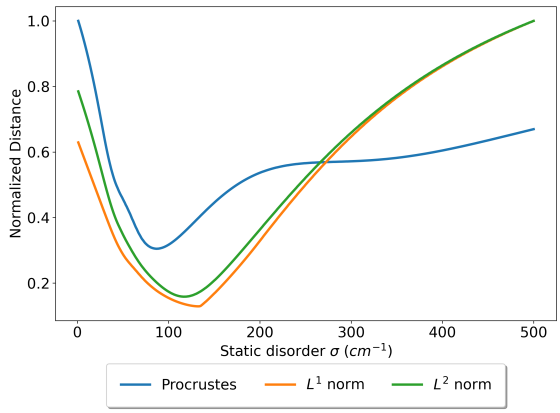

(a) Gaussian Profile

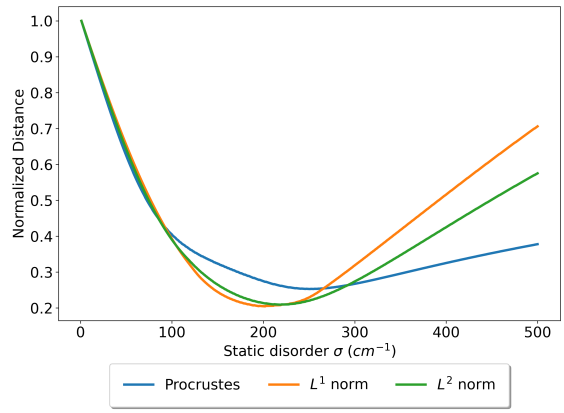

(b) Lorentzian Profile

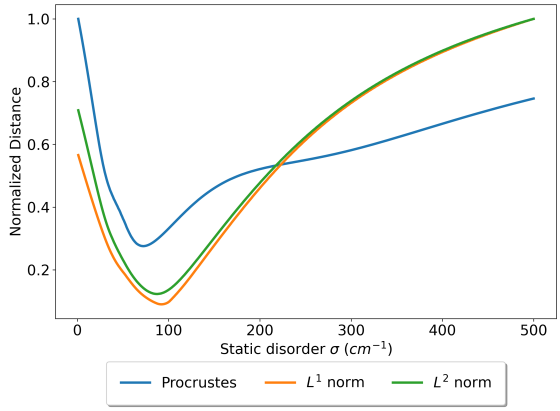

(c) Voigtian Profile

Figure C.16: Behaviour of different similarity metrics for the optimization of approximate spectral lineshapes. Effect of the statistical distribution and static disorder parameter σ. *Conditions:* experimental site energy and diabatic excitonic coupling using functional TPSS.

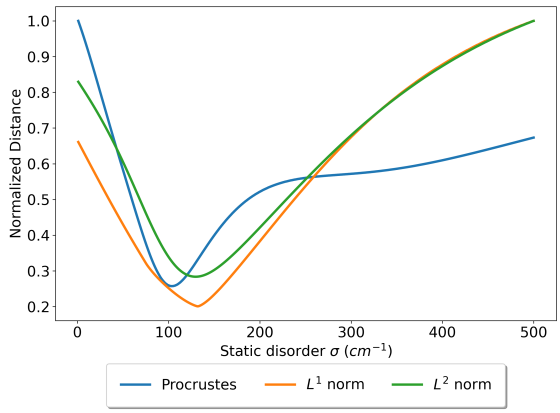

(a) Gaussian Profile

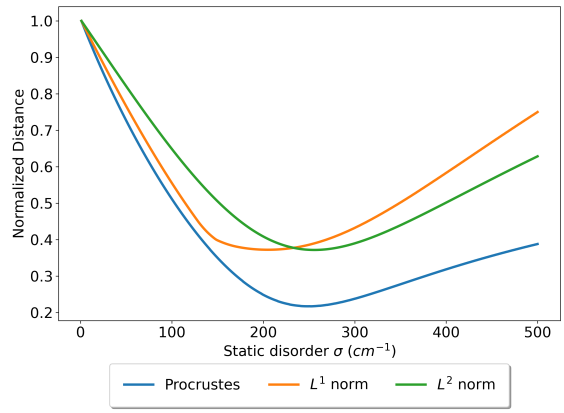

(b) Lorentzian Profile

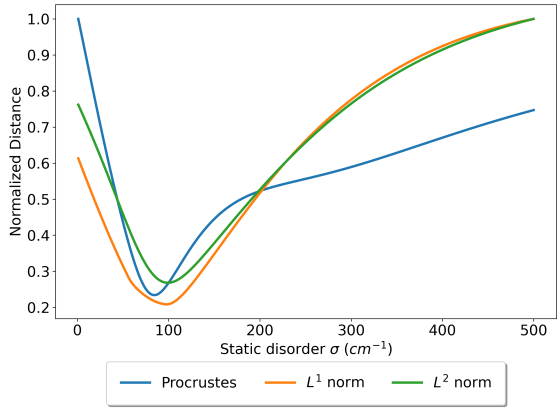

(c) Voigtian Profile

Figure C.17: Behaviour of different similarity metrics for the optimization of approximate spectral lineshapes. Effect of the statistical distribution and static disorder parameter σ. *Conditions:* experimental site energy and diabatic excitonic coupling using functional BHHLYP.

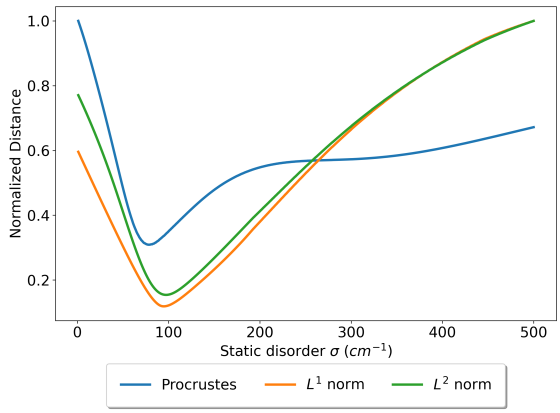

(a) Gaussian Profile

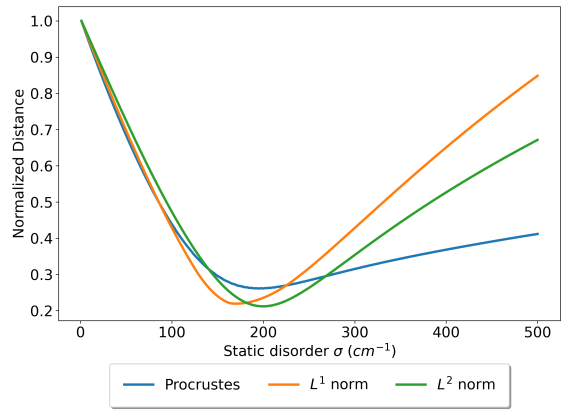

(b) Lorentzian Profile

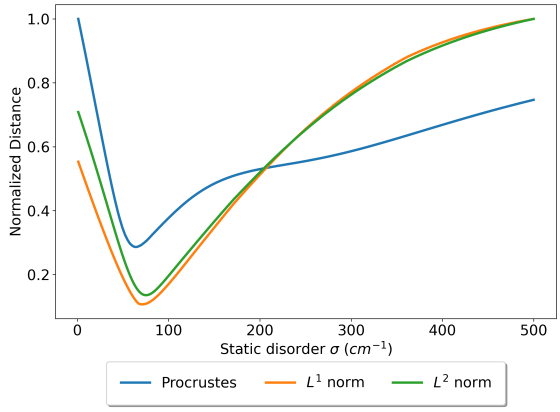

(c) Voigtian Profile

Figure C.18: Behaviour of different similarity metrics for the optimization of approximate spectral lineshapes. Effect of the statistical distribution and static disorder parameter σ. *Conditions:* experimental site energy and diabatic excitonic coupling using functional B3LYP.

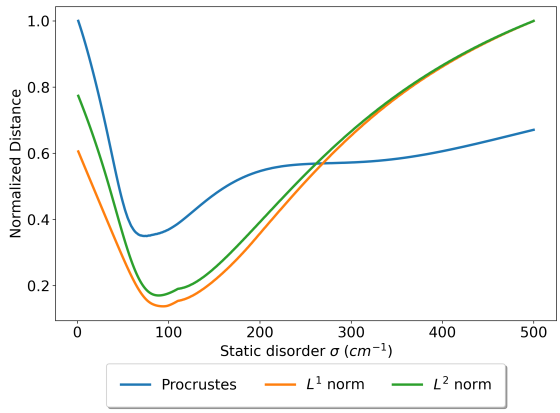

(a) Gaussian Profile

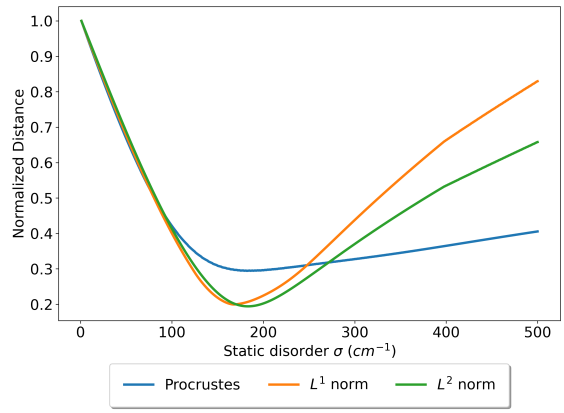

(b) Lorentzian Profile

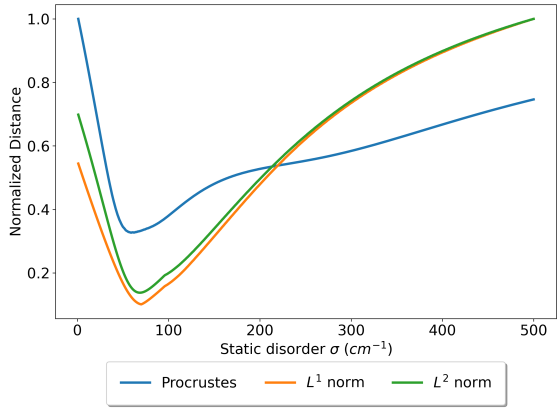

(c) Voigtian Profile

Figure C.19: Behaviour of different similarity metrics for the optimization of approximate spectral lineshapes. Effect of the statistical distribution and static disorder parameter σ. *Conditions:* experimental site energy and diabatic excitonic coupling using functional O3LYP.

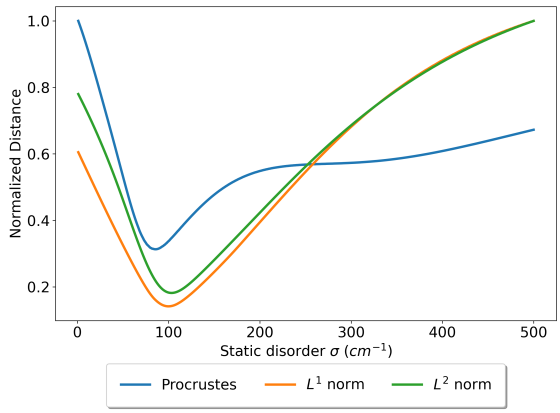

(a) Gaussian Profile

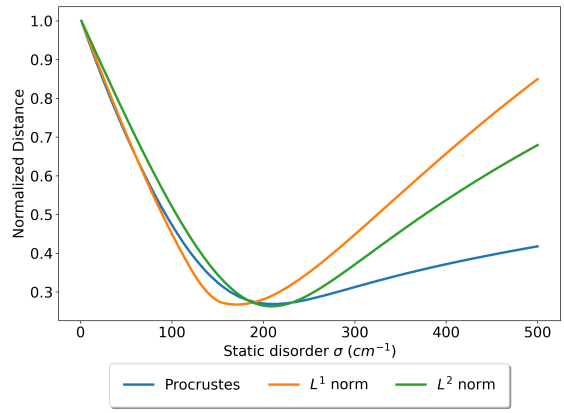

(b) Lorentzian Profile

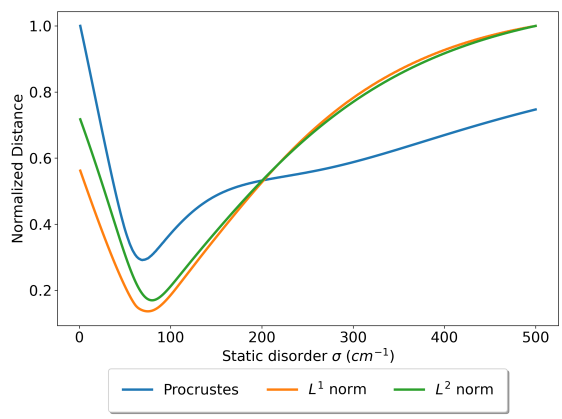

(c) Voigtian Profile

Figure C.20: Behaviour of different similarity metrics for the optimization of approximate spectral lineshapes. Effect of the statistical distribution and static disorder parameter σ. *Conditions:* experimental site energy and diabatic excitonic coupling using functional PBE0.

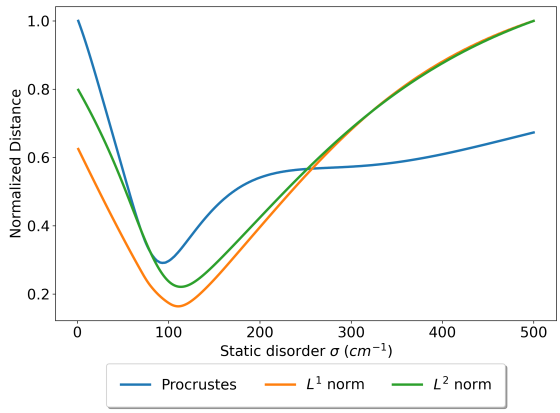

(a) Gaussian Profile

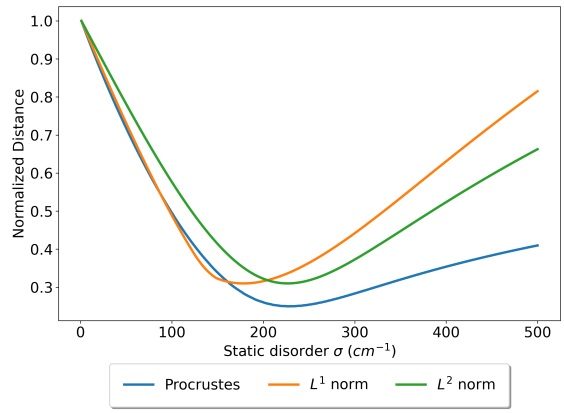

(b) Lorentzian Profile

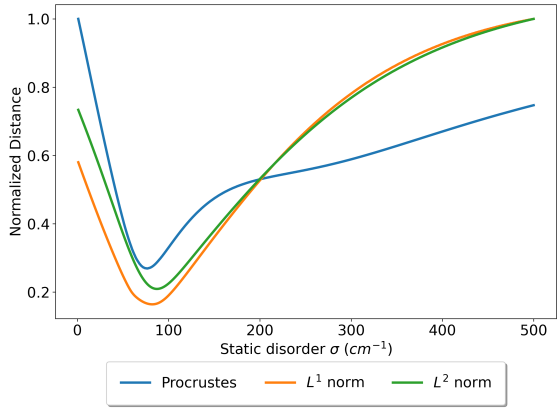

(c) Voigtian Profile

Figure C.21: Behaviour of different similarity metrics for the optimization of approximate spectral lineshapes. Effect of the statistical distribution and static disorder parameter σ. *Conditions:* experimental site energy and diabatic excitonic coupling using functional M06-2X.

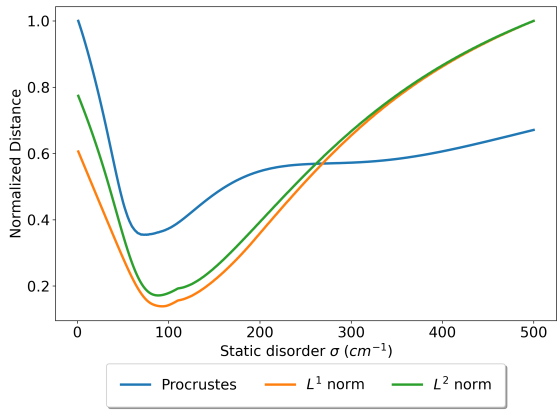

(a) Gaussian Profile

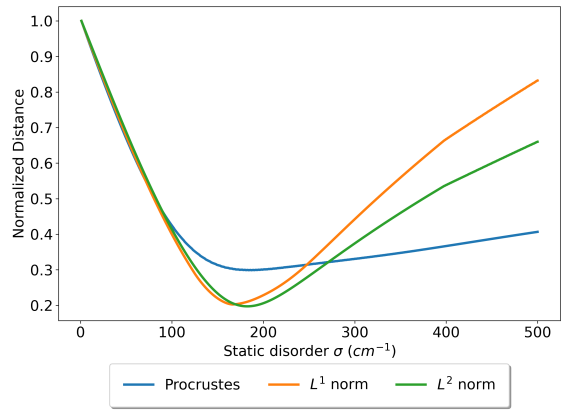

(b) Lorentzian Profile

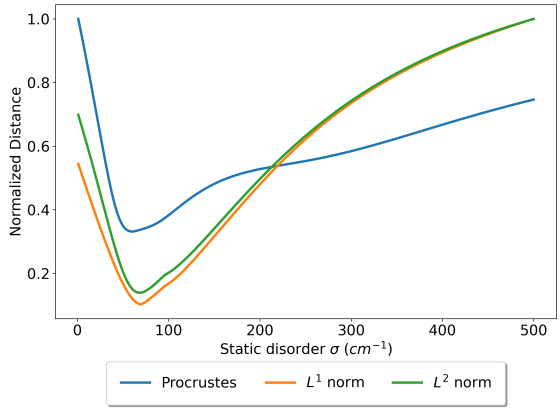

(c) Voigtian Profile

Figure C.22: Behaviour of different similarity metrics for the optimization of approximate spectral lineshapes. Effect of the statistical distribution and static disorder parameter σ. *Conditions:* experimental site energy and diabatic excitonic coupling using functional TPSSh.

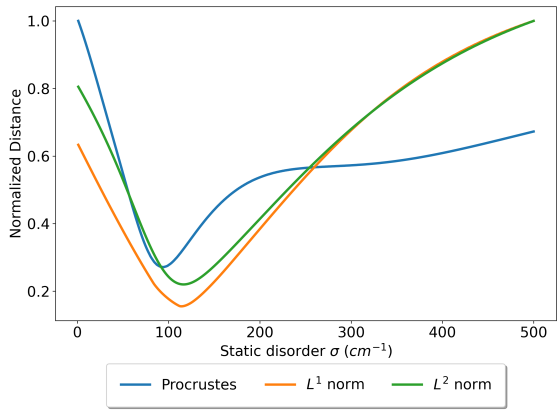

(a) Gaussian Profile

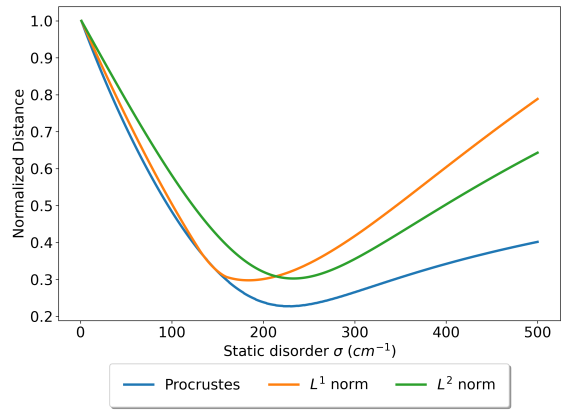

(b) Lorentzian Profile

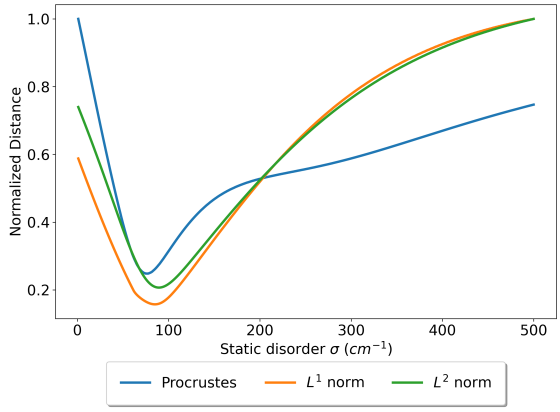

(c) Voigtian Profile

Figure C.23: Behaviour of different similarity metrics for the optimization of approximate spectral lineshapes. Effect of the statistical distribution and static disorder parameter σ. *Conditions:* experimental site energy and diabatic excitonic coupling using functional LC-BLYP.

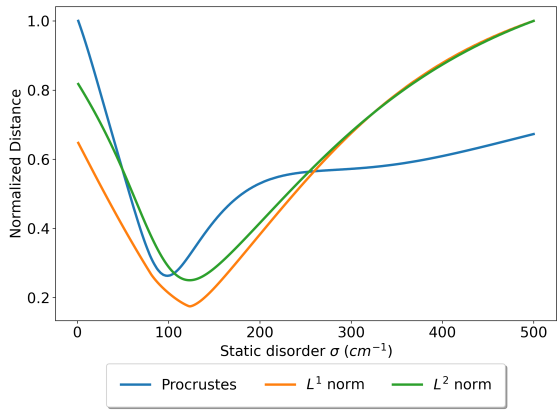

(a) Gaussian Profile

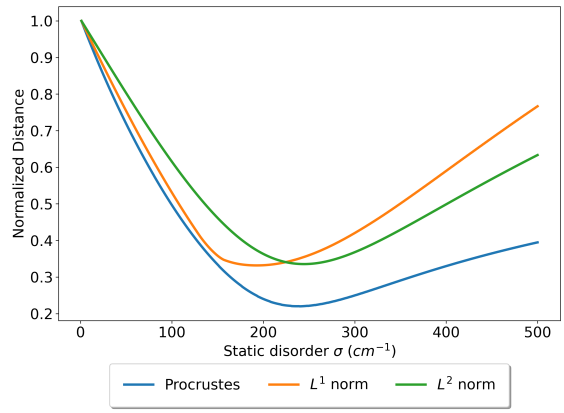

(b) Lorentzian Profile

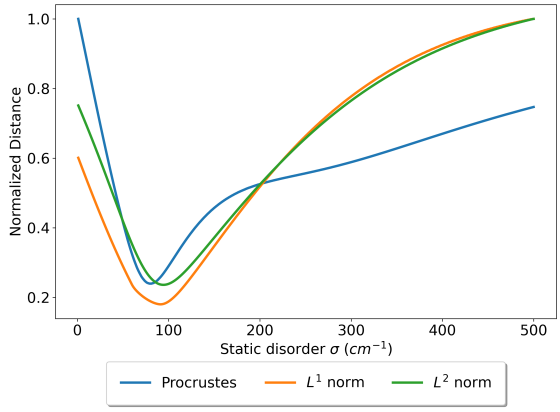

(c) Voigtian Profile

Figure C.24: Behaviour of different similarity metrics for the optimization of approximate spectral lineshapes. Effect of the statistical distribution and static disorder parameter σ. *Conditions:* experimental site energy and diabatic excitonic coupling using functional ωB97X-V.

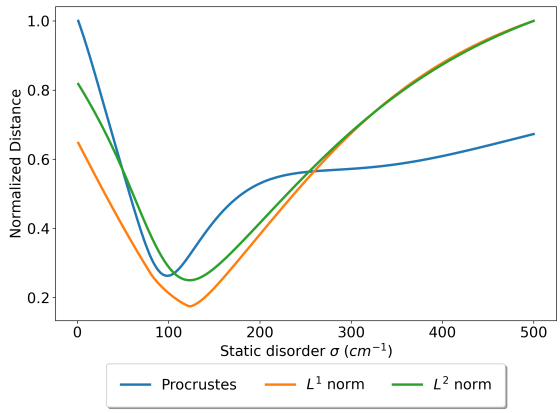

(a) Gaussian Profile

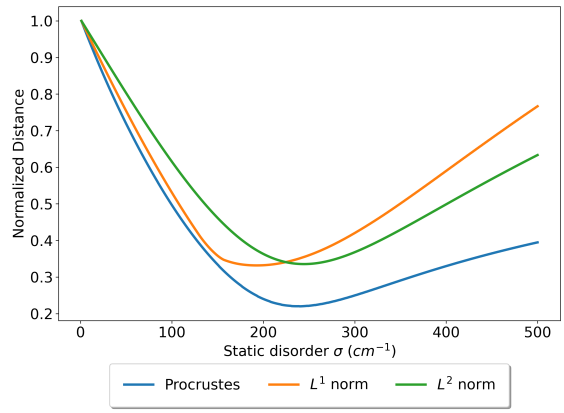

(b) Lorentzian Profile

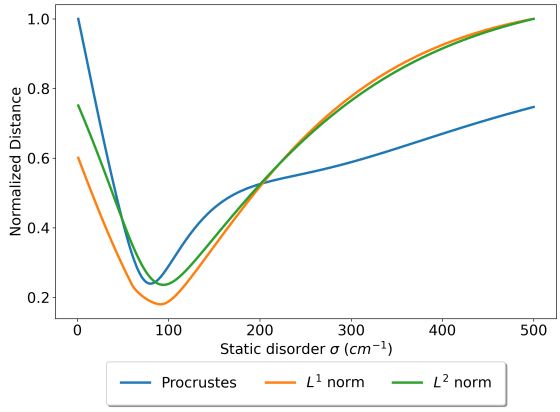

(c) Voigtian Profile

Figure C.25: Behaviour of different similarity metrics for the optimization of approximate spectral lineshapes. Effect of the statistical distribution and static disorder parameter σ. *Conditions:* experimental site energy and diabatic excitonic coupling using functional ωB97X-D3BJ.

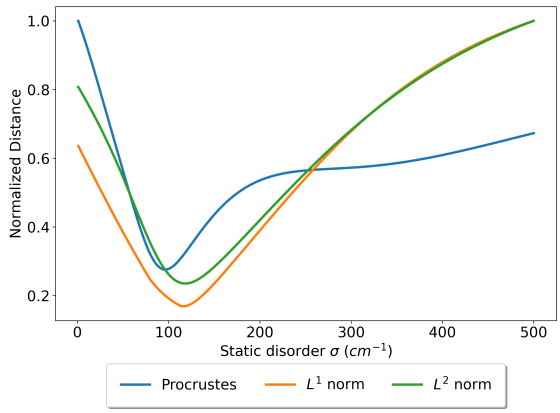

(a) Gaussian Profile

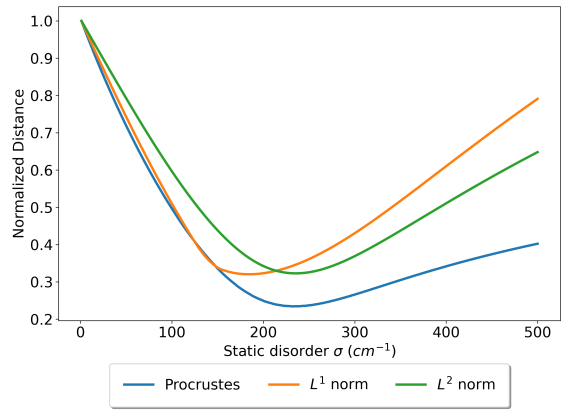

(b) Lorentzian Profile

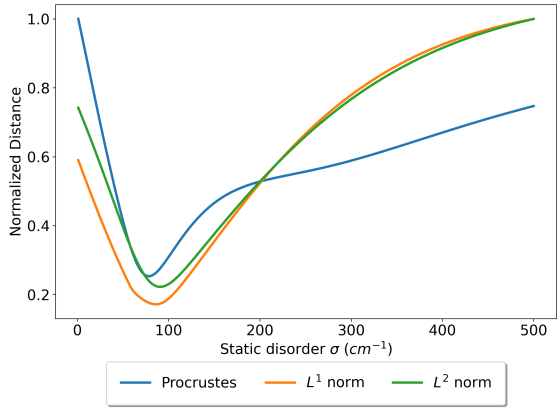

(c) Voigtian Profile

Figure C.26: Behaviour of different similarity metrics for the optimization of approximate spectral lineshapes. Effect of the statistical distribution and static disorder parameter σ. *Conditions:* experimental site energy and diabatic excitonic coupling using functional CAM-B3LYP.

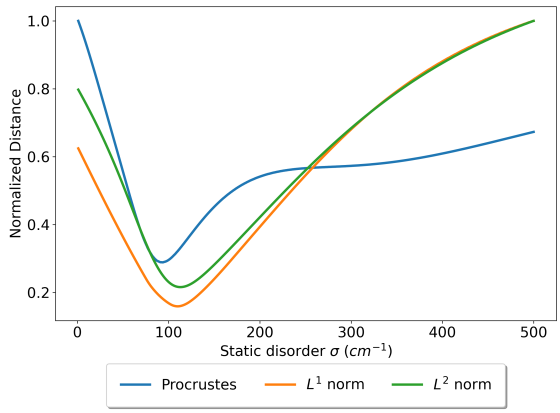

(a) Gaussian Profile

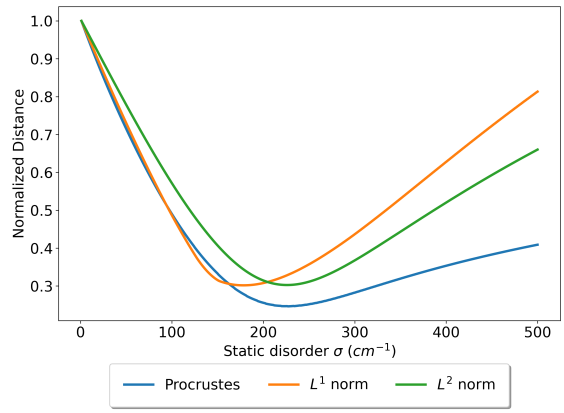

(b) Lorentzian Profile

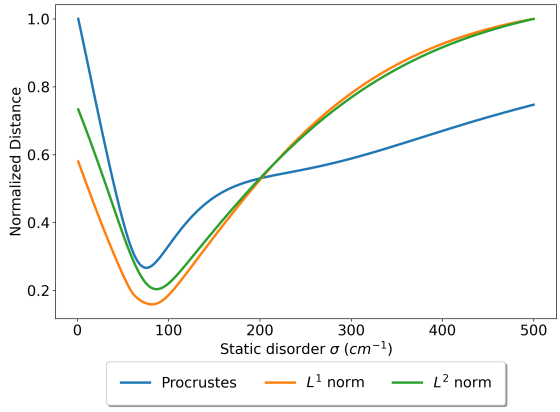

(c) Voigtian Profile

Figure C.27: Behaviour of different similarity metrics for the optimization of approximate spectral lineshapes. Effect of the statistical distribution and static disorder parameter σ. *Conditions:* experimental site energy and diabatic excitonic coupling using functional CAMh-B3LYP.

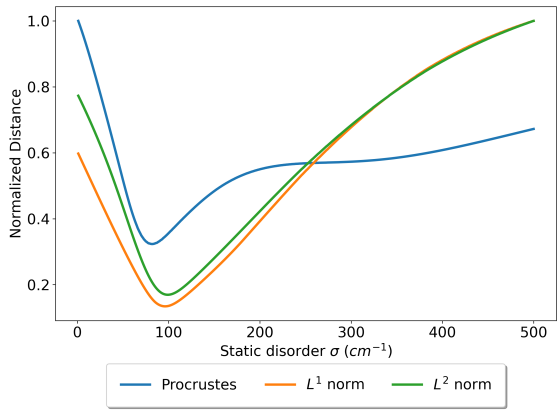

(a) Gaussian Profile

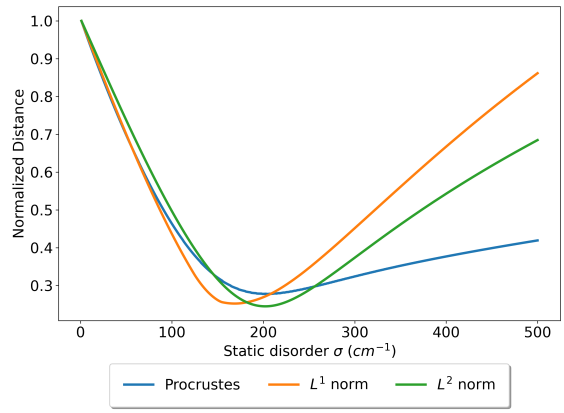

(b) Lorentzian Profile

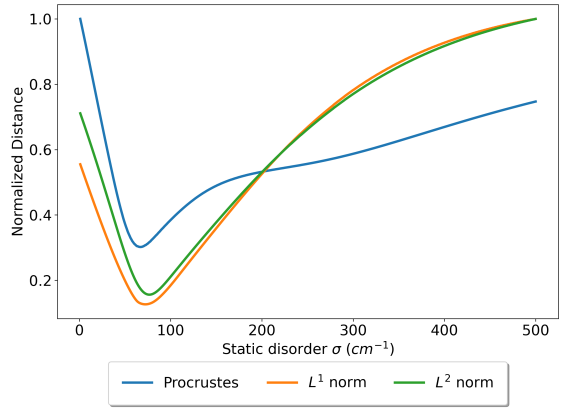

(c) Voigtian Profile

Figure C.28: Behaviour of different similarity metrics for the optimization of approximate spectral lineshapes. Effect of the statistical distribution and static disorder parameter σ. *Conditions:* experimental site energy and diabatic excitonic coupling using functional Tuned-CAM-B3LYP.

C.1.3 Static disorder optimization

Numerical optimization of the σ by minimization of the Procrustes distance is presented. This is performed for all the statistical distributions selected. All site energies have been shifted so that the site energy matches the experimental one (15198 cm^{-1}).

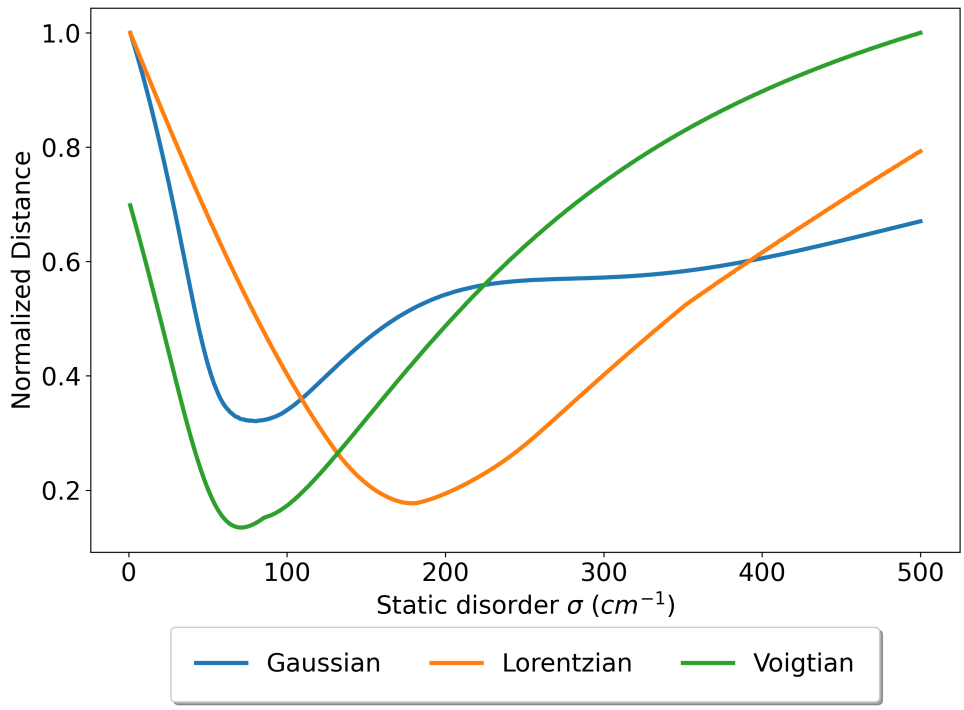

Figure C.29: Numerical optimization of σ. *Conditions:* experimental site energy (15198 cm^{-1}) and M06-L diabatic excitonic coupling.

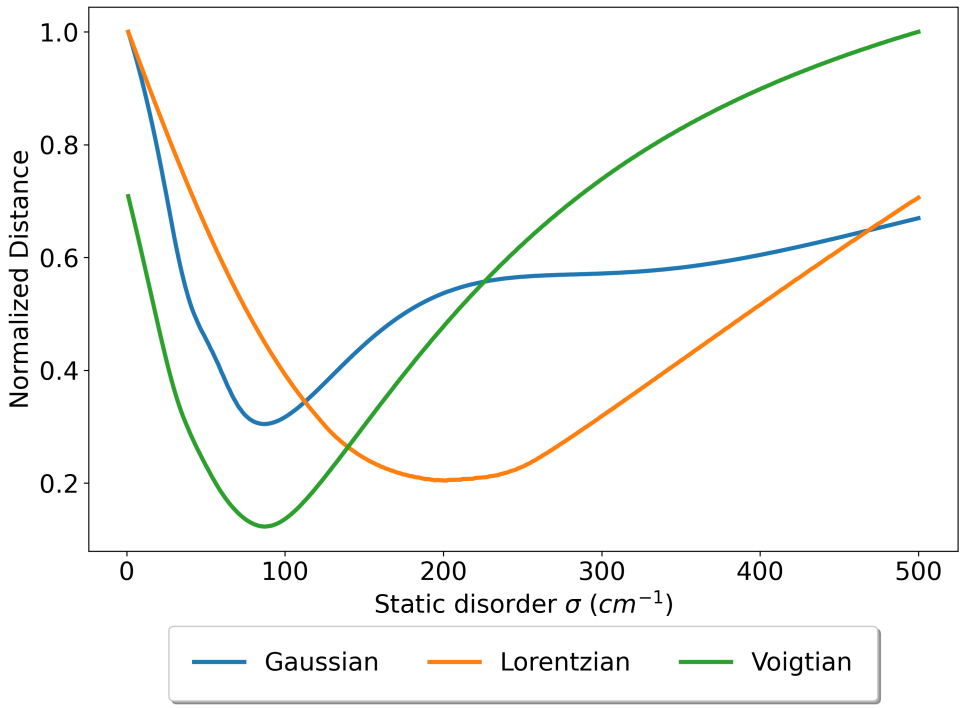

Figure C.30: Numerical optimization of σ. *Conditions:* experimental site energy (15198 cm^{-1}) and TPSS diabatic excitonic coupling.

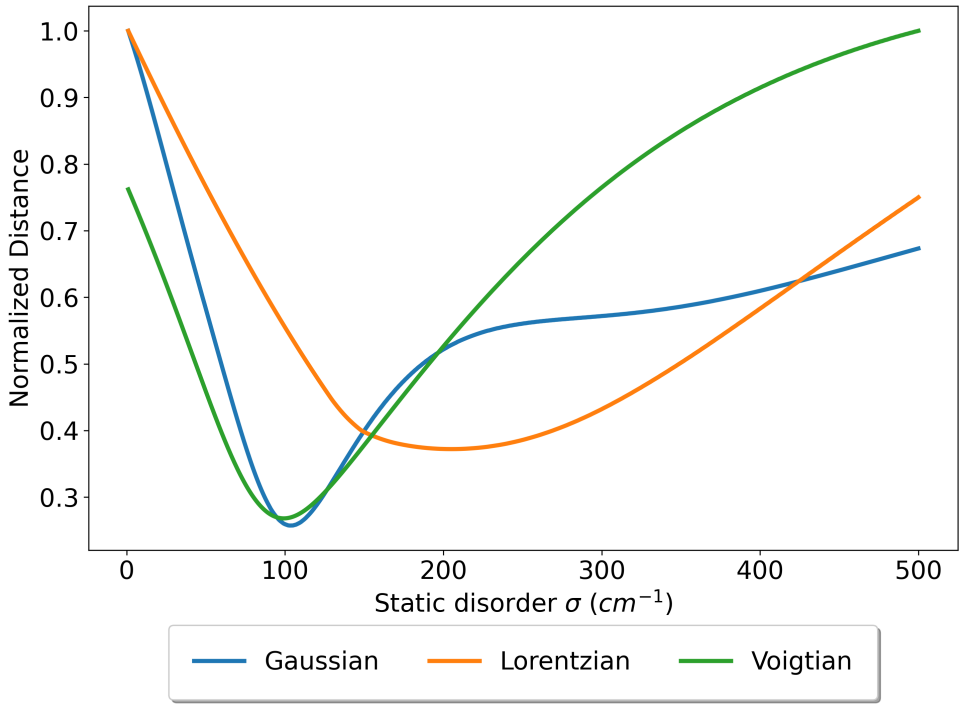

Figure C.31: Numerical optimization of σ. *Conditions:* experimental site energy (15198 cm^{-1}) and BHHLYP diabatic excitonic coupling.

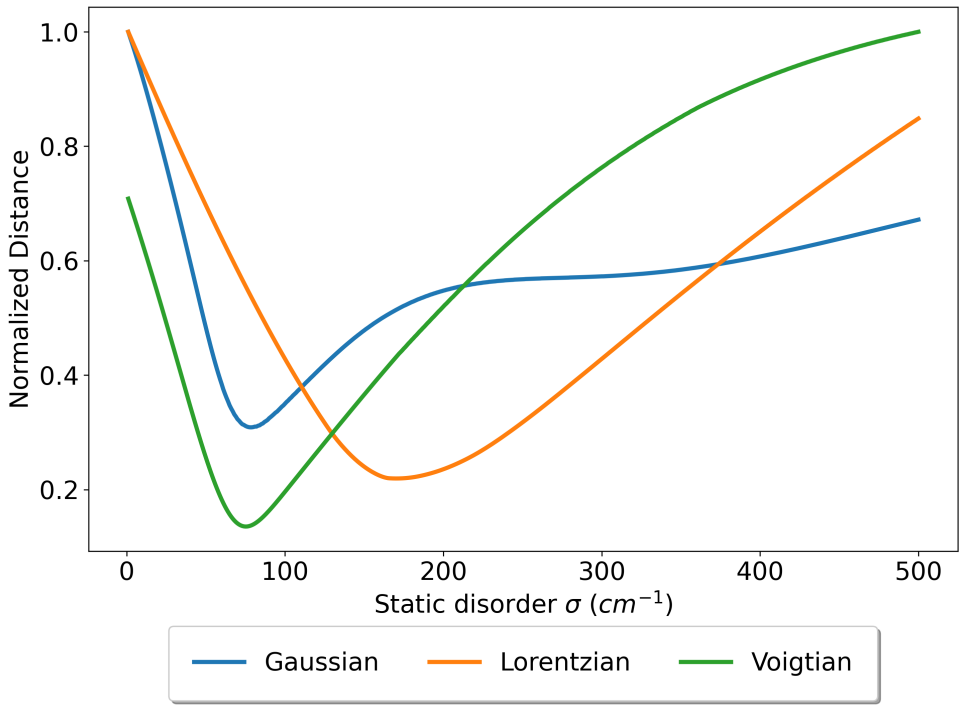

Figure C.32: Numerical optimization of σ. *Conditions:* experimental site energy (15198 cm^{-1}) and B3LYP diabatic excitonic coupling.

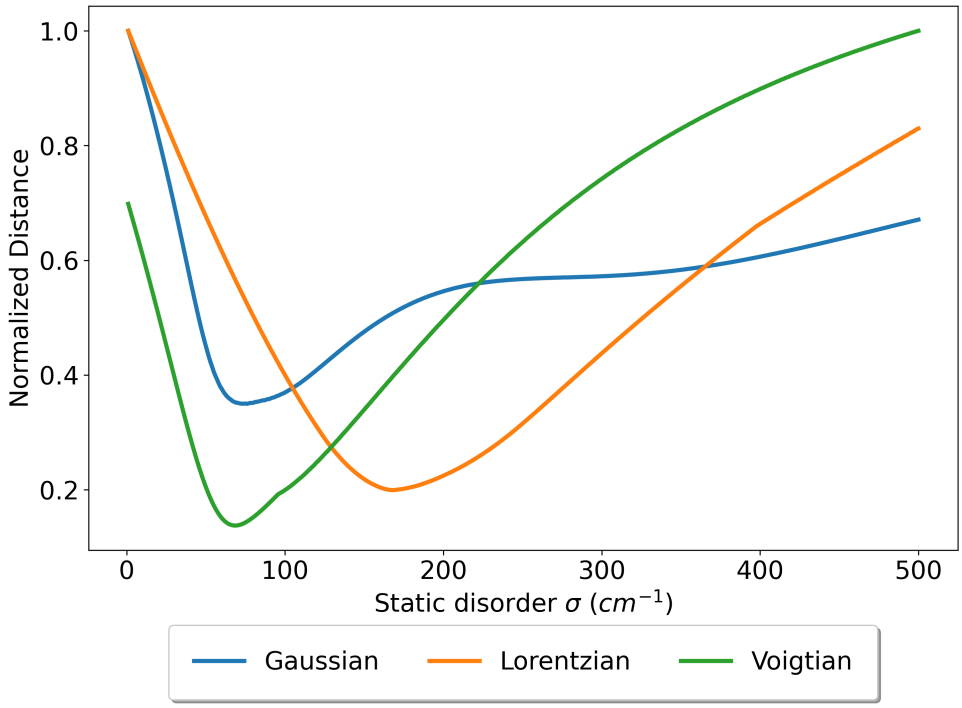

Figure C.33: Numerical optimization of σ. *Conditions:* experimental site energy (15198 cm^{-1}) and O3LYP diabatic excitonic coupling.

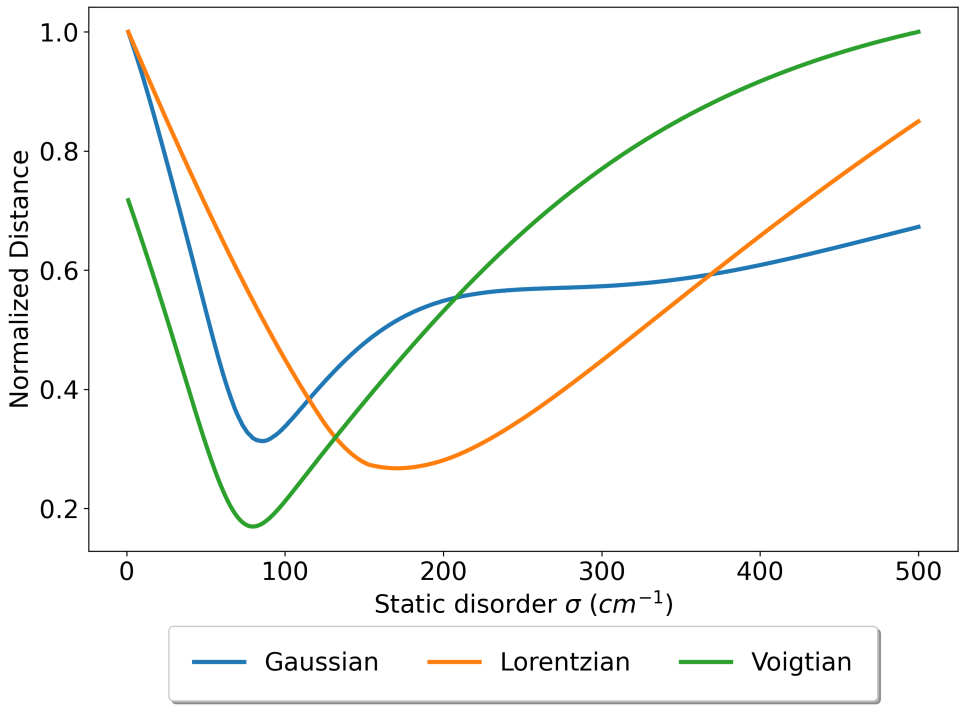

Figure C.34: Numerical optimization of σ. *Conditions:* experimental site energy (15198 cm^{-1}) and PBE0 diabatic excitonic coupling.

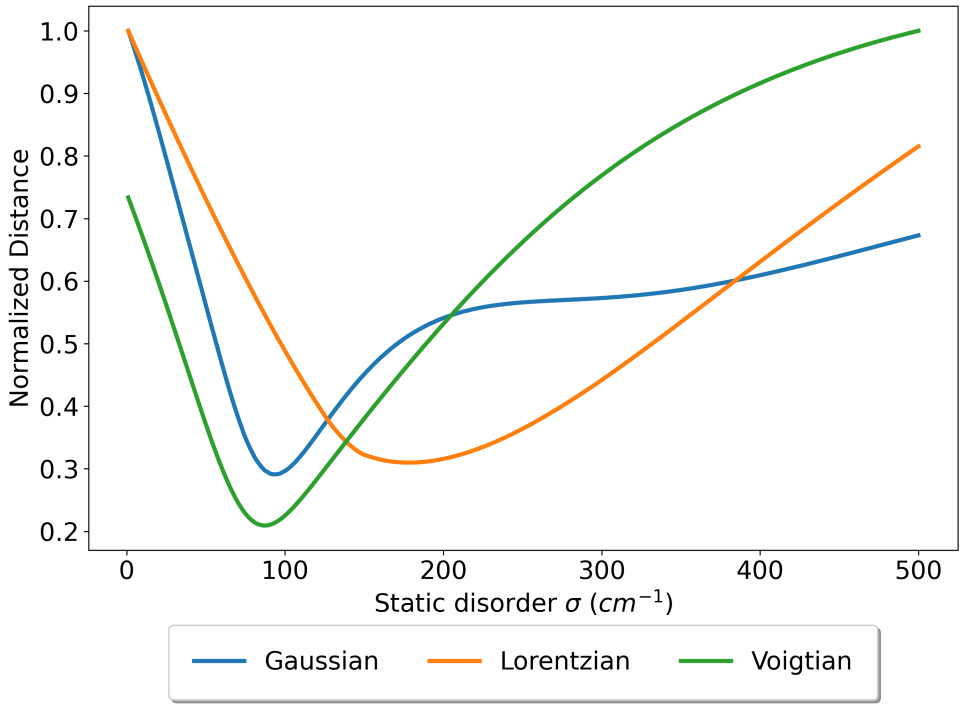

Figure C.35: Numerical optimization of σ. *Conditions:* experimental site energy (15198 cm^{-1}) and M06-2X diabatic excitonic coupling.

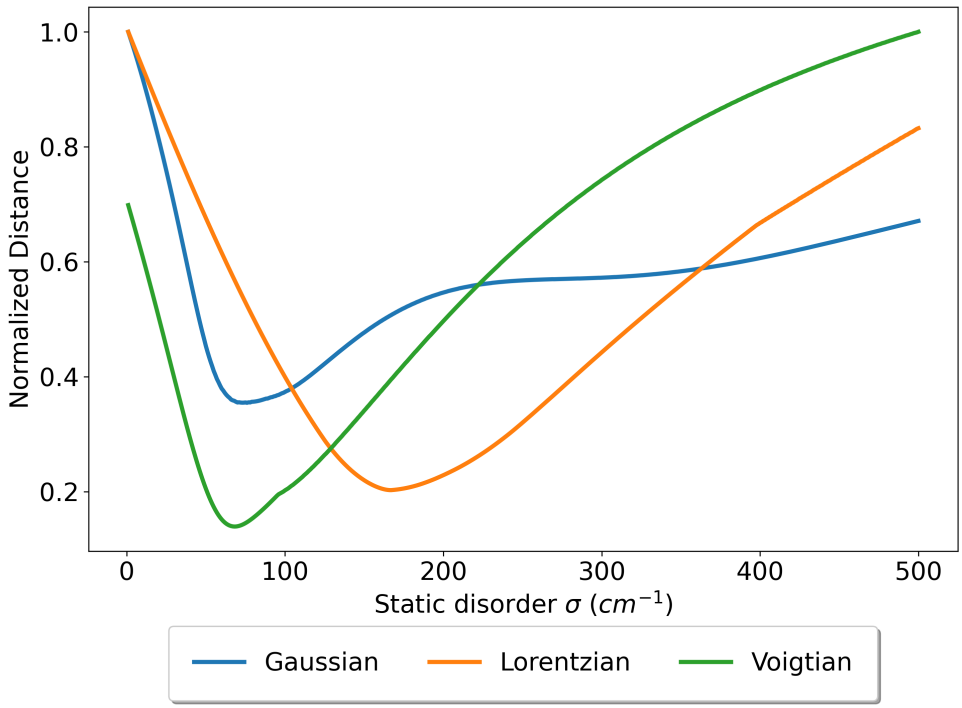

Figure C.36: Numerical optimization of σ. *Conditions:* experimental site energy (15198 cm^{-1}) and TPSSh diabatic excitonic coupling.

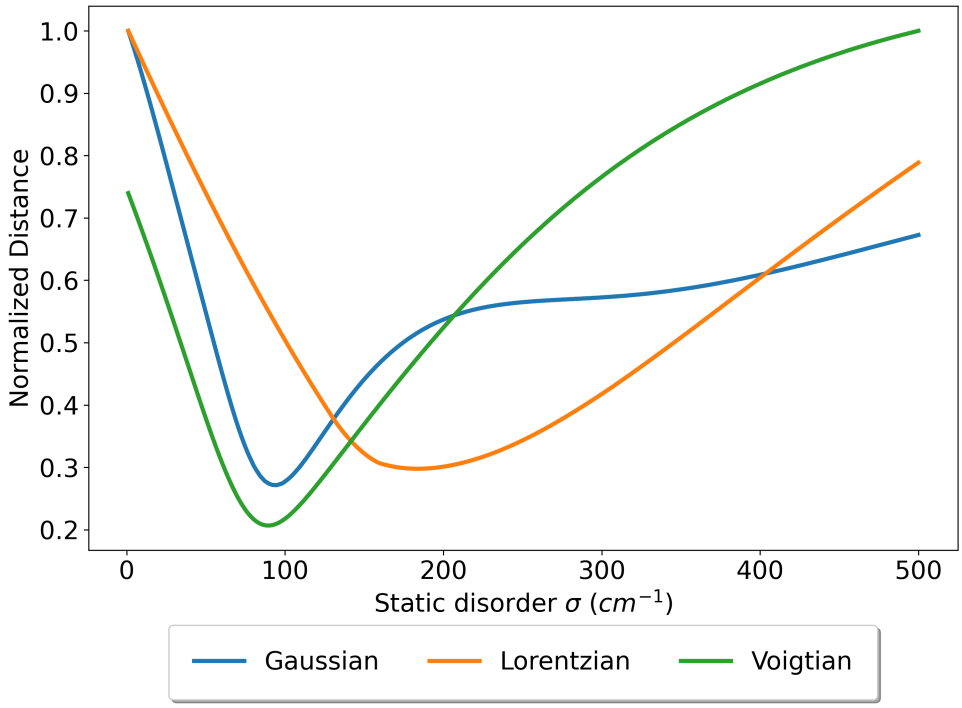

Figure C.37: Numerical optimization of σ. *Conditions:* experimental site energy (15198 cm^{-1}) and LC-BLYP diabatic excitonic coupling.

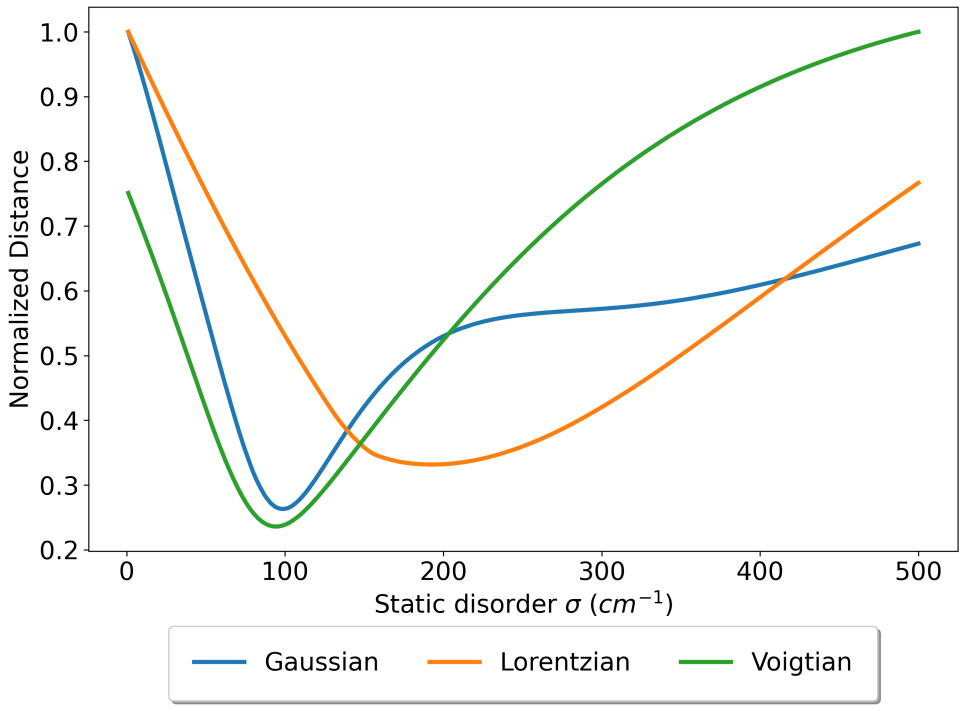

Figure C.38: Numerical optimization of σ. *Conditions:* experimental site energy (15198 cm^{-1}) and ωB97X-V diabatic excitonic coupling.

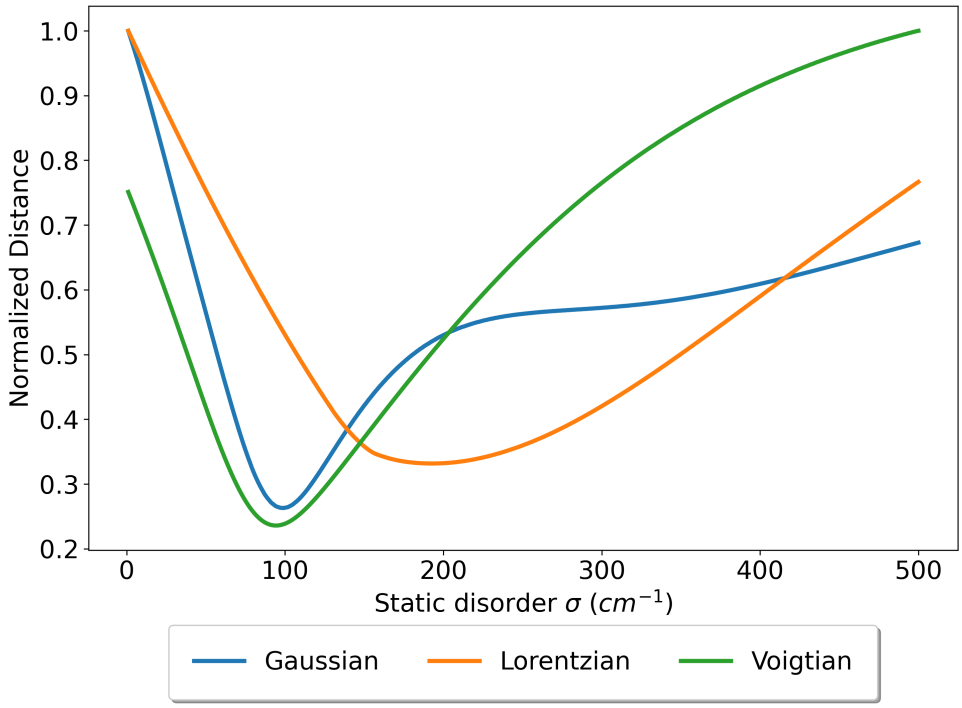

Figure C.39: Numerical optimization of σ. *Conditions:* experimental site energy (15198 cm^{-1}) and ωB97X-D3BJ diabatic excitonic coupling.

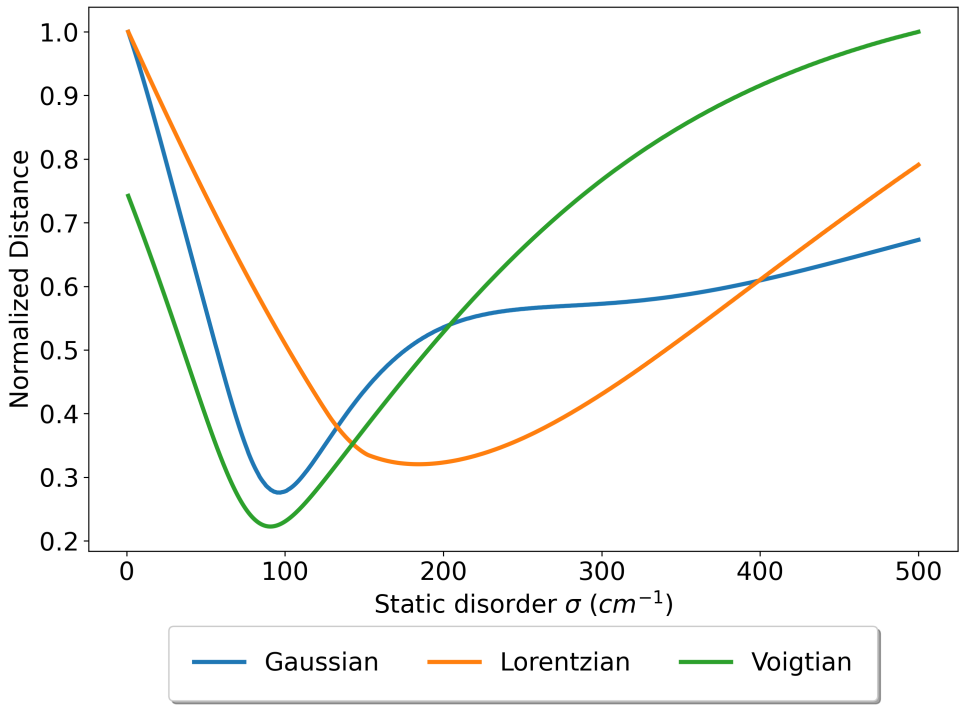

Figure C.40: Numerical optimization of σ. *Conditions:* experimental site energy (15198 cm^{-1}) and CAM-B3LYP diabatic excitonic coupling.

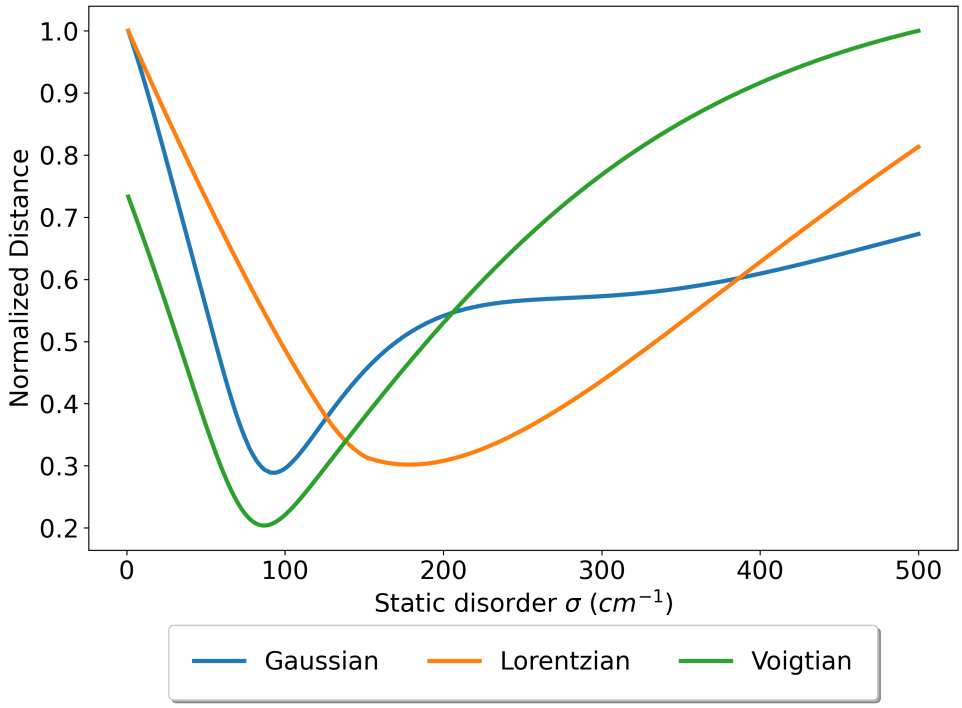

Figure C.41: Numerical optimization of σ. *Conditions:* experimental site energy (15198 cm^{-1}) and CAMh-B3LYP diabatic excitonic coupling.

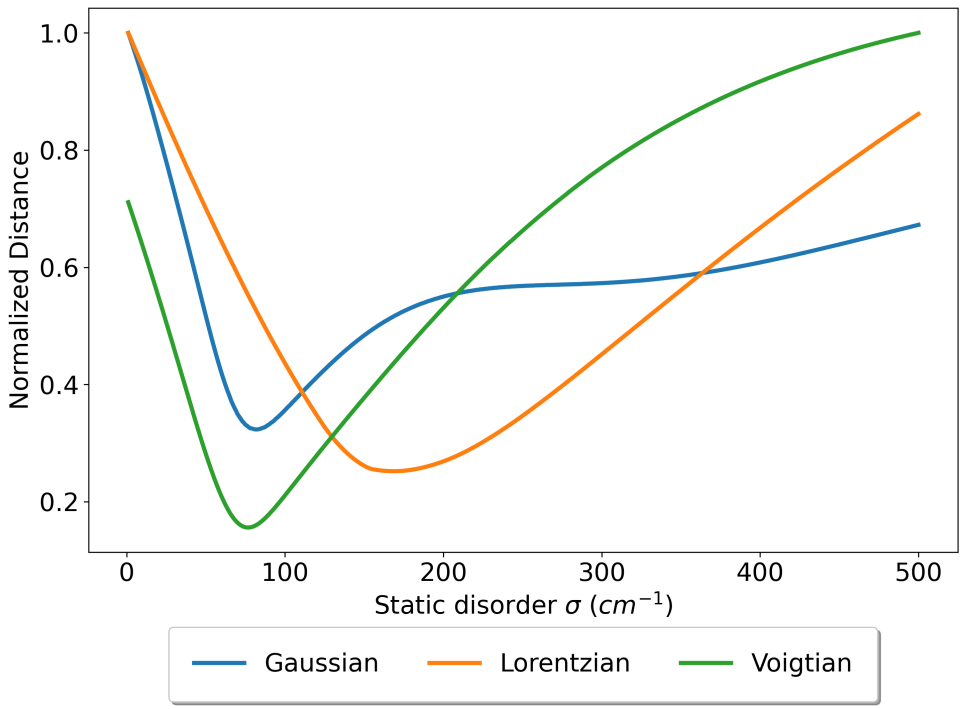

Figure C.42: Numerical optimization of σ. *Conditions:* experimental site energy (15198 cm^{-1}) and Tuned-CAM-B3LYP diabatic excitonic coupling.

C.2 Vibronic Spectra

C.2.1 HEOM spectra

Vibronic spectra was simulated using the HEOM method. This method is based on the extension of the Frenkel hamiltonian to a vibronic picture, using the excitonic spectral density to account for the exciton-vibrational couplings. This model takes as parameters the site energy, excitonic coupling, static disorder, and the opening angle between transition dipoles. In this case, all site energy have been shifted to match the highest peak with the experimental spectrum. The parameters used for the simulation are summarized in table C.1. For all simulations, σ was kept at 80 cm^{-1}.

Table C.1: Summary of parameters used in the HEOM simulation of absorption spectra. E_{calc} is the site energy as calculated by TD-DFT, E_{opt} is the optimized site energy, J is the excitonic coupling, and θ is the opening angle between transition dipoles.

Type	**Functional**	$\boldsymbol{E_{\text{calc}}}$ **(cm^{-1})**	$\boldsymbol{E_{\text{opt}}}$ **(cm^{-1})**	$\boldsymbol{J}$ **(cm^{-1})**	$\boldsymbol{\theta}$ **(°)**
meta-GGA	M06-L	15382	15887	81.8	68.7
	TPSS	15016	15909	60.4	76.6
Global Hybrid	BHHLYP	15931	15836	148.8	57.0
	B3LYP	15731	15866	104.8	66.5
	O3LYP	15469	15884	88.5	70.9
	PBE0	15956	15857	118.1	65.6
metaH-GGA	M06-2X	15846	15846	131.4	62.3
	TPSSh	15591	15884	88.9	71.2
RS Hybrid	LC-BLYP	14771	15846	131.1	60.0
	ωB97X-V	15054	15841	139.5	58.2
	ωB97X-D3BJ	15054	15841	139.5	58.2
	CAM-B3LYP	15556	15844	135.6	60.8
	CAMh-B3LYP	15919	15849	129.8	62.1
	Tuned-CAM-B3LYP	14998	15862	112.3	67.1

The simulated spectra are shown in the following.

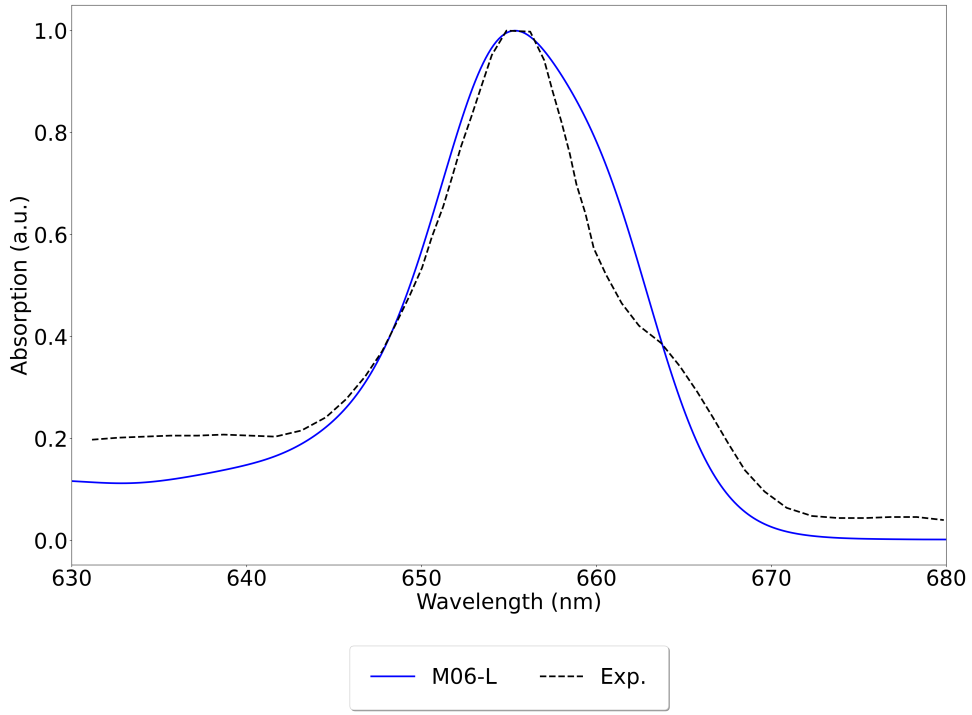

Figure C.43: Linear absorption spectra simulated by the HEOM method. *Conditions:* site energy shifted and M06-L diabatic excitonic coupling.

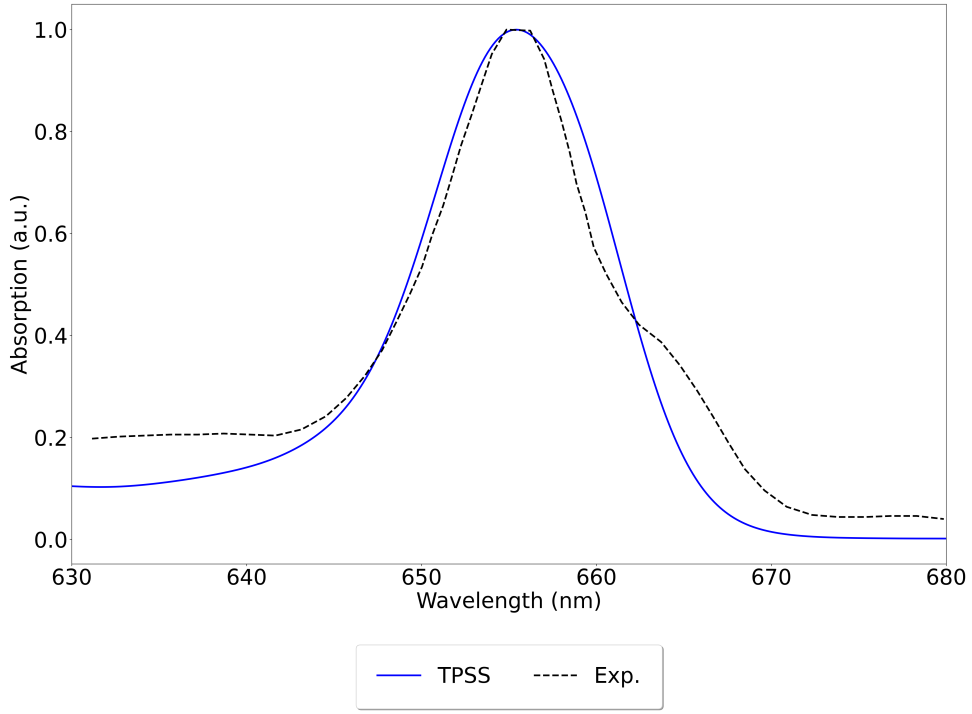

Figure C.44: Linear absorption spectra simulated by the HEOM method. *Conditions:* site energy shifted and TPSS diabatic excitonic coupling.

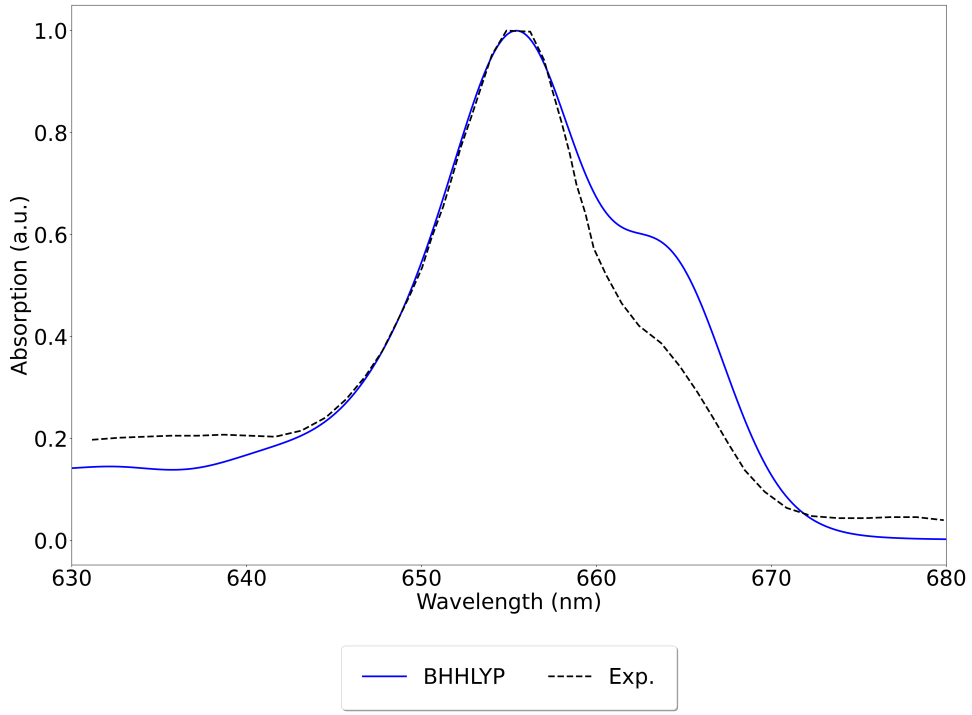

Figure C.45: Linear absorption spectra simulated by the HEOM method. *Conditions:* site energy shifted and BHHLYP diabatic excitonic coupling.

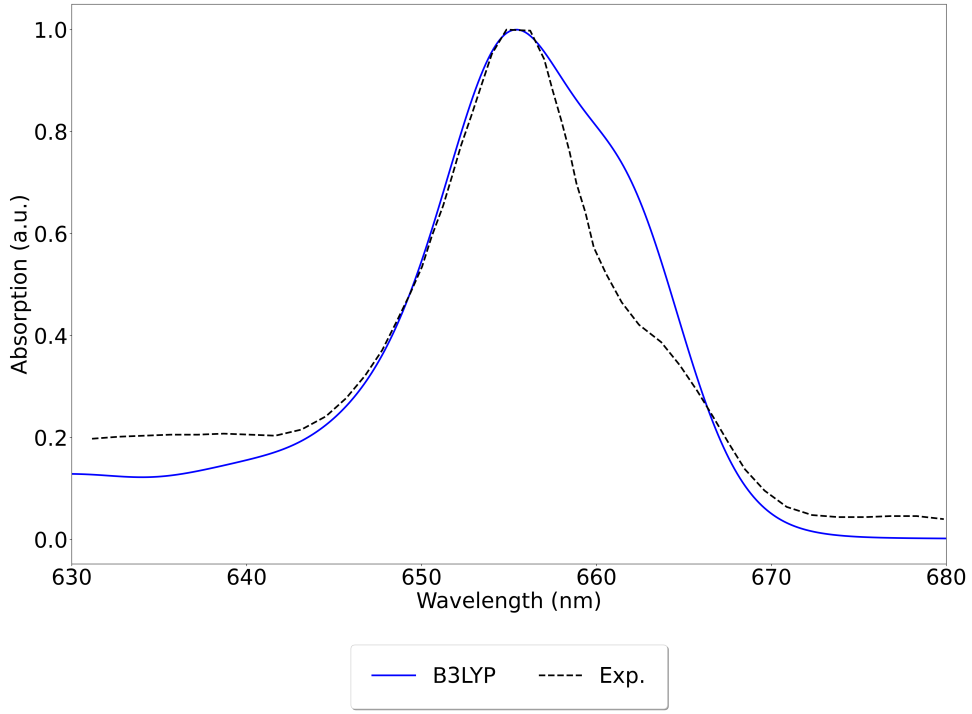

Figure C.46: Linear absorption spectra simulated by the HEOM method. *Conditions:* site energy shifted and B3LYP diabatic excitonic coupling.

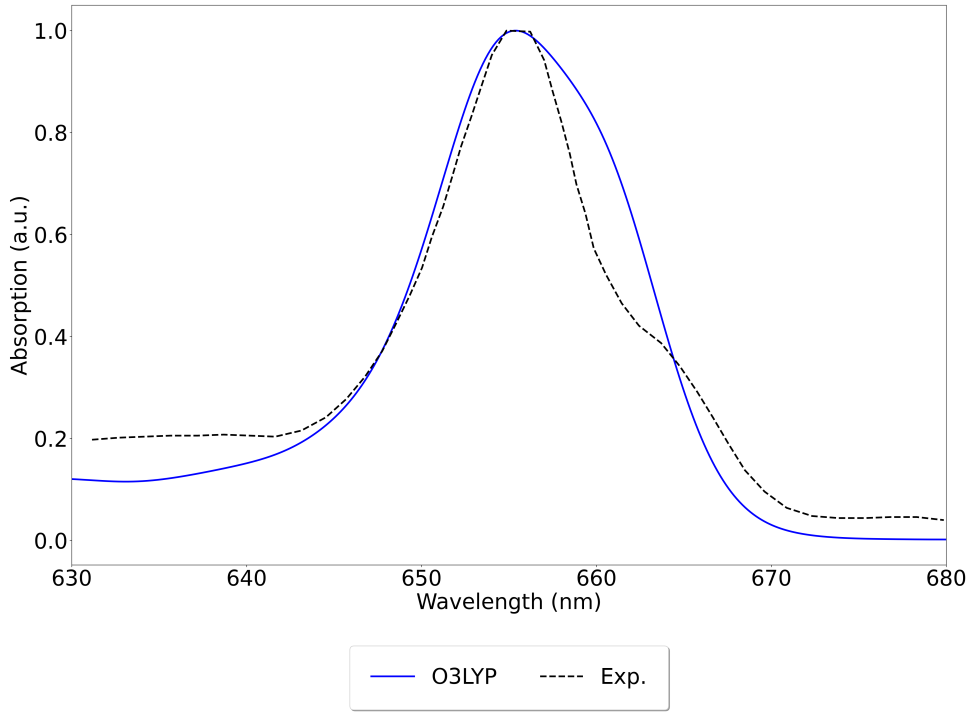

Figure C.47: Linear absorption spectra simulated by the HEOM method. *Conditions:* site energy shifted and O3LYP diabatic excitonic coupling.

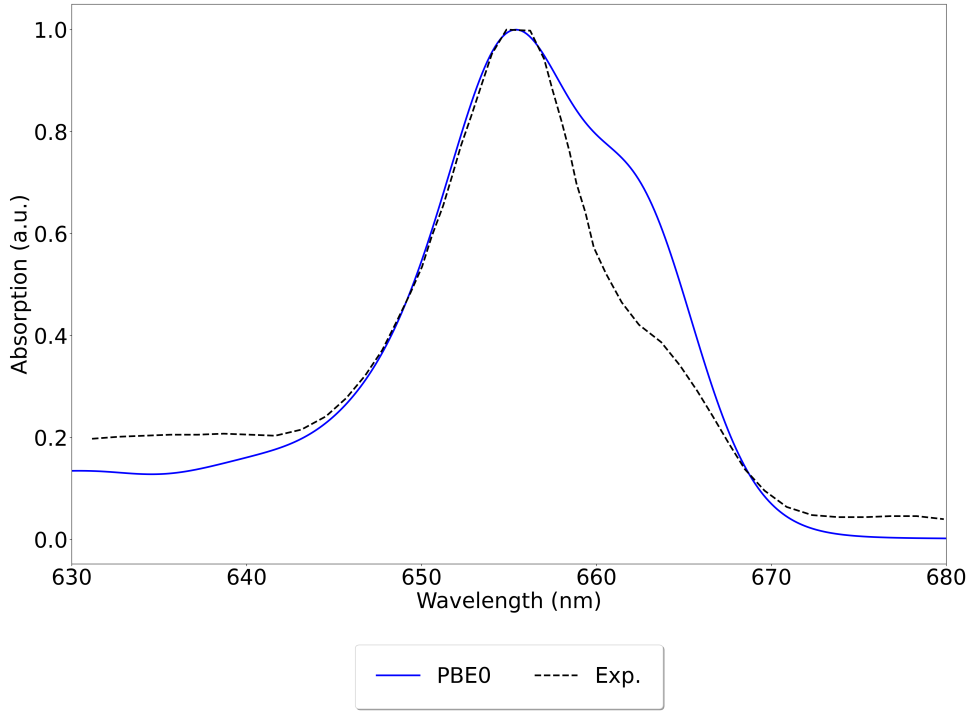

Figure C.48: Linear absorption spectra simulated by the HEOM method. *Conditions:* site energy shifted and PBE0 diabatic excitonic coupling.

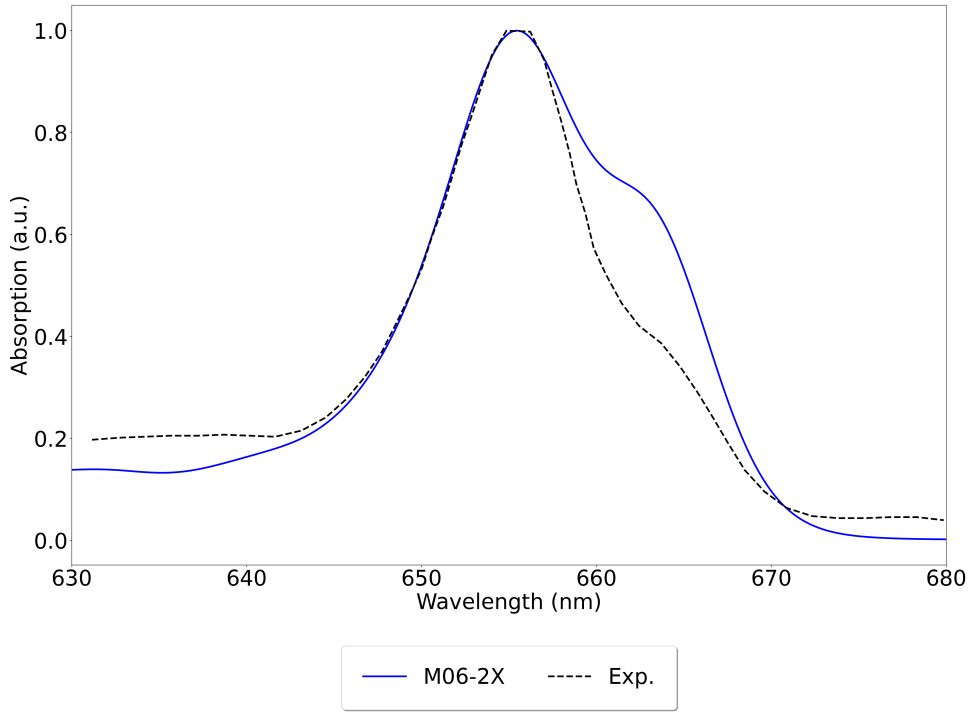

Figure C.49: Linear absorption spectra simulated by the HEOM method. *Conditions:* site energy shifted and M06-2X diabatic excitonic coupling.

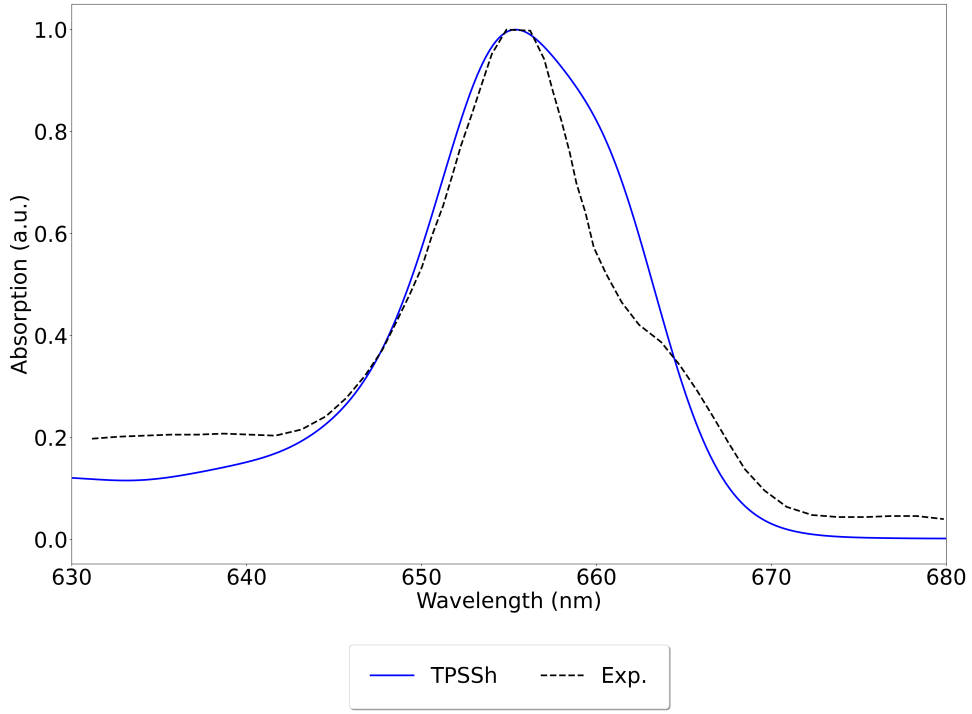

Figure C.50: Linear absorption spectra simulated by the HEOM method. *Conditions:* site energy shifted and TPSSh diabatic excitonic coupling.

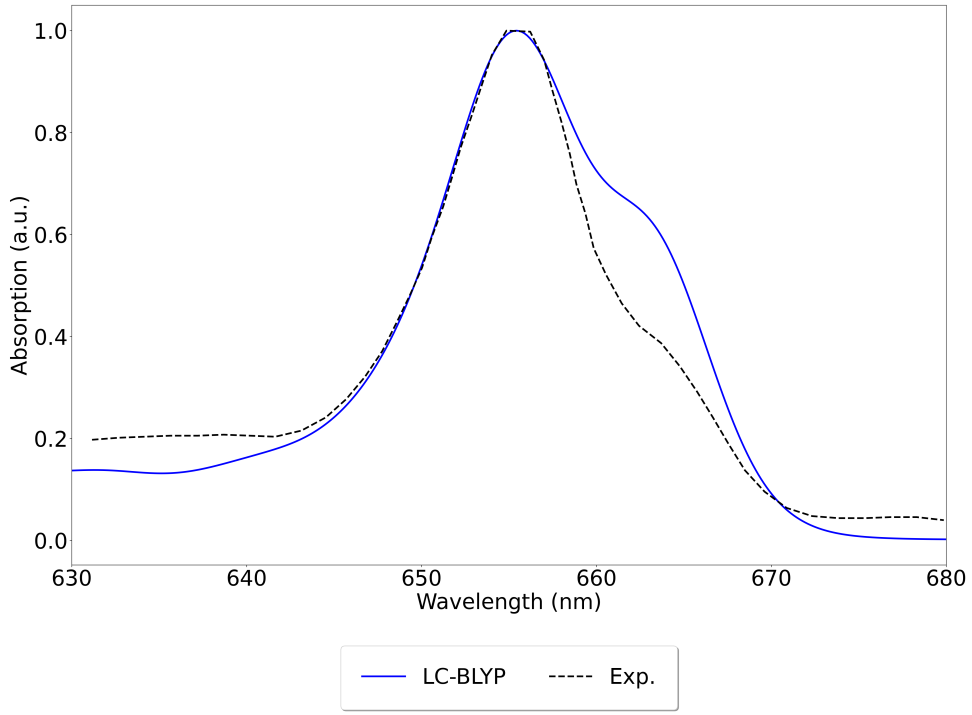

Figure C.51: Linear absorption spectra simulated by the HEOM method. *Conditions:* site energy shifted and LC-BLYP diabatic excitonic coupling.

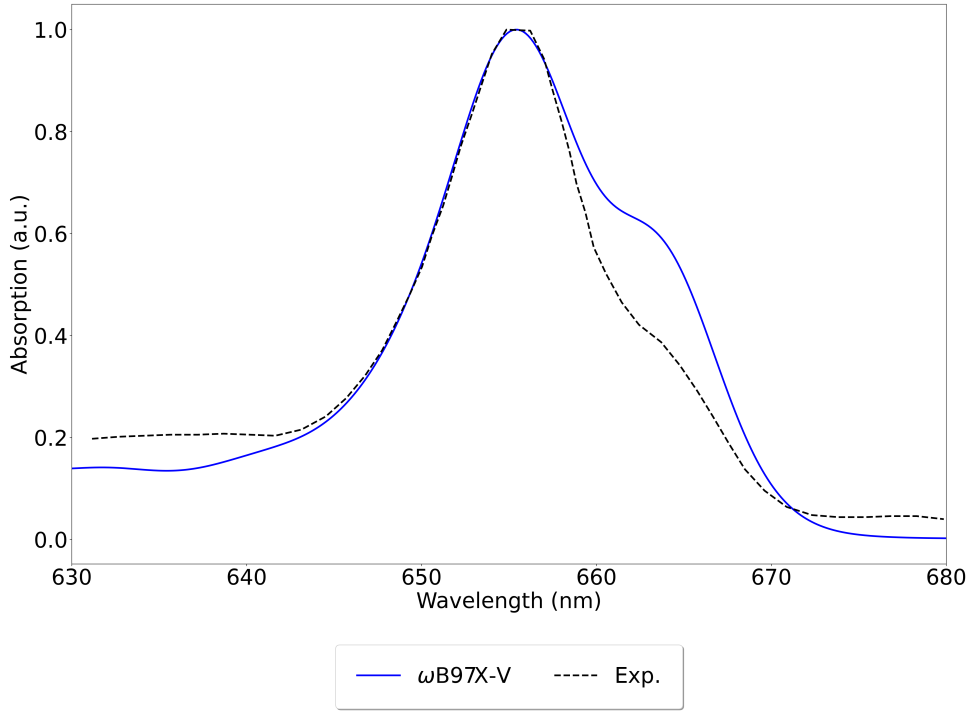

Figure C.52: Linear absorption spectra simulated by the HEOM method. *Conditions:* site energy shifted and ωB97X-V diabatic excitonic coupling.

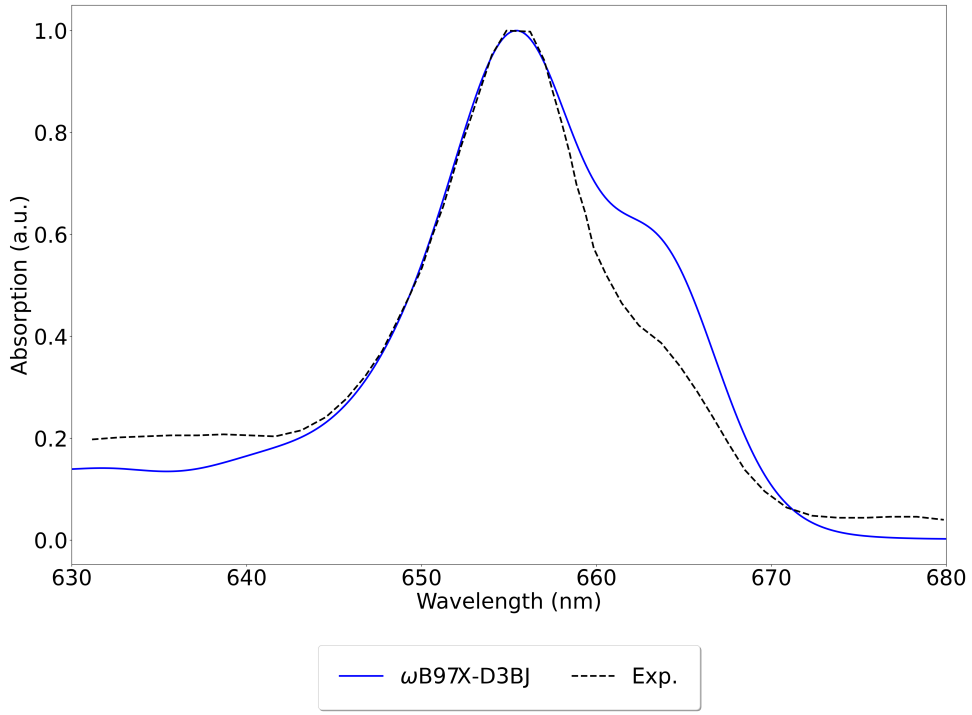

Figure C.53: Linear absorption spectra simulated by the HEOM method. *Conditions:* site energy shifted and ωB97X-D3BJ diabatic excitonic coupling.

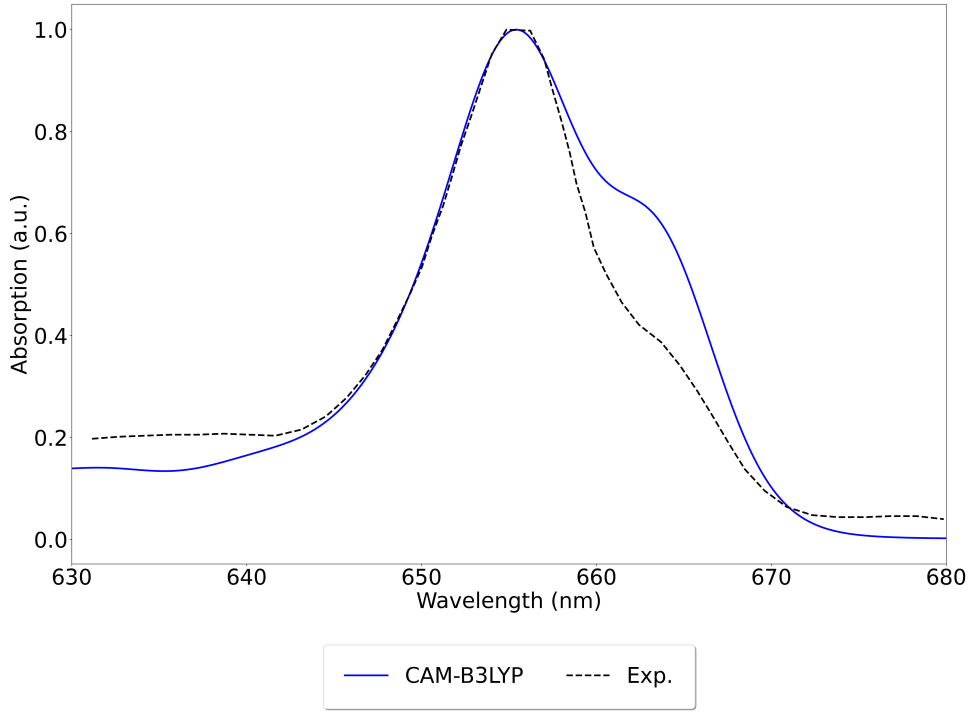

Figure C.54: Linear absorption spectra simulated by the HEOM method. *Conditions:* site energy shifted and CAM-B3LYP diabatic excitonic coupling.

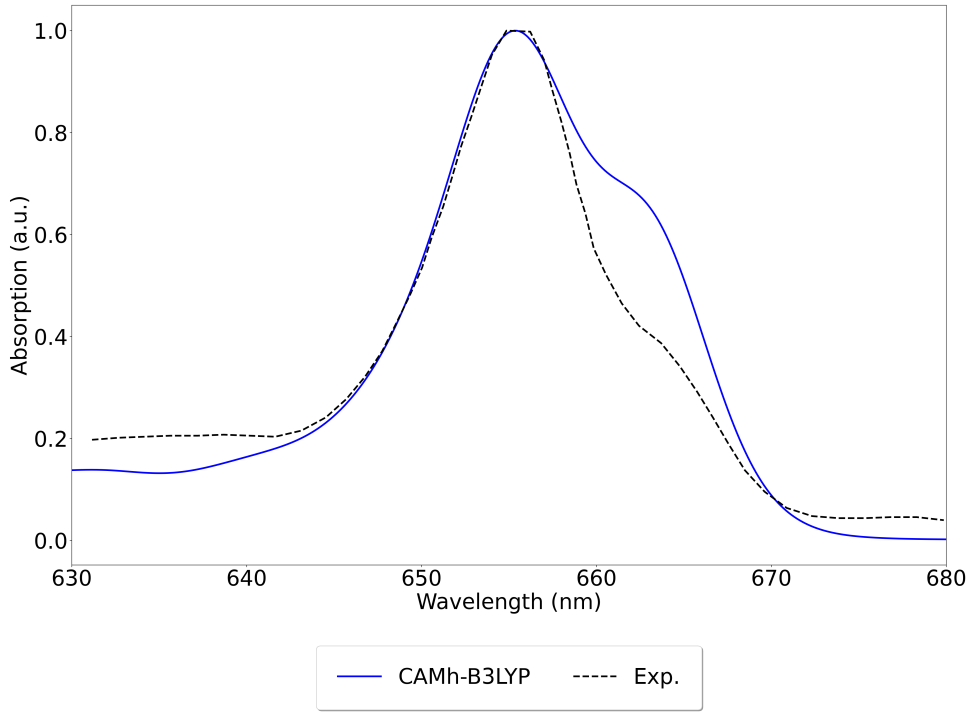

Figure C.55: Linear absorption spectra simulated by the HEOM method. *Conditions:* site energy shifted and CAMh-B3LYP diabatic excitonic coupling.

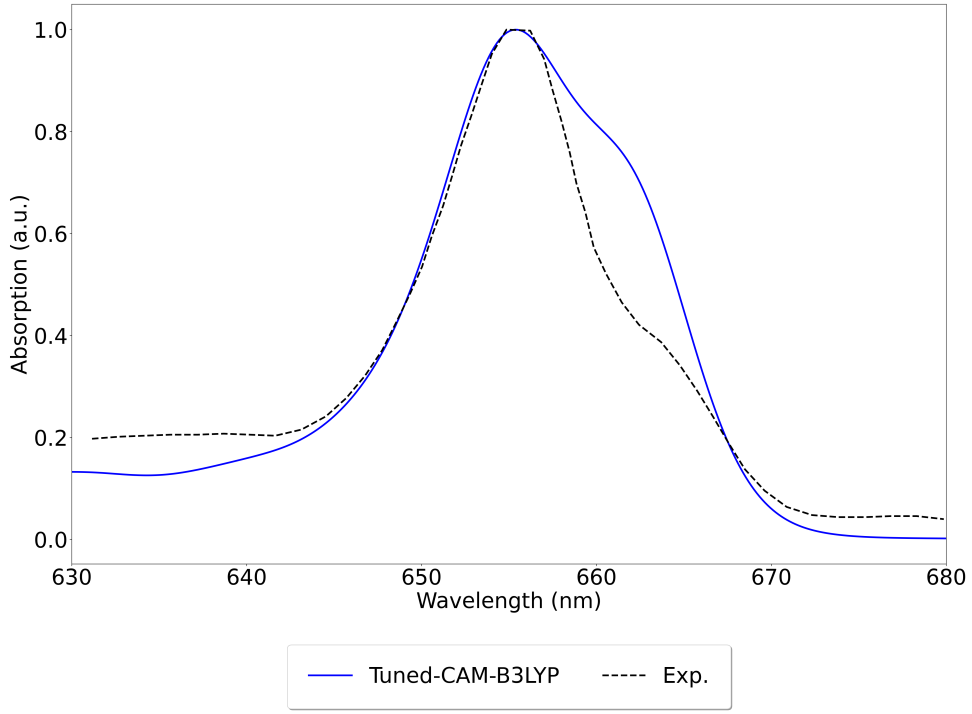

Figure C.56: Linear absorption spectra simulated by the HEOM method. *Conditions:* site energy shifted and Tuned-CAM-B3LYP diabatic excitonic coupling.

C.2.2 Deconvolution of HEOM spectra

Deconvolution of the HEOM spectra is shown, along with their fitting parameters, according to the scheme described in section 3.1.3.2 of the Main Text. In this case, all site energies have been shifted to match the highest peak with the experimental spectrum. The parameters used for the simulation are summarized in table C.1. For all HEOM simulations, σ was kept at 80 cm^{-1}. The curve-fitting was made using the least-squares procedure.

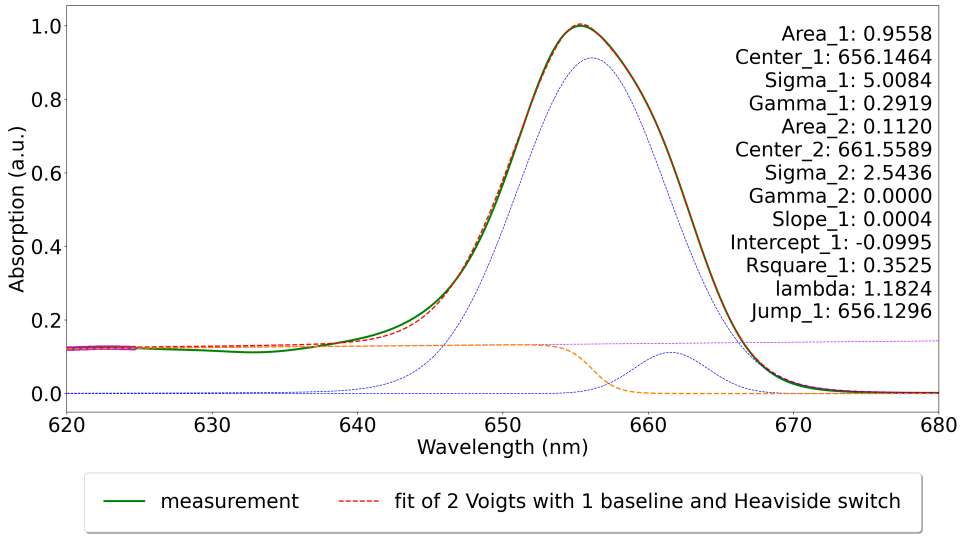

Figure C.57: Deconvolution of the linear absorption spectra simulated by the HEOM method. *Conditions:* site energy shifted and M06-L diabatic excitonic coupling.

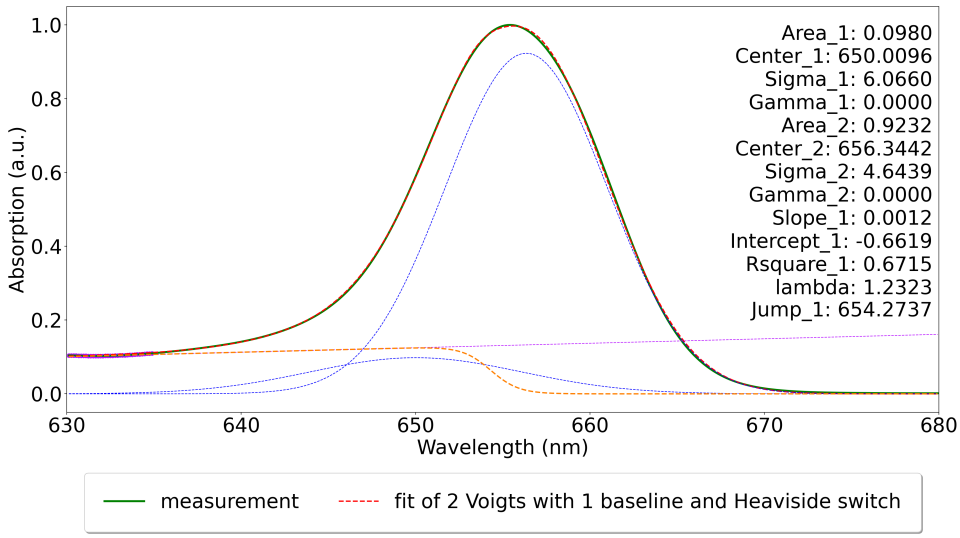

Figure C.58: Deconvolution of the linear absorption spectra simulated by the HEOM method. *Conditions:* site energy shifted and TPSS diabatic excitonic coupling.

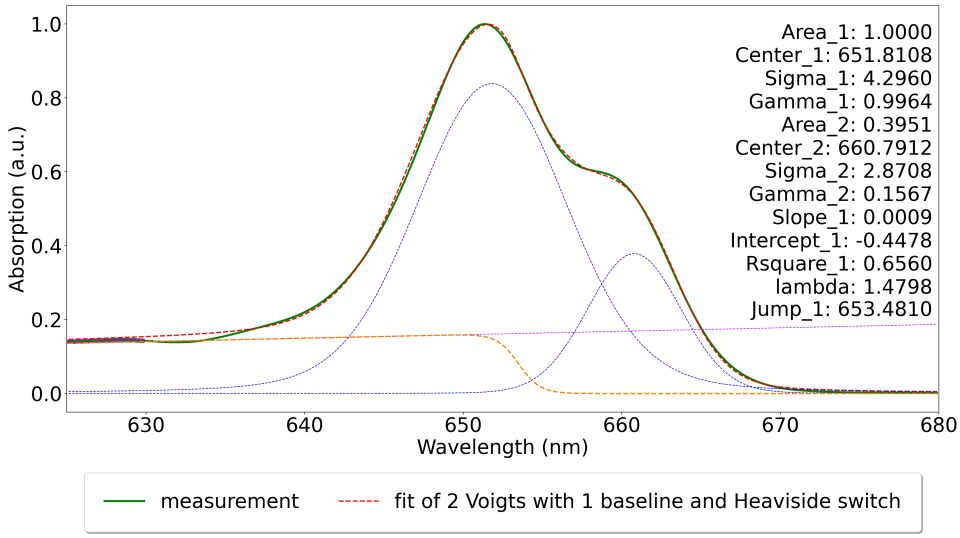

Figure C.59: Deconvolution of the linear absorption spectra simulated by the HEOM method. *Conditions:* site energy shifted and BHHLYP diabatic excitonic coupling.

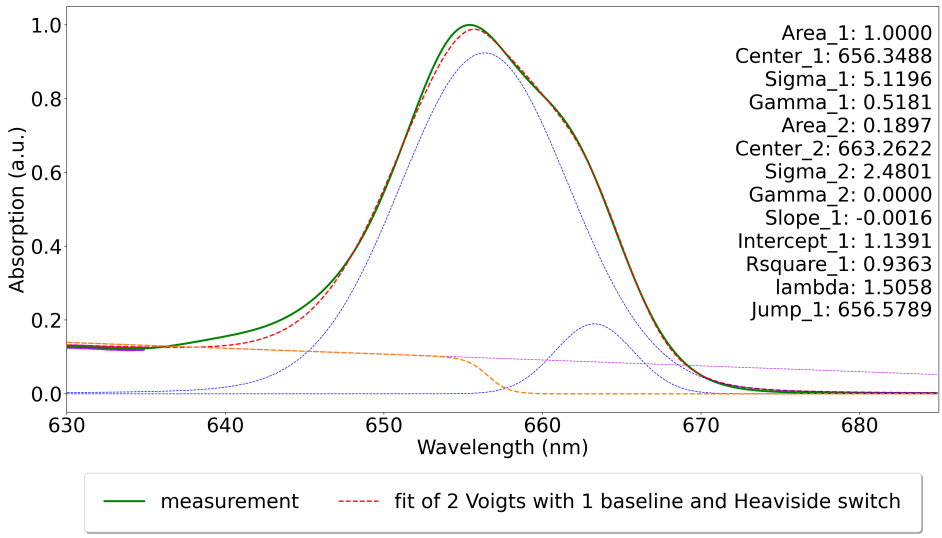

Figure C.60: Deconvolution of the linear absorption spectra simulated by the HEOM method. *Conditions:* site energy shifted and B3LYP diabatic excitonic coupling.

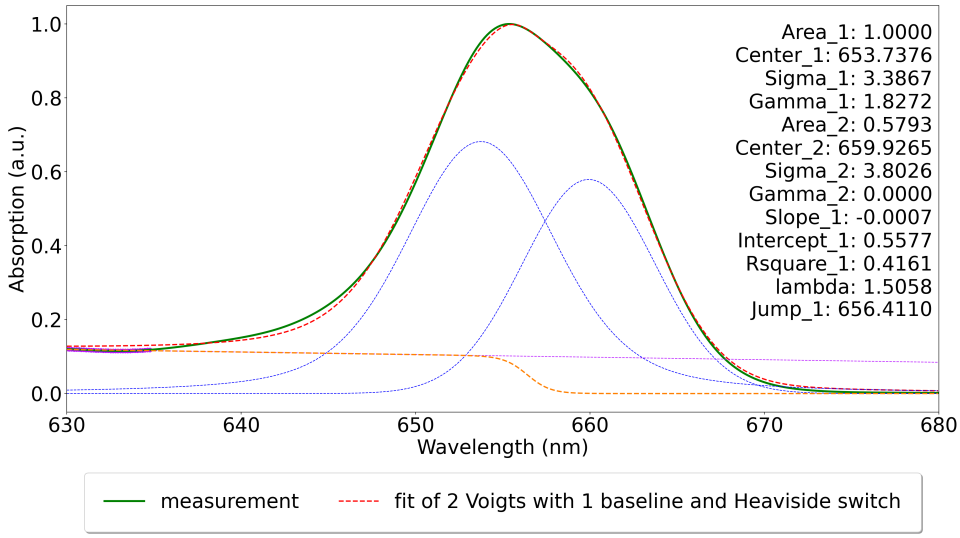

Figure C.61: Deconvolution of the linear absorption spectra simulated by the HEOM method. *Conditions:* site energy shifted and O3LYP diabatic excitonic coupling.

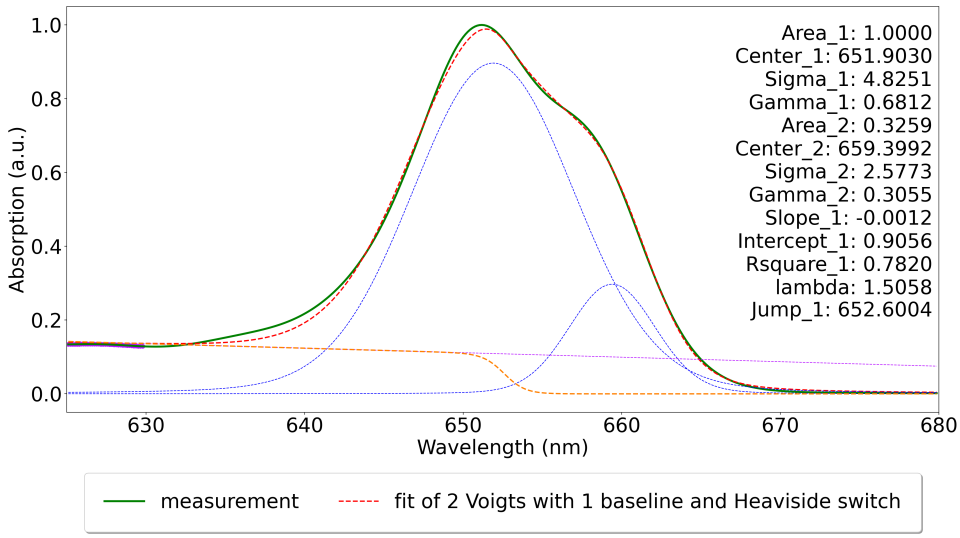

Figure C.62: Deconvolution of the linear absorption spectra simulated by the HEOM method. *Conditions:* site energy shifted and PBE0 diabatic excitonic coupling.

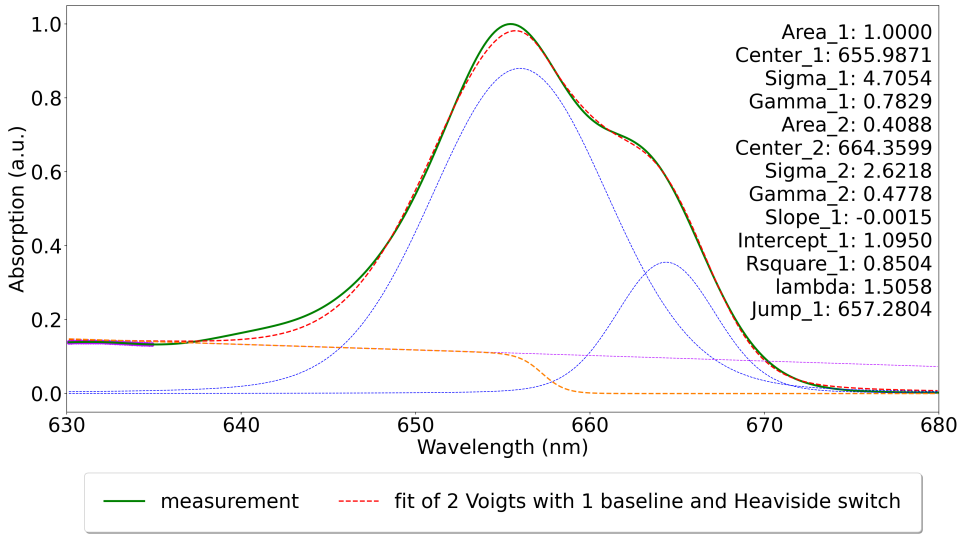

Figure C.63: Deconvolution of the linear absorption spectra simulated by the HEOM method. *Conditions:* site energy shifted and M06-2X diabatic excitonic coupling.

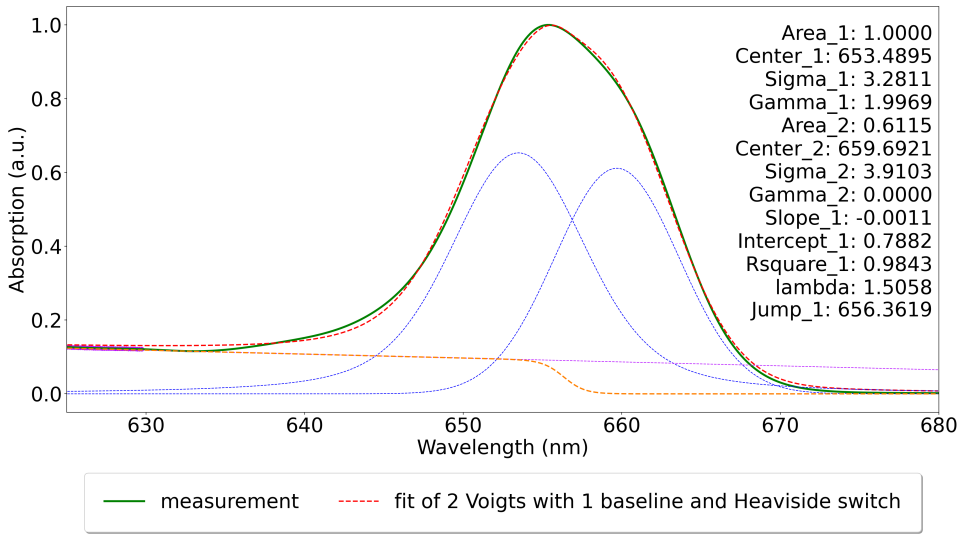

Figure C.64: Deconvolution of the linear absorption spectra simulated by the HEOM method. *Conditions:* site energy shifted and TPSSh diabatic excitonic coupling.

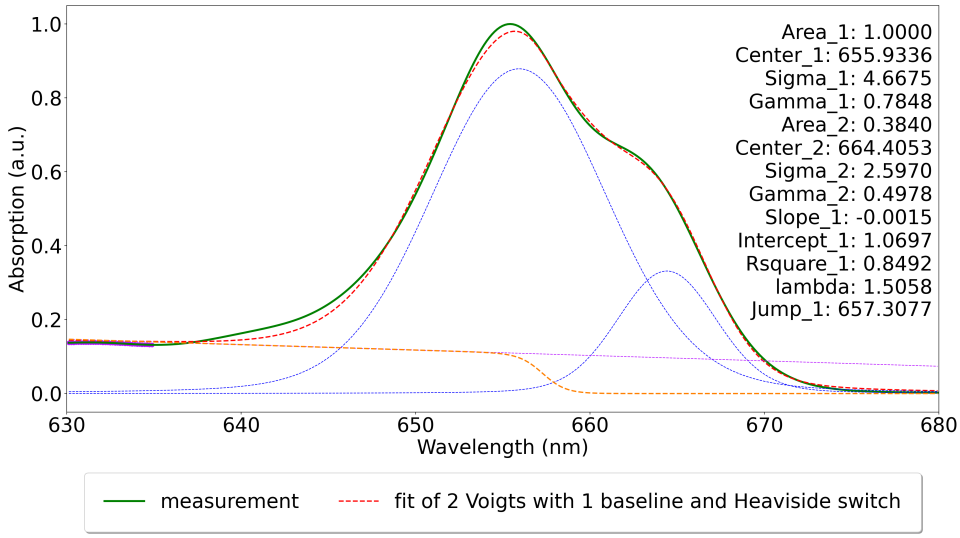

Figure C.65: Deconvolution of the linear absorption spectra simulated by the HEOM method. *Conditions:* site energy shifted and LC-BLYP diabatic excitonic coupling.

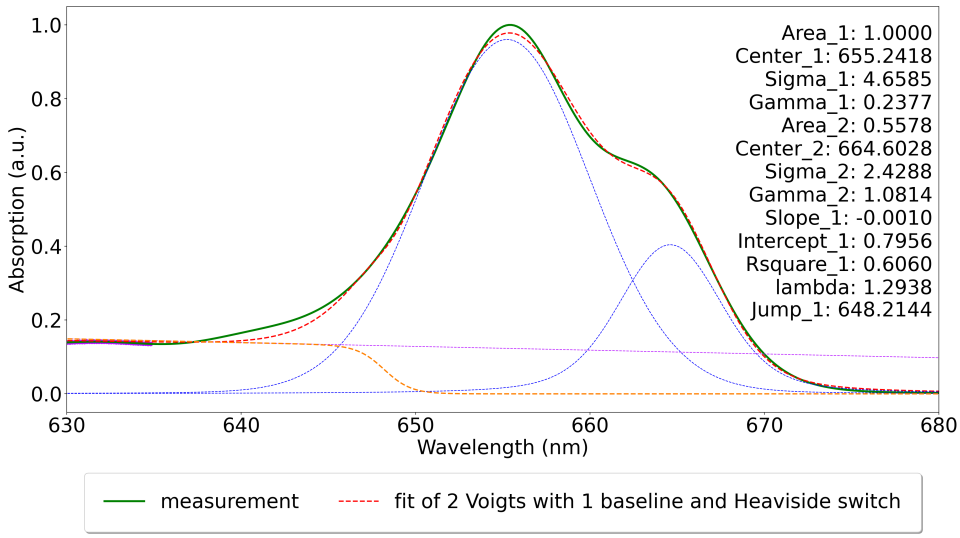

Figure C.66: Deconvolution of the linear absorption spectra simulated by the HEOM method. *Conditions:* site energy shifted and ωB97X-V diabatic excitonic coupling.

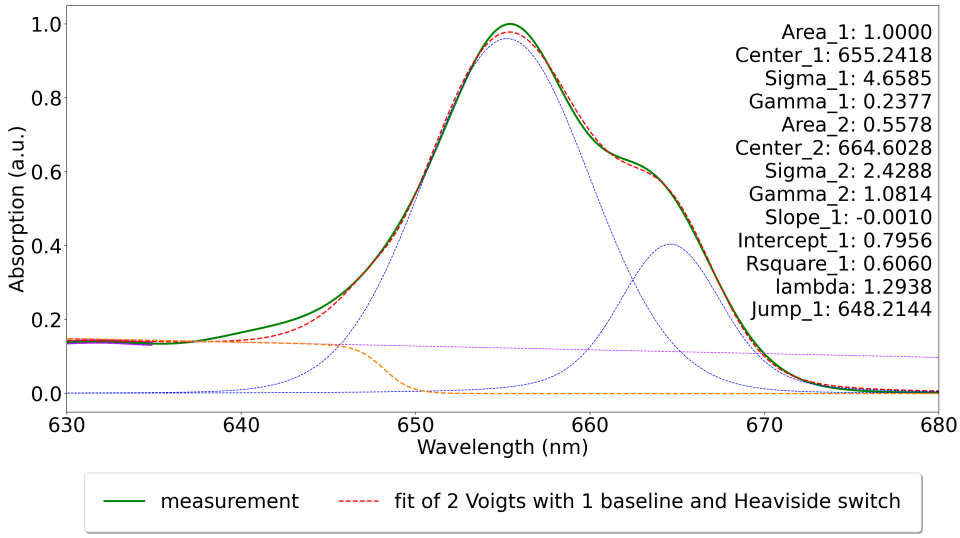

Figure C.67: Deconvolution of the linear absorption spectra simulated by the HEOM method. *Conditions:* site energy shifted and ωB97X-D3BJ diabatic excitonic coupling.

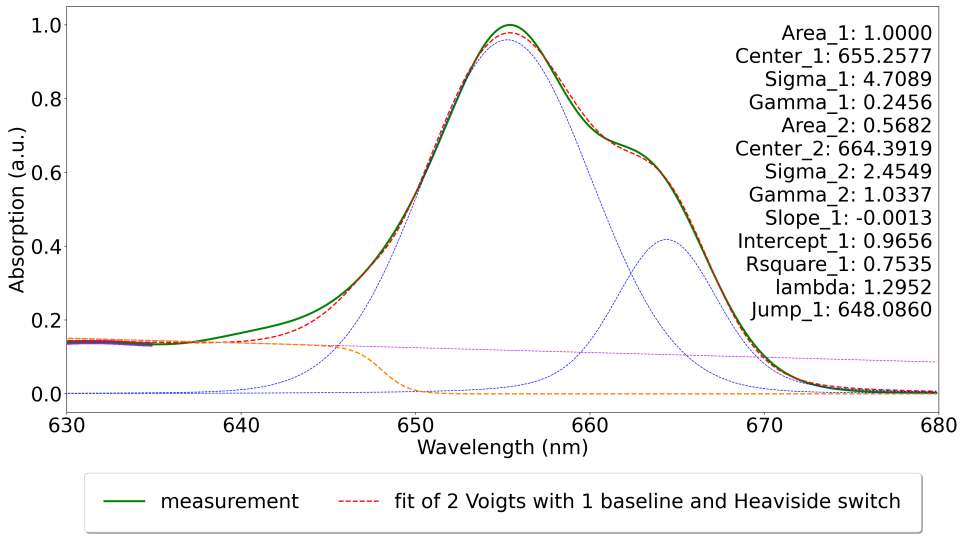

Figure C.68: Deconvolution of the linear absorption spectra simulated by the HEOM method. *Conditions:* site energy shifted and CAM-B3LYP diabatic excitonic coupling.

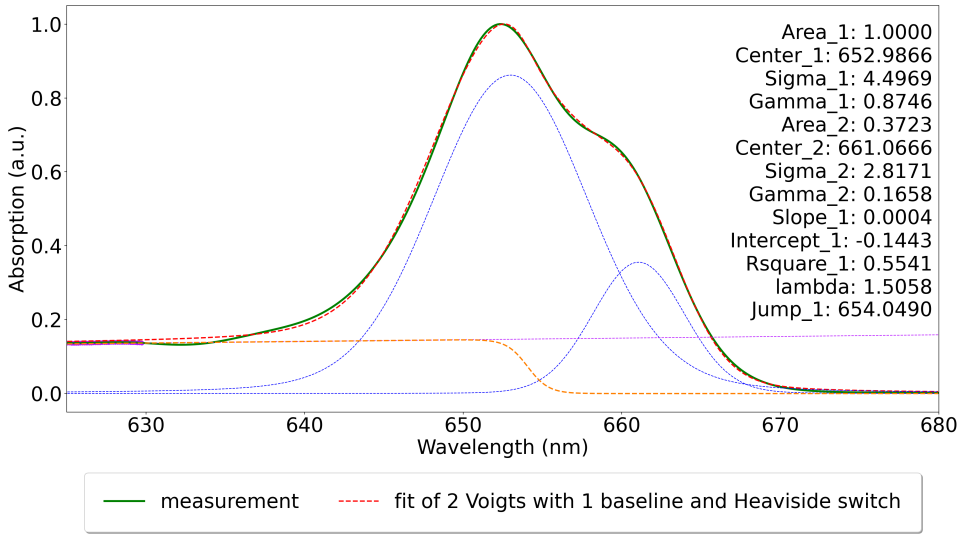

Figure C.69: Deconvolution of the linear absorption spectra simulated by the HEOM method. *Conditions:* site energy shifted and CAMh-B3LYP diabatic excitonic coupling.

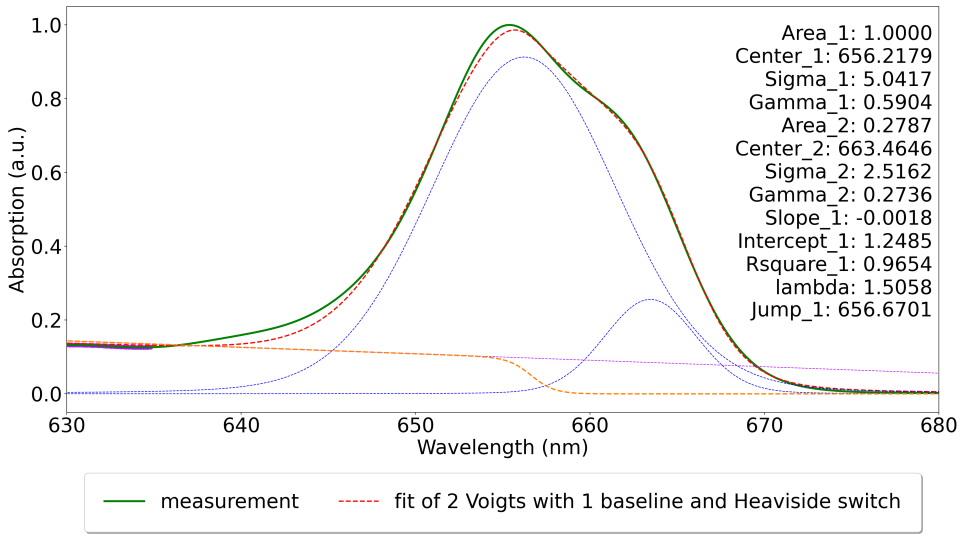

Figure C.70: Deconvolution of the linear absorption spectra simulated by the HEOM method. *Conditions:* site energy shifted and Tuned-CAM-B3LYP diabatic excitonic coupling.